KU LEUVEN

ARENBERG DOCTORAL SCHOOL
FACULTY OF ENGINEERING TECHNOLOGY

An intelligent experimental approach for the optimisation of the process parameters for the thermoforming of plastics and composites

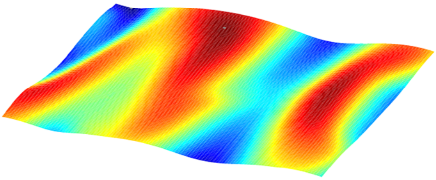

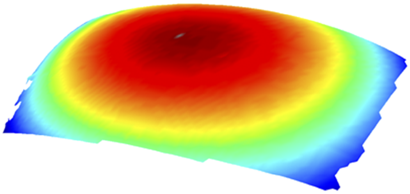

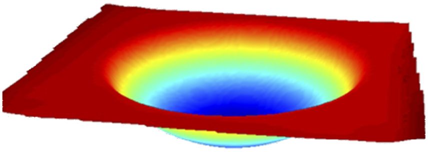

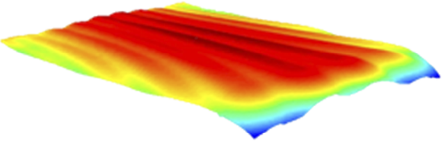

Bart VAN MIEGHEM

Supervisors:
Prof. Dr. ir. J. Ivens
Prof. Dr. ir. A. Van Bael

Dissertation presented in partial
fulfilment of the requirements for the
degree of PhD in Engineering Technology

October 2015

AN INTELLIGENT EXPERIMENTAL APPROACH FOR THE OPTIMISATION OF THE PROCESS PARAMETERS FOR THE THERMOFORMING OF PLASTICS AND COMPOSITES

Bart VAN MIEGHEM

Supervisors:
Prof. Dr. ir. J. Ivens
Prof. Dr. ir. A. Van Bael

Members of the Examination Committee:
Prof. Dr. ir. P. Hanselaer, chairman
Prof. Dr. ir. S. V. Lomov
Prof. Dr. ir. P. Van Puyvelde
Prof. Dr. ir. F. Desplentere
Prof. Dr. ir. W. Dewulf
ir. R. Hillaert (Samsonite)
Prof. Dr. ir. C. Bonten (University of Stuttgart)

Dissertation presented in
partial fulfilment of the
requirements for the
degree of PhD in
Engineering Technology

October 2015

Uitgegeven in eigen beheer, Bart Van Mieghem, Lummen

Voorwoord

Voor u ligt het eindresultaat van wat mij de afgelopen 4 jaar heeft kunnen passioneren. Zoals tijdens elke doctoraat zijn er menig up en downs geweest maar gelukkig hebben de ups de bovenhand gehaald, want anders had dit proefschrift er wellicht vandaag niet gelegen. Tijdens deze periode heb ik op de steun van een heel aantal mensen kunnen rekenen. Ik wil daarom van deze gelegenheid gebruik maken om iedereen te bedanken. Een aantal personen verdienen toch een extra vermelding.

In eerste instantie wil ik mijn promotoren Prof. Dr. ir. Jan Ivens en Prof. Dr. ir. Albert Van Bael bedanken voor de kans die ze mij hebben geboden om dit doctoraat te kunnen uitvoeren. Daarnaast wil ik hen ook bedanken voor hun ondersteuning, wetenschappelijke input en de constructieve (lunch)meetings. Mijn dank gaat ook uit naar de leden van mijn begeleidingscommissie: Prof. Dr. ir. S. V. Lomov, Prof. Dr. ir. P. Van Puyvelde, Prof. Dr. ir. F. Desplentere en ir. R. Hillaert voor hun kritische blik op mijn werk. Ook de bijkomende leden van de examencommissie, Prof. Dr. ir. W. Dewulf, Prof. Dr. ir. C. Bonten en Prof. Dr. ir. P. Hanselaer, zou ik willen bedanken voor de tijd die ze hebben genomen voor de evaluatie van mijn proefschrift.

Daarnaast mag ik ook de collega's van Cel Kunststoffen niet vergeten te bedanken voor de fijne tijd die we samen hebben doorgebracht, zowel tijdens als na het werk. Gert-Jan, Jan, Jozefien, Koen, Ludo, Maarten, Martijn, Raf, Sofie en Yves, bedankt! Onze tijd samen vormt een belangrijk stuk uit mijn leven en zal nooit vergeten worden. De vele kebabs die mij meer dan eens namiddag dipjes hebben opgeleverd trouwens ook niet.

Gedurende het doctoraat heb ik ook ondersteuning gekregen van mensen uit verscheidene onderzoeksgroepen. Vooreerst zou ik Pascal Lava van de technologiecampus Gent willen bedanken voor het gebruik van MatchID en de uitgebreide ondersteuning op gebied van digitale beeldcorrelatie. Ook Bart en Marijke, van de onderzoeksgroep Propolis van technologiecampus Oostende, zou ik willen bedanken voor hun ondersteuning op vlak van simulaties en thermische berekeningen. Daarnaast wil ik ook iedereen van de composieten groep van het departement MTM bedanken.

Ook mijn vrienden, ex-Helvoet collega's en mede-sommelier cursisten wil ik bedanken om ervoor te zorgen dat het werk toch af en toe naar de achtergrond verdween. Dat daar zo nu en dan wat alcohol aan te pas kwam heeft daar zeker niets mee te maken.

Tot slot richt ik nog een woordje van dank tot mijn familie.
Mama, papa, bedankt om mij te steunen en de kans te hebben gegeven om uit te groeien tot de persoon die ik vandaag ben. Tim (bro), jouw uitzonderlijke bijdrage aan het wetenschappelijk onderzoek valt niet te evenaren maar is zeker een drijfveer geweest om deze uitdaging ten volle aan te gaan.
Liesbeth, mijn prinsesje, bedankt voor alle steun die ik van jou heb gekregen tijdens mijn doctoraat en er hier en daar een vrouwelijke touch aan te geven. Je gedrevenheid en doorzettingsvermogen op sportief vlak hebben mij ook met periodes energie en inspiratie gegeven. Bedankt om te begrijpen dat mijn werk soms voorrang moest krijgen. En vooral bedankt om mij tijdens mijn doctoraat drie schatten van kinderen te schenken. De combinatie gezin-werk zorgde op momenten wel voor een extra uitdaging voor ons alle twee, maar Lex, Lien en Sander hebben er voor gezorgd dat de afgelopen 4 jaar een unieke periode werd.

Voorlopig gaat mijn avontuur aan de KU Leuven nog eventjes verder, dus de meerderheid van bovenstaande mensen verdwijnen niet uit het zicht en dus zeker ook niet uit het hart.

Strive not to be a success, but rather to be of value – Albert Einstein

Bart, oktober 2015

Abstract

Commercial thermoforming as known today began about 75 years ago. Unlike other major thermoplastic production processes such as injection moulding and extrusion that went through significant technological improvements, thermoforming on an industrial scale still remains a processing technique that is mainly based on operator experience and trial and error. The reason for this is mainly the lack of knowledge on the influence of process parameters and surrounding conditions on the material behaviour.

Insight in thin gauge thermoforming, a thermoforming variant for the processing of thin sheets and foils that is mainly applied in the packaging industry, has recently been improved by the introduction of in-mould monitoring systems. These systems allow for an in-situ measurement of among others: pressures, temperatures, positions and forming forces. In heavy gauge thermoforming however, such tools are not yet available. Typically, the quality of heavy gauge products is assessed on the basis of (manual) tactile, point by point thickness measurements in cross sections or parts of the final product. This makes it hard to define the relation between a specific process setting and the resulting thickness distribution, influenced by all (non-ideal) boundary conditions.

In this thesis, an experimental methodology to increase process insight in heavy gauge thermoforming is developed and validated using in-situ, full-field measurements of deformations, combined with pressure and temperature measurements. First, the specific details on how to apply the methodology in thermoforming applications are thoroughly elaborated. Next, it is demonstrated that the use of the methodology provides valuable insights in every step of the thermoforming process and that the proposed approach allows to define the process settings that are responsible for the quality of the final product. Besides this direct benefit, the approach can also be used to (i) identify specific thermoforming simulation parameters, (ii) establish the link between simulation and process parameters and (iii) facilitate the comparison of simulation results with results from production.

From an industrial point of view and with the increasing urge for automation it is clear that this enhanced insight into the process and the possibility to more accurately execute simulations can make heavy gauge thermoforming more stable, reduce start-up and cycle times and minimise the need for operator experience.

Samenvatting

Thermovormen zoals vandaag de dag gekend vindt zijn oorsprong ongeveer 75 jaar geleden. In tegenstelling tot andere belangrijke kunststofverwerkingstechnieken zoals spuitgieten en extrusie die door een significante technologische revolutie gingen, blijft thermovormen op industriële schaal nog steeds een verwerkingstechniek die gebaseerd is op de ervaring van de operator en *trial and error*. De voornaamste reden is het gebrek aan kennis over de invloed van proces parameters en randvoorwaarden op het gedrag van het materiaal.

Procesinzicht in *thin gauge* thermovormen, een variant voor de verwerking van dunne plaat en folies die voornamelijk wordt toegepast in de verpakkingsindustrie, werd recent verbeterd door de introductie van *in-mould* monitoring systemen die toelaten om in-situ metingen uit te voeren van onder andere drukken, temperatuur, posities en vormkrachten. Voor *heavy gauge* thermovormen werden dergelijke systemen echter nog niet ontwikkeld. De kwaliteit van *heavy gauge* producten wordt typisch beoordeeld op basis van (manuele) punt voor punt tactiele diktemetingen op doorsnedes of delen van het eindproduct. Deze manier van werken beperkt de mogelijkheden om relaties te leggen tussen een bepaalde procesinstelling en de resulterende dikteverdeling.

In deze thesis wordt een experimentele methodologie ontwikkeld en gevalideerd die gebruik maakt van full-field vervormingsmetingen, gecombineerd met druk- en temperatuurmetingen om het inzicht in *heavy gauge* thermovormen te verbeteren. Allereerst worden de richtlijnen om de methodologie toe te passen binnen thermovormapplicaties toegelicht. Nadien wordt gedemonstreerd dat deze methodologie voor waardevolle inzichten in elke stap van het thermovormproces kan zorgen en dat de procesinstellingen die verantwoordelijk zijn voor een goed eindproduct met deze aanpak bepaald kunnen worden. Naast dit rechtstreekse voordeel kan de methode ook gebruikt worden om (i) specifieke thermovorm simulatieparameters te bepalen, (ii) de link tussen simulatie- en proces parameters te vinden en (iii) de vergelijking tussen simulatieresultaten en productieresultaten te vereenvoudigen.

Uit industrieel oogpunt en met de toenemende tendens naar automatisatie is het duidelijk dat dit verbeterd inzicht in het proces en de mogelijkheid om accurater simulaties uit te kunnen voeren, het *heavy gauge* thermovormproces stabieler kan maken, de opstart- en cyclustijden kan verkorten en de nood aan operatorervaring kan minimaliseren.

Contents

List of symbols and abbreviations

Arabic symbols

Symbol	**Description**	**Unit**
a_k	Relaxation modulus	Pa
B_i	Biot number	-
c	Speed of light	m/s
C	Correlation criterion	-
C^{-1} *or* V	Left Cauchy-Green strain tensor	-
C_1, C_2	Constants of the WLF model	-
C_p	Specific heat capacity	J/kgK
D_f	Far distance of acceptable sharpness	mm
D_n	Near distance of acceptable sharpness	mm
f	Focal length	mm
F	Deformation gradient tensor	-
H	Hyperfocal distance	mm
h	Convective heat transfer coefficient	W/m^2K
$h(I_1, I_2)$	Damping function depending on first and second strain invariants	-
h_c	Height of circle c	m
h_P	Planck's constant	J/s
I	Spectral radiance	W/m^2 sr μm
k	Thermal conductivity	W/m. K
k_B	Boltzmann's constant	J/K
L_c	Characteristic length	m
m_i	Mass of a layer i	kg
$m(t-t')$	Memory function	Pa
N_A	Aperture f-stop number	-
N	Number of relaxation modes	-
Q_{in}	Inflowing energy	J
Q_{netto}	Netto amount of energy	J
Q_{out}	Outgoing energy	J
R	Correlation coefficient	-

Symbol	**Description**	**Unit**
r_c	Radius of circle c	m
s	Distance from the lens to the target	mm
T	Temperature	°C or K
t	Time	s
T_{amb}	Ambient temperature	°C
t_f	Final thickness	mm
T_g	Glass transition temperature	°C
t_i	Initial thickness	mm
T_m	Melting temperature	°C
T_{ref}	Reference temperature	°C
x_n	x-coordinate of node n	m
z_n	z-coordinate of node n	m

Greek symbols

Symbol	**Description**	**Unit**
α, β	Constants from the damping function	-
δz	Difference in z-direction	m
δx	Difference in x-direction	m
ε_1	Maximum principal strain	-
ε_2	Minimum principal strain	-
ε^{lnEA}	Strain expressed in the logarithmic Euler-Almansi convention	-
ε_{xx}	Strain in x-direction	-
ε_{yy}	Strain in y-direction	-
ε_{zz}	Strain in z-direction	-
θ	Time increment	s
Θ_{t1}	Temperature at time t1	°C
Θ_{t2}	Temperature at time t2	°C
λ	Wavelength	m
λ	Extension	-
λ_k	Relaxation time	s
λ_{xx}	Extension in x-direction	-
μ	Coefficient of friction	-
ρ	Density	kg/m³
τ	Stress tensor	Pa

Abbreviations

Symbol	**Description**
ABS	Acrylonitrile butadiene styrene
AISI	American Iron and Steel Institute
ANSSD	Approximated normalised sum of squared differences
$CaCO_3$	Calcium carbonate
CC	Cross correlation
CCD	Charge-coupled device
CFL	Courant, Friedrichs, Lewy
CoC	Circle of confusion
DIC	Digital image correlation
DIN	Deutsches Institut für Normung
DMA	Dynamic mechanical analyser
DOF	Depth of field
DSC	Differential scanning calorimetry
EVOH	Ethylene vinyl alcohol
FEA	Finite element analysis
FOV	Field of view
GEA	Geometric element analysis
HDPE	High density polyethylene
HDT	Heat deflection temperature
HIPS	High-impact polystyrene
IHCP	Inverse heat conduction problem
IKT	Institut für Kunststofftechnik
ISO	International standards organisation
K-BKZ	Kaye – Bernstein, Kearsley, Zapas
LDPE	Low density polyethylene
NCC	Normalised cross correlation
NRC	National Research Council
NSSD	Normalised sum of squared distances
PA12	Polyamide 12
PC	Polycarbonate
PC/PBT	Polycarbonate/polybutylene terephthalate blend
PE	Polyethylene
PEI	Polyetherimide
PET	Polyethylene terephthalate
PLC	Programmable logic controller
PMMA	Polymethyl methacrylate

Symbol	**Description**
PP	Polypropylene
PPO	Polyphenylene oxide
PS	Polystyrene
PTFE	Polytetrafluorethylene
PVC	Polyvinylchloride
PVDC	Polyvinylidene chloride
SPIF	Single point incremental forming
SRS	Spatial resolution of strain
SS	Subset size
SSD	Sum of squared distances
ST	Step size
SW	Strain window
TFI	Thermoformability index
TiO_2	Titanium dioxide
TMC	Thermoforming material characterisation
VSG	Virtual strain gauge
WLF	Williams, Landel, Ferry
ZNCC	Zero-normalised cross correlation
ZNSSD	Zero-normalised sum of squared distances

List of figures

List of tables

Chapter 1 - Introduction

1.1 General introduction

The thermoforming process is the third most widely used polymer processing technique, preceded only by injection moulding and extrusion. The product range of thermoformed final products is mostly divided into two categories, depending on the thickness of the material and the application: thermoformed foils (thin gauge < ~1 mm) and thermoformed sheets (heavy gauge > ~1 mm). The former are mainly applied in the packaging industry whereas the latter can be found (i) in just about every sector where the order quantity is too small to be profitable through injection moulding, (ii) in applications where the size of the product is such that it physically cannot be made by injection moulding or (iii) in applications where the advantages of thermoforming can be exploited. Some of these advantages are the ease of changing colour, print or finishing almost on the level of individual parts or the possibility to use multi-layer polymer sheets in a single forming step. As in every commercial production technique, the aim is to deliver the highest possible output at acceptable quality and minimal cost. The way to achieve this is to operate as lean as possible and to optimise and stabilise the processes in order to reduce start-up reject rate and cycle time while avoiding downtime during production.

1.2 Problem statement and motivation

Since heavy gauge thermoformed products are often produced in relatively small batches with frequent product changes, a lot of time is required for the identification of the optimal process conditions. The setting of the process parameters is usually realised on the basis of a trial and error approach which is highly dependent on the experience and expertise of the thermoformer. The trial and error approach is adopted because of the limited degree of process insight and shortcomings of the available thermoforming simulation tools. This frequently results in long start-up phases with lots of waste, suboptimal production parameters, unstable processes, considerable downtimes and poor quality products which is actually the exact opposite of what one strives for.

Simulation software in thermoforming can be used for two purposes: in the design phase of a new product to evaluate the effect of design changes on the final thickness distribution and thus performance of the product, or in the production phase for virtual process optimisation. Unfortunately simulation software is hardly ever used for several reasons. Next to the lack of knowledge of the real material behaviour and the exact boundary conditions, there is no direct link between several simulation parameters and the actual machine/process parameters. Such link can only be established using additional in-situ measurements.

From an industrial point of view, there is a great need for enhanced insights into the forming process to become less operator dependent, reduce start-up and cycle times for new products and ensure a stable production quality. Besides for in-process optimisations, the use of realistic simulations is essential for the development phase of new products. The combined use of recent technological improvements such as high speed thermal cameras, advanced deformation measurement systems, novel methods for material characterisation and state of the art finite element software that is able to model all the boundary conditions and complex material behaviour, can fulfil these needs.

1.3 Objectives and approach

The aim of the doctoral study is to develop and validate a methodology to get enhanced process insight in heavy gauge sheet thermoforming (mostly vacuum forming). This insight should enable for the thermoformer to define the most optimal process settings in an accurate and unambiguous way. To achieve the aim, an experimental methodology has been developed and validated using in-situ, full-field measurements of deformations and temperatures, combined with pressure measurements of the inflation air in the lower cabinet of the thermoforming machine. It is demonstrated that this methodology provides valuable insights in every step of the thermoforming process, in particular the clamping, heating, forming and cooling stages. This approach allows to precisely define the process settings that are responsible for the quality (in particular, the wall thickness distribution) of the final product. The thermoformer can then focus on the appropriate parameters to optimise the process or to improve process robustness. Also, the effects of modified settings (for example the use of patterned heating instead of uniform heating) can be mapped in every step of the process. By measuring over the entire surface during the process and on the actual production machine, undesirable influences on the material deformation, such as the effect of a malfunctioning heating element or the influence of material processing history, can be detected and quantified.

The measurement setup can also be used to identify specific thermoforming simulation parameters or to establish the link between the simulation parameters and the process parameters. As an example: on a typical machine, the temperature setting of the sheet is based on percentage settings of the power of infrared heating elements whereas the simulation software needs the full-field sheet temperature, while temperature is usually only measured at one location in the centre of the sheet, or not measured at all. Finally, the developed methodology also facilitates the comparison between simulation results and the results from production.

1.4 Thesis outline

Chapter 2 describes the state of the art concerning experimental optimisation of thermoforming processes and thermoforming simulation.

In Chapter 3, a comprehensive description of the newly developed methodology combining deformation, temperature and pressure measurements is given. For the deformation measurement digital image correlation is used enabling not only to visualise the deformation but also to define the full-field thickness and thickness evolution during the process.

Chapter 4 elaborates on how to use digital image correlation in the context of thermoforming in an industrial environment and a solution is proposed for the difficulties that arise.

Chapter 5 focusses on the application of the methodology in experimental optimisation of the thermoforming process. The methodology is validated for the different steps of the thermoforming process, i.e. clamping, heating, inflation, forming and cooling, demonstrating how it contributes to the general process insight.

Chapter 6 explains how the measuring methodology can be used for simulation optimisation. An overview is given on how critical simulation parameters can be extracted from the process and used within dedicated thermoforming simulation software.

Conclusions are drawn in Chapter 7 and an overview of possible future implementations of the methodology in both industrial and academic environment is given.

Chapter 2 - State of the art in thermoforming

This chapter gives an overview of the current experimental and simulation state of the art within thermoforming. First, the fundamentals of thermoforming are briefly explained.

2.1 Thermoforming

Thermoplastic thermoforming is a generic name for a number of processes that involve the reshaping of a polymer sheet on or in a mould at elevated temperature. Most of the time these processes are vacuum or pressure assisted [1]. Thermoforming can be used for both unreinforced and (short) fibre reinforced thermoplastics. Reinforced plastics can be shaped using pressure forming or matched die forming, whereas unreinforced plastics can also be shaped by free forming, vacuum forming or drape forming (variant of vacuum forming for male/positive products). The latter three variants are considered in this research. Twin sheet forming, a thermoforming variant able to produce hollow products, completes this list as an advanced combination of two vacuum forming / drape forming processes.

Figure 1 shows the different steps of the vacuum/drape forming process. The sheet is first clamped at its perimeter and heated to a temperature range where it is easily deformable (1). For amorphous thermoplastics this is theoretically above the glass transition temperature (T_g), whereas semi-crystalline polymers tend to have a rather narrow processing window with an ideal forming temperature close to the melting temperature (T_m). The heating of the sheet is nowadays mainly done by infrared radiation generated by ceramic, halogen or quartz elements installed in an upper and/or lower heater bank. In current equipment, the temperature of the sheet is measured throughout the heating step with an infrared sensor at a location in the centre of the sheet on top and/or bottom. Older machines do not have these possibilities and control the temperature of the sheet by choosing either the temperature or the power of the heating elements for a predefined amount of time. During the heating step the sheet stiffness decreases and the sheet starts sagging due to gravity. This sagging can be counteracted by injecting pulsated compressed air underneath the sheet, a technique called sag compensation. Next, the sheet is transferred to the moulding area. In a cabinet type machine, where heating and forming are done in a single station, the heaters are moved backwards, away from the sheet (2a). For male (positive or drape formed) products, the sheet is then typically inflated to form a bubble in order to uniformly pre-stretch the sheet and to achieve a more homogenous thickness distribution (2b). The necessary pressure for this inflation is generated by a compressed air flow controlled by a, mostly manually set, throttling valve. Finally the sheet is stretched in (for female products) or on (for male products) a mould by means of a differential pressure (typically -50 to -95 kPa). Due to the heat exchange with the cold mould on one side and with the surrounding air - sometimes assisted by air fans or water mist - on the opposite side of the sheet, the sheet is cooled to a temperature where it retains the shape of the mould (3). Finally the formed part is unclamped and removed from the mould and the excess material is trimmed away (4).

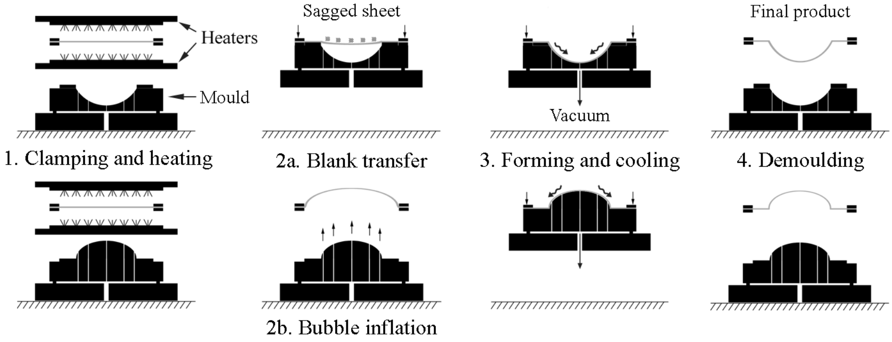

Figure 1 Thermoforming process steps; top: vacuum forming, bottom: drape forming

When considering the thickness of the initial sheet, a distinction can be made between heavy-gauge (thick sheet > ~1 mm) and light-gauge (thin sheet < ~1 mm) sheets. Typical light-gauge products are mass produced packaging for both food and technical products. Heavy-gauge products are typically made in smaller series and mostly used in transport and construction applications or in consumer goods. The homogeneity of the wall thickness (distribution) of the final product is generally taken as be the most critical parameter in the quality assessment of a product but, depending on the application, sometimes also optical appearance (transparency, gloss), resistance to compression and oxygen transmission rate, properties that are all closely related to the thickness distribution, are used.

Thermoforming has three major drawbacks compared to injection moulding. The first is the unavoidable variation in product thickness, which is an inherent characteristic of the shaping process. The second drawback is the necessity for cast or extruded sheets as the starting material instead of polymer pellets like it is the case in injection moulding. This pre-processing adds an additional cost to the final product, but also, especially for extruded sheets, this contributes to the processing history of the material and ultimately the sheet properties. More details on this phenomenon and the consequences are given in Section 5.2.2. The last drawback is the waste percentage created by trimming away the sheet area needed for the clamping. Fortunately most of this waste can be recycled.

2.2 Improvements of the thermoforming process through experiments

Although thermoforming has always been, and still is, a trial and error based technology, experimental efforts that have been done to bring the knowledge a step further are discussed in the first section. In the second section, some shortcomings of the experimental research so far are discussed.

2.2.1 Current state of the art

To make a clear overview of the experimental thermoforming improvements, a distinction is made between the experimental improvements on the polymer side and the improvements on the process side. The latter can be subdivided into: the study of the influence of the extrusion process, the influence of the heating method of the sheet and the influence of the forming process parameters on thermoformability. Before starting this overview, it is necessary to define what is meant by "thermoformability".

2.2.1.1 Thermoformability

Researchers have tried to characterise "thermoformability" of sheet materials in an unambiguous way both quantitatively and qualitatively. "Thermoformability" is a term that combines resistance to sag, ease of flow, adequate mould replication, deep draw capability, uniformity of thickness distribution after thermoforming, post-forming shrinkage and dimensional stability. It is common practice to test the thermoforming behaviour (and processing window) of a material by performing thermoforming trials on generic moulds such as cup-shapes or rectangular boxes. Nevertheless, some scientists have tried to couple intrinsic material characteristics to the thermoforming behaviour. Several researchers state that a (non-reinforced) material is considered to be thermoformable when it has a shear modulus of around 1 MPa [2, 3] and an elongational viscosity during stretching of 10^5-10^8 Pa.s [3-5]. Material exhibiting strain hardening behaviour is definitely in favour when one strives for a homogenous wall thickness distribution [5]. In 1991 Hylton [3] mentioned techniques such as uniaxial hot tensile tests, viscosity measurements and biaxial inflation techniques for the prediction of material "thermoformability". Next to the thermoforming trials, the rheological characterisations and Hylton's techniques that are still used extensively, other "thermoformability" definitions and material characterisation techniques have been explored. Table 1 gives a concise overview of some dedicated techniques that have been reported to be relevant for thermoforming. Some of them ([6-11]) are developed to define material parameters for thermoforming simulation (through reverse engineering) or (temperature) processing windows, but these techniques can, in the author's opinion, also be used to define the "thermoformability" of a material.

Term or technique	**Description**	**References**
Melt strength tester	The melt strength is measured with a Gottfert “Rheotens” melt strength tester and correlated to sagging resistance.	[12]
Thermoformability index (TFI)	The TFI is defined as the viscosity multiplied by the compliance (=creep recovery time) and is measured with a rheometer.	[13]
Bubble inflation / Bulging	Biaxial extension test by bulging of a circular-shaped specimen clamped at its perimeter.	[14-16]
Biaxial extension	Dedicated biaxial extension machine. Tensile tests performed at different speeds and temperatures.	[10, 11, 17]
Plug testing (Thermoforming material characterisation apparatus (TMC))	A sheet is clamped in an oven and plugging tests at different temperatures and speeds are performed.	[7, 9, 18, 19]
Small deformation rheological tests	Combination of dynamic mechanical tests (DMA) at different temperatures and frequencies covering the thermoforming range with creep (recovery) tests and sag measurements in a heat deflection temperature (HDT) device.	[6, 8, 20]

Table 1 Overview of terms and techniques to define thermoformability

In an industrial context however, all abovementioned techniques to characterise thermoformability are either too expensive for the typical heavy gauge thermoformers which are usually SME’s, require complex equipment or are not representative for the deformation that the material undergoes during thermoforming.

2.2.1.2 Experimental improvements of thermoforming polymers

As already mentioned in the previous section, it is obvious that not every material can be formed easily. Amorphous polymers are intrinsically easier to deform due to the absence of complex meltable crystalline phases and are hence the polymer type of choice in former studies. Some amorphous polymers can be stretched at forming temperature up to 10 times their initial length. Schmidt et al. [21] reported already in the 1970’s that for high-impact polystyrene (HIPS) (still one of the most used materials in thin gauge thermoforming) polar extension ratios up to 11 are achievable during inflation tests. The authors also reported that other amorphous materials such as polycarbonate (PC) and polymethyl methacrylate (PMMA) for instance cannot be deformed more than the hemispherical level without being subject to bursting.

To create materials that satisfy the desired stretching specifications, people have been working on modifying polymers in different ways. In the last 20 years the main published advances on polymer modification that have proven to be useful in thermoforming applications, next to the mostly undisclosed developments by the material suppliers on the pure chemical side, are:

- the addition of nucleating agents (TiO_2) to polypropylene (PP) during extrusion to improve the level of crystallinity and to form a delicate spherulitic structure [22];

- the addition of discrete long glass fibres to PP through a ‘self-assembling fibre reinforcement’ technology making reinforced PP sheets with significantly broadened processing window, even above the melting temperature of the matrix [23];
- the blending of HDPE with cross-linked HDPE to enhance melt strength and strain hardening behaviour in elongational viscosity in order to decrease sagging and improve wall thickness uniformity [4];
- the long chain branching of PP to significantly increase the strain hardening behaviour with little impact on the molecular weight [24];
- the addition of beta nucleating agents under the form of a masterbatch to create a high amount of beta-phase crystals in PP and improve the strength and rigidity of the material [25];
- the crosslinking of PA12 by irradiation to broaden the processing temperature window and making it an alternative material for vacuum forming [26, 27].

It is no surprise that all abovementioned topics address semi-crystalline polymers and that they all have intrinsically the same goal: the broadening of the processing window and the improvement of the stretching characteristics of the polymer sheets. This goal is mainly achieved by increasing the melt strength in different ways. Increased melt strength results in decreased sagging (or even delayed melting) during the heating stage of the thermoforming process [12, 28] and thereby enlarges the processing window.

2.2.1.3 Influence of the extrusion process

The starting material for (heavy gauge) thermoforming is mostly cast, extruded or rolled sheet. Casting is used for very thick sheets (> 10 mm) or for applications that require a stress-free starting blank. It is often used for example for PMMA, used in window applications, to reduce the effect of light refraction caused by internal stresses. When the sheet is extruded or rolled, the shaping process induces a degree of molecular orientation that is retained within the sheet due to the subsequent fast cooling, a phenomenon called stress freezing. It is obvious that the quality of incoming raw sheet material is critical for the quality and consistency of the thermoformed final product. Nowadays, the thermoformer has to rely on the material supplier and the standard material datasheets which mention specifications on the mechanical, thermal and electrical properties of the virgin polymer itself but less on the properties of the extruded sheet. Usually, the material supplier also provides data on length- and thickness tolerances, sheet flatness and squareness, sheet orientation and visual quality (gloss, colour,...). Information on extrusion speed, draw ratios, temperatures, cooling rate, amount of regrind,... which all strongly affect the crystallinity and residual stresses and thus the subsequent thermoforming behaviour are not provided. When quality problems arise at start-up or during production, discussions between the thermoformer and the material supplier arise with late delivery and customer complaints as a consequence. This is why, next to the modification of polymers to increase thermoformability as mentioned in the previous sections, researchers have been looking at the influence of different extrusion parameters on the thermoforming behaviour. Extrusion process parameters including die and melt temperature, extrusion speed / line speed, draw ratio and chill roll temperature affect the direction specific stresses and could result in anisotropic material behaviour, having an influence on the wall thickness distribution of the thermoformed product. Relevant studies in this context [19, 29-31] investigated the effect of the extrusion process settings on thermoformability and mechanical properties of PP and PVC sheet. Significant differences between the extrusion direction and the transverse direction were found. This was also confirmed by other researchers for ABS [32] after shrinkage tests and for PP [11] through biaxial tensile tests. The overall conclusions were that the extrusion direction exhibits the highest shrinkage and shows the highest load bearing capacity compared to the transverse direction. Dong et al [33] confirmed that anisotropic material properties may greatly affect simulation results when applying an isotropic material model, however they found no significant differences for their grades of PMMA after shrinkage tests.

2.2.1.4 Influence of the heating of the sheet material

Heating heavy gauge sheets is most of the time done by infrared radiation provided by ceramic, halogen, quartz or metal foil heaters installed in an upper and lower heater bank. The heating balance is composed of the radiant energy, convection at the surfaces of the sheet and conduction within the sheet. Sometimes, very thick sheets are preheated in a convection or contact oven before they are transferred to the main heating station. The overall aim is to heat the sheet in a homogeneous (in-plane and through the thickness) way as fast as possible without overheating the surfaces. In some cases, when high strain is necessary in certain parts of the product or when some parts are not allowed to stretch, a non-homogeneous heating pattern can be applied. This can be achieved by introducing a pattern in the form of welded wire screens to block parts of the radiation or by locally applying more or less intense heating to certain zones. This kind of patterning can be obtained by the appropriate setting of the individual heating elements, which is possible on most of the state of the art thermoforming machines, or by introducing an additional heating source. The latter can be in the form of contact heating as described by Levey [34] and Nied [35] and more recently by the researchers of the Fraunhofer Institute [36] or it can be in a non-contact way by means of local laser heating [37]. If patterned or zoned heating are omitted and homogeneous heating is the aim, typical heating strategies involve a first period of intense heating followed by a phase of reduced heating power in order to give the sheet time to transfer the heat flux from its surface to the core of the sheet. The power reduction ensures that the surface is not overheated. In modern thermoforming equipment, the sheet surface temperature is controlled by a centrally located non-contact infrared sensor (pyrometer) on one or both sides of the sheet. It is generally accepted that the absolute measured sheet temperature during heating is not very accurate. Nevertheless, these devices are common practice in the field of plastics processing. The inaccuracy is due to the fact that the captured electromagnetic radiation waves are not solely generated by the heated sheet itself but the signal is polluted by reflected and possibly transmitted, in the case of a dual heater, radiation waves. Very recently, Neubig et al. [38] suggested a clever solution for this problem by combining sensors with different wavelength ranges. Knowledge of the in-plane temperature distribution or the through-thickness temperature is limited to non-existent in an industrial context. Recently developed virtual tools such as the model-based virtual sensors and core-temperature observers from Modirnia and Boulet [39] could perhaps provide improved thermal knowledge without excessive costs.

Since heating is the first step in the thermoforming process and it has a huge effect on the following steps, researchers have dedicated significant efforts to try and understand the heating phenomenon. The following overview gives the state of the art on thermoforming related topics which, in one way or another, are based on experimentally generated thermal data.

The research goes back to the 1970's with significant works from Progelhof et al. [40, 41] trying to explain transient heat conduction in combination with surface (convective) cooling and radiant heating showing the difference between different heating methods including symmetric, asymmetric and pulsed heating and proving the importance of radiant absorption. Later work from Cunningham et al. [42, 43] included a mathematical model to predict temperature profiles, heat-up curves and transfer phenomena for infrared, contact and convection heating of flat composite sheets that can also be used for thermoplastic sheets. Monteix et al. [44] investigated experimentally the influence of halogen heaters on PET while Schmidt et al. [45] studied the influence of different heat sources, i.e. halogen (short wave), quartz (medium wave) and ceramic (long wave), on polystyrene (PS). Yousefi et al. [46] performed extensive experimental tests on 1.6 mm thick ABS to define the sensitivity of heating parameters on the sheet temperature. The main conclusions were that the temperature of the radiant heater (oven temperature) as well as the emissivity, the view factor and the specific heat of the polymer affected significantly the sheet temperature. For heavy gauge thermoforming, the thermal conductivity should also be added to this list. The heat transfer coefficient, the air temperature of the surrounding air and the spacing between sheet and heater affect to a smaller extent the temperature of the sheet as function of heating time. This is schematically represented in Figure 2.

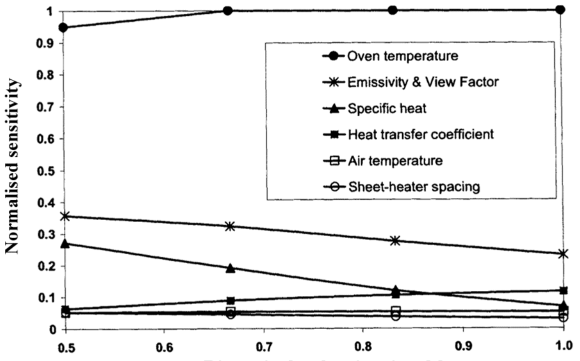

Figure 2 Normalised sensitivity of heating parameters as a function of a dimensionless heating time, with overall heating time = 180 s [46]

Moreover, they stated that all those parameters are hard to define and are dynamic in nature during the reheat phase. They also added that all kinds of surrounding conditions such as the non-uniform air temperature, the difference in air temperature between upper and lower side of the sheet and the difference in convective heat transfer coefficient between upper and lower side, make the process even more complex to model. Duarte and Covas [47] confirmed the findings of Yousefi for a PS/HIPS blend and added that also sheet sagging significantly affects the temperature. T-Sim (Accuform) forming simulations with several in-plane temperature distributions led to completely different thickness distributions of a simulated two step container-like part. From their findings it is not clear however if these findings correspond to experimental measurements and are related to sag or to (uncompleted) forming. Moore et al. [48], Girard et al [49], Boulet et al. [50] and Gauthier et al. [51] developed a system to control the heavy gauge sheet temperature by combining in-situ measurements of temperature, pressure and sag/bubble height using laser ranging sensors and linked the measurement data to simulation software (FormSim). In that way, they could optimise the sheet temperature distribution. FormSim is the predecessor of the now commercially available software Formview distributed by Rheoware Simulation Inc. The optimised temperature distribution was then converted to machine heater settings. The system was tested experimentally based on in-oven sag data and proved to be good for short heating times, but at longer heating times large deviations arose, which the researchers related to problems with the simulation model. More recently different simulation strategies to model the radiative flux were published: Cosson et al. [52] published their ray tracing method for PET and Labeas et al. [53] developed a methodology to define the position, density and power of quartz heaters. The latter was developed in order to reach optimal heating during the diaphragm forming of carbon/polyetherimide (PEI) composite sheets of different thicknesses. These studies have demonstrated once again that a representative simulation can only be performed if the radiative properties of both the emitter and the receiver are well known. Unfortunately this is not the case in industrial reality; moreover the radiative properties of the heating elements are subject to wear and contamination and thus far from constant through their lifetime. Khan et al. [54] investigated the influence of temperature dependent material properties (density, specific heat, thermal conductivity and thermal diffusivity), sheet colour (transparent and black), oven air velocity and oven temperature on the sheet heating phase of HDPE. They concluded that when the temperature dependent properties of the material were incorporated, a significantly better match with experiments was found. They also found that sheet (thermal) colour has a significant effect and that, in contradiction to all previous studies, the temperature variation of the air inside the oven had no significant influence on the results but that the air velocity was dominant. Finally, the researchers from the Upper Austria University of Applied Sciences have also contributed significantly to the knowledge and validation of the heating phase in thermoforming mainly focussing on the influences of material parameters (reflection, density, specific heat capacity, heat conductivity) [55], material filler and on the importance of the optical penetration depth when simulating heating following Bouguer Beer Lambert's law [56].

2.2.1.5 Influence of the thermoforming process parameters

Next to the material, the extrusion parameters and the heater settings a vast amount of research was devoted to the thermoforming process and the forming parameters. Table 2 summarises relevant publications where the thickness of the final product is considered as the quality parameter. To more easily draw conclusions from the considerable amount of data, not only the process parameters but also the mould shape, the sheet material and thickness and the instrument used for the thickness measurement are mentioned (when mentioned in the publications).

Mould shape	Material	Thickness	Process parameter	Thickness measurement instrument	Ref.
Box shape with undercut	ABS	3 mm	Vacuum evacuation rate Sheet temperature Mould temperature Slip	Hall effect sensor (*) on an unknown number of points	[57]
Cup with variable depth	HIPS	2 mm	Vacuum evacuation rate Sheet temperature	Ultrasonic device on 4 points	[58]
Container with draw ratio 3.18	HIPS	0.34 mm	Plug speed Plug temperature Sheet temperature	Calliper on 8 points	[59, 60]
Container	HDPE PMMA	1 mm	Sheet material Mould draw depth Plug geometry Forming temperature	Calliper on 20 points	[61]
Food container (200 ml)	Multilayer: HIPS / PVDC / LDPE	1.4478 mm	Forming temperature Forming pressure Heating time	Micrometer on 6 points in 4 directions	[62]
Yoghurt pot	PP	1.45 mm	Plug geometry Plug material Plug velocity Plug displacement Plug temperature Air pressure Air dwell time Air temperature Mould temperature Sheet temperature	Hall effect sensor on lip, shoulder, side walls and base in 3 directions	[31]
Part of a refrigerator liner	ABS	2.5 mm and 3 mm	Sheet temperature distribution	In the centreline of the part in 85 points	[63]
Open mould	PP	1.45 mm	Plug temperature Plug material	On 12 points	[64]
Open mould	HIPS PP	1.45 mm	Sheet material Plug temperature Plug material	On 12 points	[65]
Cup	PP foam	Not mentioned	Heating temperature Vacuum pressure Plug material Plug velocity Plug displacement	On 6 points	[66]

(*) A Hall effect sensor is an electronic semiconductor, integrated next to a powerful magnet in a measuring probe, which varies a voltage across its surface as a response on changes in a magnetic field. These changes are introduced by a test piece that is held in between the probe and a target, which is mostly a small magnetic ball.

Mould shape	Material	Thickness	Process parameter	Thickness measurement instrument	Ref.
Cup	PP with 30 % $CaCO_3$	0.5 mm	Plug velocity Plug material Plug displacement Vacuum pressure Sheet temperature	On 6 points	[67]
Tray	Multilayer: PS / EVOH / PE A-PET / PE PS / PE PP / PE	0.6 mm – 0.75 mm	Sheet material Mould draw depth Forming temperature Forming time Process type (pressure of plug assist)	Mitutoyo 543 digimatic indicator on 5 points	[68]
Cup	PP	1.3 mm	Plug material Plug temperature Sheet temperature	Hall effect sensor on 17 points	[69]
Cup	PET	0.5 mm	Heating temperature Vacuum pressure Plug velocity Plug displacement Plug material	On 6 points	[70]
Flower pot	PP	1.45 mm	Plug geometry	On 13 points in 4 directions	[71]
Shallow cup	PC	0.125 and 0.200 mm	Mould temperature Sheet temperature Plug displacement Plug holding time Plug velocity Sheet thickness	Thickness gauge on 5 points	[72]
Dairy pot	HIPS	1.25 mm	Sheet temperature Plug displacement Plug temperature Plug geometry Plug velocity Air pressure	Ultrasonic device on 33 points in 3 directions	[73]
Square container (500 ml)	PET	0.580 mm	Plug velocity Forming time Heating temperature	On 3 points: bottom, side, corner	[74]
Cup	HIPS	0.5 mm	Sheet temperature Vacuum pressure Mould type (male / female)	Micrometer on 5 points	[75]
Refrigerator door cover	Multilayer: HIPS	2.54 mm	Heating time Plug velocity Moulding time Mould temperature	On 1 point	[76]

Table 2 Summary of published papers on experimental thermoforming process optimisation using the final wall thickness as the principal quality parameter

Including a summary of the conclusions of every single paper listed above makes no sense as the results are much too specific for the type of process (vacuum forming, pressure forming, plug-assisted forming or multi-step forming), the material characteristics (including the thickness) and the product shape. This even sometimes results in the fact that the conclusions between different researches on the same parameters are not consistent, making it very difficult to draw general conclusions. However, an attempt is made to deduct the most interesting facts from the mentioned publications:

- Most of the studies are based on plug-assisted thermoforming.
- The majority considers small, academic, axisymmetric shapes (cups, yoghurt pots,...).
- Depending on the type of machine and control method, the parameters are related but different: some people use heater time and temperature whereas others use the sheet temperature; another example is the plug velocity that is sometimes addressed as plug lowering time without mentioning the speed or vice versa: mentioning the velocity but without mentioning the distance to the sheet or the acceleration, making it even more difficult to interpret the results.
- All thickness measurements are performed on the final products.
- All thickness measurements are point-wise measurements.
- Most of the thickness measurements are tactile measurements.
- All thickness measurements are performed on cross-sections: some times more than one cross-section is considered and the average of the different cross-sections is reported.
- Authors report that even in a laboratory environment there is asymmetry in wall thickness due to material (pre-processing) properties or inhomogeneous heating.
- Only a single study [63] addresses the subject of pattern heating.
- The conclusions that more than one reference agree on are:
    - sheet temperature and an accurate knowledge and control of the temperature (sheet, mould, plug) is critical;
    - the friction between the polymer sheet and the mould (or plug) has a significant influence on the wall thickness distribution;
    - the (Coulomb) friction coefficient is highly temperature dependent and generally the friction will rise at higher temperature of the sheet. The temperature difference between the sheet and the mould (plug) is also of importance. In plug-assisted thermoforming friction is often needed since it temporary and locally stops the sheet from being stretched, improving the wall thickness distribution at the bottom of deep products. Next to the temperature dependency, also the plug speed, plug force and to a lesser extent the surface finish has an influence on the friction coefficient [31, 77].

2.2.2 Critical reflections on experimental approaches in literature

The previous section gave an overview of relevant experimental aspects of the thermoforming process that have been under investigation until now. The following are some critical reflections on these studies.

Concerning the influence of the extrusion parameters on thermoforming quality, it is found that the extrusion induces a certain anisotropy and that it can have an impact on the thermoformed product. The magnitude of the impact however is not specified in a comprehensive guideline since it is too dependent on the material itself, the material history (extrusion parameters) but obviously also on the thermoforming processing conditions. From literature the only general conclusion that can be drawn is that the anisotropy should be as low as possible in order to have a uniform quality of thermoformed final products. In general, the thermoformer should always use the same sheet orientation for a specific part i.e. either in the machine direction or transverse to it. When mixing both directions in one batch, chances are high that quality inconsistencies will arise mainly originating from anisotropic shrinkage or from direction dependent strain resistance.

Concerning the heating of the sheet, people were quite successful attempting to model the transient thermal effects from different types of heaters and compare them to experimental measurements. They included the radiant heat flux (based on temperature, emissivity, view factor), surface convection effects, material conductivity, heat capacity, density, reflection, colour,... but also experienced that the exact definition of all these parameters is hard. Besides, the parameters are dynamic in nature and some of them are even subject to the (wear) condition and to contamination of the heating elements, making it even harder to define realistic values.

On the experimental side: the majority of the tests are performed on ‘academic’ axisymmetric shapes with thin gauge sheets under laboratory conditions and the resulting thickness distribution is frequently determined experimentally by means of manual discrete tactile measurements (thickness gauge) in a cross-section or in a part of the final product. The accuracy of the calliper or micrometer measurements is affected by the pressure exerted at the measurement tips. Too high pressure would induce indentation of the sample and thus erroneous thickness measurements. The accuracy of ultrasonic measurements is strongly dependent on the parallelism of the sheet surface to be measured and the sensor head. In the author’s opinion, the Hall effect sensor measurements are the most reliable and the best option in the case of tactile measurements. Next to the technical limitation, all the abovementioned measuring techniques are slow, operator dependent and only gives data in specific points on a cross-section of the final product. In some cases a grid (square or circular) pattern is drawn on the sheets in order to visualise the in-plane strain distribution of the product after forming but without specific knowledge on the exact reason for a certain strain distribution. In a couple of cases only a video recording is made to help understand the dynamics of the process and to visualise the sliding of the material over the mould [57, 65] (Figure 3).

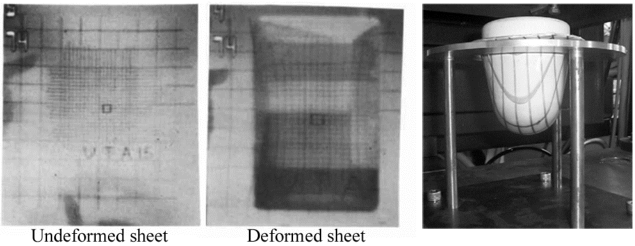

Undeformed sheet
t= 0.0 s

Deformed sheet
t = 0.90 s

Figure 3 Regular grid pattern before and after deformation in a rectangular shape [57] (left) and specimen at the end of the plugging phase (right) [65]. The deforming grids are recorded by a (high speed) camera and are used to visualize the deformation during the experiment.

Since thermoforming is a complex process characterised by many different parameters that cannot always be set independent of each other, point-wise thickness measurements in cross-sections of the final product are not ideal. This is why these kind of measurements lead mostly to complicated judgements on the causes of the thinning of the polymer sheet. When changing for example the sheet temperature, not only the rheological behaviour (Young's modulus) of the sheet will be affected, but also the contact friction between tool and sheet [78]. The current manual measurement approach makes it difficult to attribute particular observations in the thickness distribution to a specific process parameter. The results of previous studies are well suited to get better insight in the thermoforming process and the behaviour of the specific materials under investigation in their viscoelastic state, but the industrial applicability and the generic nature is rather limited.

2.3 Improvements of the thermoforming process through simulation

Next to the experimental thermoforming research, a vast amount of research is devoted to simulating the process. These research efforts combined with experimental validation have enlarged the insight in the material behaviour and the influence of process parameters on the product quality. The possibility to use thermoforming simulation software in both the design phase of new products and as a tool for process optimisation would mean a huge step forward in the evolution from an "artisanal" process to a fully virtual design and optimisation platform. Unfortunately, this is until now not the case.

Next to generic non-linear finite element modelling software solutions (ABAQUS from Dassault Systems, MARC from MSC,...) with the ability to define complex material behaviour and processes from scratch, a number of dedicated, more industry friendly thermoforming simulation software packages exist. The most well-known are: Accuform's T-Sim, Rheoware's Formview, ESI's PAM-FORM and Ansys's Polyflow. Both the generic and the commercial software solutions require similar input data, the only difference is that the effort to include the data and to model the process is considerably simplified in the dedicated packages.

In general, when only simulating the forming stage of the process, at least following input data are necessary:

- Physical and thermal material characteristics: heat capacity, density, thermal conductivity.
- Material model data: this can be in the form of a very simple rheological model such as the generalised Newtonian model, a hyperelastic model (Ogden [79], Mooney-Rivlin [80], Arruda-Boyce [81]), a linear viscoelastic model or even a non-linear viscoelastic model such as the single integral Kaye-Bernstein, Keasley, Zapas ((K-)BKZ) model [82] (with or without damping function [83]). The general trend is that the more the model becomes complex, the better it will describe the material behaviour. Unfortunately, this improved accuracy comes at the cost of more complex testing methods to generate valid input data for the models.

- Sheet characteristics: dimensions, initial temperature (distribution) and heat transfer coefficient to the surrounding air and to the mould.
- Mould and/or plug characteristics: shape, temperature (distribution), displacement speed, friction (or slip).
- Process characteristics: ambient air temperature, air pressure or vacuum pressure, timings.

Moreover, most of the abovementioned parameters can be temperature- and time-dependent.

The first section discusses the thermoforming simulation topics that researchers have addressed so far. In the second section a number of critical reflections are formulated.

2.3.1 Current state of the art

Researchers have been looking at different aspects of thermoforming simulation. Not only the influence of the material models has been investigated, but also the effect of different simulation parameters on the final thickness distribution and its comparison with experiments. Due to the large amount of information and the fact that simulation is a process that strongly evolves through time, the state of the art is presented in chronological order.

The first steps to finite element thermoforming simulations were the mathematical computations of the wall thickness distribution of PMMA sheets into conical and truncated moulds [84] in the late 1970's and later also for PS, PVC and PE [85]. These calculations are sometimes referred to as geometric element analyses (GEA). They assumed an isothermal, 2-dimensional model with sticky contact conditions (zero slip assumed on wall contact) and an isotropic and incompressible material model. Later on, computer processing power took over most of the calculation tasks, more complex constitutive equations for the material behaviour arose and different (iterative) solving methods were formulated.

DeLorenzi et al. [86] modelled the thermoforming HIPS sheet as a non-linear elastic (Mooney-Rivlin and Ogden) incompressible membrane in the ADINA finite element program and compared the thickness results with known solutions for the inflation of a bubble. They concluded that simulation and experiments showed excellent agreement. The obtained results for simple axisymmetric deep drawn parts were only in good agreement when a non-uniform temperature model was implemented (Figure 4).

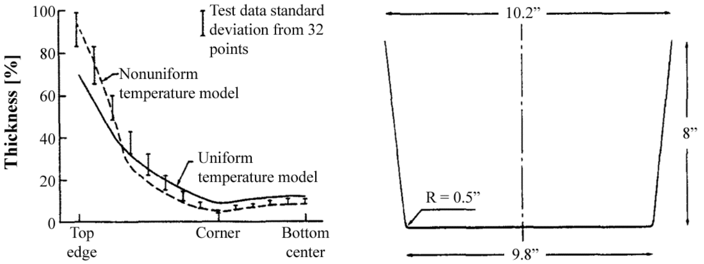

Figure 4 Comparison of measured and predicted wall thicknesses of a conical dish with a uniform and a non-uniform temperature model [86]

Nied et al. [87] developed an iterative membrane based three-dimensional FEA program for the simulation of the thermoforming process based on non-linear elastic material behaviour. They admitted that it was quite difficult for following reasons: the occurrence of large strains, the non-linear material behaviour, the contact between the polymer and the mould and in some instances due to membrane instabilities during inflation. Nevertheless, the method yielded excellent results although a relatively large number of simplifying assumptions were used (isothermal conditions, isotropy, membrane approach, simple material model).

DeLorenzi et al. [88] tried to summarise the progress in thermoforming simulation by comparing different materials (ABS, PPO, PC/PBT) using the viscoelastic Lodge material model formed in a mould shaped as a box with an undercut. The results were reasonably promising. They attributed their success to the fact that the forming process is quick and that at forming temperature the material can be treated as a nonlinear rubberlike membrane. They admitted that for slower processes, the viscous effects should probably be taken into account. They assumed sticky contact since friction data was not yet available and too difficult to measure. They also stated that temperature is the single most important parameter since differences in temperature distribution can have a major effect on the deformation of the polymer. Nevertheless, they assumed uniform temperature distribution and an isothermal process since the magnitude of the temperature distribution and the transient effects were unknown.

Song et al. [89] introduced the importance of using a finite thickness instead of a membrane approximation in cases when very thick sheets or sheets composed of different layers would be used. Almost 10 years later, Nam et al. [90] confirmed this statement for ABS proposing as a rule of thumb that membrane assumptions could only be used when the ratio of the width over the thickness exceeded a factor 100. If not, a three-dimensional approach should be followed. More recently, in 2013, Azdast et al. [91] modelled a 6.5 mm thick PMMA sheet with 5 bricks through the thickness instead of using the membrane theory to define the best combination of plug usage and air pressure in order to have the smallest thickness variation and least plug marks. Nevertheless, nearly all other papers and currently existing dedicated simulation software packages (T-Sim, Formview, Polyflow, PAM-FORM) still use the membrane (or shell) approximation for the forming simulation.

Kouba et al. [92, 93] first showed the results of the implementation of a thermoforming FEA software (predecessor of T-Sim) and then validated the incorporation of the non-linear BKZ viscoelastic material model. They proved the validity of the strain dependency by showing the differences in wall thickness based on a difference in inflation pressure.

DeLorenzi et al [94] compared in 1993 the results of extrusion blow moulding simulations, which is a process closely related to thermoforming, to experimental data. They used thermocouples inside the mould cavity to define the exact timing for the inflation of the parison and a pressure gauge to monitor the inside pressure. For the material description in simulation, they chose a nonlinear elastic 2 term Ogden model, assumed a membrane approach and sticky contact. For the material parameters, they used arbitrary values since the biaxial stress-strain behaviour for the two polymers they used (PPO and PC/PBT) were not known. The wall thickness of the parison was assumed to be uniform since they had no way to measure the thickness distribution. Although the simulation results matched reasonably well with experimental data, they admit that the understandings of the “process physics” that govern blow moulding are not at all complete. In addition, the description of the material behaviour is not yet accurate and all assumptions on material-, thermal- and parameter side should be checked with experimental data in future studies.

Bourgin et al. [95] remarked that the simulation results were sensitive to the initial deflected shape (sheet sagging), and accurate prediction of this shape might well be necessary in the future taking into account the (transient) heating of the sheet from which sagging, thermal buckling and inhomogeneous temperature arise.

By the end of the 90’s Koziey et al. devoted a chapter to review thermoforming simulation efforts so far and concluded that the material models that exist are capable to predict the thickness distribution [96]. Elastic models are attractive by their simplicity but cannot provide reliable predictions for complex plug-assisted production in deep moulds. The authors showed with thermoforming simulation examples that the Ogden model is best suited for the simulation of thermoforming into shallow simple moulds (Figure 5) while the K-BKZ model is required when the simulation includes deep-drawn forming, complex mould geometry or plug assistance (Figure 6). They also advise that future work should be focused on the development of less-complex viscoelastic models, the inclusion of time-dependent thermal effects, the integration of slip and that more experimental material data should be generated based on uniaxial and biaxial stretching, reflecting the thermoforming conditions.

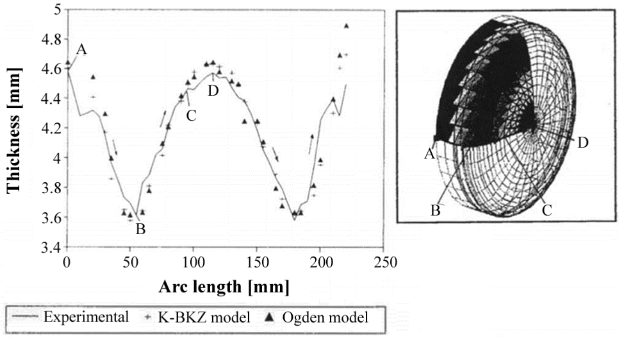

Figure 5 Comparison of predicted and experimental final thickness distribution for an automotive fuel tank component [96]

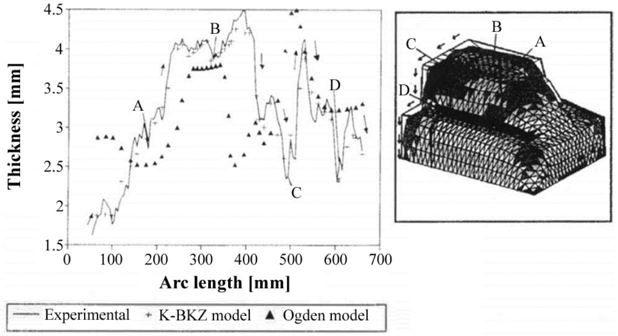

Figure 6 Comparison of predicted and experimental final thickness distribution for a casing [96]

As the first (and to the author's knowledge only), Khayat [97] modelled sheet behaviour taking into account the air flow to the vents inside the mould cavity.

Later, DiRaddo et al. [98] tried to model the sheet reheat phase and sagging as the first step of the ABS thermoforming process in combination with ceramic heaters. They indicated the importance to parametrise heater efficiency, air temperature of the oven and natural convection coefficients but did not explain how to define or measure these parameters.

Wang et al. [32] compared experimental thickness measurements of an ABS vacuum formed symmetric cup to simulation based on a viscoplastic model taking into account the effects of strain hardening, strain rate sensitivity and temperature. Instead of using (uniaxial) tensile tests, they used a Meissner type elongational rheometer to fit the material data. During vacuum forming experiments they observed shrinkage in the extrusion direction and expansion in the transverse direction. They used the average value of the measured thickness and compared it with the thickness results of the simulation which obviously did not show direction specific differences. Nevertheless, the authors conclude that the comparison between simulation and experimental data agrees fairly well and surprisingly that the forming temperature (175 – 195 °C) seems to have no effect on the thickness distribution.

That same year (1999) Stephenson et al. [99] tried to model sagging of HIPS blends of different thickness and found some discrepancies with experiments. The authors think this can be related to temperature gradients, molecular orientation of the original sheet due to extrusion or three dimensional considerations.

Laroche and Erchiqui [6, 8] started by defining the temperature process window for thermoforming in combination with finite element analysis using hyperelastic (Ogden, Mooney-Rivlin) and viscoelastic (BKZ) equations.

Later Erchiqui et al. [100-105] investigated the influence of the different material models (including the viscoelastic models of Lodge and Christensen) assuming isotropic incompressible thin sheets of ABS and membrane theory for the validation of bubble inflation and the forming of a small container. One of their major conclusions is the importance to describe the gas load during bubble inflation in terms of air flow instead of pressure, in order to efficiently describe the response of the membrane. The reason for this is that a constant pressure load is very difficult to realise in real membrane inflation experiments because the inflation process is controlled via an orifice connecting the thermoplastic membrane to a pressurised reservoir, and a constant pressure load condition would require a very large reservoir. Despite their credible results, the existing commercial simulation software packages require a pressure value and not an air flow as input parameter.

Xu et al. [106, 107] succeeded in accurately predicting post forming shrinkage of ABS by exporting the nodal information from T-Sim to Abaqus and performing a cooling and shrinkage analysis.

Collins et al. [108] and later in collaboration with Laroche [64, 109] concluded that a viscoelastic model should be chosen for plug-assisted thermoforming simulations. Contact conditions have to be taken into account including Coulomb friction effects and heat transfer between sheet and tool. The difference between the static and the dynamic friction was not yet incorporated however (and to the current author's knowledge, it still not is) since instabilities in the calculations tend to occur when they did.

Lee et al. [110] performed a parameter sensitivity study in T-Sim and concluded that rheological properties and the friction coefficient play a dominant role in determining the thermoforming performance compared to other processing parameters such as sheet and mould temperature.

Marckmann et al. [111] showed the importance of adaptive remeshing in blowmoulding and thermoforming. The material model they used is based on an incompressible nonlinear hyperelastic Mooney-Rivlin membrane with sticky contact conditions. The authors admitted that a better knowledge of material behaviour such as the influence of temperature on material stiffness is still lacking.

Sala et al. [112] used PAM-STAMP to simulate the forming of heavy gauge (4.2 mm) HIPS into a refrigerator liner. G'Sell's constitutive viscoelastic model was used and they found results differing around 20 % from the experimental measurements. The authors believed that the results could be improved by incorporating thermal exchange phenomena. They also stated that uniaxial tests are not the best for material characterisation and assume that biaxial tests are likely to give more accurate results.

Wiesche [113] simulated the sheet reheat phase including thermal radiation, convection (coefficient = 20 W/m^{2}K), thermal conduction, dynamic view factors and sagging, the forming phase and the cooling phase of a heavy gauge (8 mm) HDPE fuel tank with the single integral K-BKZ viscoelastic model. He proved by means of experimental data that modelling of the phase transition (crystallisation) during the process is highly important for predicting correct wall thickness distributions.

McCool et al. [114] tried to improve the finite element modelling of thermoforming based on experimental measurements and concluded that the process created conflicting and interrelated contact friction and heat transfer effects that largely dictate the final wall thickness distribution. A good estimate of the final wall thickness was obtained for HIPS when using high contact friction without heat transfer, but the results were bad at lower friction. When the simulation was rerun and thermal conduction was accounted for, the results at low friction where greatly improved. In their opinion further work is necessary to provide realistic measurements, input data and models for contact effects in thermoforming.

On the other hand Dong et al. [115] concluded from simulation of bubble inflation of acrylic sheets in PAM-FORM using the Mooney-Rivlin model that a perfect stick condition should be assumed and automatic mesh refinement is important to eliminate instabilities due to large deformations close to vertical wall areas.

Erchiqui et al. [116], similarly to Wiesche [113], simulated for PET, using a non-isothermal finite element approach, the radiative-conduction heat transfer during reheat, the stress-deformation during forming and the solidification during cooling. The membrane approximation and the visco-hyperelastic model were validated by equibiaxial stretching tests. In this study the convective heat transfer coefficient during heating is assumed to be 10 W/m^{2}K (for both upper and lower heater) and the transfer to the aluminium mould is estimated at 1000 W/m^{2}K. No source for these values is provided. Although they provided an analytical way to calculate heater emissivity, for their simulations a rounded value of 0.5 is taken for upper and lower heater in contrast to the values between 0.7 and 0.85 obtained by their Canadian colleagues [98].

O'Connor et al [11] simulated the thermoforming process of a PP cup in Abaqus using a hyperelastic model fitted with material data originated from biaxial stretching experiments. From these experiments they found that the extrusion direction had an increased load bearing compared to the transverse direction and that the material model was not adequate to describe the material behaviour. Besides, they encountered difficulties to simulate the sticky contact between sheet and plug.

Giacomin et al. [117] focussed especially on the sagging behaviour of the heated polymer sheet (PP, HIPS, PET) and deducted analytical equations to calculate the sagging behaviour. They also introduced a parameter called sagability. At first, the centre of the sheet descends with the cube root of time. After a particular time, the sag increases rapidly, which they refer to as sag runaway. The research on sagging was reviewed and updated for HIPS four years later by Baek [118] who found that the earliest predictions overestimated experimental sagging by a factor 14 and that recoil due to frozen-in stresses and sheet orientation should have been incorporated. Baek used Polyflow (Ansys Inc.) to validate the results (Figure 7).

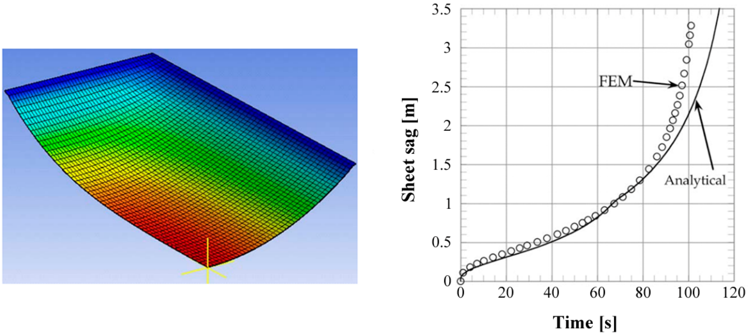

Figure 7 Analytical solution and finite element calculation for the sagging behaviour of an isothermal (915 x 1854 mm) HIPS sheet with a viscosity of 1.01 10^5 Pa.s pinned all the way around [118]

Chang et al. [119] simulated in Abaqus the vacuum forming behaviour of polycarbonate sheets in a partial hemispherical mould using different material models (Ogden, Mooney-Rivlin, Makradi [120]). Non-slip contact conditions were used and the heat-sink influence of the clamping device on the temperature distribution was investigated. They concluded that the temperature distribution of the sheet should be modelled in order to get adequate results. No conclusion can be drawn from the difference in thickness obtained with the three material models since it can only be attributed to the complete or incomplete replication of the mould.

Girard et al. [121] suggested to equip the thermoforming machines with pressure and flow rate sensors to be able to describe the inflation process in terms of power instead of a pressure. They also claimed that their technique can be used to fine tune material parameters during the forming process. More specific details on the technique were however, to the author's knowledge, not disclosed.

Finally, Brepols et al. [122] compared different hypo- and hyperelastic models in Abaqus on different industrial forming processes, i.e. deep drawing, draw bending and thermoforming. For the thermoforming process of a polymer sheet that undergoes considerable elastic strains (cup drawing) he concluded that only slight differences were found in the results between the considered models.

Summarising the most important aspects of the chronological overview and sorting it for the different materials that have been under investigation gives Table 3. All studies in that table assume material isotropy, incompressibility and mould symmetry except for a single paper that covered material (transverse) isotropy [101] and another [113] that indicated that crystallisation and the resulting changes in specific heat and density needed to be incorporated in order to predict the correct material behaviour. In most cases the simulation results are satisfying. In the cases where deviations from experiments were found, they were attributed to either thermal effects (to the mould, the clamping frame or the surrounding) or contact issues related to friction/slip effects. The importance of including heating and sagging into simulation is also repeatedly cited.

Material	Material model	Material parameter definition	Thermal assumptions	2D/3D	Contact conditions	Results / Conclusions	Ref.
ABS	Mooney-Rivlin	Hot uniaxial tensile tests	Isothermal and non-isothermal	Finite thickness	Sticky (although slight slip was seen in experiments)	Results are not perfect, but are much better with non-isothermal conditions.	[90]
ABS	K-BKZ	K-BKZ data from Rheometrics Mechanical Spectrometer measurements	Non-isothermal Non-uniform temperature distribution	Membrane	Unknown	Results are good but there are discrepancies at the boundaries probably due to the heat-sink effect of the clamping frame.	[98]
ABS	Viscoplastic including strain hardening	Meissner extensional rheometer	Isothermal Non-uniform temperature distribution	Membrane	Sticky	Good agreement with experiments. The initial forming temperature (175-195 °C) has no real effect on thickness distribution.	[32]
ABS	K-BKZ (Wagner)	Meissner extensional rheometer Oscillatory shear tests	Non-isothermal	Membrane	Friction (not specified)	Tested through simulation the sensitivity to friction and concluded that it was important. No adequate comparison to experiments available.	[110]
ABS, HDPE, HIPS	Mooney-Rivlin, Ogden (ABS) Viscoelastic: Lodge (HIPS), Christensen, K-BKZ (HDPE)	Biaxial extension (inflation)	Isothermal	Membrane	Sticky	Only small differences in final resulting thickness for the four models. Gas load during inflation has to be described as an airflow instead of a pressure.	[100-105]
ABS, HIPS	Mooney-Rivlin, Ogden Viscoelastic: Christensen and K-BKZ	K-BKZ (HIPS): small amplitude oscillatory tests Hyperelastic (ABS): inflation	Non-isothermal	Membrane	Not mentioned	Good correspondence was found between the minimum forming temperature in experiments and in simulation.	[6, 8]

Table 3 Summary of research on thermoforming simulation

Material	Material model	Material parameter definition	Thermal assumptions	2D/3D	Contact conditions	Results / Conclusions	Ref.
ABS, PC/PBT, PEI, PPO	Mooney-Rivlin, Ogden	Hot uniaxial tensile tests	Isothermal	Membrane	Sticky	Excellent results for all materials.	[87]
ABS, PC/PBT, PEI, PPO	Mooney-Rivlin, Ogden Viscoelastic Lodge	Hot uniaxial tensile tests	Isothermal	Membrane	Sticky	Promising results but the integration of temperature is probably the single most important parameter to include in FEA if thermal data were available.	[88]
HDPE	K-BKZ (Papanastasiou)	Not mentioned	Non-isothermal Specific heat and density are also temperature dependent	Membrane	Not mentioned	Simulated sheet reheat and sagging, forming and cooling. Modelling of the phase transition (crystallisation) is necessary. Due to crystallisation, the temperature decrease slows down and therefor, the material behaves differently.	[113]
HIPS	Mooney-Rivlin, Ogden	Approximated data from inflation experiments (not taking into account the cooling of the sheet during inflation) from Schmidt et al. [21]	Isothermal Uniformal and non-uniformal temperature distribution	Membrane	Frictionless for forming simulation Sticky contact for inflation and forming	Excellent agreement for bubble inflation, forming and the combination of both.	[86]
HIPS	Mooney-Rivlin, Ogden	Hot uniaxial tensile tests	Isothermal	Membrane	Sticky	Influence of the initial deflected shape defined by transient heating effects is important and should be taken into account.	[95]

Table 3 Summary of research on thermoforming simulation (continued)

Material	Material Model	Material parameter definition	Thermal assumptions	2D/3D	Contact conditions	Results / Conclusions	Ref.
HIPS	Mooney-Rivlin	Inflation data from DeLorenzi and Nied [86]	Isothermal	Membrane	Sticky	Adaptive remeshing is of importance. They found good predictions, but temperature influence on material behaviour should be investigated more into detail.	[111]
HIPS	G'Sell with Arrhenius dependency	Parallel plate rheometer	Isothermal Non-uniform temperature distribution	Membrane	Friction (not specified)	Results are not bad (max. 20% average error) but could be improved when accounting for thermal exchange, improving the temperature distribution and selecting the correct coefficient of friction. They remarked that the thickness is remarkably influences by the friction coefficient.	[112]
HIPS	Newtonian	N/A	Isothermal	Membrane	N/A	Simulation of sagging. Prior study [117] was an overestimation and frozen-in stresses and sheet orientation should be incorporated for correct sag prediction.	[118]
HIPS blends	Generalised Maxwell model	Parallel plate rheometer to measure G' and G'' at different temperatures	Isothermal	Membrane	N/A	Simulation of sagging. Discrepancies due to temperature effects, molecular orientation or 3D considerations	[99]
HIPS, PET, PP	Newtonian	N/A	Isothermal	Membrane	N/A	Simulation of sagging.	[117]

Table 3 Summary of research on thermoforming simulation (continued)

Material	Material model	Material parameter definition	Thermal assumptions	2D/3D	Contact conditions	Results / Conclusions	Ref.
Any material that obeys Mooney-Rivlin model	Mooney-Rivlin	Unknown	Isothermal	Membrane	Sticky	Conclude that air flow of the air evacuating from the mould has an effect on the sheet and should be accounted for. Comparison is made with prior studies from literature, not with own experimental tests.	[97]
PC	Mooney-Rivlin, Ogden, Makradi	Hot uniaxial tensile tests	Isothermal Non-uniform temperature distribution	Membrane	Sticky	Investigated the heat-sink effect of the clamping frame. The temperature distribution should be modelled to get accurate details. From their results it is impossible however to validate the difference in thickness between the different material models since the mould is not always correctly replicated.	[119]
PC/PBT, PPO	Ogden	Parameters where chosen arbitrary since no biaxial stress-strain data was available	Isothermal	Membrane	Sticky	Reasonable match. The discrepancies that are available are thought to be coming from the unknown initial parison geometry (and thickness).	[94]
PE, PS, PVC	Pure geometrical formulas	NA	N/A	2D	Sticky	Good prediction for a conical mould and a truncated cone	[85]
PET	Visco-hyperelastic (Christensen-Yang like [123, 124])	Equibiaxial stretching tests	Non-isothermal	Membrane	Sticky	Their finite-element code for the simulation of thermoforming or blow-moulding is validated. The code includes radiative-conduction, heat transfer during reheat, the stress-deformation during forming and solidification during cooling.	[116]

Table 3 Summary of research on thermoforming simulation (continued)

Material	Material model	Material parameter definition	Thermal assumptions	2D/3D	Contact conditions	Results / Conclusions	Ref.
PMMA	Neo-Hookean, Mooney-Rivlin	Equibiaxial stretching data from Treloar [125]	Isothermal	Finite thickness	Only inflation	Good agreement for free inflation of axisymmetric sheet and comparable to results from literature. Since thermoforming is fast, the sheet can be assumed to be (non-linear) elastic and the viscous part can be neglected.	[89]
PMMA	Mooney-Rivlin	Hot uniaxial tensile data from Dong et al. [115]	Isothermal	Finite thickness	Sticky	These authors found through simulation the best combination of pressure and plug usage for optical quality PMMA parts.	[91]
PMMA	Neo-Hookean, Ogden	From fitting stress-strain data	Isothermal	Membrane	Sticky or slipping (not specified)	Ogden model provided good results, the Neo-Hookean showed instabilities.	[93]
PMMA	Mooney-Rivlin, Ogden	Uniaxial tensile tests	Isothermal	Membrane	Sticky	Inflation tests using a hyperelastic model compared well with experimental data. The authors state that also when forming more complex shapes (container) the model is fine and that perfect stick condition should be assumed. Automatic mesh refinement is important to eliminate instabilities.	[115]
PP	K-BKZ (Papanastasiou)	Small amplitude oscillatory tests	Non-isothermal	Membrane	Both static and dynamic (Coulomb) friction with temperature dependency	For plug assisted thermoforming, a viscoelastic model needs to be chosen, friction and heat transfer to the plug should be accounted for.	[64, 108, 109]

Table 3 Summary of research on thermoforming simulation (continued)

2.3.2 Critical reflections on simulation approaches in literature

The previous section gave an overview of relevant aspects of thermoforming simulation that have been under investigation until now. The following are some critical reflections on these studies.

From the previous section and the overview in Table 3 it is clear that the simulation of the thermoforming process is a rather difficult task requiring a significant amount of assumptions such as material isotropy, thermal homogeneity, incompressibility and on all but a few exceptions the applicability of the membrane theory. In addition, the choice of the material model able to capture the complex behaviour of the heated polymer sheet and the calculation method (direct or iterative, with or without automatic mesh refinements,...) in order to avoid instabilities make the task even more complex. Next, a number of effects that are difficult to parametrise do not necessarily contribute to the final accuracy. These effects can be the contact conditions and friction, the (through-thickness) temperature distribution, sheet side dependent convection coefficients, radiation parameters and heater efficiencies, the use of air pressure or air flow as input data for the inflation process and the possible necessity to incorporate the evacuation of the air from the cavity into the simulation model. It is clear that the simulation of the thermoforming process is not straightforward and that it is hard to almost impossible for the industrial thermoformer to find a specific set of research results that apply directly to his case. Either the material, the material thickness, the process conditions, the mould shape, the process variant,... is not corresponding to what has been described in literature leading to non-usable results and forcing him back to the typical trial and error approach.

Similar to the conclusions of the experimental research, an attempt is made to deduct the most interesting facts out of the mentioned publications. Researchers agree that depending on the type of process that is used (plug-assisted thin gauge thermoforming or heavy gauge vacuum forming) with the same material, the choice of the material model may be different. Unfortunately, they do not always agree on what model to choose. Some believe that heavy gauge thermoforming simulation is mainly shape driven making simple constitutive equations applicable, whilst others find it necessary to use non-linear viscoelastic equations. The former is also the opinion of current author, especially since the process is much slower compared to thin gauge (plug-assisted) thermoforming. For almost every material model listed in Section 2.3.1, reasonable to good agreement with experiments has been found. It is in most cases however not clear if this is directly related to the material description or whether some simulation parameter were adjusted to improve the fit with experiments, since some parameters have to be estimated. However, researchers agree that good constitutive equations are those that consist of a simple expression that can model the rheological characteristics of a material with sufficient accuracy and for which the input data is easy to determine. Unfortunately, this is in contradictions with current constitutive equations and material testing techniques.

Different studies confirm the findings of Section 2.2.1.3 concerning the influences of material history and frozen-in stresses, but do not present a practical solution on how to cope with these effects in simulation. For axisymmetric parts, the simulations are typically performed on one quadrant of the product and the results are then mirrored to the other quadrants. Unfortunately, due to process variation or material related issues such as frozen-in stresses during the prior extrusion process of the sheet, this assumption does not necessarily correspond to reality [126, 127].

During the comparison of simulated results with experiments the difference between simulation parameters and machine settings can also be a major source of error since the link between the two is not always clear. Finally, nearly all authors assume incompressibility and mass conservation. This is a simplification that is also used by all the dedicated thermoforming software packages mentioned in the introduction of this chapter.

Simulation software that predicts final wall thickness distribution based on product drawing, material parameters and process conditions, can and should be used in the design phase of new products and moulds or during production (start-ups) for process optimisation. Although dedicated simulation software is available and has proven to be valuable, it is not that often used by the industry because of several reasons. Firstly, the software mostly describes an idealised situation, differing from the real industrial environment. For example, the heating of blanks and cooling of tools is expected to be uniform in-plane and homogenous through the thickness in simulations but this is rarely the case in reality. Secondly, the simulation software does not take into account all thermal and physical aspects of this complex process within its material models since not all characteristics of the large amount of possible thermoforming materials, at thermoforming conditions, have been researched and parameterised for usage in simulation software. Thirdly, variation of process parameters in practice jeopardises the process robustness and requires higher safety margins and initial blank thicknesses. Finally, when all abovementioned conditions are met, i.e. when the process parameters are under control and a material model is chosen that accurately describes the material behaviour, one other issue remains in order to adequately execute a simulation that yields results that can be linked back to the process itself. This issue is the matching of the thermoforming machine settings to the parameters to be set in the simulation software. This matching is a critical part of the simulation since it is impossible to obtain realistic results when starting with the wrong simulation parameters; no adequate method to define this link has been found in literature by the author. In all cases where simulation is used, one should keep in mind that an accurate knowledge of the process variables and the link between the parameters in the simulation software and the parameters that can be set on the machine is mandatory to validate the obtained virtual data with experimental measurements.

2.4 Conclusions

The state of the art on thermoforming reveals that the research is far from complete and that a number of topics have not been addressed to full extent. Besides, especially in simulation, a reasonable amount of assumptions are to be taken since realistic values for a number of parameters cannot be retrieved from literature. Either the data is just not available, or the data is not fit for the specific thermoforming machine, material, process conditions one is looking for.

The experimental methodology that is proposed in Chapter 3 serves to clarify a certain amount of the above-cited uncertainties.
Following topics will be addressed:

- the effect of sheet anisotropy on heating, sagging and forming;
- the heating of the sheet and how to predict on-line the through-thickness and in-plane temperature distribution;
- the equilibration effects and asymmetric heating;
- the magnitude and asymmetry of sagging;
- the quantification of friction/slip;
- the visualising of slip at the clamping frame;
- the parametrisation of convection coefficients to the surrounding and thermal exchange to the mould;
- the simulation of bubble inflation and forming processes with the available material parameters;
- how to uncontestably link a final thickness distribution to a certain process parameter.

The approach is demonstrated and validated on industrial moulds and on an industrial thermoforming machine. A full-field non-contact measurement technique is used to avoid the disadvantages of manual measurements in a tactile way. The methodology ultimately guides the thermoformer to advanced process knowledge making it possible to optimise the thermoforming process both experimentally and through simulation.

Chapter 3 - Methodology

3.1 Introduction

It is clear that there is a need for a more robust and industrially oriented approach to enable more process insight in thermoforming and to efficiently:

- Understand the on-going mechanisms making it possible to choose the right process parameters based on real surrounding conditions, real machine settings and applicable for non-axisymmetric production moulds and non-isothermally heated sheets.
- Define realistic simulation parameters that allow for the modelling of the process as it occurs in reality, based on a realistic surrounding and boundary conditions.
- Compare simulation results to experimental data.

This approach should be, if possible, material independent or at least without the necessity of complex material models.

In thin gauge thermoforming, process insight has proven to be highly important to evaluate the effect of process parameter settings on the final product quality. Martin et al. [128] recently published details of a prototype multivariable instrumentation system for use in thermoforming and highlighted its added value. This instrument combines in-mould measurements of plug force, temperature and displacement with air pressure and air and sheet temperature. A similar commercial instrument called ToolVision, distributed under that name in Europe and under ToolVu (uVu Technologies) in the USA, is on the market since 2010 [129].

In heavy gauge thermoforming on the other hand, little to no effort has been reported to obtain more in-process data. Heavy gauge thermoforming does not strictly refer to the thickness of the sheet (≥ 1 mm), but more to a class of processes that involve large products, most of the time formed by simple vacuum forming or free forming and which are cut-sheet fed. These thermoforming process variants have the advantage that the sheet is visible during every step of the process: heating, sheet transfer (or heater retraction depending on the type of machine), bubble inflation for positive products, forming, cooling and demoulding. The only research group that tried to develop a 'smart' measurement setup is that of the National Research Council (NRC) of Canada together with the researchers of McGill University [48-51]. They developed a control system that consists of a combination of temperature, pressure and height measurement, the latter based on laser optics (Figure 8).

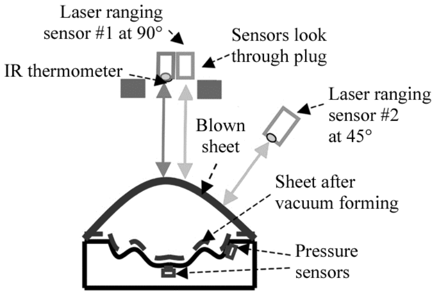

Figure 8 Multi-variable monitoring setup for the adaptive control of sheet heating [49]

The system is primarily focused on the heating step of the thermoforming process and tries to match the temperature map at the exit of the oven to an optimal heat map as predicted by simulations.

To respond to the lack of process insight in heavy gauge thermoforming, a new setup has been developed in this thesis (Figure 9 and Figure 10).

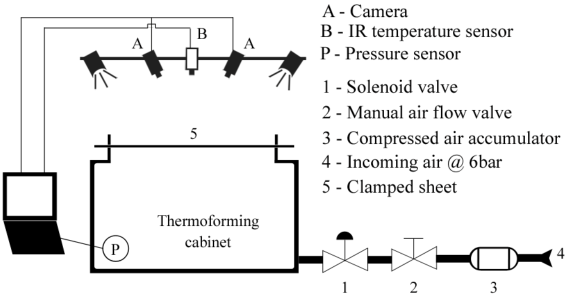

Figure 9 Schematic representation of the monitoring setup

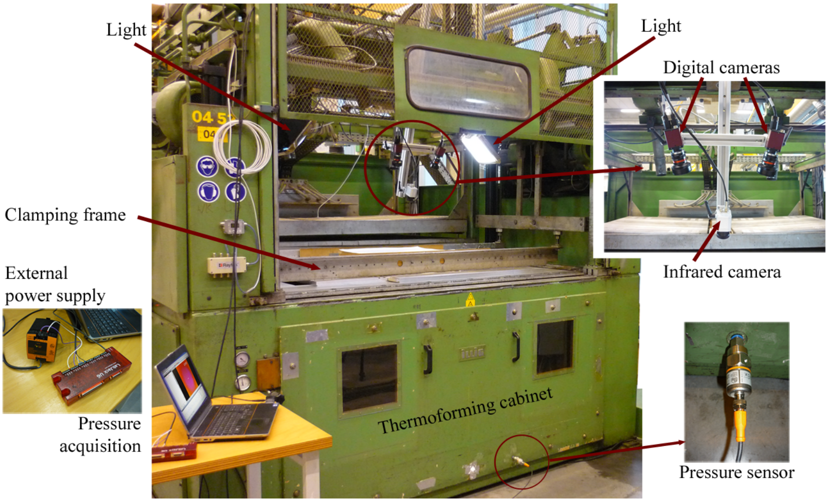

Figure 10 Experimental setup on an Illig UA200 thermoforming machine

The arrangement shown in Figure 9 consists of three measurement systems. The first measures the pressure of the cabinet underneath the sheet, the second measures the sheet surface temperature (on a single point in the middle or over the entire surface) and the third measures the full-field deformation of the sheet. All measurements are performed in-situ during the complete process-cycle and on an industrial thermoforming machine. Pressure, temperature and deformation data are synchronised on a single laptop. The pressure sensor is externally powered by a 12 V DC source, the digital cameras are powered over the (Firewire) bus, the infrared acquisition device is powered through USB. The individual components of the setup are further described in detail in Section 3.2.

3.2 Materials and methods

The next sections will explain in detail the materials and equipment used for the setup and why this particular combination of temperature, pressure and deformation is chosen.

3.2.1 Thermoforming equipment

For all experiments in this thesis, an industrial sheet fed heavy gauge thermoforming machine from ILLIG, UA200ED from 1988, was used. The mould and plug movements are hydraulic and the movements of the clamping frame and the heater banks are pneumatically driven. The maximum sheet dimensions that can be processed are 2000 mm by 1000 mm with a thickness up to 10 mm. The maximum mould height cannot exceed 580 mm. The system has a maximum clamping force of 8 tonnes and can be used as a twin-sheet forming machine. It is a cabinet type machine, meaning that the heating and forming takes place within the same enclosure. During heating the dual heater banks are moved forward in order to heat the sheet. The top heater consists of 160 ceramic elements with a total power of 53.75 kW. Each element can be individually assigned to one of three temperature controlling master elements in the upper heater bank. The lower heater consists of 112 ceramic elements with a total power of 28 kW. These are all assigned to one controlling master element in the lower bank. The vacuum system is driven by a Büsch R5 pump connected to two 350 liter buffer vessels providing sufficient capacity for fast extraction of the air between the sheet and the mould. Finally, the machine is equipped with an air injection system with accumulator for sag compensation and bubble inflation and 8 fans attached at the top of the machine to provide cooling air.

3.2.2 Pressure measurement

In thin gauge thermoforming, air pressure is often used as the forming force while vacuum is only applied to evacuate the air from the chamber underneath the product. In heavy gauge thermoforming however, vacuum is used to form the product and air pressure is used for other purposes: i.e. for sag compensation, for bubble inflation or for both. For this reason and when one wants to simulate the inflation process, an accurate knowledge of the pressure is important since it has a direct influence on the thickness of the final product. Current state of the art thermoforming machines control the air flow by a throttle valve connecting the area underneath the clamped thermoplastic sheet to a pressurised reservoir. The positioning of the valve is either done by a manual lever or by a PLC controlled actuator. As stated by Erchiqui et al. [100] and Girard et al. [121] a constant load is very difficult to realise in real experiments due to the type of pressure control. Moreover, the resulting pressure profile is rarely measured. The link between the position of the valve and the actual occurring pressure that can be used in simulation should be known to predict the correct setting of the pressure valve for both sag compensation and bubble inflation.

For the experiments in this thesis, a relative 0-1 bar pressure sensor (IFM electronics PA9027) is installed in the lower cabinet of the machine and coupled to a 16 bit data acquisition system (Labjack U6). The sensor has a resolution of 0.1 mbar and a repeatability accuracy lower than 0.1 % of the measuring range. Experiments showed that the position of the pressure sensor in the cabinet is of insignificant importance on the pressure values. The pressure build-up during bubble inflation is affected by the general air pressure on the incoming pneumatic air line, the diameter and resistance of the piping, the setting of the air flow valve, the volume of the compressed air accumulator vessel (if present), the volume of the lower cabinet that needs to be filled and the losses due to non-perfect air-tight closure of the cabinet. In the current setup, the incoming air (pressurised at about 6 bar) is accumulated in a 90 liter pressure vessel followed by a manual valve for the air flow setting and a solenoid valve to determine the duration for the pressure to build-up (Figure 9). The free volume of the lower cabinet of the thermoforming machine and the piping connecting the cabinet to the accumulator is approximately 5170 liter. In an ideal situation and assuming air as an ideal gas, the maximum pressure without edge losses that can be achieved when connecting the air accumulator to the lower cabinet would be 103 mbar. A typical profile, measured with different settings (1-10) of the pressure valve and a rigid sheet clamped in the machine to close the cabinet of the Illig UA200 industrial thermoformer is displayed in Figure 11.

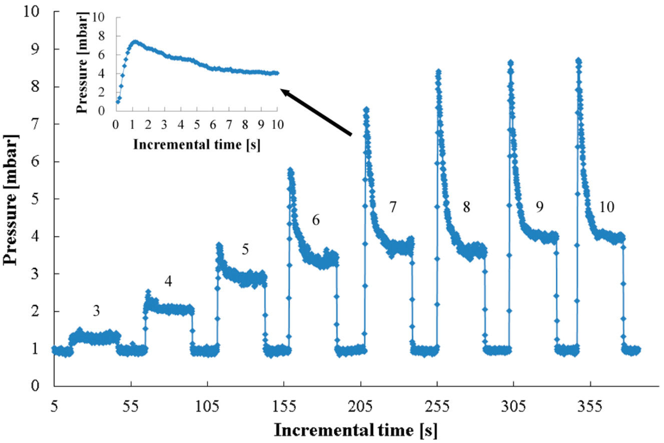

Figure 11 Typical pressure profile during bubble inflation for different settings of the pressure valve

Small differences are to be expected in a production (heated) context since the clamped sheet is not rigid. Due to the pressure the sheet will be lifted and expanded, increasing the free volume underneath the sheet and affecting the slope of the pressure profile. Important to remark is that even with the highest setting of the valve, the pressure reaches less than a tenth of the calculated value as a consequence of the considerable losses. It is certainly useful to perform this measurement if realistic values are to be obtained for simulation.

With valve settings 1 and 2, the opening of the valve is too small to overcome the losses, the pressure gradients are therefore not represented in the graph. As a general observation on Figure 11, it can be noticed that irrespective the setting of the valve, in the first 500-1000 ms a quick pressure is built-up due to the fast decompression of the air inside the accumulator vessel. The higher the setting of the air flow valve, the higher the peak value becomes. Once the accumulator is empty, the pressure only depends on the direct flow rate from the incoming pneumatic line, affected by the throttling effect of the valve and reduced by the leakage losses. The pressure value decreases to a stable value representing the equilibrium between the leakage losses and the fresh incoming air. From setting 7 and above, the pressure in the equilibrium phase is practically identical. Important to remark is that for some faster applications where the bubble inflation step takes less than 1 second, the pressure gradient will still be in the rising part of the curve. In most of the heavy gauge applications however, inflation takes more time meaning that not only the rising part but also the descending or even the horizontal part of the profile needs to be used as input for simulation.

3.2.3 Temperature measurement

The temperature (distribution) of the polymer sheet is, next to the strain rate, one of the most important parameters in thermoforming since it is directly related to the sheet behaviour and it defines whether the sheet is thermoformable or not. Researchers do not fully agree on which of the two is dominant or if strain rate is even of importance at all for the, mostly slow, heavy gauge processes (cf. Chapter 2). They do agree however that the sheet should be heated as fast as possible through the thickness without overheating the surface. When only taking infrared radiation heating into account, two different types of heating control methods exist: power controlled elements and temperature controlled elements. Power control is typically used for quartz or halogen heating elements where the power setting represents a fraction of the time that the elements are activated at full power. Temperature control is usually used for (slow) ceramic heating elements that have embedded thermocouples inside the elements monitoring the temperature of the element itself. Both control types do not tell anything about the temperature of the sheet. On older machines, the temperature of the sheet is not measured at all, newer thermoforming machines are equipped with one or a couple of non-contact infrared temperature sensors in the top and bottom heaters. These sensors give an approximated point value for the surface temperature of the sheet [38]. Temperature measurement can be 1D spot measurements, 2D array measurements or even 3D measurements when the 2D temperature is mapped over the product geometry.

For the experiments in this thesis auxiliary infrared sensors are used since the thermoforming machine is not equipped with built-in pyrometers. For this reason, the temperature of the sheet can only be measured while the heaters are in their backward position in the case of dual heater operation. When a temperature measurement is necessary during heating a single heater bank is used. The temperature is then either measured from the top or from the bottom, depending on which heater bank is used. The first temperature sensor that is used is a Fluke 576 spot infrared thermometer with a spectral response between 8 and 14 µm. The data is read out at a rate of 10 Hz, but since the response time is of the order of magnitude of 250 ms, the actual acquisition rate is 4 Hz. The distance to spot size ratio is 60:1 with a focal point of 19 mm at 1150 mm from the sensor. The sensor has an accuracy of ±0.75 % of the reading, a repeatability of ±0.5 % and a reading resolution of 0.1 °C. A second instrument that is used is a FLIR T335 thermal camera which has a resolution of 320 x 240 pixels, a thermal sensitivity of 50 mK, an accuracy of ±2 % of the reading and a resolution of 0.1 °C. A third device that is used is the OPTRIS PI400 thermal camera which is able to record full-field thermal images at a frame rate of 80 Hz. The sensor has a resolution of 382 x 288 pixels, a thermal sensitivity of 80 mK and an accuracy of ±2 % of the reading. This device is represented on Figure 10 but is in the context of this thesis, however, only used for test measurements. Since the absolute accuracy of all infrared measurement devices is largely affected by the setting of the sensor emissivity, this parameter is based on material emissivity measurements (for values, see Section 3.2.5.2).

3.2.4 Deformation measurement

Nowadays, the thickness distribution of a thermoformed product is measured on the final product and in cross sections. As described in Chapter 2 this mostly tactile approach has several drawbacks and makes it quite difficult to relate the effect of a process parameter to the obtained thickness distribution since it is not clear what the influence of each process step is. To overcome this, non-contact full-field deformation measurements can provide an added value. Deformation measurement can be considered as an advanced version of non-contact shape measurement technologies like point-based laser triangulation measurements or structured-light 3D scanners. Next to full-field shape reconstruction, deformation measurements also provide insight in the displacement components of the material and thickness distribution throughout the sheet. This is done by using (stereo) digital image correlation (DIC), following displacements of a random speckle pattern on the sheet surface.

The term digital image correlation refers to the class of non-contact measurement methods that acquire surface images of an object, store them in digital form, and perform image similarity metrics to extract full-field shape and deformation data [130]. It allows for a sub-pixel measurement accuracy of displacements and strains on complex parts. To be able to perform stable and sub-pixel accurate correlation, a random, non-repetitive, isotropic and high contrast speckle pattern has to be applied to a blank in order to ensure distinction between the pixels. Next, since a (grey scale) pixel-value is not a unique signature, a so-called subset is introduced which is a small, mostly square, surface of pixels that contains a combination of speckles and represents a unique signature in the picture (Figure 13). It is that subset that is compared between the undeformed state (flat blank) and the deformed state (thermoformed product). The subset is shifted step by step (step size) and for each step the comparison between reference and deformed picture is made until it covers the complete surface of the specimen. Since the subset can change position, shape and size during the forming process, the coordinates are related through a deformation function (shape function) which is dependent on the expected deformation mode. For a rigid body motion, only a first order term is considered, but when an affine or irregular transformation is expected, higher order terms need to be used (Figure 12).

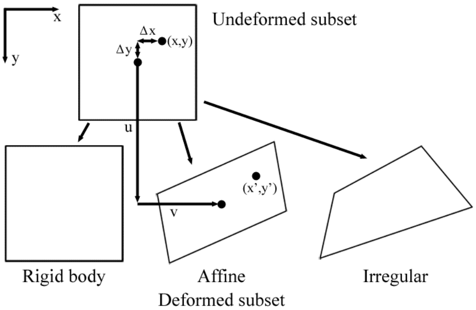

Figure 12 Possible transformations to be fitted by the appropriate shape functions

When for example an affine transformation is expected, the relation between the coordinates of the undeformed (x, y) and the deformed coordinate (x', y') can be approximated by:

$$x' = x + u + \frac{\partial u}{\partial x}\Delta x + \frac{\partial u}{\partial y}\Delta y \tag{1}$$

and

$$y' = y + v + \frac{\partial v}{\partial x}\Delta x + \frac{\partial v}{\partial y}\Delta y \tag{2}$$

where u and v represent the translation of the centre of the subset in x and y direction respectively. The distance from the centre of the subset to the point (x, y) is denoted as Δx and Δy.

The correlation results in a full-field displacement map, an example of such a displacement map with U- and V-displacements, corresponding to x- and y-directions respectively, of a uniaxial extension is represented in Figure 13. In a stereo setup, displacements in the third direction, perpendicular to the U-V plane are also possible and are denoted as W-displacements. Since the measurements are performed in-situ, transient effects during heating, sag depth and shape, bubble height and shape and final product shape can be measured. The strain that results from the displacement map can be used subsequently as an input parameter for subsequent full-field thickness calculation. A detailed description of this procedure is developed in Section 4.2.5.

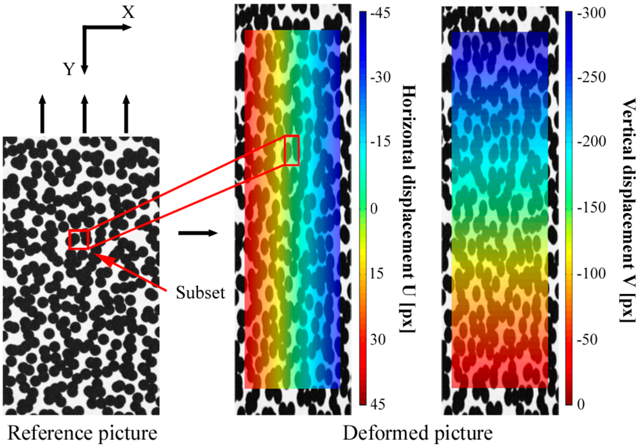

Figure 13 Horizontal (U) and vertical (V) displacement fields of a specimen in uniaxial tension

For this research the academic digital image correlation software MatchID3D V4.1 [131] developed by the research group Mechanics of Materials, Products and Processing of the KU Leuven Technology Campus Ghent, is used. The 2D module of the software is independently benchmarked to the results of commercial systems [132] and it was found that for the bias error, MatchID is in an identical range as VIC (Correlated Solutions [133]) whereas an improved lower standard deviation by a factor of four was achieved. The results are based on the comparison of the correlation of numerically shifted images. When comparing to Aramis (GOM [134]), similar conclusions on the standard deviation can be drawn but besides also the bias error of MatchID is significantly lower. For the stereo camera calibration, the calibration module of the MatchID software is used. The default Zhang [135] calibration approach is used and the maximum reprojection error in all cases never exceeds 0.3 pixels. The correlation settings for the displacement calculations that are used throughout the thesis are: a zero-normalised sum of squared differences algorithm (ZNSSD), a bicubic polynomial interpolation, an affine transformation both in 2D and stereo, a spatial correlation with updated reference and Gaussian noise handling. The ZNSSD algorithm is represented by Equation (3):

$$C_{ZNSSD} = \sum_{i=-M}^{M} \sum_{j=-M}^{M} \left[\frac{f(x_i, y_j) - f_m}{\Delta f} - \frac{g(x'_i, y'_j) - g_m}{\Delta g} \right]^2 \tag{3}$$

with

$$\Delta f = \sqrt{\sum_{i=-M}^{M} \sum_{j=-M}^{M} \left[f(x_i, y_j) - f_m \right]^2} \tag{4}$$

$$\Delta g = \sqrt{\sum_{i=-M}^{M} \sum_{j=-M}^{M} \left[g(x'_i, y'_j) - g_m \right]^2} \tag{5}$$

$$f_m = \frac{1}{(2M+1)^2} \sum_{i=-M}^{M} \sum_{j=-M}^{M} f(x_i, y_j) \tag{6}$$

$$g_m = \frac{1}{(2M+1)^2} \sum_{i=-M}^{M} \sum_{j=-M}^{M} g(x_i', y_j') \tag{7}$$

The discrete functions $f(x_i, y_j)$ and $g(x_i', y_j')$ correspond to the undeformed and deformed state, respectively. The subset area is represented by $(2M+1)^2$ where M is expressed in pixels.

As to the standard strain calculation algorithm, the logarithmic Euler Almansi strain tensor is used (Equation (8)), combined with a bilinear quadrilateral interpolation.

$$\varepsilon^{\ln EA} = ln(V) = \sqrt{FF^T} \tag{8}$$

In Equation *(8)*, V is the left deformation tensor obtained via the Cauchy-Green theorem of polar decomposition and F is the deformation gradient matrix (cf. Figure 38). More details on the DIC process flow and the choice of the correlation algorithms are presented in [136] and [137]. The parameters chosen in this thesis are based on literature; the evaluation of every single correlation parameter on the quality of the results is outside the scope of this thesis. Subset, step and strain window sizes are specified throughout the thesis since these parameters are more dependent on the field of view of the camera and the speckle size but care has been taken to always have at least 3 x 3 pixels per speckle and three speckles per subset. These values are a commonly adopted rule of thumb to ensure accurate matching and reasonable intensity pattern reconstruction via interpolation without aliasing [130, 138, 139]. A summary of all used values is included in Appendix C.

Two AVT Stingray F-201 cameras with Pentax high resolution, low distortion, 8 mm or 25 mm focal length lenses, depending on the required field of view, are mounted vibration free on top of the thermoforming machine. At the beginning of each experiment and after camera calibration, a noise evaluation is carried out to estimate the influence of noise. This implies that the averaged standard deviation on the grey values between the region of interest of a reference picture and several still, unloaded, pictures is calculated. This technique is referred to as a self-correlation test and the result is an estimate of the camera noise. Noise impacts the measurement accuracy and should be kept as low as possible. An interesting paper concerning this issue is published by Wang et al. [140]. The average noise values in all cases in this thesis range between 0.5 and 1 % depending on the setup. Up to 1 % standard deviation on grey values is commonly acceptable when using decent image acquisition hardware.

The DIC technique is chosen to measure surface deformation instead of interferometry based methods (speckle interferometry, Moiré, shearography,...) since the latter tend to be more sensitive to rigid-body motion [141-144]. Other drawbacks of these other methods are the complexity of the setups and the investment costs.

The grid method [145-149] could be an alternative for DIC since both techniques rely on the same concept of image feature tracking, but the grid method requires a perfectly regular grid pattern which is much more difficult to prepare than the random pattern necessary for DIC. DIC is definitely the most flexible method in an industrial environment. An advantage of the grid method is that it requires less computational power making it faster and probably more convenient for almost real-time measurements. The latter are however not the purpose of this research. A drawback of both (non-interferometric) techniques is that the pattern remains on the specimen after the measurement.

Specific details on the application of DIC for in-situ full-field deformation measurements during the thermoforming process are described in Chapter 4.

3.2.5 Thermoplastic material

The material of choice for the tests is extruded high impact polystyrene (HIPS) from Metzeler: Metzoplast SB/HK. HIPS, still one of the most used materials for thermoforming, is quite easy to form since it is an amorphous material. The most important specifications, extracted from the material supplier datasheet are listed in Table 4.

Mechanical properties		
Yield strength (DIN 53455)	N/mm²	17.5
Elongation at yield (DIN 53455)	%	2.0
Tensile strength at break (DIN 53455)	N/mm²	17
Elongation at break (DIN 53455)	%	> 30
Flexural modulus (DIN 53457)	N/mm²	1850
Thermal properties		
Thermal conductivity (DIN 52612)	W/mK	0.17
Thermal coefficient of linear expansion (DIN 53752)	10^{-5}/K	8-10
Specific heat	kJ/kgK	1.2
Other properties		
Density (DIN 53479)	g/cm³	1.05
Sheet thickness tolerance	mm	< 0.03 + 0.04 x thickness

Table 4 HIPS (Metzoplast SB/HK) properties from supplier's (Metzeler) datasheet

To check the validity of some results since the material specifications of the supplier are based on the raw material at ISO conditions instead of on the extruded sheet and at thermoforming conditions, additional tests are performed.

3.2.5.1 Differential scanning calorimetry

Differential scanning calorimetry (DSC) measurements are performed to quantify the glass transition temperature (T_g) and the specific heat (C_p) of the material. The latter value is needed for (thermal) simulation. The equipment used is a DSC Q2000 from TA instruments. Samples of 5-10 mg were subjected to a heat-cool-heat cycle at a rate of 10 °C/min under nitrogen atmosphere to avoid thermal degradation. At each cycle transition the temperature of the sample is kept constant during five minutes guaranteeing a uniform and constant temperature throughout the sample. The DSC experiments reveal a T_g of 97 °C and a specific heat capacity between 1.34 and 2.5 kJ/kgK depending on the temperature (Figure 14).

In the forming temperature range of HIPS (130-160 °C), the average C_p is 2.25 kJ/kgK, a value that can be used for simulation purposes.

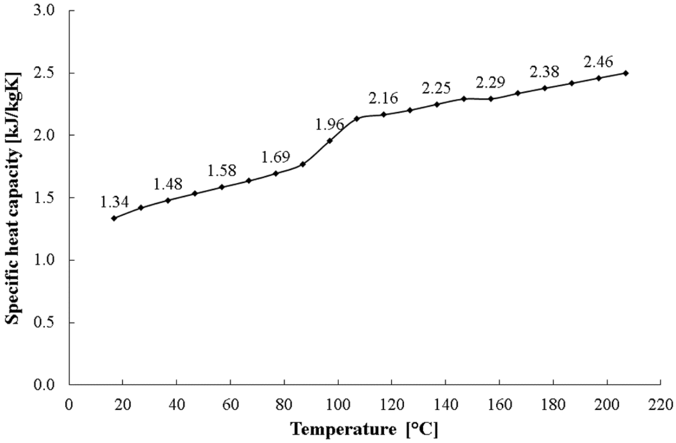

Figure 14 Specific heat as function of temperature for HIPS

3.2.5.2 Emissivity measurements

Material emissivity is measured by heating the HIPS sheet inside a convection oven to a temperature of around 70 °C and measuring the temperature of the sheet and that of a part of the sheet covered with a tape with known emissivity with a thermal camera. The setup is placed in a cardboard box (painted black on the inside) to avoid reflections from the oven enclosure affecting the measurements. A temperature of 70 °C instead of ambient temperature is chosen to maximise the effect of the differing emissivity. The higher the surrounding temperature, the higher a small difference in emissivity will be noticeable on the measured temperature. This temperature is also the upper limit due to the thermal specifications of the used tape. In our experiments, black vinyl electrical insulation tape is used with a known emissivity of 0.97. The insulation tape is a cost effective and easy to use alternative compared to using a perfect black body [150]. After an initial heating time of 30 minutes, allowing the oven and the material to acquire a homogeneous temperature, the oven window is opened and a thermal camera (OPTRIS PI400) records, at a frame rate of 27 Hz, thermal images during 10 seconds (Figure 15).

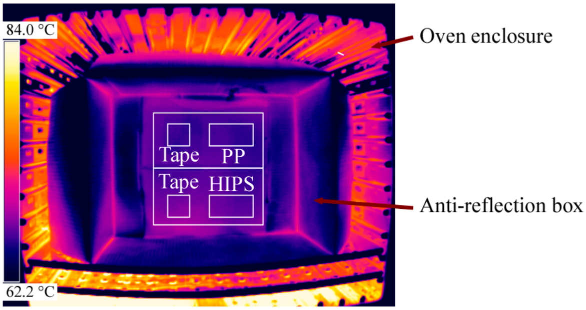

Figure 15 Infrared image taken at an emissivity 0.97 and used to define the emissivity of HIPS

The maximum temperature drop during this time is below 2 °C. The recording of the tape is performed at the known emissivity (0.97), leading to the correct temperature reading of the zone that is covered by it (taking into account the ±2 °C accuracy of the sensor). The average emissivity of the uncovered part of material during the 10 seconds period is defined by adjusting the emissivity of that area until the same temperature profile is found as for the tape. By using this approach, the average emissivity of 5 measurements for HIPS is recorded to be 0.96±0.02 (95 % confidence interval). This emissivity value is used for all thermal measurements on HIPS in this thesis.

3.2.5.3 Mechanical characterisation of the material at ambient temperature

Due to the extrusion and subsequent calendaring process, the latter being inherent to get a smooth surface and accurate thickness, a preferential orientation in the extrusion direction is induced in the sheet. This results, after restricted cooling, in residual internal stresses. If this orientation effect in the sheet is excessive, the residual stresses in the clamped sheet can be so elevated that it can be physically pulled from the clamping frame during the heating cycle of the thermoforming process [1]. To quantify the magnitude of the residual stresses, tensile tests are performed on ten ISO 527 tensile specimens cut in the extrusion direction and ten samples cut in the transverse direction. The samples are both cut and tested in a randomised way to minimise systematic errors (Figure 16).

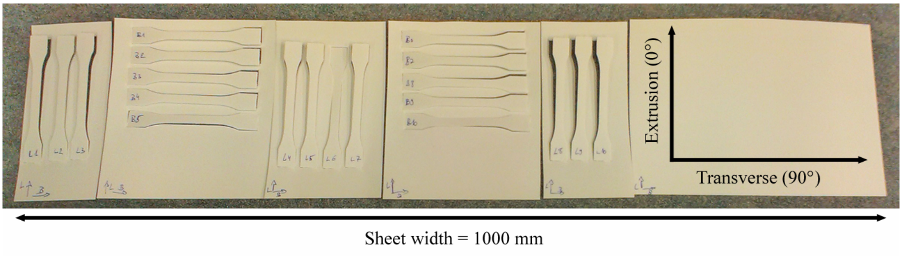

Figure 16 Randomised ISO 527 tensile specimens in extrusion and transverse direction

The tensile test is performed under ISO conditions in an acclimatised room (23 °C and 50 % humidity) on a Galdabini tensile machine equipped with an extensometer and a 50 kN load cell. The samples are pre-loaded up to 25 N at a speed of 2 mm/min, drawn at 1 mm/min for the first 250 µm in order to have an accurate Young's modulus measurement and finally the tensile test is immediately sped up to 50 mm/min until failure. The results of the tested samples are presented in Figure 17 (left). From the stress deformation curves it is clear that there is a significant difference in the amount of tension needed to deform the samples cut in both directions. Higher tensile stresses are required to deform the samples in extrusion direction. Also a slightly higher Young's modulus and elongation at break is measured for the samples in extrusion direction. The obtained values are compared with the data from the manufacturer's datasheet stating a stress of 16 MPa at 3 % elongation which lies in between the experimental values at 0° and 90°. The technical specs also state an elongation at break above 35 %, which is in both cases confirmed.

For comparison, the same tensile test is executed with annealed samples in both 0° and 90° directions. The annealing procedure is as follows: virgin sheets are placed unclamped between two friction free aluminium plates spaced at 1.5 mm from each other. The sandwich structure is placed in a forced convection oven at 150 °C during 5 minutes, allowing for the residual stresses to relax and the sheet to shrink. Possible excessive curling of the sheet is prevented by the aluminium plates. After cooling down the sheets and repeating the same procedure 3 times, all residual stresses can be considered reduced to a minimum. The tensile samples are punched from the annealed sheet and the results of tensile tests show, as expected, negligible differences between the two directions (Figure 17, right).

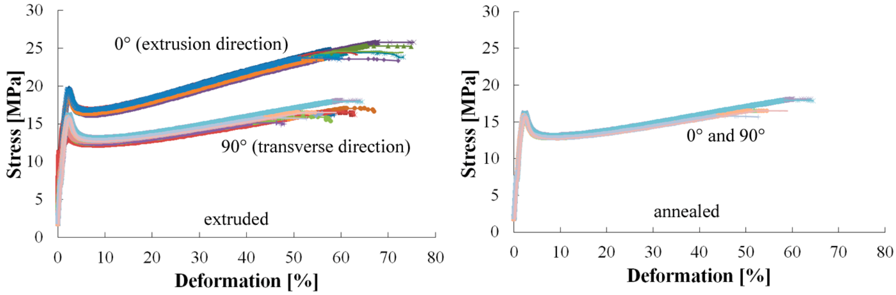

Figure 17 Left: stress deformation curves for 0° and 90° extruded ISO 527 tensile specimens; right: stress deformation curves of annealed samples in both 0° and 90°

To quantify the effect of this anisotropy, shrinkage experiments have been performed. Six samples of 150 x 150 mm are cut from different locations in the width direction of a 1 mm thick extruded HIPS sheet. A 50 x 50 mm square grid pattern is drawn on the surface and the thickness is measured on the 9 crossing points of the square grid with a Mitutoyo Digimatic indicator ID-130M with a resolution of 0.001 mm and an accuracy of 0.002 mm (Figure 18).

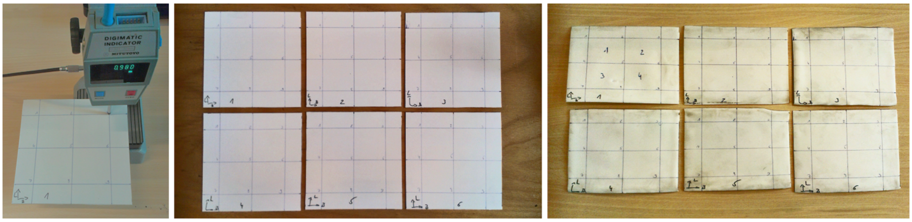

Figure 18 Left: thickness measurement on the 9 nodes of the 50 x 50 mm square pattern; Middle: virgin 150 x 150 mm sample plates; right: annealed sample plates

The initial average thickness is 0.980±0.025 mm (95 % confidence level), lying well within manufacturing specifications (1±0.07 mm). Worth mentioning is a decrease in initial thickness depending on to the location of the cut samples. Samples cut on one side of the sheet are thinner than samples on the other (Figure 19, middle). This is a result of the extrusion process. The small difference in thickness obviously influences the volume of the sheets and the final thickness after forming, but this does not affect further volume measurements. After a similar annealing procedure as for the tensile specimen, the width and length of the drawn squares are measured with a Mitutoyo CD-series calliper with a resolution of

0.01 mm and an accuracy of 0.02 mm. The thickness of the sheet is again measured similarly to that of the virgin sheets. All values are compared to the initial values to be able to quantify the directional dependant shrinkage (Figure 19). In the extrusion direction a shrinkage ratio of over 20 % is measured, in transverse direction the samples are expanded approximately 5 % and in thickness direction the sheet expanded on average 21.5 %. When comparing initial volume and volume after annealing based on previous values, it can be concluded that, keeping in mind the standard deviation, the volume remains unchanged.

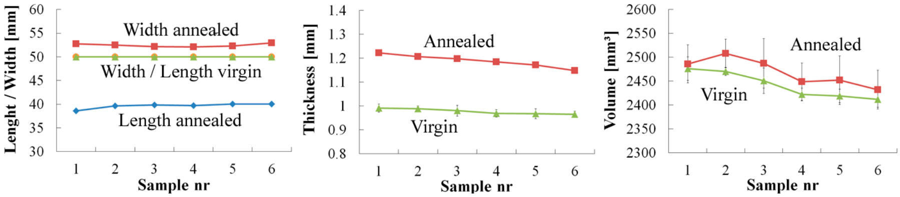

Figure 19 Shrinkage values for the considered HIPS (virgin versus annealed sheet): in length and width direction (left) in thickness direction (middle) and the effect on the total volume (right)

One critical reflection on this test has to be made. Since the test is performed in quasi-static conditions, possible strain rate related phenomena such as void formation and severe chain alignment which could occur in actual forming processes are not included. The same is valid for crystallisation effects for semi-crystalline polymers. On the other hand, heavy gauge thermoforming most of the time does not involve very high strain rates and those phenomena are therefore less expected. Nevertheless, the resulting thickness from DIC measurements is validated with conventional thickness measurements in Section 4.2.5.2.

3.2.5.4 Mechanical characterisation of material at forming temperature

Next to the material characterisation at ambient temperature, data on the behaviour of the material around forming temperature is also of importance, especially for simulation purposes. Most of the dedicated thermoforming simulation software packages use a non-linear viscoelastic material model (K-BKZ). In this context, characterisation of the material used in this thesis is performed by the researchers of the Institut für Kunststofftechnik (IKT) in Stuttgart using a dedicated thermoforming material characterisation apparatus (TMC, Figure 20, [9]).

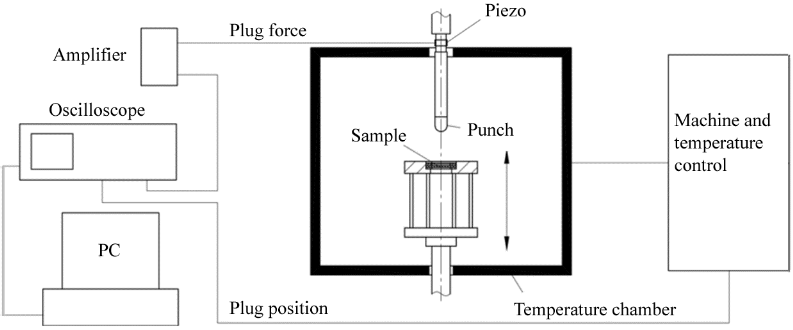

Figure 20 Schematic representation of the TMC apparatus (translated from [9])

The test starts by clamping a small sample of the material (100 x 100 x 1 mm) inside a temperature chamber at a certain temperature for a predefined period allowing the sheet to heat homogenously through the thickness. Next, a hemispherical steel punch is moved at a predefined speed into the material. The force and displacement data of the plunger is recorded for 3 different temperatures (130, 140 and 150 °C) and three different speeds (20, 200 and 500 mm/s). The obtained data is then used in an automated fitting program based on simulations that iteratively fits (Least Square Method) the K-BKZ parameters until the same material behaviour as that from the plugging experiment is obtained. This iterative fitting is performed by Accuform, a company in the Czech Republic. The schematic of such a fitting and an example of the match between measured and simulated force as function of deformation are represented in Figure 21. A detailed explanation of the fitting procedure can be found in [151].

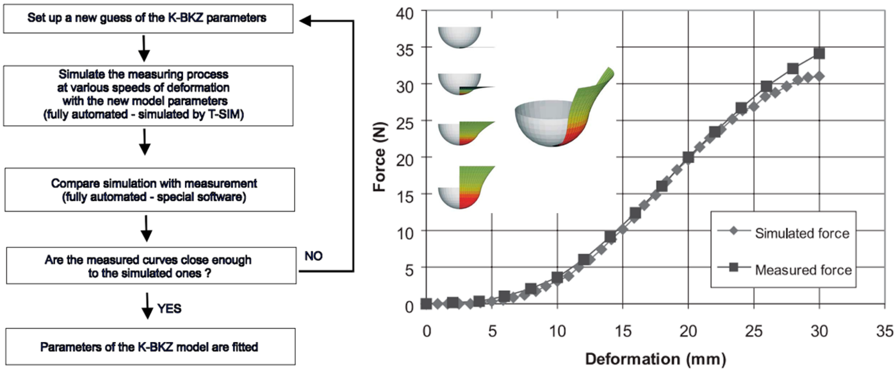

Figure 21 Schematic representation of the K-BKZ fitting procedure [151]

The adopted material model is the K-BKZ Wagner II model, a modified version of the Wagner I model including strain hardening effects [152], with 12 pairs of relaxation moduli as function of time. Temperature effects are included by the Williams-Landel-Ferry (WLF) temperature dependency of the material parameters [153]. The time-integral constitutive K-BKZ equation is described by Equation (9):

$$\tau = \int_{-\infty}^{t} m(t-t')h(I_1,I_2)C^{-1}(t')\,dt' \tag{9}$$

where τ is the resulting stress, *m(t-t')* is the memory function, *h* is in this case the Wagner II damping function and C^{-1} is the left Cauchy-Green strain tensor. The memory function can be written as a sum of exponential functions involving couples of relaxation times (λ_k) and relaxation moduli (a_k) for *N* relaxation modes (Equation (10)):

$$m(t-t') = \sum_{k=1}^{N} \frac{a_k}{\lambda_k} e^{\left(-\frac{t-t'}{\lambda_k}\right)} \tag{10}$$

The Wagner II damping function h is defined by two parameters α and β and the two strain invariants I_1 and I_2 (Equation (11) [154]):

$$h(I_1,I_2) = \frac{1}{exp(\beta\sqrt{\alpha I_1 + (1-\alpha)I_2 - 3})} \tag{11}$$

An overview of the fitted material parameters are listed in Table 5. Damping is not included since the α and β coefficients from the damping function are set to zero. Unfortunately, the accuracy of the fitted parameters cannot be assessed since the simulated force-displacement curves are not disclosed by Accuform.

k	**λ_k [s]**	**a_k [Pa]**
1	0.0237	78.58
2	0.0273	647.50
3	0.0316	4200.13
4	0.0365	13939.10
5	0.0421	18707
6	0.0486	8389.19
7	0.0562	865.75
8	0.1	303762
9	1.3335	430.16
10	1.5399	68708.60
11	1.7782	26794.80
12	2.0535	191.19

Table 5 Relaxation spectra for HIPS (Metzoplast SB/HK) from material testing at IKT; α and β = 0, WLF parameters: $C_1 = 5$ *K,* $C_2 = 80$ *K with reference temperature* $T_{ref} = 140$ *°C*

Next to the characterised data, also the default material parameters for HIPS from the material databases of T-Sim (Accuform) and Formview (Rheoware) are used (Table 6). For T-Sim these are characterised by the K-BKZ Wagner I model with 8 pairs of relaxation moduli as function of time. The Wagner I damping function can be written as (Equation (12)) [83, 155]:

$$h(I_1, I_2) = \frac{1}{1 + \alpha\sqrt{(I_1 - 3)(I_2 - 3)}} \tag{12}$$

k	**λ_k [s]**	**a_k [Pa]**
1	0.0001	934853
2	0.0012	206823
3	0.017	177543
4	0.24	122675
5	3.3	36507
6	47	4653
7	640	80
8	8920	7.23

Table 6 Relaxation spectra for HIPS from the T-Sim material database; α = 0.001, WLF parameters: $C_1 = 17.44$ *K,* $C_2 = 51.6$ *K with reference temperature* $T_{ref} = 140$ *°C*

Formview also uses a K-BKZ model but with Papanastasiou damping [156]. The damping function is described in Equation (13), the material parameters in Table 7.

$$h(I_1, I_2) = \frac{\alpha}{\alpha - 3 + \beta I_1 + (1 - \beta) I_2} \tag{13}$$

The material parameters for Formview, with WLF dependency, are defined by oscillatory shear tests, the damping parameters are based on elongational characterisation.

k	λ_k [s]	a_k [Pa]
1	0.0028	506200
2	0.0346	83300
3	0.4212	69300
4	5.1270	52400
5	62.4010	18200
6	759.4881	400

Table 7 Relaxation spectra for HIPS from the material database of Formview; $\alpha = 20$ and $\beta = 0.9$, WLF parameters: $C_1 = 10.09$ K, $C_2 = 66.81$ K with reference temperature $T_{ref} = 140$ °C

3.2.6 Thermoforming simulation software

During the research several dedicated simulation software packages are used. i.e. T-Sim version 4.82 (Accuform), Polyflow release 15 (Ansys) and Formview version 9.1 (Rheoware). Those packages all use a membrane (or shell) representation and assume constant volume. The constant volume assumption has been recently questioned by Nixon and Menary [157] based on measurements of PET for blow moulding applications. They proved that in uniaxial extension the volume decreases, while for biaxial extension, the volume increases. The authors attribute this effect to strain rate induced crystallisation. Since for all tests in this thesis an amorphous material is used, these changes in the Poisson ratio are not expected and are therefore neglected. As mentioned in Section 2.3, different thermoforming simulation software packages require in general similar input data. The typical input values and software specificities for a standard thermoforming simulation including heating and cooling but excluding warpage for the different software solutions are given in Table 8. For the sake of completeness, data from ESI's PAM-FORM is also added.

The ease of performing a simulation is in descending order: T-Sim, Formview, PAM-FORM and Polyflow. It has to be remarked that ease of use is a priori not a guarantee for good simulation results. A typical simulation in T-Sim requires 5 steps: definition of the sheet, definition of the mould, definition of the material parameters, definition of the process condition and finally, definition of friction and convection coefficients. The mesh for both sheet and mould is automatically generated. Simulation in Formview is similar except that also the heater banks can be modelled and the heating step can be simulated. Besides, the process settings include variable surrounding conditions (temperature, convection) in every step of the process, parameters that are fixed values during the complete simulation in T-Sim. Polyflow is not as user friendly and visually attractive and needs some more experience and time both for process setup and for meshing. Additionally, parameters for slip including penalty coefficients and penetration accuracy need also to be provided by the user. The ease of use of PAM-FORM is similar to that of Polyflow.

The output parameters from all software packages are comparable, the most important are the thickness and temperature distribution, resulting stresses, sheet extension and a visualisation of the contact nodes making it easier to evaluate whether the mould is completely replicated or not. All results are consultable for every intermediate calculation step and can be exported to other finite element codes for post-processing purposes.

An accurate knowledge of all the parameters that are mandatory to start a simulation is critical. Without process insight those parameters need to be retrieved from literature or are based on the expertise of the person making the simulations. Combined measurements of temperature, pressure and deformation can help in the better understanding of the parameters and in improving the process. Details on how this can be done are given in Chapter 6.

3.3 Conclusions

An overview was presented of the reasons why the combination of temperature, pressure and deformation measurements is important and how these measurements are implemented. Knowledge of what is happening during heating and forming is mandatory to get more process insight and to improve the process itself or to be able to estimate realistic values for heavy gauge thermoforming simulations. Chapter 5 and Chapter 6 will elaborate on how this is achieved during respectively experimental optimisation and optimisation through simulation, but first the DIC methodology is explained in detail in Chapter 4.

	Accuform - T-SIM	Ansys - POLYFLOW	Rheoware - FORMVIEW	ESI - PAM-FORM
Sheet definition				
Sheet length and width	User defined			
Initial sheet thickness distribution	Locally adjustable			
Initial sheet temperature distribution	Locally adjustable			
Clamping	User defined on node level	User defined on node level	Contour clamped or 2 edge clamped	User defined on node level
Sheet mesh	2D triangle elements	2D triangle or quad elements	2D triangle elements	2D triangle or quad elements
Multilayer material	No	Yes	Yes	Yes
Material definition				
Available models	K-BKZ Wagner I or Wagner II	Generalised Newtonian, Hyperelastic, linear viscoelastic, K-BKZ	K-BKZ Papanastasiou, Christensen, Mooney, Ogden	G'Sell and Ogden
Temperature dependency	WLF	WLF, Arhenius	WLF, Arhenius	Linear interpolation from test data
Density	Fixed value	As function of temperature	As function of temperature	As function of temperature
Heat capacity	Fixed value	As function of temperature	As function of temperature	As function of temperature
Thermal conductivity	Fixed value	As function of temperature	Fixed value	As function of temperature
Linear expansion coefficient	No	As function of temperature	As function of temperature	As function of temperature
Crystallinity	No	No	Yes	No
Mould definition				
Temperature	Uniform or in zones			
Heat transfer coefficient	Fixed value for whole mould	Variable per zone	Variable per zone	Variable per zone
Thermal conductivity within tool	No	Not within Polyflow	No	Yes
Friction coefficient with sheet material	Fixed Coulomb friction	Friction pressure, temperature and velocity dependent	Coulomb friction as function of temperature	Coulomb friction as function of temperature, pressure and velocity
Contact	Software defined	User defined	Software defined	User defined
Heating simulation				
Model heaters	No	Not within Polyflow	Yes	Not within PAM-FORM
Simulate IR heating	No	Not within Polyflow	Yes	Not within PAM-FORM
Heating parameters	N/A	N/A	Oven size, distance, number of elements, emissivity, temperature	N/A
Transfer from heating to forming	Waiting time at forming temperature	Waiting time at forming temperature	Yes, including convection coefficients	Waiting time at forming temperature
Process parameters				
Mould	Position as function of time			
Pressure (positive and negative)	As function of time			
Ambient air temperature	Fixed	As function of time	As function of time	As function of time
Convective heat transfer coefficient ambient air / material	Fixed	As function of time and different for upper and lower side of sheet	As function of time and different for upper and lower side of sheet	As function of time and different for upper and lower side of sheet
Gravity	Always included	Used defined	User defined	Used defined
Various				
Mesh refinement	Manually after each simulation iteration	Automatic during simulation	Manually after each simulation iteration	Automatic during simulation
Calculation time for 18000 triangular elements and equivalent simulation settings on a standard laptop	+/- 10 minutes	+/- 60 minutes	+/- 40 minutes	+/- 60 minutes (data from ESI)

Table 8 Overview of limitations, possibilities and input values for the four most used dedicated thermoforming simulation software package

Chapter 4 - Stereo DIC in thermoforming

4.1 Introduction

Digital image correlation is an optical non-contact technique to measure surface displacements and strains that started its development in the 1980’s [158-162]. In later years the quality of the correlation results were assessed, more powerful correlation algorithms were developed and compared [136, 137, 163-169] and the importance of stereo correlation [170] rose thanks to the application of a simple and flexible calibration procedure developed by Zhang [135]. DIC and especially the virtual fields method [171] have proven to be extremely important to characterise local strains and stresses in anisotropic materials. More recently the focus is more and more on the evaluation of the calculation accuracy, the estimation of sources of errors and the matching of DIC data to finite element code simulations [132, 136, 140, 172-177]. The most recent publications on DIC which could be interesting for thermoforming, combine different imaging techniques [178] or self-adaptive global DIC in combination with an adaptive mesh instead of using fixed subsets as in local DIC [179]. The main advantage of this self-adapting approach is that the results of the correlation are less dependent on the size of the chosen subset and thus on the experience of the user, making DIC easier applicable in an industrial environment.

DIC is widely used in experimental mechanics and in material science. It is one of the most applied optical measurement technologies and demonstrates increasingly broad application prospects [137]. Application of stereo digital image correlation in thermoforming is nevertheless limited. Besides the author’s publications on that topic [126, 127, 180, 181], only one related work is known to the author [182]. In the latter study the full potential of in-situ measurements is not exploited since only the full-field strain field at the end of the thermoforming process is evaluated. In order to apply DIC for thermoforming processes, a number of specific challenges need to be overcome. An overview of the challenges and the solutions are given in the next sections. A practical guide for the use of stereo DIC in thermoforming applications is attached in Appendix A.

4.2 DIC applied to thermoforming

Stereo digital image correlation applied to thermoplastic thermoforming involves a number of specific challenges. This section explains how to: (i) apply suitable speckle patterns, (ii) ensure appropriate lighting conditions, (iii) deal with the effect of heat waves, (iv) tackle large three dimensional displacements resulting in large depth of field (DOF) and field of view (FOV), (v) convert measured strain into full-field sheet thickness distributions.

4.2.1 Speckling

4.2.1.1 Paint and application technique

A ‘good’ speckle pattern is critical for image correlations. Different studies on the quality of a speckle pattern have been conducted in the last 10 years [183-188]. A common rule for stable DIC measurements is that the speckle pattern should be random, non-repetitive and isotropic, the contrast with the substrate should be high and it must deform together with the sample without reinforcing or weakening the substrate. For thermoforming applications in particular, some additional criteria come into play. The speckle pattern should be temperature resistant: no discoloration is allowed and it should be non-toxic at the forming range of the polymer sheet (an overview of typical forming ranges for the most common thermoforming polymers is added in Appendix B). The pattern should be able to withstand high strains up to 500 % and strain rates between 0.01 and 10 /s without cracking [1]. It should be able to impeccably bind with the polymer sheets and last but not least when looking at it from an industrial context, it should be cheap, fast and easy to apply. Since matte white HIPS sheets are used during the thermoforming experiments, only the speckle itself needs to be applied and the sheet serves as the contrasting background. To evaluate the different speckling formulations and techniques, an experimental qualitative test scheme is drafted and carried out. The procedure consist of evaluating the speckle pattern after high strain (up to 400 % where possible) tensile tests of injection moulded polymer samples (polypropylene for its poor bondability and high extensibility, polystyrene for its wide usage in thermoforming and polycarbonate for its high forming temperature) at room and at forming temperature (Figure 22).

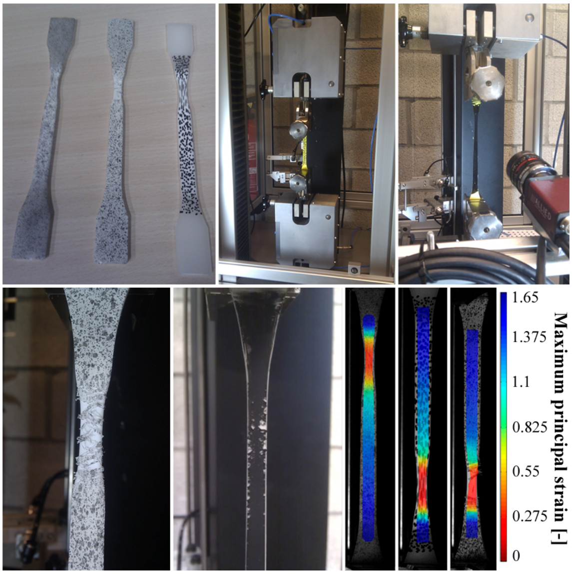

Figure 22 Some examples of tensile specimens with different speckling techniques

Next, an evaluation is made of three different speckling techniques: spraying, (silkscreen)printing and hand marking. The combination of all tests leads to a qualitative ranking (Table 9).

		Temperature resistant (no discoloration)	Strain resistant (no cracking or discoloration)	Good bonding with thermoplastic	Ease of application	Speed of application	Price	Applicable as a random, non-repetitive, isotropic, high contrast speckle	Non toxicity
1	Standard spray can paint (Motip)	🟥	🟥	🟧	🟩	🟩	🟩	🟩	🟩
2	High temperature spray can paint (Dupli-Color)	🟩	🟧	🟧	🟩	🟩	🟩	🟩	🟩
3	Standard spraygun paint (water based)	🟧	🟥	🟥	🟧	🟩	🟩	🟩	🟩
4	Manually applied permanent marker	🟩	🟧	🟩	🟩	🟧	🟩	🟧	🟧
5	Manually applied printing toner	🟩	🟩	🟧	🟥	🟧	🟧	🟩	🟩
6	Silicone applied with toothbrush	🟩	🟩	🟧	🟥	🟥	🟩	🟧	🟩
7	Custom-made polymer spraygun paint (Flanders Color)	🟩	🟩	🟩	🟧	🟩	🟩	🟩	🟩
8	Silk screen printing with custom-made paint	🟩	🟩	🟩	🟩	🟩	🟥	🟩	🟩
9	Digital printing (UV curable inks)	🟩	🟩	🟩	🟩	🟩	🟥	🟩	🟩

Table 9 Properties comparison between different speckling materials and application techniques

The boxes in the table are visually categorised in good (green), medium (orange) and bad (red) agreement with the requirements. Since the standard speckling solutions found in literature (number 1 to 6 in Table 9) all have one or more critical drawbacks, a spraypaint based on an elastic acrylic emulsion is made. It is filled with additives to reduce the surface tension and to optimise the flow by reducing the viscosity and was chosen to be the best match for all requirements except for the ease of application. The base colour of the custom-made acrylic spraypaint is transparent, so by adding the necessary pigment, any colour can be made, the same is valid for the (unwanted) gloss level of the paint. The paint is produced by Flanders Color and known under the name F122304 WB Elastic ACRYLIC. The advantage of using a spraygun instead of spray cans is that it allows more control over the speckle size since the nozzle and the applied pressure can be chosen according to the needs. For industrial applications however, spraygun application is not really an option. In that case, silkscreen printing (with the custom paint) or digital printing are more recommended but come at a higher cost. In the former case a printing template is necessary. Digital printing is the most expensive option, but from an industrial point of view probably the most favourable. Printing inks that meet all the abovementioned requirements are commercially available, one example is the VUTEk GS-TF ink from EFI [189]. The recently developed UV curable ink Uvijet KV from Fujifilm also promises to be applicable, claiming strains over 500 % without cracking [190]. Stretchable self-adhesive films are omitted from the list since they tend to separate from the surface at higher temperatures due to unequal thermal expansion and shrinkage.

If a transparent thermoforming material would be used, a base coat of paint covering the whole surface should be applied prior the application of the speckles. To investigate the influence of such a thin base coat on the substrate material, uniaxial tensile tests are performed on samples with and without the coating. The resulting stress and strain differences proved to be insignificant.

4.2.1.2 Speckle size

Next to the appropriate paint and application technique, also the size of the speckles should be well under control. Spray painted speckles are the easiest to apply but do not allow control over the size of the speckles. In some cases during this research, the speckles were painted using a laser cut masking pattern or they were printed directly on the substrate. In the case a masking or printing pattern is used, the speckles are designed to be stochastic elliptical or circular. In the case of the elliptical pattern, the minor axis of the undeformed speckles at starting distance from the cameras corresponds to at least 4 x 4 pixels. This size is just above the minimum speckle size of 3 x 3 pixels as described in Section 3.2.4. The oversizing of the speckles already takes into account the increasing distance of the blank with respect to the cameras for example during sagging, leading to speckle size reduction without going below the 3 x 3 pixels limit. A typical subset compromises approximately 3 x 3 speckles. The step size is chosen so that a reasonable accuracy in the subset matching process is ensured. A typical value is 1/3rd of the subset size or lower. To validate the proposed pattern, a qualitative comparison between spray-painted and printed (or pattern sprayed) speckles is presented in the next section.

4.2.1.3 Printing versus spraying

To evaluate the influence of printed speckles instead of spray painted speckles on the correlation accuracy, a 2D laboratory setup with a single camera, a 25 mm fixed focal length lens and an aperture f-number of f/1.4 (small depth of field) is used. The f-number is the ratio of the lens's focal length to the diameter of the entrance pupil. Three sample plates of 100 x 100 mm are prepared: one with a lightly sprayed pattern (low speckle density), one with a dark sprayed pattern (high speckle density) and one with a dot-printed speckle of 0.78 mm diameter, which corresponds in this particular setup to a diameter of 29 pixels per dot at a distance from the camera of 150 mm. The dot size is vastly larger than the minimum 3 x 3 pixels but artificial compressions up to 130 % are expected in this test, so the safety margin is taken proportional to this value. Each of the three plates are positioned successively perpendicular to the lens. After focusing, a first picture is taken, the plate is moved 1 mm backwards from the camera and the lens is refocused. This procedure is repeated in steps of 1 mm for the first 5 mm, in steps of 5 mm until 170 mm, in steps of 10 mm until 200 mm, in steps of 25 mm until 300 mm and finally in steps of 50 mm until 500 mm. The consecutive pictures are correlated with updated reference pictures (incremental) in MatchID2D using a subset size of 58 pixels (twice the speckle size) and a step size of 9 pixels (1/3th of the speckle size). The calculated average artificial strain (logarithmic Euler-Almansi, strain window 15) values and their corresponding standard deviations over the region of interest, which are in a 2D setup based solely on the backward movement of the plate and the resulting reduction of the speckle size, are plotted in a chart relative to the distance from the camera (Figure 23). More detailed correlation settings can be found in Appendix C. Artificial strain can only be observed in a 2D setup since in a stereo setup the calibration of the cameras and the knowledge of the extrinsic camera parameters would ensure the detection of the imposed backward movement, resulting in rigid body motion instead of increasing compressive strain values. It can be seen that the results of average artificial strain are identical and independent of the speckling method, while the standard deviation of the printed speckle pattern is even lower than that of the sprayed patterns. This small difference is assumed to be a result from the uncontrolled speckle (size) distribution in the sprayed samples in combination with the fixed subset size which leads to results that are more likely to deviate from the mean.

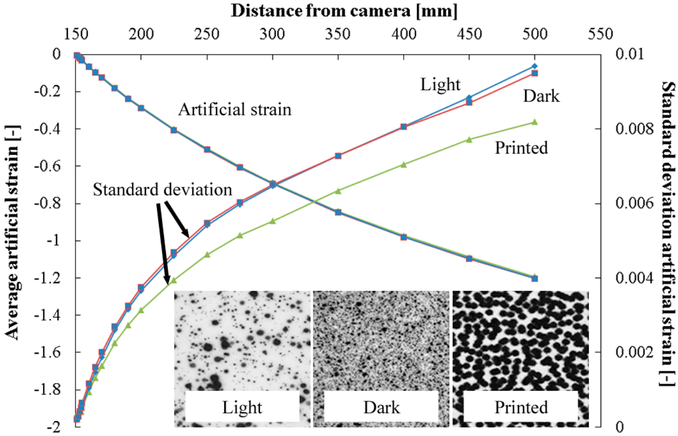

Figure 23 Average artificial strain and standard deviation as function of the camera distance for three different speckle patterns

Artificial strain is used as the correlation quality parameter, since other parameters, such as the average correlation coefficient (R), cannot be used as a qualitative comparison between speckle patterns since it is too much affected by lighting, speckle size, subset size and step size. The correlation coefficient is a measure of the quality of a correlation and the purpose of correlation software is to maximise this coefficient, or to minimise the correlation criterion: $C = 1\text{-}R$ (cf. Equation (3)). Moreover, the correlation coefficient in a correlation using updated references, such as this one, gives an indication of the correlation capabilities between two consecutive pictures but is meaningless when evaluating the overall correlation quality. From these results, it can be concluded that the dot printed pattern, which can be designed according to the needs (size, distribution, density) and which is exactly repeatable, can be used as a good alternative for accurate DIC measurements next to the standard spray painted patterns.

4.2.2 Lighting

4.2.2.1 Histogram

A second, not to be underestimated factor of the DIC measuring principle is the uniformity of the lighting conditions. The choice of optimal lighting conditions in a dynamic process such as thermoforming is not easy since light should be as uniform as possible at the start of the process and it should be so that changes in light, caused by shadows or reflections during the forming process, affect the correlation results as little as possible. The use of diffuse light is strongly recommended. To evaluate the influence of lighting, correlation tests (similar to those of Section 4.2.1.3) are performed with pictures of a fixed spray painted speckle pattern mounted perpendicular to the camera at different shutter times in order to simulate different lighting conditions (shorter shutter times give darker pictures and vice versa). The shutter time is used instead of adjusting the intensity of the light source because it can be controlled much more accurately, uniformly and repeatedly. It was found that the best agreement between correlation capabilities, which means a high average spatial correlation coefficient and a low number of correlation iterations, and shutter time (lighter or darker pictures) should be chosen so that a grey value histogram is achieved with a wide base and no grey values reach the edges of the range (0-255 for an 8 bit camera where 0 is black and 255 is white) even when shadow or reflections occur. These conclusions are in line with those of Pan et al. [187] and Hua et al. [188]. The easiest way to start with this kind of histogram is to choose a fixed lighting and lens aperture (depending on the desired Depth of Field (DOF), see Section 0) and then modify the shutter time until agreement is obtained with the ideal histogram bearing in mind that if the shutter time is increasing, motion blur can occur. When the forming process is too fast and motion blur appears, the main lighting should be increased so that the shutter time can be decreased proportionally and motion blur is minimised. The histograms in Figure 24 clarify this for a spray painted speckle pattern pictured with a shutter time of 4 ms and 6 ms. The brighter the picture (longer shutter time), the more the curve shifts to the bright side (right) of the histogram. When light reflections would occur, the background of the picture taken at 6 ms will directly saturate (grey value >= 255) and this will result in lost correlation. The histogram taken with a shutter time of 4 ms will also shift to the right but will remain within the unsaturated zone.

If small light changes cannot be prevented, the choice of the correlation algorithm can also play an important role. Pan et al. [137] compared in their publication the different correlation criteria (both cross-correlation and squared differences criteria) and concluded that the zero-normalised sum of squared differences (ZNSSD) or the zero-normalised cross-correlation (ZNCC) criterion offer the most robust noise-proof performance and are insensitive to the offset and linear scale in illumination lighting. The normalised sum of squared differences

(NSSD) and the normalised cross-correlation (NCC) criterion are similarly insensitive to the linear scale in illumination, but are sensitive to the offset of the lighting. The sum of squared differences (SSD) and cross-correlation (CC) criterion are on the other hand sensitive to all lighting fluctuations and are therefore not suitable for thermoforming applications. For the consistency of the thesis the most robust (ZNSSD) criterion is chosen for all correlations (see Equation (3)). A summary of the mathematical expressions of the foregoing correlation criteria can be found in [137].

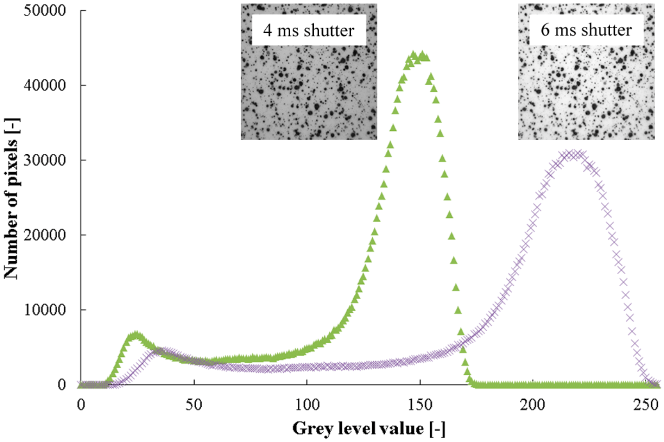

Figure 24 Histogram of a spray painted speckle pattern imaged with 4 ms and 6 ms shutter time

4.2.2.2 Histogram equalisation

When all precautions have been taken to illuminate the object as diffuse and uniform as possible, the right histogram is chosen and the most light insensitive correlation algorithm is used, it is still possible that light changes are in the order of magnitude that the correlation yields correlation coefficients below an acceptable value (0.9 is a good guideline). When retesting is not an option, a final option can be to digitally modify the pictures until correlation converges again. Every digital modification of the picture will come at the cost of a lower accuracy, but in certain cases it is better to have a result that has to be assessed with the necessary precautions than to have no result at all. One way to deal with this is to match the histogram of the reference picture to the pictures that fail to correlate. This can be done with the *histeq* function that is available in Matlab. It is a pixel intensity matching function that can be used to equalise the histogram of the deformed picture to the one of the undeformed picture. Figure 25 shows the effect of this equalisation procedure on the histogram of a reference image (with a perfect grey value distribution taken with a 25 mm focal length lens at 300 mm from the camera with a similar setup as the one used in Section 4.2.1.3) that was darkened by lowering the shutter time, simulating a possible shadow effect.

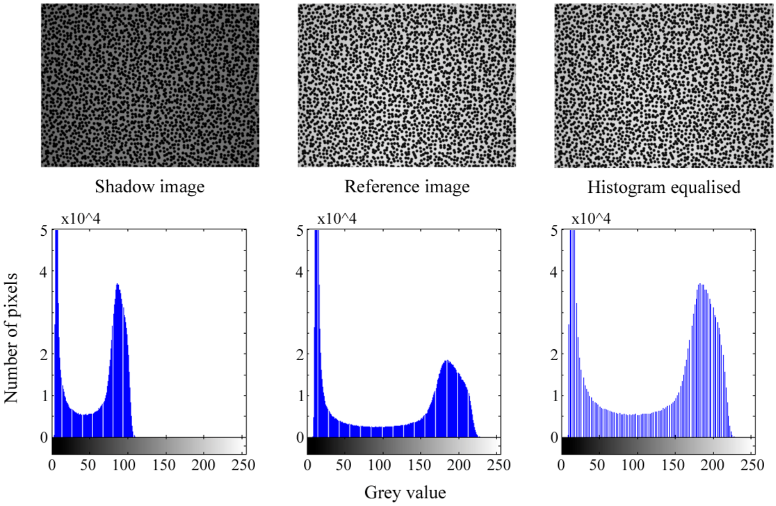

Figure 25 Images and histograms before (left) and after(right) image equalisation. The centre picture is the reference used for equalisation.

In this virtual example, no displacement or strain occurs in reality. A static unloaded self-correlation test revealed a standard deviation of maximum principal strain of 43 µm/m and a mean of the same order of magnitude due to image noise and variations in the surrounding lighting. Those values are evidently negligible to the strains that occur in thermoforming experiments. When correlating the reference picture to the shadow picture with a normalised sum of squared differences algorithm (NSSD), the mean and the standard deviation of maximum principal strain are a factor 10 larger and the average correlation coefficient drops significantly. Some parts of the region of interest are even not correlated at all. When applying the *histeq* function to the darkened picture and correlating the equalised picture to the reference, the total area of the region of interest yields correlation results above the 0.99 threshold and both the mean and standard deviation of strain result in values of the same order of magnitude as those of the self-correlated reference picture. Similar results were found for brighter pictures or pictures that were partially darkened or brightened. Only when parts of the picture are saturated (grey value > 255), the correlation coefficient starts dropping and virtual strain values rise, proving again that care has to be taken not to saturate the pictures.

To demonstrate the effect of the histogram equalisation and the sensitivity of the correlation algorithm, a 2D correlation of a range of pictures going from dark (1 ms shutter time) to bright (19 ms shutter time) is performed with the NSSD, approximated NNSD (ANSSD [191]) and ZNSSD correlation algorithm for both initial pictures and pictures after the equalisation procedure. Figure 26 shows the results in terms of correlation coefficient and calculated thickness. The latter demonstrating what the effect would be if the correlation results are used for thickness calculation starting from a 1 mm initial thickness sheet.

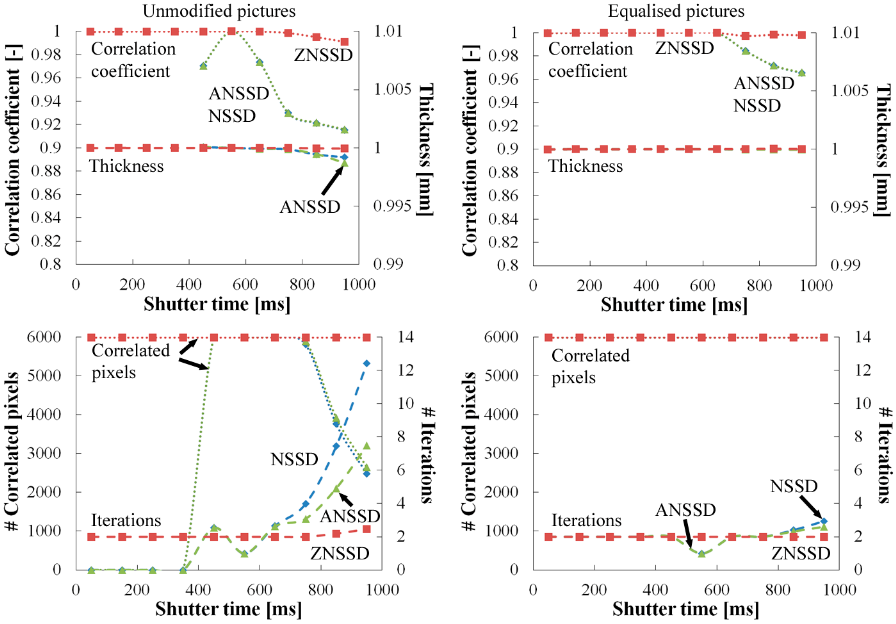

Figure 26 Performance comparison of different correlation algorithms on initial and equalised pictures

From the number of correlated pixels (which equals in the ideal case 5984) it is clear that the equalisation script makes correlation possible for all pictures whereas correlation was not possible or only possible for a part of the picture with the initial pictures. Before equalisation all results for shutter times below 450 ms yielded results below the 0.9 correlation threshold whereas after equalisation all pictures could be correlated. Moreover, the number of iterations reduces drastically after equalisation, making the correlation faster. The impact on the calculated thickness is in this case minimal. Finally this also demonstrates that the ZNSSD algorithm is definitely the most stable when light fluctuations occur. The NSSD needs on average more iterations than the ANSSD for the same result accuracy.

The obtained results reflect the most optimal situation since the effect of displacement and deformation are not included. To illustrate that the equalisation approach is also capable of improving correlation results when displacement and deformation would be included, the experiment is repeated but instead of using the histogram of the picture that is used as the reference for the correlation, the histogram from a totally different speckle pattern (larger speckles) but with approximately the same intensity distribution is chosen (Figure 27). The original reference picture is again correlated with all equalised pictures and the results are plotted in Figure 28. Once again it can be concluded that all pictures can be correlated with a fewer number of iterations and the impact on the thickness is minimal.

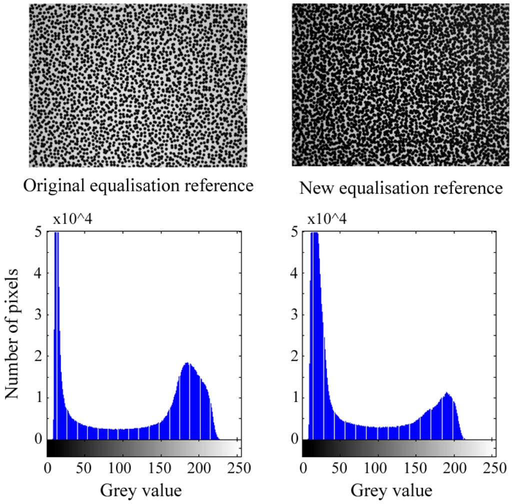

Figure 27 Original and new equalisation reference

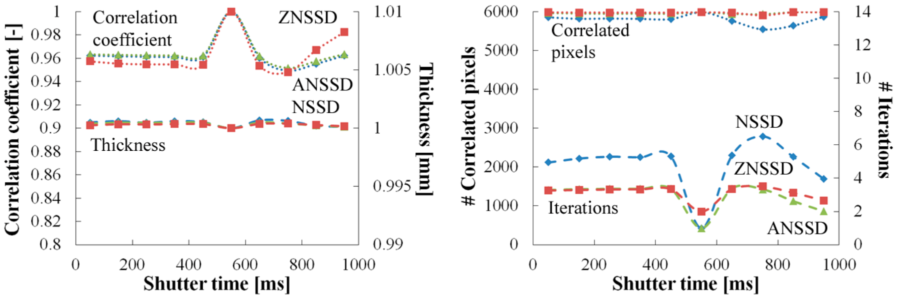

Figure 28 Performance comparison of different correlation algorithms on pictures equalised with a histogram from a different speckle pattern

4.2.3 Influence of temperature

DIC is most of the times used for complex material characterisations where localised strains are to be expected. Typically, the tests are executed in a temperature controlled environment. When using DIC during thermoforming, the aspect of temperature creates an additional difficulty. The heating of the sheet could result in erroneous correlations due to image distortions originating from heat waves or due to brighter or darker images from radiation at higher temperatures. Both effects are explained below.

4.2.3.1 Heat waves

In the ‘90s, Lyons et al. [192] investigated the possibilities of using DIC for high-temperature (600 °C) deformation measurements and concluded that the technique is able to measure deformations but that precautions must be taken to avoid heat waves. Since they measured through the glass window of a furnace, they suggested mixing the air at the proximity of the oven with cooler air in order to minimise the effect of the heat waves. The results of their thermal expansion and tensile tests yielded the same level of accuracy as measurements obtained under ambient conditions. Grant et al. [193] even performed DIC measurements up to 1400 °C but used filters and special blue light. Chen et al. [194] used monochromatic light and special high heat resistant flexible paint for successful metal heating experiments. The paint they developed is however not usable for thermoforming applications since the maximum strain is too low (15 %) and a curing procedure is necessary up to 340 °C for the coating to reach its heat resistance, a temperature that is way above the forming temperature of most of the thermoformable polymers.

To investigate the magnitude of the effect of the heat waves on correlation accuracy, a speckled steel sheet is heated from the bottom side in the thermoforming machine to an average temperature of 200 °C. Once the sheet reaches a stable temperature, a series of 49 pictures (1 Hz) is taken with a single camera mounted perpendicular to the sheet at a distance of 1200 mm inside the thermoforming machine. These pictures are spatially correlated in MatchID2D (more detailed correlation settings can be found in Appendix C). A similar experiment is performed while blowing air gently over the surface of the sheet in order to minimise the heat waves, similar as the approach of Lyon's et al. [192]. The resulting thickness assuming a 1 mm initial thickness, based on the equations from Section 4.2.5, is plotted together with a linear regression curve in Figure 29. With a perfect imaging system and perfect temperature control, the thickness should be equal to 1 mm for all samples since there is no strain, but in realistic circumstances and with the available imaging hardware (resolution and noise) there are some expected variations.

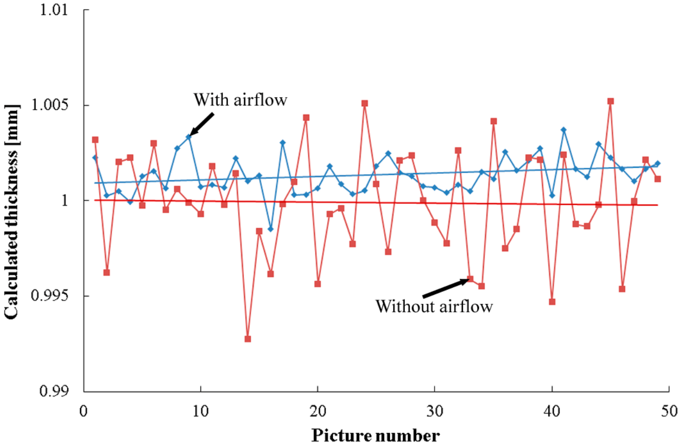

Figure 29 Calculated thickness with and without airflow of a speckled steel sheet at 200 °C

When comparing both data sets, it is clear that the standard deviation on the measurements without air is much higher (by a factor 3) than the dataset with air blown over the surface. The mean is almost equal fluctuating around 0.1 %, which is for heavy gauge thermoforming not an issue since the allowable tolerances on the initial sheet thickness are already much higher. The effects of the heat waves are therefore considered to be negligible and no additional precautions are taken during further experiments to prevent them.

4.2.3.2 Radiation

A second factor that affects measuring accuracy is caused by the fact that when the polymer sheet is heated, the portion of energy that it is radiating will shift more and more from the infrared region (> 0.78 µm) to the visible region. Due to this shift, the imaging sensor will also receive more 'visible' electromagnetic radiation that could affect the measurements. To investigate the extent of this effect, the quantum efficiency of the used imaging sensor (Sony ICX274 progressive scan CCD), which is a measure of the effectiveness of an imaging sensor to produce electronic charges from incident photons, and the spectral radiance as function of temperature and wavelength (according to Planck's law of black body radiation Equation (14)) are overlaid on top of each other in Figure 30.

$$I(\lambda,T) = \frac{2h_P c^2}{\lambda^5}\frac{1}{e^{\left(\frac{h_P c}{\lambda k_B T}\right)}-1} \tag{14}$$

with λ the wavelength, h_P Planck's constant (6.626 x 10^{-34} J/s), c the speed of light (2.998 x 10^8 m/s), k_B the Boltzmann constant (1.381 x 10^{-23} J/K) and T the temperature in Kelvin. It can be seen that the quantum efficiency of the used imaging sensor at standard thermoforming temperatures (below 400 °C) is small and the effects of the shifting spectral radiance peak can be neglected. If the camera would be more sensitive to the infrared zone, an alternative would be to use an infrared cut-off filter.

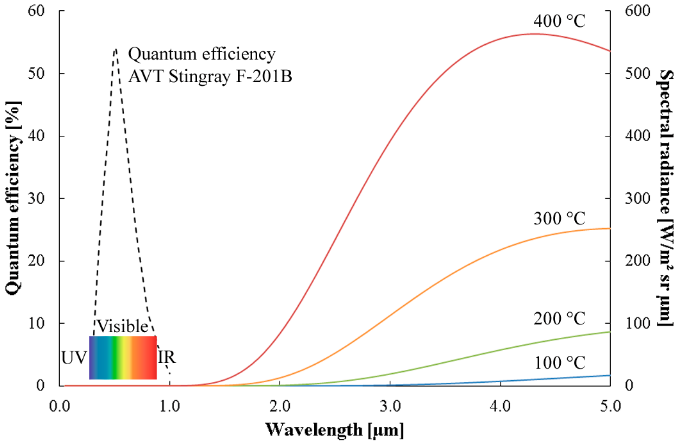

Figure 30 Blackbody radiation curves for different temperatures plotted together with the quantum efficiency of an AVT Stingray F-201 camera sensor as function of wavelength

4.2.4 Field of view and depth of field

Still today, most of the DIC applications involve a 2D single camera setup and special care is taken to position the camera exactly perpendicular to the specimen. The purpose is to reduce out-of-plane displacements since they will be seen as 'virtual' strain in a 2D setup and results will be erroneous. There are a couple of solutions to reduce these errors: the first one is the use of a telecentric lens, a second is to place the camera as far as possible from the specimen since this distance is proportional to the occurring error. When combining a large distance with a lens with a longer focal length, the resolution over the field of view can be optimised. A third solution to reduce the errors originated from a non-perpendicular camera alignment is to use a second camera and perform stereo correlation. With this approach, the out-of-plane displacement will be quantified and will not be evaluated by mistake as 'virtual' strain. Of course adding a second camera and the necessary calibration procedure associated with it, will introduce new sources of errors. It is therefore important to evaluate which of the proposed solutions yields the results with the smallest errors. Interesting papers on error estimation of a non-perpendicular camera alignment are published by Lava et al. [174] and Sutton et al. [195].

4.2.4.1 Theoretical depth of field

In applications where out-of-plane displacements are to be expected, such as in the case of thermoforming, a stereo setup is mandatory. A problem that arises with large out-of-plane displacements is that, since DIC systems typically work with fixed focal length lenses, the pictures can become unsharp and correlation problems may arise. It is well known from photography that the sharpness of a picture can be quantified. One of the many definitions is that a picture is considered sharp as long as it remains within the depth of field (DOF) of the imaging system. The DOF is defined as the range of object distances within which objects are imaged with acceptable sharpness [196]. The DOF is a function of the lens focal length, the distance to the target and the setting of the aperture. High aperture (f-stop) numbers, which means that the aperture is more closed, longer distances to the target and shorter focal lens lengths lead to higher depth of fields. Vice-versa, lower aperture numbers, shorter distances and longer focal length lenses lead to smaller depth of fields. Equations to calculate the DOF of an imaging system were developed long ago but are today still valid [197]. These equation are based on the circle of confusion (CoC) which is an optical spot caused by a cone of light rays from a lens not coming to a perfect focus when imaging a point source. The DOF is then defined as the region where the CoC is less than the resolution of the human eye or of the display medium. In photography, the CoC diameter limit is often defined as the largest blur spot that will still be perceived by the human eye as a point. A visual representation of the depth of field (DOF), the focal length (f) and the circle of confusion (CoC) is shown in Figure 31. The object is focussed at a distance s from the lens, D_n and D_f represents the near and far distance of acceptable sharpness respectively.

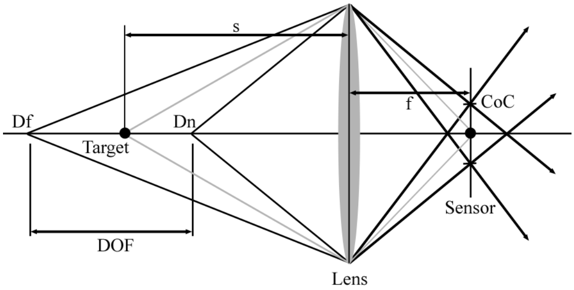

Figure 31 Representation of the depth of field (DOF)

When using the abovementioned definitions, the DOF can be expressed mathematically using Equation (15):

$$DOF = D_f - D_n \tag{15}$$

with

$$D_f = \frac{s * (H - f)}{H - s} \tag{16}$$

$$D_n = \frac{s * (H - f)}{H + s - 2 * f} \tag{17}$$

where *H* represents the hyperfocal distance (in mm) which is mathematically defined as:

$$H = \left(\frac{f^2}{N_A * CoC}\right) + f \tag{18}$$

With N_A the aperture number. The hyperfocal distance is the distance beyond which all objects can be brought within acceptable focus. The results thus obtained are strongly dependent on the chosen CoC, which on its turn depends on the visual acuity of the person who's judging the picture, the viewing conditions and possible enlargements [198]. Typical values for the CoC lie between 0.001 mm for small sensors to almost 0.1 mm for high resolution systems with large imaging sensors. The smaller the CoC is, the more critical the definition is whether an object is within acceptable focus or not and the smaller the resulting DOF will be. Since the CoC value of the Sony ICX274 sensor that is used in this research is not specified on the technical datasheet of the sensor, the generally accepted approximated calculation using the so-called 'Zeiss' formula is used: *CoC = chip diameter (mm) / 1730*. This leads to a CoC of 0.0052 mm. Figure 32 shows the relation between the depth of field, the distance of the object to the camera and the aperture for such a CoC and an 8 mm (left) and a 25 mm (right) focal length lens.

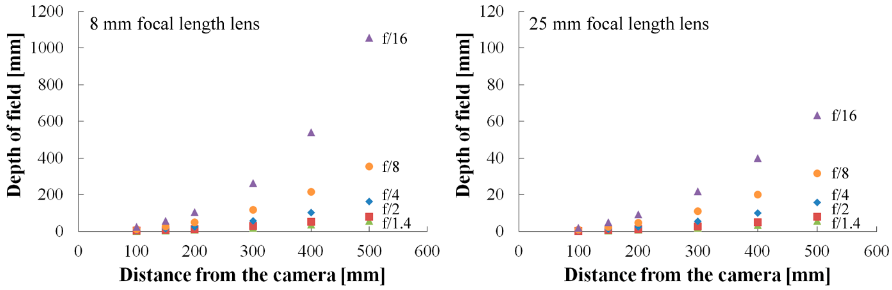

Figure 32 Theoretical depth of field as function of the distance to the camera and aperture for an 8 mm lens (left) and a 25 mm focal length lens (right). Notice the factor 10 difference in scaling for the vertical axis.

4.2.4.2 Experimental depth of field

People performing DIC measurements and expecting large out-of-plane displacements either trust on their experience or use the abovementioned equations to estimate which lens to choose, where to position the camera and how to set the aperture. This approach is of course not bad, but the definition of sharpness based on the CoC, which is a human defined parameter, does not reflect the performance of the correlation system. Besides, it is a well-known fact that pictures that are not perfectly sharp tend to yield better correlation results since the interpolation between pixels, which is necessary to get sub-pixel information, is better when there is a smooth transition in image gradients (soft edges) than with sudden transitions (sharp edges) [132, 199].

Since the pictures used for DIC measurements are not judged on sharpness by people, but are only depending on grey value differences between pixels, the mathematical calculation of the DOF are an approximation and cannot be used as is. To get the correct DOF value that is useful for DIC, a standardised testing method has been designed based on real camera and lens combinations and based on actual image correlation results. To find the exact depth of field that is relevant for DIC applications, as function of focal length, the starting distance and the chosen aperture, a similar 2D setup as used in Section 4.2.1.3 for the evaluation of the difference in quality of a printed and a sprayed speckle pattern is used (more detailed correlation settings can be found in Appendix C). A reference picture of a focussed dot-printed target (dot diameter 29 pixels) is taken at a starting distance from the lens of 150 mm (dot diameter 0.78 mm) using the smallest possible aperture since this corresponds with the smallest depth of field, making focussing easier. Next, the sample is moved backwards and pictures are taken, each time after refocussing. The pictures are correlated in MatchID2D (spatial combined with updated reference correlation) using a subset size of 58 pixels and a step size of 9 pixels. The same procedure is repeated for two other starting distances, i.e. 300 mm and 500 mm with respective dot diameters of 1.56 mm and 2.6 mm, maintaining always the same dot diameter in pixels, making the results independent from the subset and step size. The resulting average, minimal, maximal and standard deviation of the maximum principal strain values (logarithmic Euler-Almansi, strain window 15) are expressed relative to the distance from the starting point in Figure 33. For the sake of completeness: the effect of a smaller or larger subset and step size as well as the strain window size has been assessed. Differences were found in the absolute strain magnitude but the relative results were comparable to those of Figure 33.

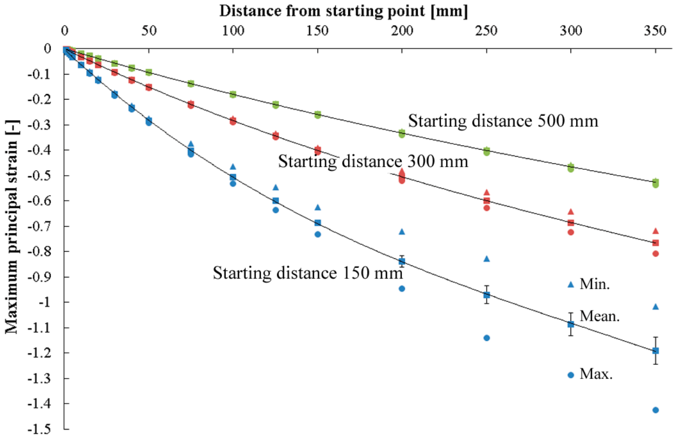

Figure 33 Virtual strain values as function of the distance between the camera and the target for an AVT Stingray F-201 camera with a 25 mm focal length lens and three different starting distances (150, 300 and 500 mm)

A third order polynomial regression function is fitted to the average strain values for each starting distance. This function is used as the reference for further calculations, providing interpolated results on a millimetre scale. In a second step, the same procedure is repeated but without focussing after each displacement. This test is repeated for the combination of different aperture settings (1.4, 2, 4 and 8) and the different starting distances. Once all unfocussed pictures are taken, they are correlated using MatchID2D (using a spatial correlation or a spatial correlation with updated references) and the resulting exported raw data is loaded in an automated custom-made Matlab script. The script loads the maximum principal strain data from the imported results and calculates a cut-off point (see Figure 36) for the achievable depth of field by comparing the third order polynomial regression function of the strain plot of the focussed pictures to the average strain values of the unfocussed pictures.

The cut-off point is based on a deviation from the average fitted function (e.g. 5 %) or on an excessive standard deviation (e.g. twice that of the focussed pictures) of the strain values, depending on which one is first exceeded. These arbitrary values can be increased or decreased depending on how many deviation is tolerated, a factor that depends on the application and the correlation accuracy that is requested. This working principle can be seen as a camera/lens characterisation procedure. Once the cut-off distances are known for different starting distances and apertures, the complete working range in terms of depth of field can be calculated for a specific camera-lens combination. The above procedure needs to be performed only once for each camera-lens combination and provides the user with the complete DOF, interpolated to greater, industrial, distances than the ones used during the laboratory setup and more representative than those calculated based on the CoC.

A typical resulting graph for the setup as described earlier for a 25 mm focal length lens is represented in Figure 34.

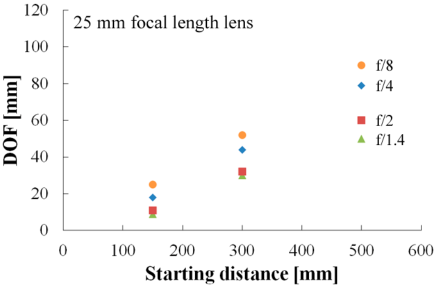

Figure 34 Experimental depth of field as function of the distance to the camera and aperture for an AVT Stingray F-201 camera with a 25 mm focal length lens and a printed 29 pixels speckle pattern

In the author's opinion, although the results are strongly dependent on the chosen parameters that define the cut-off, this new approach gives more reliable results than the approach based on the theoretical calculations and the CoC since this new approach is based on real camera/lens combinations, real speckle patterns and correlation result including the effect of the chosen correlation criteria. When comparing Figure 32 with Figure 34 it can be seen that the achievable DOF is larger than what theoretical calculations predict, making it possible to place the cameras closer to the target (when the FOV allows this), gaining in resolution.

Two critical remarks have to be made on this approach: in order to use the results for actual thermoforming experiments, care has to be taken to use the same settings as used during the camera/lens characterisation (speckle, subset, step, strain window and correlation settings). A second remark is that it is assumed that these tests, based on a 2D setup, can also be used in a stereo setup. This is plausible when a good stereo calibration is performed, since stereo correlation is in fact nothing more than two 2D correlations combined by triangulation and cross-camera matching.

Besides the characterisation of a camera/lens combination and in order to make the approach industrially more applicable, the Matlab code is converted into a graphical user interface and also calculates, when chip size, resolution and lens focal length are given, the field of view as function of the distance to the target. The field of view is easy to approximate with the well-established equations from photography (Equation (19) and (20)):

$$FOV_{width} = \left(\frac{s * sensor\ width}{f}\right) \tag{19}$$

$$FOV_{length} = \left(\frac{s * sensor\ length}{f}\right) \tag{20}$$

When the dimensions of the product to be thermoformed are given, the software provides the user with a minimal distance to place the camera, the lens focal length to choose and the setting of the aperture to use to be able to see the complete FOV and to see with sufficient sharpness during the complete forming process, based on the characterisation measurements. It will always suggest the closest possible location for the camera (based on FOV) to provide the user with the highest possible resolution. When, due to mounting restrictions, the cameras cannot be installed at the proposed distance, the user can manually select a different distance and the software will display the FOV, resolution and DOF at the chosen distance. The program also calculates the appropriate diameter of the speckles to be printed for that specific setup (camera, lens, distance) and it generates a corresponding random speckle pattern with the correct speckle size. Figure 35 shows the graphical user interface that is available for download on the Matlab file exchange website (http://www.mathworks.com/matlabcentral/fileexchange/). The diagram in Figure 36 schematises the complete working principle.

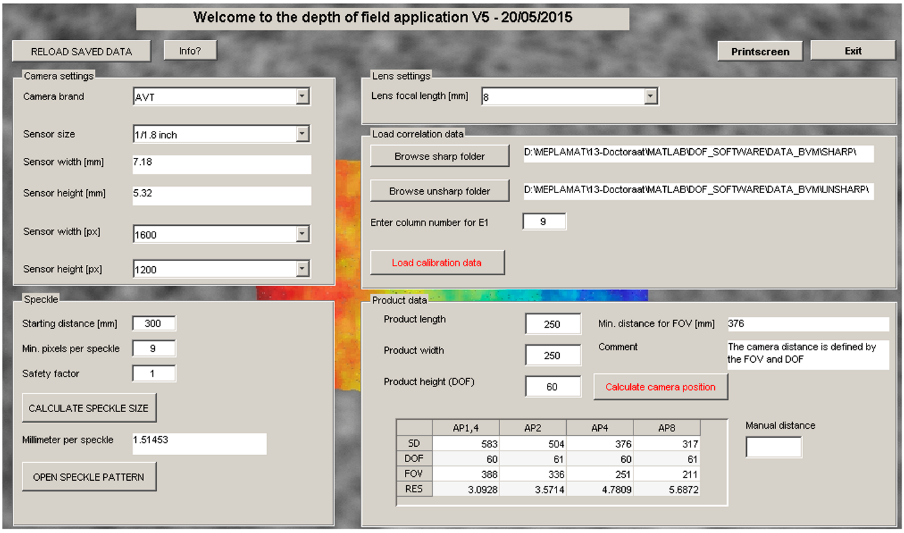

Welcome to the depth of field application V5 - 20/05/2015

Camera settings

Camera brand: AVT

Sensor size: 1/1.8 inch

Sensor width [mm]: 7.18

Sensor height [mm]: 5.32

Sensor width [px]: 1600

Sensor height [px]: 1200

Speckle

Starting distance [mm]: 300

Min. pixels per speckle: 9

Safety factor: 1

Millimeter per speckle: 1.51453

Lens settings

Lens focal length [mm]: 8

Load correlation data

Browse sharp folder: D:\MEPLAMAT\13-Doctoraat\MATLAB\DOF_SOFTWARE\DATA_BVM\SHARP\

Browse unsharp folder: D:\MEPLAMAT\13-Doctoraat\MATLAB\DOF_SOFTWARE\DATA_BVM\UNSHARP\

Enter column number for E1: 9

Product data

Product length: 250

Product width: 250

Product height (DOF): 60

Min. distance for FOV [mm]: 376

Comment: The camera distance is defined by the FOV and DOF

	AP1,4	AP2	AP4	AP8
SD	583	504	376	317
DOF	60	61	60	61
FOV	388	336	251	211
RES	3.0928	3.5714	4.7809	5.6872

Manual distance:

Figure 35 Graphical user interface of the depth of field and field of view calculator created in Matlab

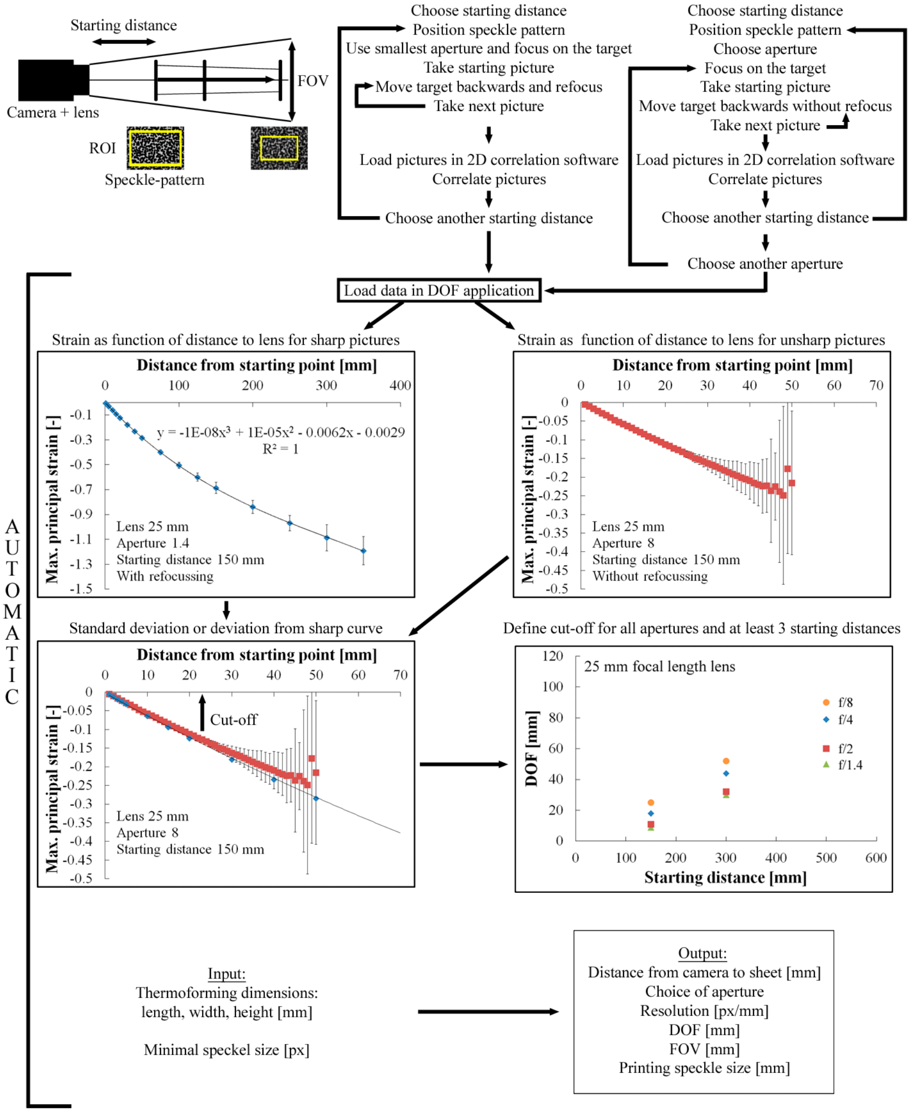

Figure 36 Procedure for the definition of the depth of field of stereo cameras based on 2D DIC measurements. The part indicated as 'automatic' is integrated in the Matlab user interface.

4.2.5 Thickness calculation

As mentioned in the introduction, the thickness distribution is by far the most critical quality parameter of a thermoformed product. To extract full-field thickness distribution from surface strain measurements an important assumption needs to be made. This assumption is that the volume of the sheet is kept constant during thermoforming. This hypothesis is an approximation since during the thermoforming process the sheet reaches a temperature above the glass transition temperature for amorphous polymers or close to the melting temperature for semi-crystalline polymers and this is associated with a certain thermal expansion. Especially for semi-crystalline polymers, the specific volume is therefore affected during heating, forming and cooling. Intermediate thickness calculations would therefore be less accurate than thickness calculations after the product reaches its cooled state. Besides, the crystallinity which also influences the thermal expansion is defined by the cooling rate. Also the draw ratio and the strain rate can influence chain orientation and crystallisation jeopardising the constant volume assumption. Since a significant number of factors influencing the constant volume assumption exist, the validity for the used HIPS grade has been confirmed in Section 3.2.5.3. This is done by comparing initial volume and volume after several annealing cycles of an unclamped HIPS sheet. The resulting thickness from DIC measurements is validated with conventional thickness measurements in Section 4.2.5.2 and 5.3.1.5. Moreover, all main dedicated thermoforming simulation software packages (cf. Table 8) rely on the assumption of volume conservation for thickness predictions.

4.2.5.1 Strain definitions used to calculate the thickness

Stereo digital image correlation software typically calculates (3D) displacements. Surface strains are extracted after a local polynomial smoothing (using a so-called strain window) of the displacement data and interpolating the results with a, typically bilinear or quadratic, function. Based on the constant volume assumption these surface strains can be combined to calculate the strain in the thickness direction. A schematic principle of this procedure is shown in Figure 37.

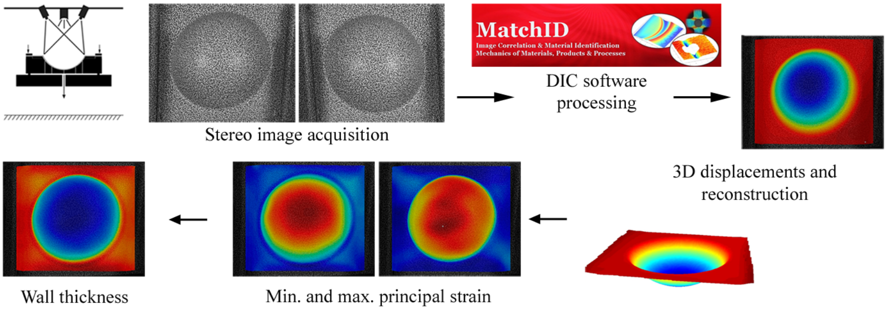

Figure 37 Principle of thickness definition based on stereo DIC measurements

The different equations to calculate the thickness, based on the different strain definitions that are available in correlation software in a simple cross sectional configuration, are developed below. The investigated strain definitions are [172, 200-202] Green-Lagrange strain (default for large strains), Hencky strain (also called logarithmic, true or natural strain), Biot strain (similar to engineering strain), logarithmic Euler-Almansi strain and Euler-Almansi strain. The latter two are finite strain definitions that are defined in terms of the pure deformation of the translated and rotated material. It is known that the deformation is normally expressed in matrix form since it is a second order tensor, but for the simplicity and understanding, the following part reduces the problem to a first order problem. First an imaginary cubical pattern is applied to a flat sheet. The properties of each cube can be defined by its length *x*, height *y* and depth *z*, the latter being the thickness of the sheet. After deformation, one single element can again be defined by its length *x+dx*, height *y+dy* and depth *z+dz* and its deformation and rotation which can be represented in the global coordinate system or in the local coordinate system (Figure 38).

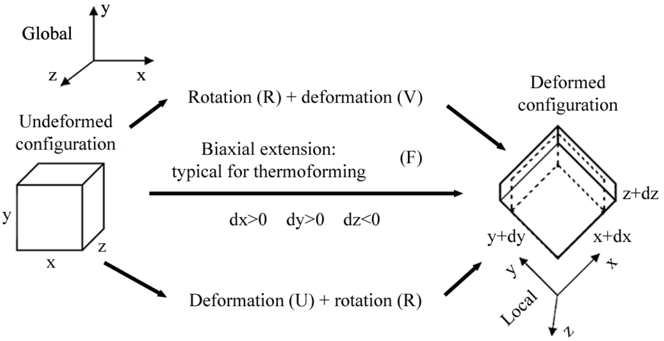

Figure 38 Schematic representation of undeformed and deformed conventions

When assuming volume constancy, the following equilibrium applies:

$$xyz = (x + dx)(y + dy)(z + dz) \tag{21}$$

When calculating strain (ε) according to the Green-Lagrange strain definition, the general definition is:

$$\varepsilon = \frac{1}{2}(\lambda^2 - 1) \tag{22}$$

where λ refers to the ratio of the final length over the initial length; in the x-direction this gives:

$$\lambda_{xx} = \frac{x + dx}{x} \tag{23}$$

And after substitution:

$$\varepsilon_{xx} = \frac{1}{2}\left[\left(\frac{x + dx}{x}\right)^2 - 1\right] \tag{24}$$

Similarly, ε_{yy} and ε_{zz} can be defined as:

$$\varepsilon_{yy} = \frac{1}{2}\left[\left(\frac{y + dy}{y}\right)^2 - 1\right] \tag{25}$$

$$\varepsilon_{zz} = \frac{1}{2}\left[\left(\frac{z + dz}{z}\right)^2 - 1\right] \tag{26}$$

Combining Equation (21) with (24), (25) and (26) gives:

$$\varepsilon_{zz} = \frac{1}{2}\left[\left(\frac{1}{\sqrt{(1+2\varepsilon_{xx})(1+2\varepsilon_{yy})}}\right) - 1\right] \tag{27}$$

Combining Equation (26) with (27), replacing $z+dz$ by t_f, z by t_i and expressing it in terms of maximum principal ε_1 and minimum principal strain ε_2 gives:

$$t_f = t_i\left(\frac{1}{\sqrt{(1+2\varepsilon_1)(1+2\varepsilon_2)}}\right) \tag{28}$$

with t_f, the final wall thickness and t_i the initial wall thickness.
A similar approach can be applied to other strain algorithms leading to the following equations for the Hencky (or logarithmic) strain:

$$\varepsilon = \ln(\lambda) \tag{29}$$

This leads to the following for the final thickness:

$$t_f = t_i e^{(-\varepsilon_1 - \varepsilon_2)} \tag{30}$$

The same equation is valid for the logarithmic Euler-Almansi expression.
The Euler-Almansi strain equation is defined as:

$$\varepsilon = \frac{1}{2}(1 - \frac{1}{\lambda^2}) \tag{31}$$

with corresponding thickness equation:

$$t_f = t_i\left(\sqrt{(1-2\varepsilon_1)(1-2\varepsilon_2)}\right) \tag{32}$$

And finally the Biot and Engineering strain definition:

$$\varepsilon = \lambda - 1 \tag{33}$$

with corresponding thickness equation:

$$t_f = t_i\left(\frac{1}{(1+\varepsilon_1)(1+\varepsilon_2)}\right) \tag{34}$$

The choice of the strain definition is important when comparing strain results to results from strain gauge measurements or simulations but the residual wall thickness should be identical irrespective of the choice of the definition when using the appropriate equation ((28), (30), (32), (34)).

To demonstrate the effect of the different strain definitions on strain magnitude and on final thickness, the equations are adopted to calculate analytically the strain values and the resulting wall thickness of a cross-section of an imaginary 2 mm thick sheet that is deformed into a perfect half sphere by means of a hemispherical plug and assuming sticky contact conditions. Figure 39 illustrates this deformation principle.

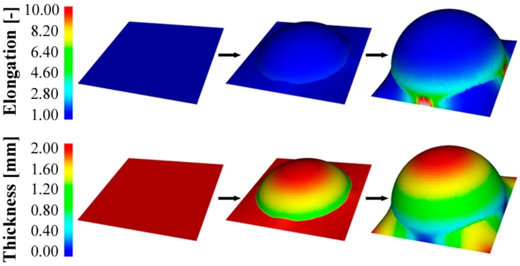

Figure 39 Simulation of a hemispherical plugging experiment on a 2 mm thick sheet. Top: elongation values; bottom: resulting thickness distribution.

The cross-section is divided into a finite number of small sections delimited by nodes. It is assumed that all nodes on the initial flat sheet are subject to a vertical projection to the spherical surface of the plug. The boundary nodes are fixed and the nodes closest to the boundary will therefore deform the most.

When considering a cross section in the centre of the sheet (y = 0), the z-coordinates of the projected nodes (z_n) can be calculated by Equation (35):

$$z_n = \left(\frac{x_n}{\tan(\sin^{-1}(\frac{x_n}{r_c}))} \right) - (r_c - h_c) \tag{35}$$

The radius of the circle is represented by r_c, the height of the final hemisphere, which not necessarily has to be equal to the radius of the circle, by h_c. The approximated arc length of a projected segment on the spherical surface is then:

$$arclength \approx \sqrt{\delta z^2 + \delta x^2} \tag{36}$$

with $\delta z = z_n - z_{n+1}$ and $\delta x = x_{n+1} - x_n$ this leads to following expression for a uniaxial elongation:

$$\lambda_{section} = \frac{arclength}{\delta x} \tag{37}$$

A visual representation is shown in Figure 40.

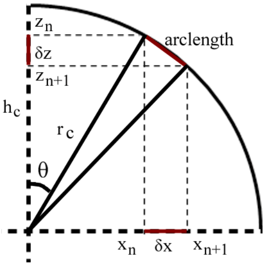

Figure 40 Elongation based on the vertical projection on a spherical surface

Figure 41 (top) shows the strain as function of the distance to the centre of the sphere. It can be seen that the strain at the centre node equals zero and increases with increasing distance from the centre to have a maximum value between the final node and the boundary node. At small strain, all definitions are practically equal, but when increasing, the difference between the different strain definitions gets significantly larger. The logarithmic Euler-Almansi strain increases in an exponential way while the Euler-Almansi strain increases quasi linearly.

The wall thickness based on the different strain definitions is represented in Figure 41 (bottom). This simple analytical example demonstrates that the residual wall thickness can be calculated by the equations above for either one of the strain algorithms and is consistent irrespective of the choice of the strain definition when assuming volume constancy.

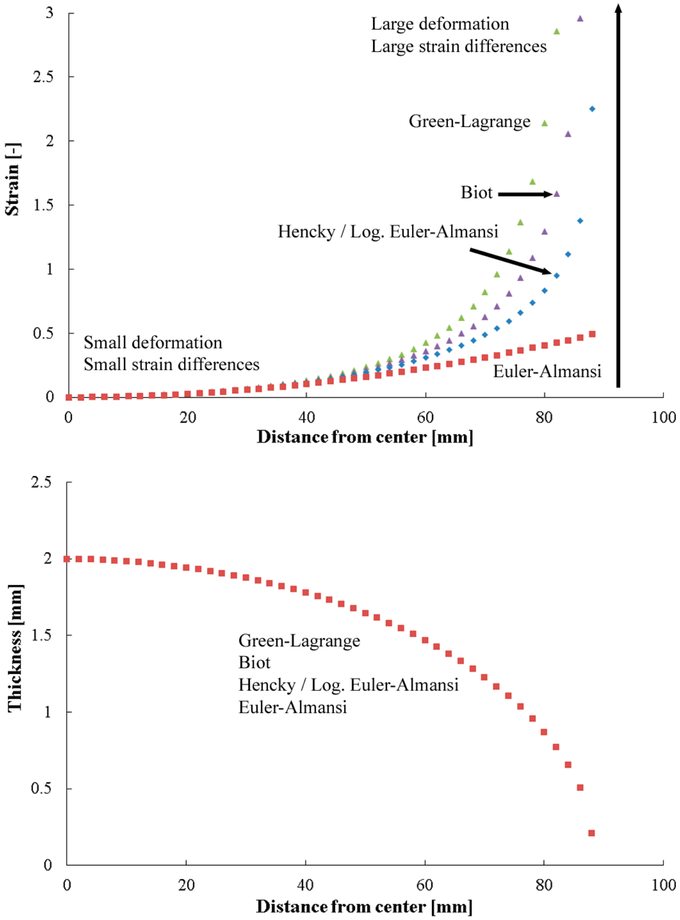

Figure 41 Top: strain magnitudes for the different strain algorithms in a cross-section of a half-sphere with a radius of 90 mm as function of the distance to the centre; bottom: corresponding residual wall thickness

4.2.5.2 Validation of the thickness calculation from DIC measurements

To prove that the approach is not software specific, two correlation software packages are used side by side to assess the wall thickness distribution of a HIPS vacuum formed partial hemisphere (mould: see Figure 42), using the strain definitions from previous section. The results of the academic code MatchID3D are compared with those obtained by the commercial software VIC-3D [203], version 2012, originally developed by researchers at the University of South Carolina and to conventional thickness measurements. For this experiment two cameras equipped with 25 mm focal length lenses are mounted on the thermoforming machine at 1190 mm from the sheet surface. This setup, combined with an aperture f-stop number of f/8 and two diffuse spotlights mounted in a 45° angle above the sheet ensures that the sheet will be completely visible in the field of view (FOV: 338 x 254 mm) of the cameras and the necessary depth of field (DOF: 229 mm) is achieved. The pixel resolution at this distance is 4.7 pixels per mm. To be able to judge the effect of the forming without having to bother about the influence of the speckle pattern, a dotted random, non-repetitive, isotropic and high contrast speckle pattern is printed (cf. Section 4.2.1.3) on 1 mm thick 330 x 330 mm HIPS sheets using a modified inkjet HP Deskjet 1100C printer. The dots have a diameter of 1 mm, corresponding to a resolution of 4.7 pixels per dot, as seen by the cameras in undeformed state. To be able to compare the correlation results independently of the calibration results, the images of the distorted speckle patterns are correlated in both VIC-3D and MatchID3D using identical intrinsic and extrinsic calibration parameters (intrinsic: focal length, principle point, skew, distortion; extrinsic: inter camera position and rotation angles). The correlation settings used in both software packages are given in Table 10 (full details on the correlation settings used in MatchID3D can be found in Appendix C).

Software	**VIC-3D**	**MatchID3D**
Correlation algorithm	Zero-normalised sum of squared differences	Zero-normalised sum of squared differences
Interpolation	Optimised 8-tap	Bicubic polynomial interpolation
Stereo transformation	Not specified	Affine
Correlation progress	Incremental	Spatial + update reference
Subset weight / Noise handling	Gaussian	Gaussian
Subset size [pixels]	21 x 21	21 x 21
Step size [pixels]	3	3
Filter size or Strain window [pixels]	9	9
Spatial resolution [pixels]	45	45

Table 10 Comparison of the correlation settings used in VIC-3D and MatchID3D

The product that is formed is a partial hemisphere with a radius of 180 mm, a die fillet radius of 5 mm and a depth of 65 mm. The single point incremental formed (SPIF) 2 mm thick aluminium (AlMg3, AA5754) mould is represented in Figure 42. A centrally located small hole (0.5 mm) connects the mould to the central vacuum system of the thermoforming machine. Digital stereoscopic images are taken at a frame rate of 4 frames per second during vacuum forming.

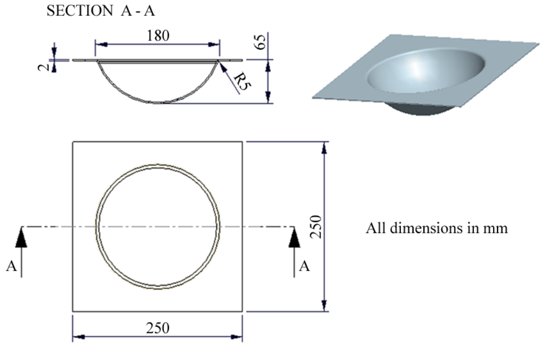

Figure 42 Partial hemispheric mould

Since proper strain values can only be calculated when displacements are accurate, the displacement results are validated by loading, meshing, fitting and comparing the resulting point clouds from both correlation software packages in an inspection and mesh processing software, GOM Inspect V7.5 [204]. Figure 43 shows that both point clouds match well, the local small differences are due to lost correlation (using a correlation threshold of 0.90) in VIC-3D.

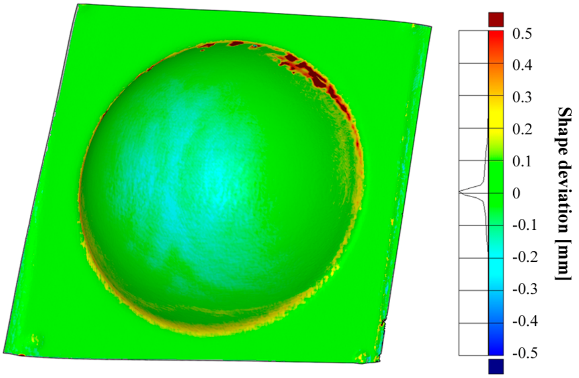

Figure 43 Mesh matching between VIC-3D and MatchID3D point clouds show good agreement

A vertical cross section is considered through the centre point of the final part and the resulting maximum principal (ε_1) and minimum principal (ε_2) strains are extracted and displayed as function of the radial position. Principal strains are used instead of strain components (ε_{xx} and ε_{yy}) to eliminate errors caused by misalignment of the coordinate systems between the software packages. By using these strains in the equations described in the previous section, the full-field wall thickness distribution is calculated. Figure 44 represents the final thickness distribution of the cross-section as calculated by MatchID3D and VIC-3D (2012) respectively, superimposed with a manual thickness measurement on a discrete number of points along the cross section. The manual measurements are performed with a Mitutoyo 209-573 dial calliper gage with a resolution of 0.01 mm and an accuracy of 0.02 mm and are the average of 3 repeats. The thickness distributions of both correlation software packages correspond well to the manual measurement and as expected the results of the different strain definitions are identical. This validates the initial assumption and the equations of the previous section.

It can be noticed that the thickness distribution is not perfectly symmetric. This is caused by a combination of non-uniform heating and material pre-processing history. More details on this phenomenon can be found in Section 5.2.2.

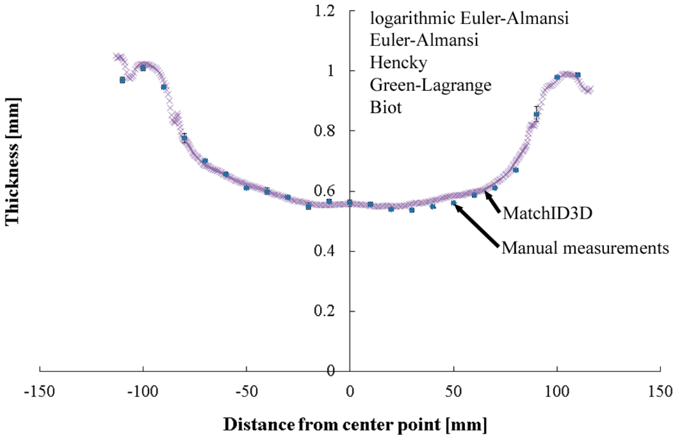

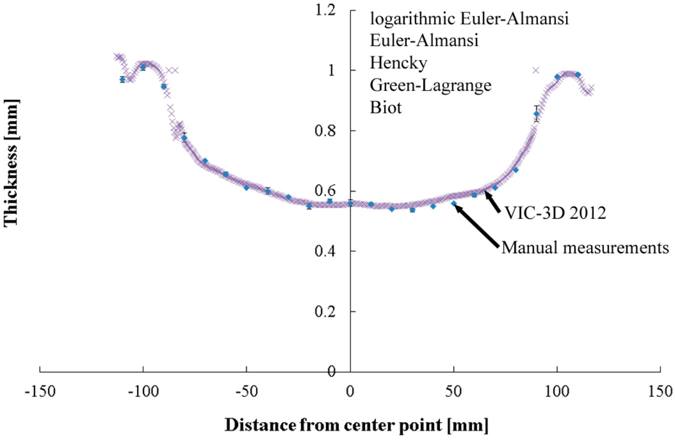

Figure 44 Top: thickness of a cross section as calculated by MatchID3D superimposed with the manually measured thickness profile; bottom: thickness of a cross section as calculated by VIC-3D 2012 superimposed with the manually measured thickness profile.

4.2.5.3 Inconsistency of the results in VIC-3D version 2009

Since VIC-3D 2012 has been issued only recently and a number of research institutes and companies still use the 2009 version, the exact same experiments were carried out with the older software version. When recalculating all different strains in version 2009 based on the correlation results obtained in version 2012, surprisingly completely different results were obtained for the thickness distribution (Figure 45). The thickness calculated on the basis of the Biot strain tensor is omitted since this strain definition was not yet available in version 2009.

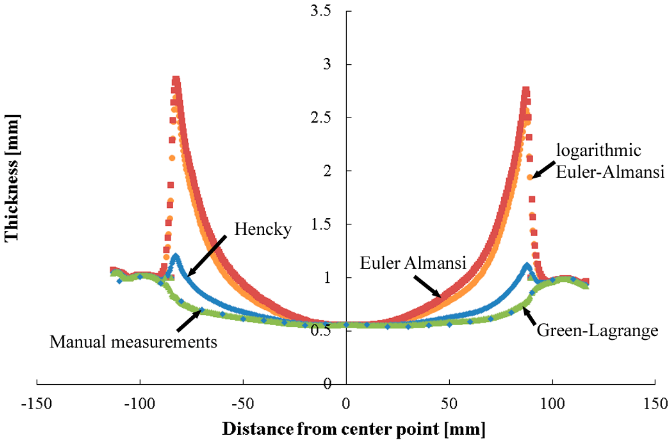

Figure 45 Thickness of a cross section as calculated by VIC-3D 2009 superimposed with the manually measured thickness profile

To uncover the reason behind this inconsistency, a closer look is taken at the strain components. Figure 46 and Figure 47 represent the maximum principal and minimum principal strain in the cross section calculated by MatchID3D and VIC-3D version 2009 respectively. Three observations can be made based on these graphs: firstly, the maximum principal strains obtained with both software packages are of the same order of magnitude, but the profiles are not identical (Figure 46). Secondly, the minimum principal strains differ tremendously, especially when looking at the Euler-Almansi and logarithmic Euler-Almansi strains where very high compressive strains are found for VIC-3D (Figure 47, bottom), which is physically meaningless. Thirdly, at the centre point the corresponding strain magnitudes are equal, regardless of the software used. The excessive compression strains for the VIC-3D correlation give unrealistic wall thickness values reaching up to 2.5 mm for the Euler-Almansi strain and logarithmic Euler-Almansi strain definition, when starting with an initial thickness of 1 mm (Figure 45). When comparing these results to the thickness profiles calculated with MatchID3D or VIC-3D version 2012 (Figure 44), it can be concluded that the only thickness result in VIC-3D 2009 that corresponds quasi exactly to the reference, is based on the Green-Lagrange strain definition.

The reason for the mismatch in VIC-3D version 2009 is mainly due to exaggerated minimum principal strain components, which the author believes to be caused by an erroneous conversion of strain data from the local coordinate system to the global coordinate system. This assumption is primarily based on the fact that at the centre point, which is the point that stays quasi orthogonal to the initial position of the sheet and therefore undergoes no rotation, gives realistic results for all strain definitions in VIC-3D version 2009.

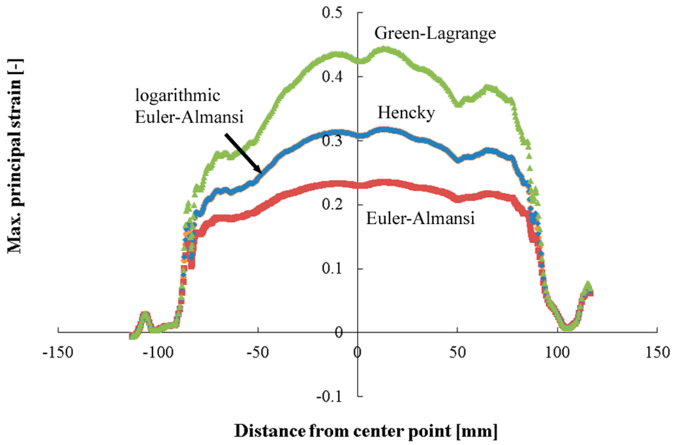

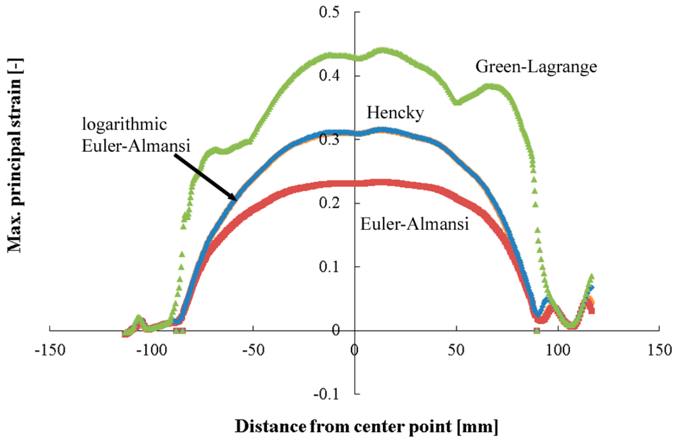

Figure 46 Top: maximum principal strain as calculated by MatchID3D as function of the distance to the centre; bottom: maximum principal strain as calculated by VIC-3D 2009 as function of the distance to the centre.

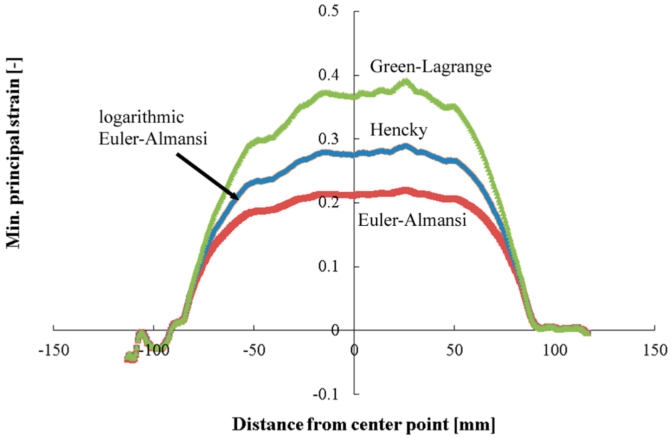

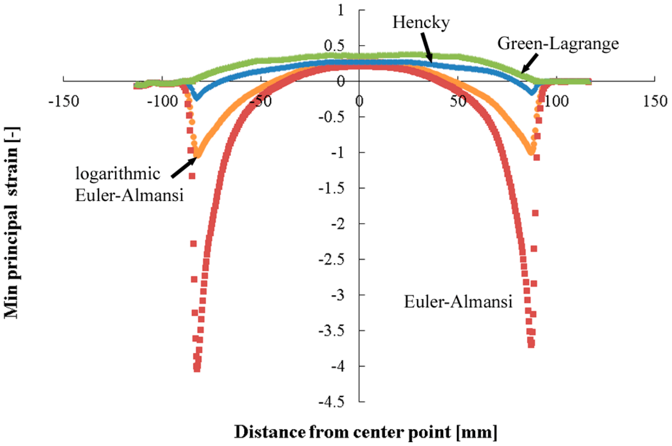

Figure 47 Top: minimum principal strain as calculated by MatchID3D as function of the distance to the centre; bottom: minimum principal strain as calculated by VIC-3D 2009 as function of the distance to the centre.

4.2.6 System resolution and accuracy

The terms used to quantify the measuring capabilities of a DIC system (resolution, spatial resolution and accuracy) are sometimes rather confusing. This section therefore clarifies the most common terminology.

4.2.6.1 Resolution and spatial resolution

Resolution is defined as the smallest change in a quantity being measured that causes a perceptible change in the corresponding indication [205]. In DIC, the displacement resolution is defined by the level of noise (camera and surrounding) and can be quantified by taking still undeformed pictures and calculating the deformation (self-correlation test). This deformation should normally be around zero. The resolution of the displacement is then defined as the standard deviation on this zero displacement [179]. The same approach is adopted for the strain resolution.

Spatial resolution is defined as the shortest distance between two spatially independent measurements. For displacements this is the subset size. Smaller subset sizes increase the spatial resolution but decrease the resolution since the standard deviation will increase [206]. Since strains are derived from displacements, the spatial resolution of strain is dependent on the subset size (SS), the step size (ST) and the strain window (SW) that is adopted to smooth the displacements and reduce displacement noise. Spatial resolution of strain (SRS) can be calculated as [207]:

$$SRS = [(SW - 1) * ST] + SS \tag{38}$$

Another often used term to compare strain from DIC to strain gauge measurements is the virtual strain gauge, which is a term originating from finite element analysis. In FEA software it is quite easy to compare strain gauge measurements to simulation results since the average strain from the surface mesh below the gauge can be used. In DIC a similar approach can be adopted. The size of the virtual strain gauge (VSG) can be written as [207]:

$$VSG = [(SW - 1) * ST] + 1 \tag{39}$$

Resolution, spatial resolution and virtual strain gauge lengths of all test setups are reported in Appendix C.

4.2.6.2 Accuracy

Measurement accuracy is defined as the closeness of agreement between a measured quantity value and a true quantity value of a measurand [205]. Measurement accuracy is not a quantity and can therefore not be represented by a numerical value. The only value that can be reported is the measurement error which is the measured quantity minus a reference quantity value. The measurement error can be split up in the systematic measurement error which varies in a predictable manner and a random error. The influence of correlation parameters on the measurement error of optical measuring systems has been the topic of many studies in the last decades. Not only the correlation parameters (correlation algorithm, interpolation, choice of the shape function, prefiltering, polynomial smoothing, subset size,...) affect the accuracy but also the lighting conditions, the quality of the speckle pattern (aliasing) and the quality of the (hardware) setup (noise, contaminations, sensor self-heating [165]) have an influence on the final accuracy. In addition, when working in a stereo setup, systematic errors can be introduced by the calibration procedure and the cross-camera correlation. Uncertainty quantification is so complex that even a complete doctoral thesis is dedicated to the topic [207] and still it is not fully tackled yet. Besides, most of the work is focussed on the quantification of 2D DIC uncertainties. A restricted amount of literature is available on multi-camera DIC error quantification [208-210].

Nevertheless, to get a rough estimate of the displacement accuracy, some target values can be used. Depending on the setup, displacement accuracies have been reported between 1/100 pixel in lab environment [164] to 1/20 pixel in more harsh environments. For strain, values in the order of 100 µm/m (0.01 %) are common.

In concreto, this means that when positioning a 2 megapixel camera (1600 x 1200 pixels) equipped with a 25 mm focal length lens at a distance of 1200 mm from the target (field of view = 341 x 256 mm) and considering 1/20 pixel displacement accuracy, it should be possible to correctly measure displacements of 10 µm. Overall, for most heavy gauge thermoforming applications, displacement and strain accuracies are more than enough especially when taking into account the errors already originating from the variance on the nominal thickness of the extruded sheet, which is in the range of +/- 5 % (cf. Table 4). As a proof: when comparing the DIC thickness calculations to the manual measurements on a discrete number of points (for the deformation presented in Figure 44), the average thickness deviation for a 1 mm thick HIPS sheet is approximately 0.5% with a local maximum of around 2.5 %.

4.3 Conclusions

In Chapter 4 an extensive explanation is given on how to correctly apply stereo digital image correlation in thermoforming. First, the choice of the correct speckle pattern, the speckling method and the correct lighting is highlighted. A solution is provided to cope with drastic changes in lighting conditions and the influence of heat waves and radiation has been investigated. Next a comprehensive comparison between theoretical depth of field calculations and depth of field calculations based on DIC measurements is provided. An automated methodology on how to select the correct camera, lens and distance to the target according to the size of the product to monitor is presented, taking into account the depth of field performance of the chosen hardware. In the final section of this chapter, a methodology to determine wall thickness distributions in thermoformed products derived from in-situ surface strain measurements obtained with stereo digital image correlation (DIC), under the assumption of material incompressibility, is presented. Wall thickness equations have been derived and validated on an analytical example for different strain definitions i.e. the Green-Lagrange, Hencky, Biot, logarithmic Euler-Almansi and Euler-Almansi strain definitions. These equations were then used to calculate the wall thickness from digital image correlations with a commercial software (VIC-3D) and with an academic software (MatchID3D, version 2009 and 2012). The comparison uncovered that for MatchID3D and VIC-3D, version 2012, the wall thickness values prove to be identical, regardless of the strain definition that was used. On the other hand in VIC-3D, version 2009, all but the Green-Lagrange strain definition bring forth unrealistic minimum principal strain results, leading to erroneous values for the wall thickness.

When following the methodology of Chapter 3 and combining it with the tools provided in this chapter, the thermoformer should be able to independently apply the methodology on his process. Chapter 5 will explain how the methodology can be used to experimentally optimise the process. Chapter 6 will show how to use the methodology to parametrise thermoforming simulation software. This is done by means of detailed examples.

Chapter 5 - Methodology application during experimental optimisation

5.1 Introduction

Chapter 4 explained how a novel combined measuring approach can be set-up during the thermoforming process and what measures need to be taken. The aim of this chapter is to describe the added value of this new approach and the new insights it offers in the thermoforming process. This is done by dividing the thermoforming process in different steps and demonstrating with examples how the measurement results generate deepened insight in each of the processing steps. The process is divided in following steps: clamping, heating, transfer, bubble inflation, forming and cooling (cf. Figure 1). Since heating, transfer and cooling are all temperature related, they are discussed in a single section.

5.2 Clamping

In a first section, the novel DIC based methodology will be used to assess the quality of clamping during thermoforming and to visualise and quantify sheet slip and wrinkling. The section ends with a brief note on the assets of combining DIC with thermal and pressure measurements for the optimisation of sheet clamping. In a second section, the methodology will be used to investigate the influence of the extrusion anisotropy and the clamping direction on product wall thickness distribution.

5.2.1 Clamping quality

The first step when thermoforming a product is to fix the sheet with a clamping device. This device has two purposes. The first is to retain the sheet during heating and forming since substantial forces may occur when the mould is pressed against the sheet, especially when forming positive products. The second purpose is the air-tight sealing of the gap between the sheet, the lower cabinet and the mould. When forming positive products and a pre-blowing phase is necessary, the clamping device must make sure that no air can escape between the lower cabinet and the sheet. When applying vacuum, the clamping device must ensure a vacuum-tight connection between the mould and the sheet. If a tight closure is not realised, air or vacuum can escape and the product will either not be corresponding to the thickness specifications or will not be formed at all.

In heavy gauge thermoforming, the initially flat sheet is placed on top of a seal mounted all around the upper surface of the lower clamping frame. When the process is started, the upper clamping frame, which is in many cases equipped with pointed pins, is lowered and the pins slightly penetrate the sheet ensuring that no slip in the clamping frame occurs during the forming step. Already during heating, relaxation of residual stresses in the clamped sheet could result in the sheet being pulled from underneath the clamping frame. This can occur when the clamping force, which is a parameter that is depending on the sheet thickness and the height adjustment of the clamping frame, is not properly chosen. Apart from slipping of the complete sheet, parts of the sheet can also be drawn in between two neighbouring pins when the distance between the pins is too large. This pin to pin distance typically ranges from 25 mm for amorphous polymers to 12 mm for semi-crystalline polymers and even 6 mm for thermoplastic elastomers [1]. The material surplus that needs to be foreseen all around the clamps is typically thickness dependent ranging from 12 mm for sheet thicknesses less than 2.5 mm to 50 mm for heavier gauge sheet when using 0.35 MPa clamping pressure [1]. These values are however rules of thumb that are based on experience and most of the industrial machines are only equipped with a single clamping set making it practically impossible to change the inner-pin distance each time the material is changed. Besides, the clamping force is mostly unknown. Consequently, a safety margin in sheet area is often applied to ensure that the sheet stays clamped during forming and that the vacuum cannot escape. This makes the final product more expensive since this surplus material is cut off after forming and is most of the times considered as scrap.

5.2.1.1 Visualisation of sheet slip and wrinkling

When using DIC during thermoforming, shape and displacements can be measured and sheet slip and wrinkling can be visualised. This makes it easier to define the clamping parameters such as the clamping force, the material surplus that is necessary outside the clamped area and the distance between the clamping frame and the product side of a (positive) mould. The way this is done, is demonstrated with a thermoforming example.

A 1 mm thick HIPS sheet is thermoformed two consecutive times into a partial hemisphere (for dimensions see Figure 42). In both experiments the sheet is heated single sided with the bottom heater set to 300 °C, resulting in an average sheet top temperature of 150 °C after approximately 60 seconds. The difference however between the two cases is the clamping force. Whereas in the first experiment, the sheet is adequately clamped, in the second experiment the clamping force is reduced making it possible for the sheet to (partially) slip in the clamps. Figure 48 illustrates the shape of the partial hemisphere right after the first mould contact and the start of the vacuum. In the first case (top left), the sheet is correctly restrained and the mould replication is started without sheet slipping in the clamping frame. The flat top shape of the mould and the gap between the mould and the lower clamping frame can be clearly distinguished. At the end of the process the product is adequately formed (Figure 48, bottom). In the second case however (Figure 48, right), the centre part of the hemisphere starts its reproduction, but since the sheet is allowed to partially slip in the clamping frame, undulations are formed, allowing the vacuum to escape. In that case, no product is formed.

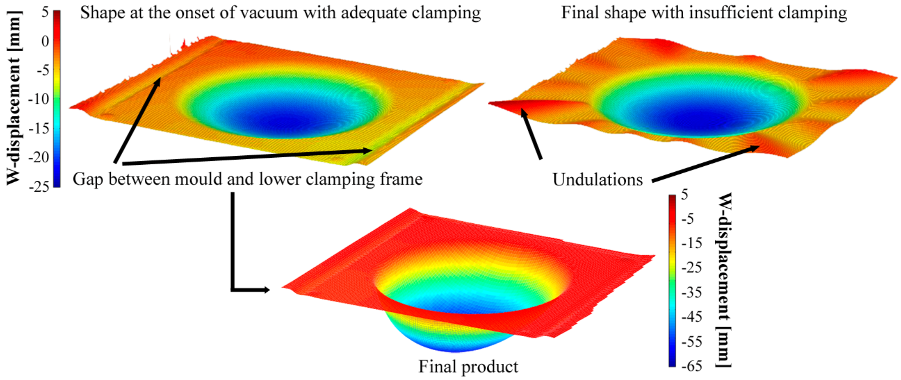

Figure 48 3D representation of the vertical displacement (W-displacement) immediately after mould contact of a correctly clamped (top left) and insufficiently clamped sheet (top right)

The previous comparison is meant as an exaggerated example. It is clear that the difference between the two final products could easily be noticed without the use of a DIC system but the example only serves to demonstrate the possibilities. Smaller (local) effects due to for example poor clamping or the wrong choice of the distance between the (positive) mould and the clamping frame resulting in high local strains and stresses can also be easily detected and moreover be quantified. Besides incomplete forming, slipping of the sheet can also induce the formation of wrinkles. Wrinkles can also be the result of an incorrect choice of inflation pressure. By using the DIC approach the cause and origin of the formation of wrinkling can be attributed to either inflation or insufficient clamping.

5.2.1.2 Quantification of sheet slip and wrinkling

In some cases it is more interesting to quantify the amount of sheet slip instead of just visualising it. To demonstrate that DIC can be used to quantify the effect of sheet slip, a second experiment is conducted.

In this case, a punching test is performed with an unclamped 3D orthogonal woven E-glass flax reinforcement. The non-impregnated flat textile sheet is deformed by a double-dome mould as described in [211, 212] into a three-dimensional shape. The experiment is executed at room temperature. This example is meant as an illustration since the deformation is similar to (plug assisted) thermoforming.

A stereo camera setup follows the deformation of the bottom side of the sheet during the test. The setup is represented in Figure 49. The sheet is initially placed unclamped on top of a blank holder (black line in Figure 50) shaped slightly bigger than the double-dome mould itself. The centre of the sheet is slightly sagging through the blank holder due to gravity (Figure 50, left). During a downwards punching stroke of approximately 55 mm, the sheet slides inwards over the blank holder. After the test, the slip can be calculated by extracting the displacement components. The result can be seen in Figure 50 (right). The borders slip locally up to 30 mm to the centre of the shape.

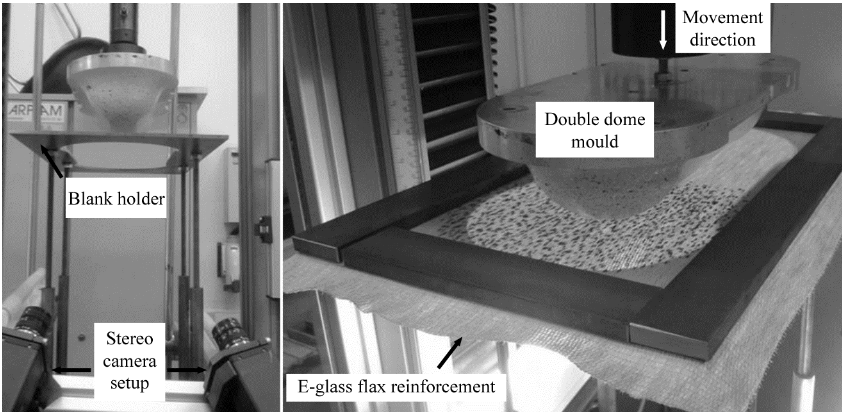

Figure 49 Double dome draping setup with stereo vision system [212]

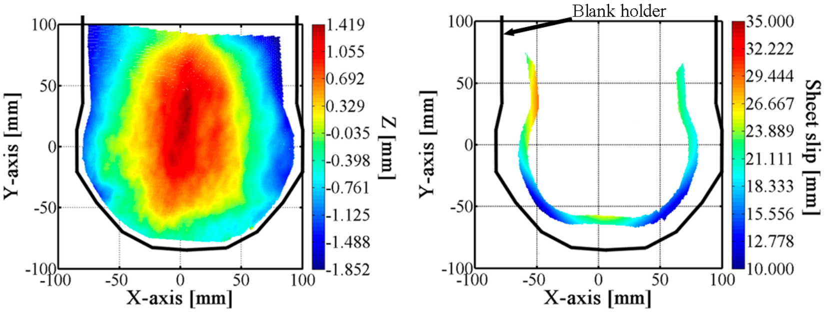

Figure 50 Left: initial flax sheet sagged through the blank holder before deformation by a double dome shape (only one half is represented); right: slip values after deformation. The black line represents the blank holder.

This example shows that the slip can also be quantified. Obviously, the clamping parameters can be modified depending on the outcome of this quantification.

5.2.1.3 Clamping optimisation by combining DIC with pressure and temperature measurements

In the previous two examples dealing with sheet clamping, only the DIC part of the combined measuring methodology is used. When combining DIC with a pressure (or vacuum) measurement, the monitoring of the air-tight closure of the gap between the sheet and the lower cabinet during bubble inflation, or the sheet and the mould during forming, can only be more accurate.

The same is valid for the use of a thermal camera together with DIC. This combination makes it possible to monitor the heat-sink effect of the clamping device. With the knowledge of both the temperature and the displacement data, it is even possible to turn the heat-sink effect of the clamping frame into a positive aspect. The strategy makes it possible to define the necessary temperature in the vicinity of the clamping frame in order to create a local stiffer or less stiff zone. This temperature gradient can be induced by a local setting of the heaters of the thermoforming machine or by adjusting the temperature of the clamping frame, if the thermoforming machine is equipped with such a temperature controlled frame.

5.2.2 Clamping direction and extrusion anisotropy

Section 5.2.1 demonstrated that the quality of the clamping can be assessed and, if necessary, modified depending on the outcome of the novel measurement approach. When clamping parameters have been set correctly and slip does not arise, care should be taken how to orient the sheet in the thermoforming machine. This is especially true for heavy gauge thermoforming where cast or extruded sheets are used as the starting material. If the extruded sheets are not allowed to freely relax during cooling, internal stresses are inherently induced in the material. Extrusion process parameters like the extrusion temperature, the extrusion speed, the die gap and chill roll temperature affect these direction specific stresses and result in anisotropic material behaviour. Although there has been quite some research to characterise and improve thermoformability by improving material and processing conditions (cf. Section 2.2), to the best of the author's knowledge the effect of extrusion induced anisotropy on thermoforming product quality has not yet been investigated in detail. The combined measuring approach developed in this thesis provides interesting insights, described in the next sections.

5.2.2.1 Experimental setup

By applying DIC during thermoforming, the effect of residual stresses in extruded blanks can be visualised. The experiment consists of thermoforming 1 mm thick HIPS sheet in a hemispherical mould (cf. Figure 42), with the extrusion direction parallel (0°) and perpendicular (90°) to the machine direction. For each orientation, 3 experiments were performed. The blanks were 325 x 325 mm with a 300 x 300 mm clamping frame. The applied speckles and the camera setup were identical to the one used for the validation of the thickness equations (cf. Section 4.2.5), only the step size is in this case increased from 3 to 10 pixels and the strain window from 9 to 10 pixels. These modifications make that the spatial strain resolution increases more than a factor of 2 but a sensitivity analysis of these parameters showed this has no significant influence on the final results of this experiment (more detailed correlation settings can be found in Appendix C). The speckled sheets are heated up to an average temperature of 150 °C and are subsequently formed in the partial hemispherical mould. During this process, images are acquired at a frame rate of 4 frames per second. The images are afterwards correlated and a 3D point cloud of the final shape, based on displacements calculated by DIC, is extracted for each of the six samples. Next, the point clouds are meshed and matched in the 3D inspection and mesh processing software GOM Inspect V7.5. From this matching procedure, it is found that the maximum deviation within the region of interest between the final shapes is less than 0.2 mm, leading to a first conclusion that the DIC correlations are successful and the DIC and thermoforming process repeatability is consistent. Furthermore, comparable DIC results were found within the three repetitions of each orientation (0° and 90°).

5.2.2.2 Results

During the thermoforming process, which takes in total 120 seconds, three relevant points in time are highlighted: i.e. the moment the sheet reaches the glass transition temperature, the time point right after heating and before forming, and finally the endpoint of the process.

When the sheets pass through the glass transition region, undulations of the sheet surface (also called relaxation waves) are formed preferentially in the direction parallel to the extrusion direction (Figure 51, top row). It must be noted that the exact location of the undulation peaks is random. The magnitude and the direction however are comparable in each of the three repetitions. The maximum principal strain (logarithmic Euler-Almansi) observed in this step is oriented perpendicular to the extrusion direction. The explanation for this is that the internal stresses in the extrusion direction, still present at T_g, prevent the sheet from relaxing in that direction. Consequently, relaxation predominantly occurs in the transverse direction. The maximum principal strain values stay below 1.5 % for both directions. No significant thinning (a maximum value of 0.02 mm is found) can be observed in this step.

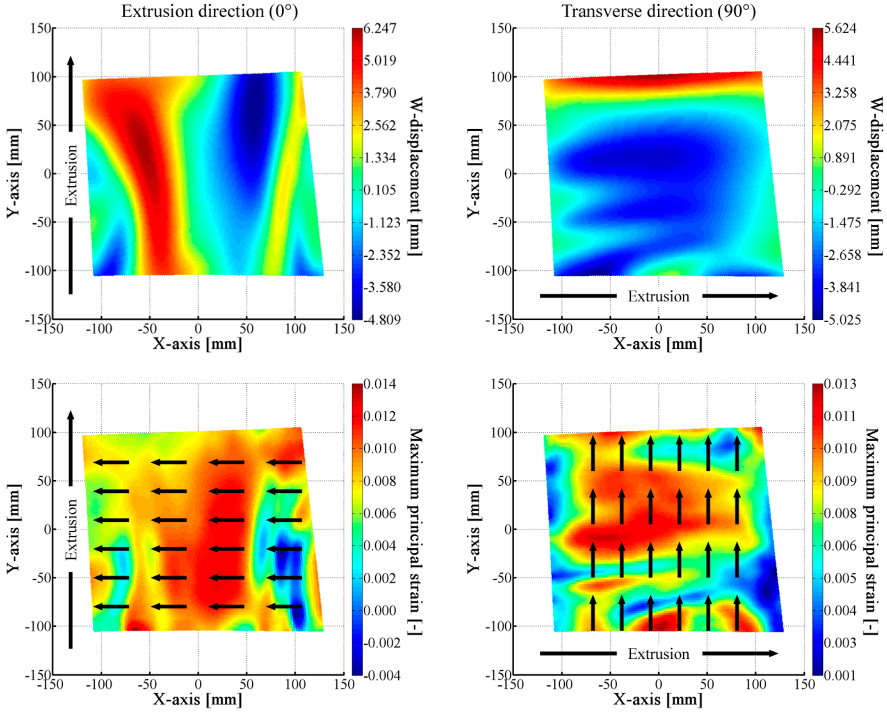

Figure 51 Undulations around the glass transition temperature for a 0° (top left) and 90° (top right) sheet appear parallel to the extrusion direction, leading to maximum principal strains (directions are represented by the arrows in the bottom pictures) perpendicular to the extrusion direction

After sagging of the sheet and right before forming, it is found that the magnitude of the sagging is independent of the extrusion direction orientation in terms of (vertical) W-displacement (-9.1±1 mm, Figure 52, top), maximum principal strain (8.6±0.7 %) and minimum principal strain (2.1±0.6 %). The direction of the maximum principal strain in the most thinned region coincides with the extrusion direction, irrespective of the blank orientation in the machine. After sagging, larger variations in thickness are found parallel to the extrusion direction than perpendicular to it. Local minimal thickness values of approximately 0.90 mm (0.1 mm thinning) are found (Figure 52, bottom). The thinning effect can be enhanced during subsequent forming since the thinnest section is expected to deform the most when subjected to the forming forces, unless strain hardening is able to compensate for the thickness reduction.

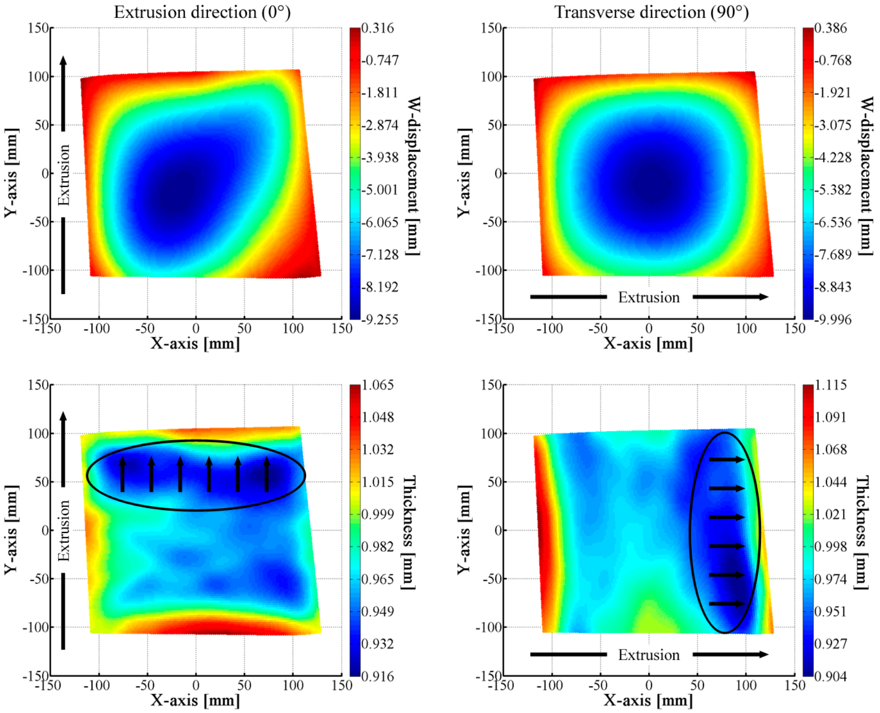

Figure 52 Sagged samples in the extrusion direction (left) and 90° samples (right) just prior forming. Sagging depth (top) and residual sheet thickness (bottom) including direction (arrows) of maximum principal strain.

To evaluate the reinforcement effect, the picture after sagging and prior to forming is used as reference, and thickness and strain changes during forming relative to this new reference are extracted. In this way, the thickness and strain changes of the forming and sagging phases can be separated. From this experiment, no significant reinforcement effect is found in this specific application and the final thickness distribution looks identical in both the 0° and 90° experiment (Figure 53).

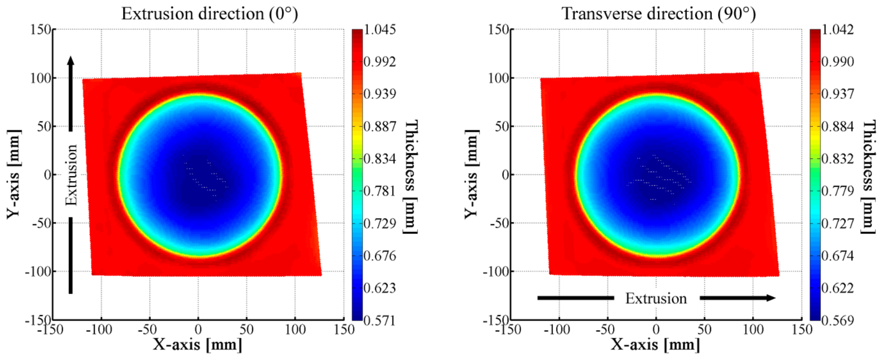

Figure 53 Formed samples in the extrusion direction (left) and transverse directions (right). Final thickness distribution without the effect of sagging.

When looking at the final thickness distribution including the effect sagging and comparing this to the thickness distribution when sagging is omitted, other conclusions must be drawn. Although the mould shape is perfectly axisymmetric and the sheet is supported by a square clamping frame, the local thinning is asymmetric and thickness differences up to 0.15 mm are found (Figure 54, bottom). The final thickness distribution of the product is shown in the top pictures.

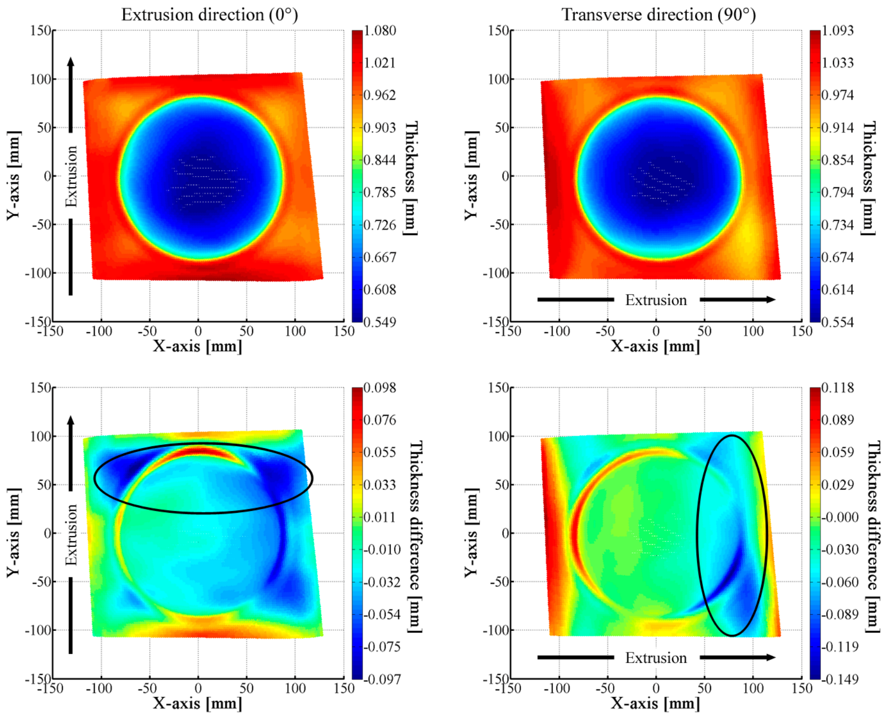

Figure 54 Formed samples in the extrusion direction (left) and 90° samples (right). Final thickness distribution including the effect of sagging (top) and thickness difference compared to the ideal thickness distribution when sagging is neglected (bottom).

In the final product, the thinnest regions correlate with the location of the thinning due to sagging (Figure 52) and are located perpendicular to the extrusion direction. The exact location of the thinnest area seems to be random. It is assumed that temperature variations can affect the location. This assumption was already brought to the attention in [126]. Local thinning is promoted in bands perpendicular to the extrusion direction because of the orientation of the local maximum principal strain. When making non-symmetrical parts, it is therefore advised to orient the extrusion direction parallel to the direction of the highest deformations, to avoid accumulation of thinning and possible tearing of the sheet. An alternative would be to apply sag compensation by blowing air underneath the sheet. More details on this technique can be found in Section 5.4.1.

5.3 Heating, transfer and cooling

The use of DIC and the combined measuring approach can provide additional relevant information during (a)symmetric heating, transfer and cooling. Since these topics are all temperature related, it is chosen to treat them in a single section. During the heating stage the thermoformer tries to heat the sheet as fast as possible in plane and through the thickness from ambient temperature to the ideal forming temperature. This can be done with or without preheating in a convection oven, depending on the thickness of the sheet. Once the sheet is (pre)heated a transfer period is started. This is the period of time between the start of the retraction of the heaters and the moment the mould touches the heat-softened sheet and is the onset of the cooling period. The above topics are discussed in Section 5.3.1.

In some cases, the thermoformer tries to locally influence material behaviour by modifying the in-plane temperature. The insight that the developed methodology can provide is discussed in detail in Section 5.3.2.

In the last section (5.3.3), attention will be attributed to the cooling step, to the accelerated cooling when using the bubble inflation technique and to the effect of mould contact on cooling rate.

5.3.1 Heating and transfer

The heating step in thermoforming is of crucial importance. The thermoformer tries to heat the sheet as fast as possible in-plane and through the thickness to the forming temperature without overheating the surface. Unfortunately, the homogeneity of the temperature over the sheet surface and through the thickness is generally unknown. Usually, only the temperature of the heating elements or the temperature of a single (central) point on the sheet surface is measured. Since the pyrometer is mounted in the heater bank, the sheet temperature is no longer measured when the heaters retract. Knowledge of the in-plane temperature distribution, the through-thickness temperature and the cooling effect of the sheet during transfer is therefore limited to non-existent in an industrial context. In the Sections 5.3.1.1 and 5.3.1.2, a thermal model that makes it possible to predict the through-thickness temperature gradient will be presented and validated.

When combining the model with in-situ temperature measurements, the core temperature of the sheet can be accurately predicted in real-time (Section 5.3.1.3). Moreover, the effect of the transfer period on the amount of sagging will be illustrated (Section 5.3.1.4).

5.3.1.1 Determination of the sheet core temperature

The knowledge of the through-thickness temperature of the sheet is, next to the in-plane temperature distribution, of crucial importance for the quality of the final product. To study the through-thickness temperature gradient in a thermoplastic sheet during the thermoforming process, a heat transfer model was developed in collaboration with colleagues from the Polymer Processing and Lightweights structures research group of the KU Leuven, Technology Campus Ostend [213]. The model is based on the finite difference method and assumes zero in-plane heat transfer. The model combines radiative heat of the heaters, convection at the top and bottom surfaces, and heat conduction of the sheet and calculates at each time increment the through-thickness temperature gradient. In this model, penetration of the radiative heat, which is thought to influence the calculations significantly [51] is not implemented but is under further investigation in an ongoing project. The density, thermal capacity and thermal conductivity of the sheet are also assumed to be constant. The sheet is divided in a finite number of thin layers (i=1..N) and assumes that the net heat (Q_{netto}) in a layer is the result of the subtraction of the amount of energy flowing out of the layer (Q_{out}) from the amount of energy flowing into the layer (Q_{in}) (Equation (40)).

$$Q_{netto,i} = Q_{in,i} - Q_{out,i} = m_i . C_p . (\theta_{t1} - \theta_{t2}) \qquad (40)$$

The mass of each layer is represented by m_i and by multiplying this with the specific heat (C_p) and the difference between the temperature at time t1 (θ_{t1}) and the final temperature (θ_{t2}), the heat flow can be calculated. Since in-plane heat transfer is neglected, the mass is represented by a unit cell with a known density. The number of layers is defined by the Courant-Friedrichs-Lewy (CFL) [214] condition in order to prevent instabilities and depends on the thermal properties of the investigated material, the sheet thickness and the applied time step. To achieve broad application, a.o. by the industry, the model can simulate the different heating phases such as a preheating phase in a convection oven, a convective cooling phase due to the transport from the preheating station to the forming station, a radiative heating phase (main heating) and a pre-forming holding phase, also called the transfer or equilibration phase.

5.3.1.2 Validation of the thermal model

To validate the model, through-thickness temperature measurements were performed during a heating and cooling experiment. For this purpose a silicone sheet composed of four silicone layers with three ultra-fine thermocouples (type K) vulcanised in-between the layers is used (Figure 55). The dimensions of the sheet are 500 x 500 x 2.5 mm. The outer thermocouples are placed at a distance of 1.5 mm with respect to each other, the third one is situated in the centre of the sheet. All three thermocouples are shifted 5 mm in-plane to reduce the interaction on each other. The heat transfer coefficient and the heat capacity of the thermocouples will slightly affect the reaction speed of the measurement but since the thermocouples are identical, the relative measurements values are assumed to be correct.

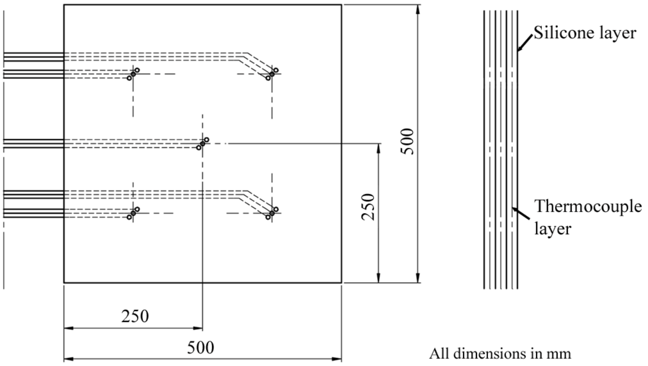

Figure 55 Silicone sheet used for the validation of the thermal model

The silicone sheet has a density of 1330 kg/m³. The thermal conductivity is measured with a thermal conductivity analyser (C-Therm TCI) and an average of 0.181 W/mK is found. A thermal capacity of 1330 J/kgK is measured by DSC. All values are applicable for room temperature. The following measurements were executed at limited temperatures (max. 100 °C) and the parameters are assumed to be constant. The sheet is placed in the centre of the thermoforming machine and the upper and lower heater banks are preheated to 200 °C. Once at temperature, the heating banks are moved forward and the silicone sheet is heated until one of the thermocouples (sampling rate 0.4 Hz) measures approximately 100 °C. The heater is then removed and the sheet is allowed to cool down. The test is repeated with a 300 °C and 400 °C setting of the heaters. The registered temperature profiles of the upper, core and lower thermocouples are plotted in Figure 56 next to the core temperature calculated with the finite difference model. The quasi perfect agreement of the calculated and measured core temperature validates the proposed approach.

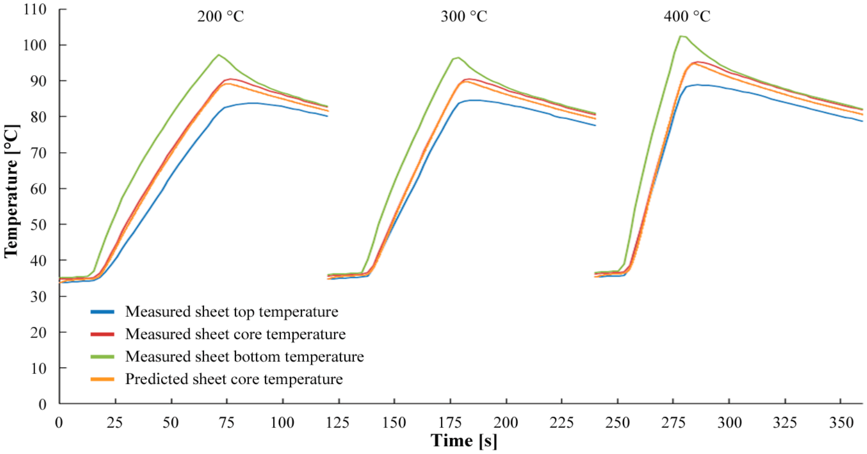

Figure 56 Measured top, bottom and core temperature of a silicone sheet superimposed with the calculated core temperature. Dual side heating with temperature settings of 200 °C, 300 °C and 400 °C.

5.3.1.3 Applicability of the model to industrial thermoforming

To prove the applicability of the thermal model in industrial thermoforming context, three examples have been worked out. The first consists of a complete process, including convective preheating. The second is meant to define the temperature gradient of a sheet heated from a single side. The third and probably the most relevant in an industrial environment is the use of in-situ temperature measurements for the prediction of the core temperature of the sheet.

Example 1. A 3 mm thick HIPS sheet is expected to be heated to 150 °C. A normal heavy gauge thermoforming heating process consists of 5 stages. The first stage is the preheating of the sheet in a convection oven. In current example 45 seconds at 100 °C is assumed. The preheating is followed by a period of 15 seconds for the transport of the sheet from the oven to the thermoforming machine at an ambient temperature of 30 °C. The main heating of the sheet is divided into two phases, reflecting the typical heating strategies involving a first period of intense heating (20 seconds) followed by a phase of reduced heating power (40 seconds) to permit the sheet to transfer the incoming heat flux from its surface to the core. Both heating steps have different power settings for top and bottom heater but the heat transfer coefficient is kept constant at 16 W/m²K. The last part of the heating is the equilibration which is the time necessary for the heaters to retract and the mould to move towards the heat softened sheet. For all the experiments in this thesis, the retraction of the heaters takes 3.7-3.8 seconds and the speed of the mould is adjusted depending on the mould height so it reaches its top position after approximately 5 seconds (the mould movement is hydraulically driven). The total transfer phase is thus approximately 9 seconds. An example plot of the temperature as function of time including all phases is displayed in Figure 57. Important to remark is that during the transport and equilibration phases, the core temperature becomes greater than the surface temperatures, a result of the convection losses.

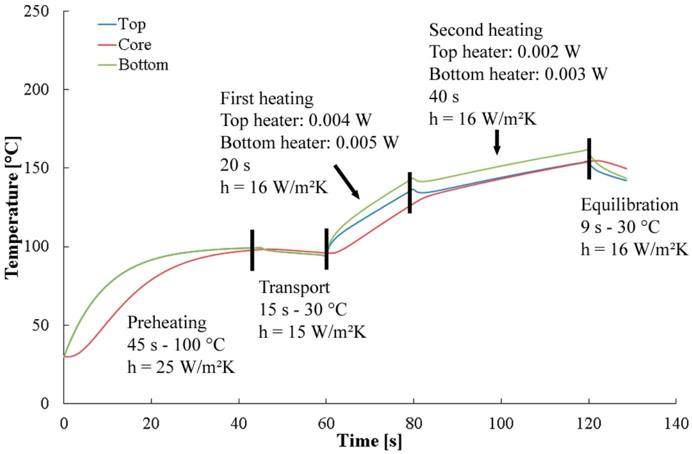

Figure 57 Predicted temperature as function of time of the top, bottom and core of a 3 mm HIPS sheet. The most important adopted settings in the model are mentioned on the figure. h represents the convective heat transfer coefficient.

Example 2. Most of the experiments in this thesis are based on 1 mm thick HIPS sheets which are heated from a single side with a heater temperature of 300 °C. To estimate the through-thickness temperature gradient and to be able to estimate the importance of this gradient on the results, the thermal model is applied for this material and these specific process conditions. Oven preheating is not used in this case and only the single side (bottom) single step radiative heating and the equilibration phase are to be simulated. When using the material values as defined in Section 3.2.5 (density: 1050 kg/m^3, specific heat capacity: 2250 J/kgK, thermal conductivity: 0.17 W/mK), a convective heat coefficient of 16 W/m^{2}K (see section 5.3.3.1), a single side radiant power setting of 0.0064 W (from a curve fitting approach knowing that the top surface of the sheet should heat up to 150 °C in approximately 60 s with a heater setting of 300 °C), Figure 58 is obtained. It shows the temperature of the top and bottom surface and of the core of the sheet. The temperature in every intermediate layer is not represented for clarity but is obviously also calculated. The maximal temperature gradient is 16 °C between top and bottom of the sheet at the end of the heating stage. After the equilibration phase of 9 seconds, the maximal gradient within the 1 mm sheet drops below 2.5 °C. This small gradient is already being achieved after 4 seconds, defining the minimum equilibration time that is necessary to take into account. Since this gradient is low, no special care has been taken to quantify the effects of this gradient in further thermoforming tests.

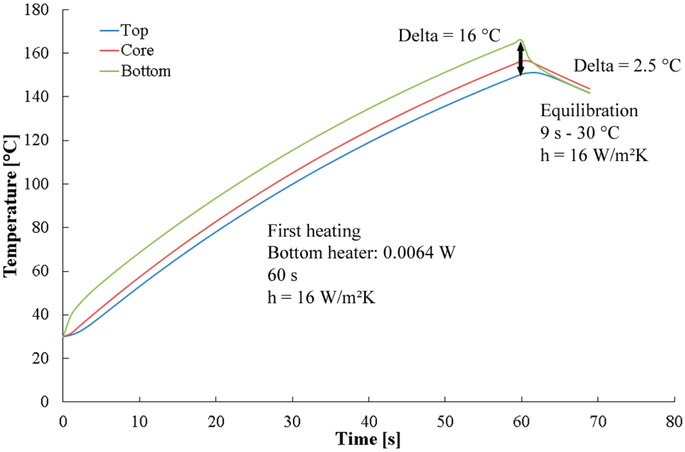

Figure 58 Predicted core and top temperature as function of time for a single step heating and equilibration of a 1 mm HIPS sheet heated with bottom heater only set to 300 °C

Example 3. A third, industrially more relevant approach to get more thermal insight, is the capability to estimate the through-thickness temperature based on measurements on the machine instead of simulations with fitted power values (cf. example 2). This approach is more robust since the efficiency of the heating elements can vary depending on the power or temperature setting of the heating elements, due to surrounding conditions or due to the wear of the heating elements. For this purpose, a modified version of the previously mentioned model is developed. The model is based on the same background and equations as before, but instead of using a power value to describe the energy of the heating element, the surface temperatures (top, bottom or both) that are registered by the pyrometers, installed in the heaters of most recent thermoforming machines, are used. These surface measurements enable the calculation of the transient heat dissipation through the thickness of the sheet using the equations of Section 5.3.1.1. Fluctuations in the temperature profile due to surrounding conditions are hereby captured and included in the calculation of the final core temperature. The procedure is illustrated in Figure 59 for a double side heated sheet. The equilibration phase can either be calculated or can also be based on thermal measurements during equilibration. This is obviously only possible when the machine is equipped with additional pyrometers (or a thermal camera) next to those in the heater banks. When single side heating is used, the heat flux is unknown and the temperature is only measured on the opposite side of the sheet the calculation is more complex since this results in an ill posed problem for the heat equation. The solution for this problem has not been worked out in this doctoral thesis, but solutions for this inverse heat conduction problem (IHCP) are fortunately available in literature, like the solution proposed by Manselli et al. [215]. The most challenging of this inverse problem is the stability of the results which is related to the presence of noise in the recorded temperature data, but also this problem has been tackled by different researchers, like Guo et al. [216].

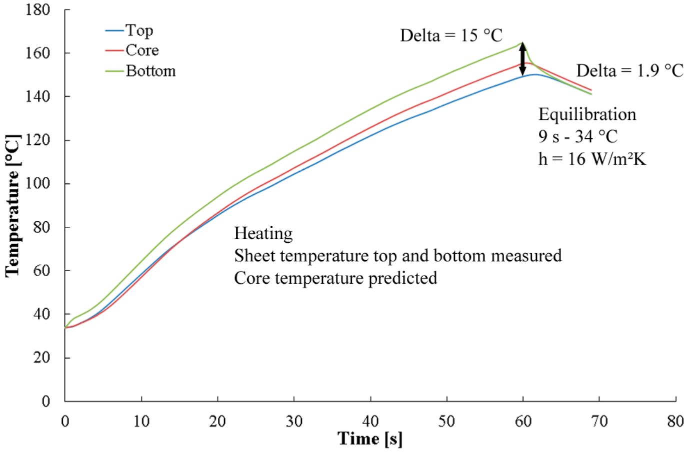

Figure 59 Predicted core temperature as function of time based on measurements of the top and bottom surface

The benefits of the tool become clear when it is applied in-situ on the machine. The real-time knowledge of the core temperature of the sheet allows the use of the core temperature to optimise the heating parameters instead of the sheet surface temperature. It is possible that the surface of a sheet reaches its predefined temperature but the core of the sheet is not yet above the lowest forming temperature in heavy gauge thermoforming when heating parameters (temperature, time, power) are not chosen correctly. Using the core temperature instead of the surface temperature as control parameter will avoid this problem.

5.3.1.4 Sagging during transfer

The combination of temperature and DIC measurements is beneficial during the transfer phase since it allows to assess the behaviour of the sheet. As an illustration, a sheet of 850 x 670 mm is clamped and heated from the bottom side with the heater temperature set at 300 °C until the sheet top surface temperature reaches 150 °C. The heaters are then retracted (this takes 3.7 s). The displacement in vertical direction (W-displacement) of the centre of the sheet is measured from the top side as function of the time throughout the heating and transfer phase (more detailed correlation settings can be found in Appendix C). At the point of retraction of the heaters, the sheet has sagged approximately 12 mm. During the heater retraction the sheets sags another 13 mm to a total mid-point deflection of 25 mm (Figure 60). Even though the large sag increase seems remarkable, it can be explained by the buoyancy effect: the convection of the hot air underneath the sheet results in an upward pressure on the sheet during heating. When the heaters retract, the lifting convection effect is no longer present and the sheet sags more. A similar phenomenon occurs if there is a delay between sheet sagging compensation and subsequent bubble inflation or vacuum forming (cf. Section 5.4.1). At a certain moment, due to convective cooling, the sheet will stabilise at an equilibrium but the importance and the consequences of this sagging effect are self-evident (cf. 5.2.2).

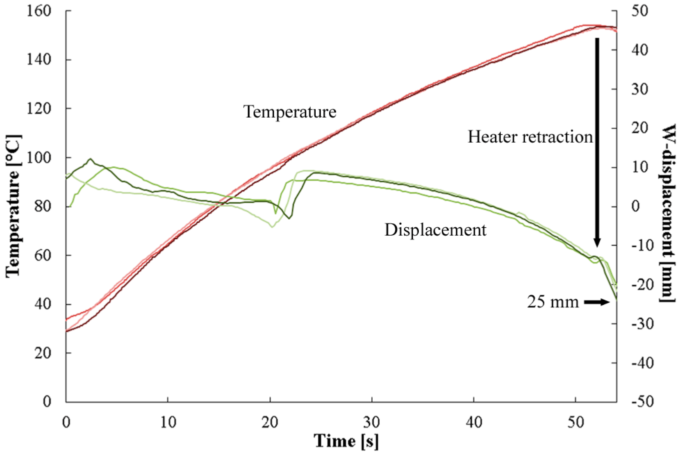

Figure 60 Temperature and W-displacement of the centre of the sheet as function of time during the heating phase (3 repeats)

5.3.1.5 Influence of step size and strain window size on thickness prediction after sagging

To conclude this section, a sensitivity study of the influence of step size and strain window size on the thickness of a sheet after heating and sagging is performed. The subset size is kept constant at 21 pixels, representing an area covering approximately 3 speckles (more detailed correlation settings can be found in Appendix C). In this case, a 1 mm thick HIPS sheet is clamped (850 x 670 mm) and heated from the bottom with a uniform heater setting of 300 °C until the top surface of the sheet reaches 150 °C. At that moment, the heater is retracted and the sheet is allowed to cool freely to the surrounding air. Once the sheet is completely cooled, the average thickness of a centre part of the sheet is measured (Mitutoyo ID-130M) and compared to the results of the digital image correlation using different step and strain window sizes (Figure 61).

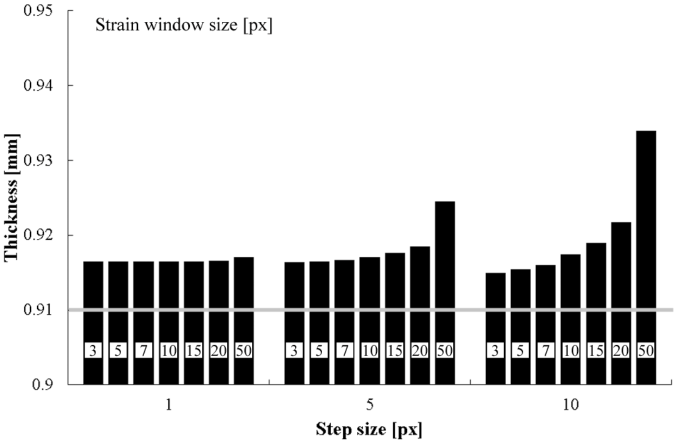

Figure 61 Effect of step size and strain window size on wall thickness of a 1 mm sagged HIPS sheet using a subset of 21 pixels. The horizontal line represents the average manually measured thickness.

The results show that the effect of the step and strain window size is almost negligible. Care should be taken when using very large strain windows or when less homogeneous deformations are expected. The DIC measurements produce thickness results comparable to the manual measurements (0.91±0.01 mm, 95 % confidence interval), keeping in mind that the thickness calculated by DIC assumes a constant initial thickness of 1 mm and measurements have proven that the average thickness is a little less: i.e. 0.980±0.025 mm (cf. Section 3.2.5.3).

5.3.2 Asymmetric heating/cooling

Attempts have been made to use local and/or asymmetric heating/cooling during the thermoforming process. Even though this approach has the potential to optimise thermoforming, the relation with final part thickness and quality is not straightforward. This is illustrated by two examples.

A first example is to keep parts of the mould at a lower temperature to ensure that once the material touches these cold parts, it freezes immediately, thus limiting local thickness reduction. However, the effects are not so obvious. On the one hand, the cooler zones will locally reduce the friction coefficient (or increase slip), i.e. the opposite of the desired effect. On the other hand, the decreased temperature of the sheet increases the local resistance to deformation. Which one of the two effects will prevail is not easy to predict since it depends on the temperature difference between the mould and the sheet, the initial thickness and material of the sheet (affecting the heat transfer), the process speed and the temperature dependence of friction coefficient and stiffness. Moreover, this approach has the limitation that it only affects the forming step which is most of the times very short. Moreover it relies on the fact that the sheet needs to cool down locally during that short period of time. Eventually, it can lead to chill marks or even to open tears.

Patterned or zoned heating of the sheet to acquire thicker or thinner zones in the final products is a second example of local and/or asymmetric heating/cooling [1]. Although this approach is not new, it is not used so much since it adds complexity to the process control. The relation between the zoned heating and the final thickness distribution is not straightforward since the final thickness is affected by every step of the process from heating (sagging), bubble inflation (when applicable), to forming.

Combining thermal camera measurements with in-situ DIC enables to create full-field strain maps and clarifies the influence of each process step on the sheet thinning. The link between the initial position of the sheet with respect to a specific zone of heating elements and the final position after forming can easily be tracked. This additional insight facilitates the optimisation of the process settings.

To demonstrate this, a 1 mm HIPS suitcase shell is formed on an uncooled, machined aluminium male mould with bounding box dimensions of 630 x 445 x 160 mm. Since a male mould is used, a bubble is inflated right before the forming step. Two experiments were performed with different heater temperature distributions.

5.3.2.1 Symmetric heating

In a first experiment, the sheet is formed with a standard homogeneous bottom heater temperature of 300 °C and the pressure necessary for the bubble is adjusted until a height of 160 mm is reached (cf. Section 5.4.2). This height is equivalent to the mould height, ensuring that the best possible thickness distribution is acquired without forming wrinkles. Stereo digital images for DIC calculations are taken throughout the whole process. This enables to visualise the 3D shape of the symmetrically heated sheet during sagging, during bubble inflation and finally during and after forming (Figure 62).

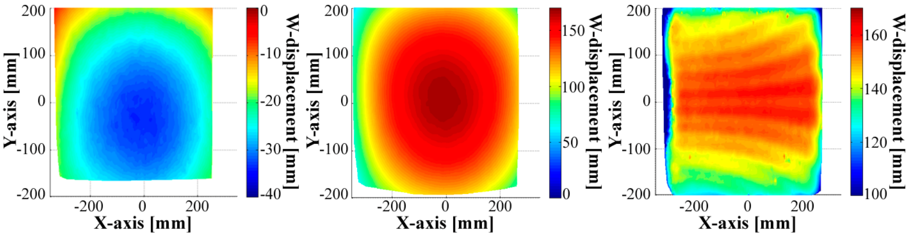

Figure 62 Top-view of a sagged sheet (left), inflated sheet (middle) and formed sheet (right) during symmetric heating

5.3.2.2 Asymmetric heating

In a second experiment, the same process settings are chosen except for the temperature setting. The sheet is heated asymmetrically with the left zone of heating elements only at 200 °C. The sheet is heated during 120 s, the hottest section of the sheet (at the right side) reaching 150 °C. The top surface of the left side is then at an average temperature of 110 °C, which is in theory slightly below the lowest forming temperature but the heated (bottom) left side of the sheet is at that time around the lowest forming temperature (130 °C). In analogy to the description in the first example, the shape can again be visualised at different points throughout the process (Figure 63). The difference in the size of the represented area between the symmetric and the asymmetric heating is due to the choice of the region of interest during the DIC calculations and has no influence on the overall result.

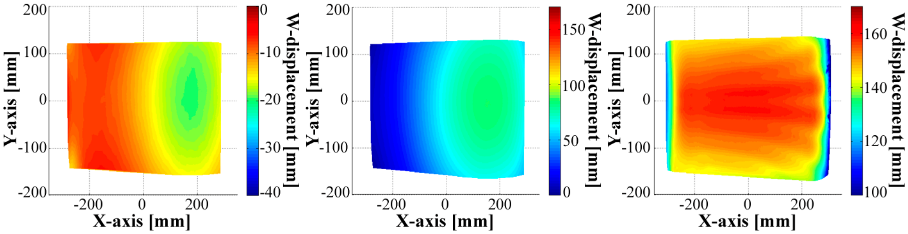

Figure 63 Top-view of a sagged sheet (left), inflated sheet (middle) and formed sheet (right) during asymmetric heating

5.3.2.3 Symmetric versus asymmetric heating

When comparing the symmetric and the asymmetric results, some of the findings are obvious. For example, the sagging of the symmetrically heated sheet is symmetric and much more pronounced than that of the asymmetrically heated sheet. The same applies for the 3D shape after the bubble inflation step: the bubble is higher in the case of symmetric heating. Both findings are related to the amount of energy that is being radiated that is higher in the first example. These findings are as expected and can be related to the difference in temperature and, therefore, the difference in material stiffness. The final shape of the formed product is in both cases comparable, meaning that the mould is adequately reproduced.

When analysing the thickness profile of a horizontal cross section through the middle of the part after the different steps of the process, the result for the asymmetrically heated product is clearly asymmetric where that of the symmetrically heated product is almost constant (Figure 64, right).

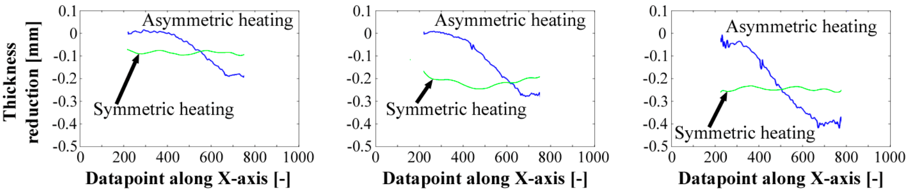

Figure 64 Comparison of thickness reduction (initial thickness 1 mm) between symmetric and asymmetric heating of a central cross section in x-direction after sagging (left), after bubble inflation (middle) and after forming (right)

The additional asset of the developed approach is that the in-situ measurements allow to determine which specific phase of the process is responsible for the sheet thinning during asymmetric heating. Most of the sheet thinning (50 %) is caused by the asymmetric sagging. The sheet thins from 1 mm to 0.8 mm on the right side, Figure 64, left), an additional 25 % is caused by bubble inflation (from 0.8 mm to

0.7 mm, Figure 64, middle) and another 25 % is caused by the forming process during mould contact (from 0.7 mm to 0.6 mm, Figure 64, right). On the other hand, the cold side (left side of the cross section) is almost not strained during sagging or bubble inflation since in these steps the available force (gravity and bubble inflation pressure (< 10 mbar)) is too low to induce deformation. It is only slightly strained (thinned) during the forming step. This example demonstrates that the proposed stereo-DIC technique provides information that cannot be experimentally defined in another way and could only be obtained through complex through-process finite element modelling. When looking at the thickness profiles of the symmetrically heated sheet, it can be seen that the forming on itself hardly affects the final thickness and that the bubble inflation and the sagging are almost entirely responsible for the final thickness distribution of the top surface of the suitcase shell. This conclusion is of course only valid for the top surface of the shell, other deformations are to be expected on the corners of the suitcase for example.

The adopted methodology proves that a variation of the in-plane temperature has a significant effect of the product thickness distribution. Patterned heating can be used for example to avoid excessive thinning provided that the location of the hotter and colder areas can be specified accurately. Fortunately, new techniques are being developed that allow a very precise local control of the temperature [36, 37]. Combining those heating techniques with a clear insight on material behaviour through DIC can mean a big step forward to faster and higher quality production.

5.3.3 Cooling

An important part of the thermoforming process consists of cooling the sheet. Cooling starts from the moment the heaters retract and the sheet temperature drops due to a combination of convective heat transfer from the sheet to the environment and some radiation losses. This is confirmed by performing a finite element transient thermal simulation (using Siemens Unigraphics NX) of the cooling of a plate with typical size and process conditions. Since radiation effects are not negligible but hard to estimate, they are often incorporated into the convection coefficient. From literature [1], the convection heat transfer coefficient (h) typically varies from 5.7 W/m²K for free surface cooling in quiescent air to 570 W/m²K when using a water spray, which is a very broad range. It is of major importance to know the correct convection coefficient and the cooling rate of the sheet, since the knowledge of the right temperature is critical for correct material behaviour during forming.

The following sections describe how the developed methodology can be used to obtain realistic heat transfer coefficients. This is done by means of three examples. The first example is a free cooling experiment, which gives a convective heat transfer coefficient that can be used during the equilibration phase. The second example produces realistic convective heat transfer coefficients during bubble inflation. The last example characterises the heat transfer to a mould. Important to remark is that all experiments were carried out on an industrial thermoforming machine witch realistic sheet sizes, environmental and boundary conditions.

5.3.3.1 Heat transfer during free cooling

Realistic convection coefficients, using the actual environmental conditions, are obtained by applying the proposed combined measuring approach: temperature and deformation are simultaneously measured during free cooling (starting temperature 150 °C) of a 1 mm thick sheet (clamping dimensions 850 x 670 mm) without application of pressure or vacuum. The temperature of the first 5 seconds of the decreasing slope, which is quasilinear, is fitted according to Newton's law of cooling, which is a reformulation of Fourier's law, with different values for the heat transfer coefficient (Equation (41)):

$$T_t = \left[\left(T_{(t-1)} - T_{amb} \right) . e^{-\frac{\theta . h}{\rho . C_p . L_{c(t)}}} \right] + T_{amb} \tag{41}$$

with temperature T, time t, ambient temperature T_{amb}, time step size θ, convective heat transfer coefficient h, density ρ, specific heat capacity C_p and characteristic thickness L_c. The characteristic thickness is the thickness of the sheet in the case of single side cooling or half the thickness of the sheet when cooling from two sides, as is the case in this experiment. As the L_c value, 0.45 mm is used which corresponds to half the sheet thickness, measured after heating (sagging). Using Equation (41) is a simplification since it does not take into account conductivity within the material. Nevertheless, it can be used when the Biot number (B_i, Equation (42)) that represents the ratio of the internal resistance of a body to heat conduction to its external resistance to heat convection, is smaller than 0.1 [217]:

$$B_i = \frac{hL_c}{k} \tag{42}$$

In this equation, k represents the thermal conductivity. For heavier gauge sheets or material with low thermal conductivity, conduction has to be integrated. This is done using the finite difference approach described in Section 5.3.1.1. To validate the equations, the cooling rates of a 1 mm and a 5 mm HIPS sheet are compared with a transient two-sided convective cooling simulation (including conduction) with identical material and convection coefficients (16 W/m^{2}K). The temperature of the surface of the sheet (and to a limited extent that of the first layers through-thickness due to thermal transparency [218]) is measured with a FLUKE 576 spot infrared thermometer (cf. Section 3.2.3). The results are plotted in Figure 65. For 1 mm thickness, the differences are negligible since the Biot number is lower than 0.1. For the 5 mm sheet on the other hand, a considerable difference between the results is observed. The FE-simulation and the results including conduction do match, proving that the equations are correct in this case.

When fitting the curve from the free cooling experiment for different values of h, Figure 66 is obtained. It is clear that the best matching convective heat transfer coefficient has a value of 16 W/m^{2}K. To illustrate the effect of the coefficient on the slope of the curve, curves for h = 5.7 W/m^{2}K and h = 30 W/m^{2}K are also shown in the figure. The identified coefficient can be used in simulation, for example to simulate the equilibration phase.

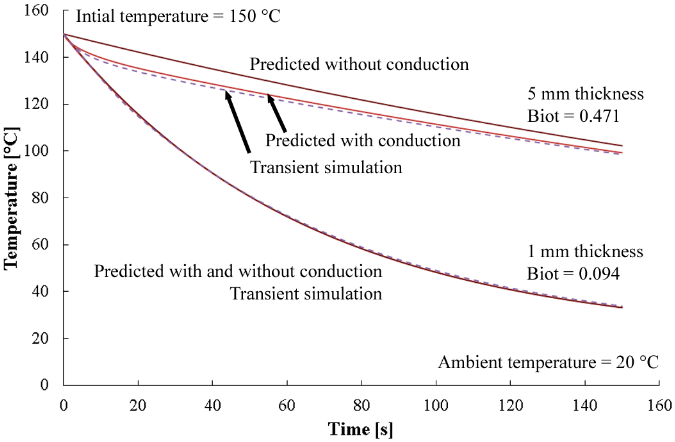

Figure 65 Cooling curves of a 1 mm and a 5 mm thick HIPS sheet calculated with and without conduction and compared to a transient thermal simulation using a convective heat transfer coefficient of 16 W/m²K. The dotted lines represent the simulations.

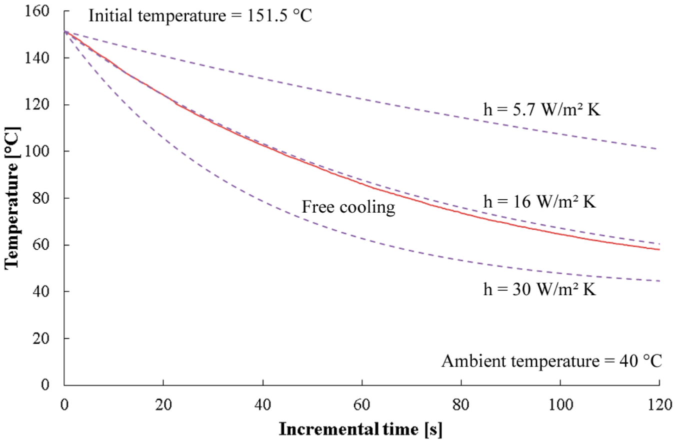

Figure 66 Fitting a free cooling curve for a 1 mm (initial thickness) HIPS sheet at starting temperature of 150 °C with different convective heat transfer coefficients. The dotted lines represent the fittings. The best fit is obtained with 16 W/m²K.

5.3.3.2 Heat transfer during bubble inflation

The heat transfer coefficient defined in previous section is of course only valid to obtain realistic surface temperatures during free cooling or equilibration. When forming positive or free-formed product however the sagged sheet is subjected to a bubble inflation step. During inflation, other convective coefficients should be taken into account. The higher the inflation pressure, the higher the bubble will be and the faster the sheet will cool down. The faster cooling response is caused by two phenomena: firstly, a higher pressure results in more turbulent air, leading to a higher convection and secondly, since the sheet thickness reduces at the same time, the local heat flux density increases inversely proportional to the sheet thickness according to Fourier's law of heat conduction.

Three different settings of the air flow valve (valve setting 3, 5 and 7 cf. Figure 11), leading to three different strain rates, bubble heights and thicknesses are used. The starting temperature is approximately 151 °C and of the first 5 seconds of the decreasing temperature slope is fitted according to Equation (41). If a constant sheet thickness is assumed, this results in convective coefficients of 29, 50 and 60 W/m²K for the three valve settings respectively. The values differ significantly from each other, considering that similar surrounding conditions (turbulent air) were used. Using the actual thickness as function of time ($L_{c(t)}$), as obtained from DIC measurements, the convection coefficients drop significantly to 26, 31 and 32 W/m²K, respectively (Figure 67). This shows that values based on a fixed sheet thickness would vastly exaggerate the cooling effect in simulations. A correct calculation of the convective heat transfer coefficient is not possible if the thinning effect during the bubble inflation is not included.

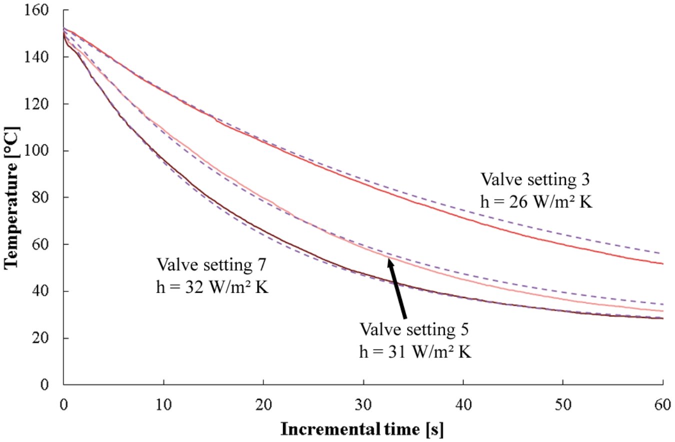

Figure 67 Fitting of the convective heat transfer coefficients to the cooling curves during bubble inflation for valve settings 3, 5 and 7 taking into account the thickness reduction due to inflation. The dotted lines represent the fittings.

5.3.3.3 Heat transfer to the mould

The previous section described the approach to determine the convection coefficients to the surrounding air, whether or not during bubble inflation, but did not describe what happens when the sheet comes into contact with the mould. In 2008, Choo et al. [219] developed an experimental lab-scale apparatus to measure the heat transfer coefficient between polymer (PP and PVC) and plug (PTFE and syntactic foam (Hytac-B1X)). They retrieved heat transfer values for a temperature range from 45 °C to 75 °C interface temperature but admitted that accuracy, repeatability and other factors such as interface roughness and pressure needed more investigation. Since then, to the author's knowledge, no further results on this topic have been published by Choo et al.

An alternative approach presented here to estimate the heat transfer coefficient between the sheet and the mould, is to fit the increased cooling rate due to mould contact using the same methodology as presented above (equation in Section 5.3.1.1). The procedure is illustrated with a thermoforming experiment with two different sheet thicknesses. Heat transfer coefficients obtained for a 1 and 2 mm sheet blown with the same pressure and formed at the same temperature (150 °C) with a positive mould at 20 °C are visualised in Figure 68. The obtained values include all boundary conditions and can be used as a starting point for simulations instead of using the values from literature which do not include effects like the temperature difference between the sheet and the mould, contact pressure, mould roughness,...

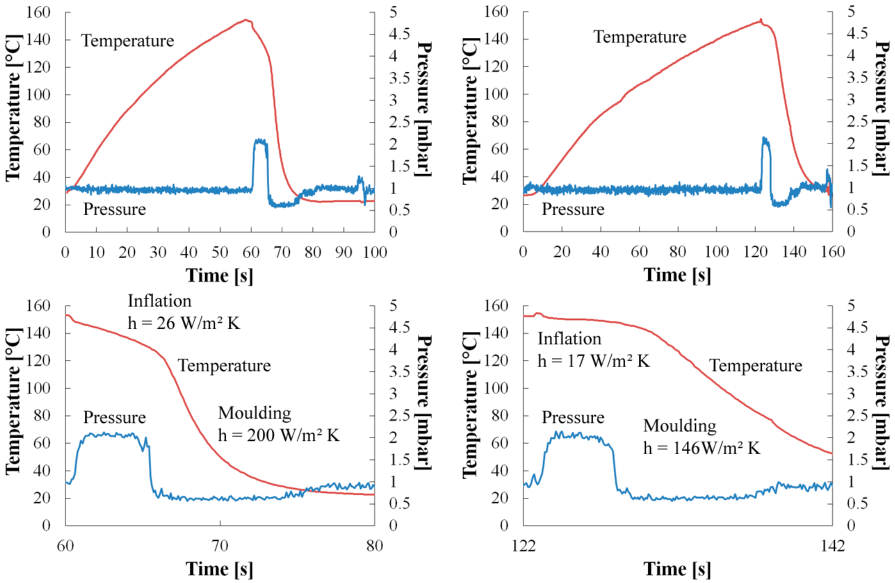

Figure 68 Temperature and pressure curves as function of time during heating, bubble inflation and forming with a male (suitcase) mould at 20 °C. Left: 1 mm sheet thickness; right: 2 mm sheet thickness. Top: complete cycle; bottom: only inflation and forming.

5.4 Sag compensation and bubble inflation

Bubble inflation is one of the most well-known techniques to increase the uniformity of the wall thickness distribution of positive thermoformed products. Pneumatic air is blown from underneath the sheet, most of the times through the vacuum holes of the mould, right after the heating step, in order to uniformly expand the sheet. This expanded sheet is then draped over the mould at the moment the pneumatic air is released. The result is a product that has a more uniform thickness distribution than products produced without bubble inflation since the latter tend to have more localised highly stretched areas. Since sag compensation uses the same technique, although with reduced air pressure, to suppress the sheet from excessive sagging during heating, this aspect will be addressed first in this section. For both topics, the advantage of using the DIC methodology will be highlighted.

5.4.1 Sag compensation

It is common practice for the thermoformer to manually or automatically inject (sometimes pulsated) air underneath the sheet in order to prevent the sheet from sagging or in the worst case from touching the lower heater bank. When an automated system is used, an opto-electronic device (for example a light curtain) mounted at a specific distance below the sheet, detects the sagging and triggers for a predefined time an air injection valve. The pressure and the effect on the sheet, which is highly temperature dependent, is however not measured. Insufficient pressure will increase the chance for the sheet to sag onto the heaters, too much pressure will pre-stretch the sheet as is the case in bubble inflation (cf. next section) or blow it against the top heater. Besides, the exact moment at which the pressure should be released and vacuum switched on is based on experience and post forming measurements. This has as a consequence that when changing the material or the clamping dimensions, the pressure setting and the correct timings need to be manually adjusted again. When using a combined measuring approach as proposed in this thesis, insight is created and lengthy manual trial and error procedures can be accordingly limited to a minimum. The approach for doing so is demonstrated with an example below.

The lower heater bank is set to 300 °C and when a stable temperature is reached, a 1 mm thick HIPS sheet at an initial temperature of 35 °C is clamped (850 x 670 mm) and a fixed pressure (pressure value setting 3 cf. Figure 11) is applied. Next, the heater is moved forward to heat the sheet until the top surface reaches a temperature of 150 °C. While heating, the pressure is kept constant and the sheet height and shape are measured using DIC (more detailed correlation settings can be found in Appendix C). Figure 69 represents the temperature, (vertical) W-displacement and thickness of a point located in the middle of the sheet.

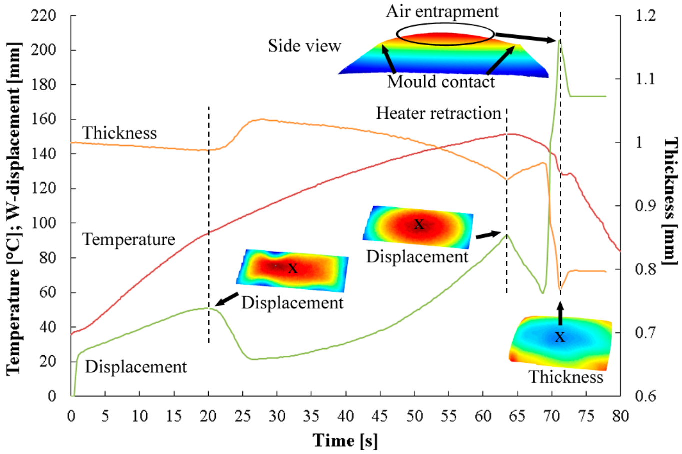

Figure 69 Temperature, W-displacement and thickness of a central point of a 1 mm initial thickness HIPS sheet submitted to a fixed pressure during heating until 150 °C and forming without vacuum

Initially, the sheet is lifted approximately 20 mm by the applied pressure. During the first 20 seconds of heating, the sheet starts to stretch and the lifting effect is gradually reinforced. Around the glass transition temperature (96 °C) the typical relaxation effects occur and sheet undulations perpendicular to the extrusion direction are observed (cf. Section 5.2.2) although they are not as pronounced due to the supporting pressure. This transition is associated with a significant compression in the length (extrusion) direction of the sheet leading to a local increase in thickness in the middle. After this transition, the sheet is stretched and lifted further until 150 °C is reached. At that moment the bottom heater is retracted, the mould starts to move upwards and the pressure is released. It can be seen that at first gravity takes over and lowers the sheet again. At the same moment, when looking at the thickness plot, there is an amount of elastic springback, increasing the sheet thickness again. The mould makes contact with the sheet after approximately 70 seconds and stretches it again. In this example it is deliberately chosen not to switch on the vacuum at mould contact, which is a general rule of thumb, to show the importance of the exact timing for the vacuum. If vacuum is switched on too late, the possibility exists that (inflation) air gets trapped between the sheet and the mould and that this entrapped air locally induces additional sheet stretching, as can be seen in Figure 69. When the vacuum is switched on too early, the sheet can be drawn down against the mould and already start too cool down rapidly increasing the chance for defects such as webbing or open tears. The insight in the material behaviour created by DIC makes it easier for the operator to determine the exact moment when to switch off the pre-blowing air and to switch on the vacuum. Besides, when performing DIC measurements such as the one described above and repeating this approach with different pressure settings, the effect of a certain setting on sagging and (unwanted) sheet expansion can be quantified. The choice of the right pressure as function of the used material and processing temperature can in this way be defined prior the process. It makes it even possible, if the machine control is capable of doing so, to modify the pressure as function of temperature, keeping it steady at a predefined height instead of having an increasing height with rising temperature, as is the case in the shown example.

5.4.2 Inflation

Next to the frequent use of bubble inflation for material model validation in academia (cf. Section 2.2) and its use to freeform product such as light domes and curved (aircraft) windows, bubble inflation is an in industry commonly adopted method to increase the wall thickness distribution uniformity of positive, drape formed, products. The bubble height is often defined by experience and trial and error and is then controlled by a laser sensor or a light curtain.

When only visually inspecting the final product for the formation of wrinkles or webbing, the search for the right pressure setting leading to the right bubble height is not that difficult and cumbersome. Figure 70 demonstrates the effect of different pressure settings on the formation of wrinkles. When using no pressure at all or small pressure settings, up to valve setting 3 (cf. Figure 11: < 1 mbar) no wrinkles can be detected. When using higher pressure levels, wrinkles typically appear at the corners of the product. From pressure setting 7 and up, the area of the bubble exceeds the area of the formed product making it impossible for the vacuum to properly redistribute the material.

When, on the other hand, bubble inflation is used to accurately define the wall thickness distribution and to investigate the effect of a chosen pressure on the thickness, a lot more measurements than just visual inspection is necessary.

Typically, products with different pressure settings are formed and the wall thickness of a cross section of the final product is measured. Although it is known that the final thickness is not homogeneous, it is just a hopeless task to measure the complete product. Besides, the thus obtained resulting thickness has not only originated from the bubble inflation, but can also come from sagging or unexpected effects during forming (cf. Section 5.4.1 and 6.2.4.2).

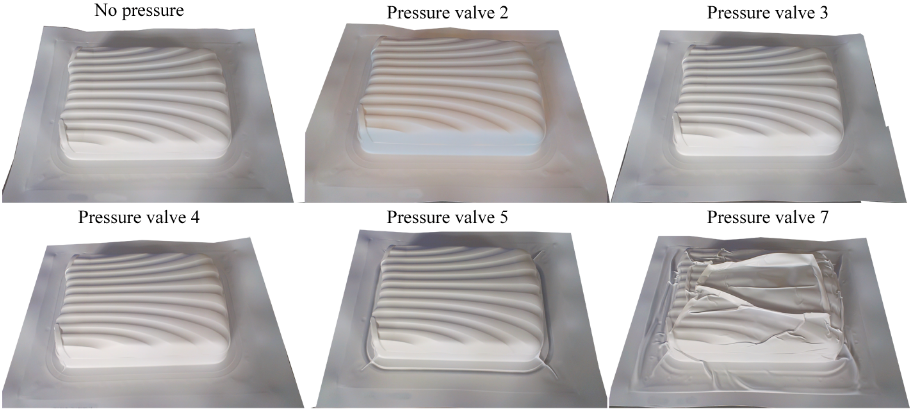
No pressure
Pressure valve 2
Pressure valve 3
Pressure valve 4
Pressure valve 5
Pressure valve 7

Figure 70 Effect of pressure valve setting during bubble inflation on wrinkling / webbing of the final product. No pressure, valve setting 2 and 3 give comparable results. For valve setting 4 and 5 wrinkles start to form in the corners. At valve setting 7 the complete product is wrinkled.

DIC makes it possible to disconnect the different effects from each other, to define the exact height and shape if a bubble asymmetry is needed and to define in a single measurement the thickness over the entire surface within the field of view. The approach for doing so is demonstrated with two examples in the next section. The first is only based on bubble inflation, the second combines bubble inflation and consecutive forming.

5.4.2.1 Bubble inflation only

A similar DIC setup as described above for the definition of the effect of sag compensation is used. A 1 mm HIPS sheet is clamped (850 x 670 mm), heated with the bottom heater to 150 °C surface temperature and after retraction of the heater, 3 variable pressure levels are applied. This pressure is kept constant until the sheet is completely cooled down to ambient temperature. After cooling, the bubble shape is retained and the sheet is unclamped (Figure 71, top row). Again, the pressure, temperature and deformation are measured throughout the process making it possible to link a certain machine setting (pressure, temperature) to a bubble height, shape and thickness. The middle row of Figure 71 represents the shape of the bubble, the bottom row the thickness distribution.

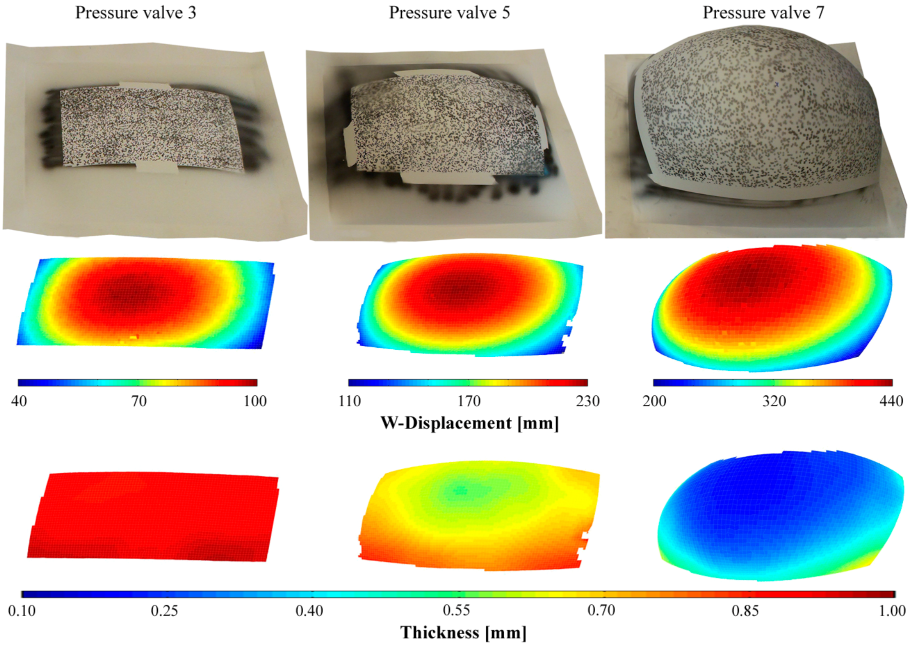

Figure 71 Top row: bubble shapes obtained with different pressure valve settings; middle row: W-displacement (shape); bottom row: thickness.

Figure 72 represents the temperature and displacement of the centre point of the sheet as function of time. The heating part of the graph, although similar to previously shown graphs, is added to demonstrate the repeatability of the heating process. The pressure and thickness plots are omitted in this graph to maintain overall clarity.

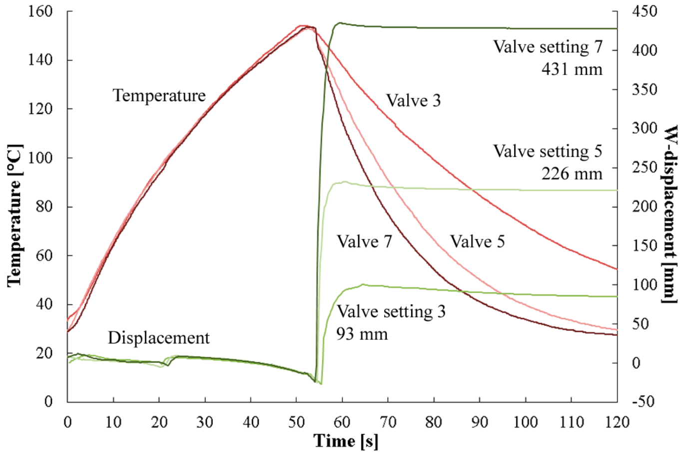

Figure 72 Temperature and W-displacement of the centre of the sheet as function of time for three settings of the pressure valve

For symmetric heating the bubble is expected to be symmetrical too. This symmetry can be seen in Figure 71 (middle row). Perfect heating is in an open mould process, such as heavy gauge thermoforming, unfortunately utopic. Small deviations from symmetry coming from surrounding conditions, variation in the quality and the age of the heating elements, the heat-sink effect of the clamping frame,... already affect the bubble shape and the optimal expected thickness distribution. When using point-based laser measurement systems or light curtains for bubble height measurements, this asymmetry is however not measured.

The assets of using DIC on a non-symmetrically heated sheet are further elaborated in the section 5.3.2.

5.4.2.2 Bubble inflation and forming

Figure 71 and Figure 72 demonstrated that the height and shape of the bubble can clearly be visualised. When the pressure is measured simultaneously, these can be coupled to process settings. The consequence for the product thickness is however not yet shown. To visualise the effect of bubble inflation on a final product, an identical thermoforming test is set up with and without the inflation step. The process and DIC settings are similar to the previous example except that in this case a suitcase shell is formed on a machined aluminium male mould with bounding box dimensions of 630 x 445 x 160 mm. Two pressures are used for the inflation step. Valve setting 4 leads to a bubble height of ±180 mm, which is slightly too high to avoid wrinkling. The second pressure setting (valve setting in between 3 and 4) is one that leads to the ideal bubble height, i.e. one in the same range as the height of the mould (160 mm). Figure 73 shows the resulting thickness distribution. When no bubble inflation is used, the thickness differences of the ribs are more pronounced since the sheet stretches by the mould upward movement and the ribs are formed at the moment the vacuum is switched on (Figure 78). The corner areas are highly stretched. If a bubble is blown, the excess material is draped on top of the mould and the ribs are not formed by the vacuum but by the draping. The stretching at the corner areas is in this case less pronounced. This results in less thickness variation, which is exactly the purpose of using the bubble inflation technique. When only judging the quality of the products based on their shape, which is common practice, they are identical. The slight differences in (vertical) W-displacement (Figure 73, top) are due to the fact that the coordinate systems of the 3 measurements are different. The W-displacement is calculated based on a best plane fit through the reference image, that is an almost flat plate, yet slightly different in each of the 3 cases. When transforming the coordinate systems so that they coincide, a maximum shape deviation of 2 mm is found over the entire surface. When looking at the thickness distribution however, a clear difference can be distinguished. The higher pressure clearly leads to a thinner top surface of the shell.

The use of DIC allows to determine the shape of the product (surface) and the thickness distribution at once. Besides thickness of the formed product, thickness and deformation data is available in every intermediate step. When using this approach during start-up or optimisation, the effect of a changing pressure (valve) setting can immediately be quantified both on the bubble height and shape as on the shape and thickness distribution of the final product, making it much easier for the thermoformer to find the optimal process settings.

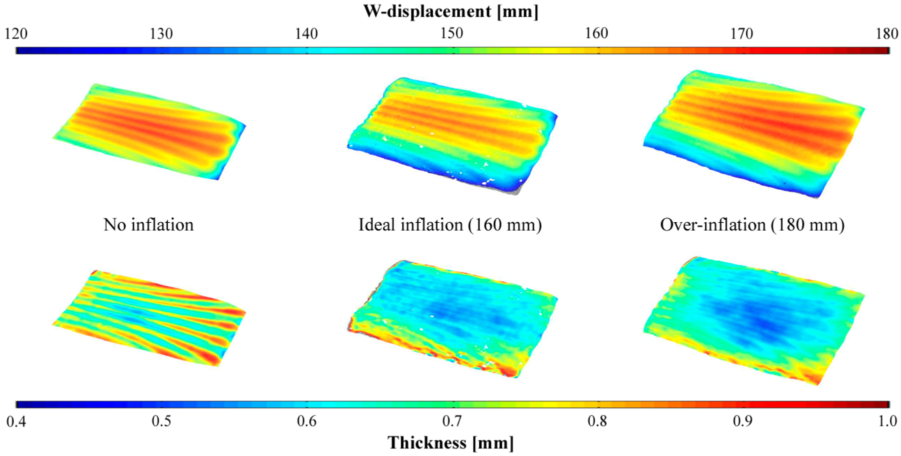

Figure 73 Top row, from left to right: W-displacements without bubble inflation, with a bubble of 160 mm height and with a bubble of 180 mm height. Bottom row: thickness values for corresponding pressure.

5.5 Forming

During forming, DIC allows for a full-field shape and thickness reconstruction. In the previous sections it was demonstrated that the full-field thickness distribution of the final part can be measured and that the influence of the intermediate steps (heating, extrusion anisotropy, sag compensation and bubble inflation) can be quantified. When one is not directly interested in the thickness distribution of the product, DIC can also be used to provide knowledge, on a spatial resolution level, of the shape of the entire sheet during the process. This knowledge can be exploited in different ways as illustrated below with three examples. The first example is included to check whether a product is completely formed or not, the second is to detect if material slip is occurring and the third shows that DIC can also be used to define whether the movement of the mould or the vacuum is responsible for the final forming of (parts of) the shape.

5.5.1 Completeness of the forming process

For most products, the question of whether it is fully formed or not is obvious and can be answered by simply visually inspecting the formed part. For shapes with double curvatures however, this is far more complex and additional measurements are often necessary. Besides, when a product is not completely formed, finding the reason for the incomplete forming is less evident since the cause of the problem can be material, temperature or process related. When applying the DIC methodology, the shape of the product is measured and can be compared to the shape of the mould. When finding abnormalities, the forming history can be consulted making it easier to define the causal relation. This is demonstrated by forming a double curved shape, i.e. a washbasin, while performing in-situ DIC measurements (more detailed correlation settings can be found in Appendix C). The mould has bounding box dimensions of 540 x 400 x 130 mm and is made by single point incremental forming (SPIF) out of an AISI 304 0.8 mm thick sheet. A centrally located small hole in the washbasin's drain connects the mould to the central vacuum system of the thermoforming machine. To be able to judge, in a later stadium, the accuracy of the thermoformed product, a laser scan (Metris LC60Dx, with an accuracy of 15 µm) of the upper side of the mould is taken. The washbasin is formed from a speckled 1 mm thick sheet of HIPS heated from the bottom to a top surface temperature of 150 °C. Based on the displacements of the speckle pattern, a 3D point cloud of the top surface of the final shape, whilst still in the mould and vacuum is not yet switched off, is exported. The part is then meshed and compared to the laser scan of the top surface of the SPIF mould, using GOM Inspect V7.5. To account for the original thickness of the polymer sheet, since DIC and laser scanning are both surface measurement techniques, the top surface of the basin is offset by its original thickness of 1 mm. Figure 74 shows that the largest difference between product and mould (up to 6.4 mm) is located at the bottom back curvature of the basin. The rest of the basin fits well the scanned surface.

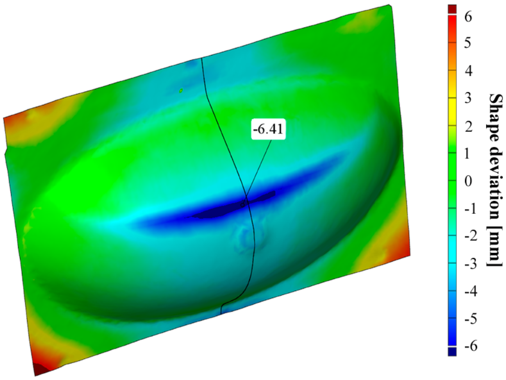

Figure 74 3D DIC measurement matched to a laser scan of the SPIF mould show differences exceeding 6.4 mm at the bottom right side

In this example the position and the reasons for these inconsistencies are of interest. One can assume that the bottom back curvature is probably not completely formed due to the wrong positioning of the vacuum holes in the washbasin's drain. This assumption is confirmed when taking a closer look at the history of a cross section in the length direction (Y-axis) of the washbasin (Figure 75). This history is retrieved from the DIC results during the forming process. The reference cross section is compared to the first picture after heating (referred to as "stop heating" in Figure 75 and Figure 76) and to other incremental steps in the forming process. Right after heating, the sheet sags symmetrically under its own weight until the start of the moulding step, but when the vacuum starts (referred to as "start vacuum"), the sheet forms asymmetrically with a preference for the front part of the mould (Figure 75). This part closely follows the actual mould surface, keeping in mind the thickness reduction and the fact that only the top of the sheet can be measured, but the back section is not. At a certain moment, the sheet closes the vacuum holes in the drain before it is able to completely take the shape of the back side of the mould. This results in an incompletely formed part. In this case it is hard to distinguish visually the incomplete forming on the final part without actual geometric measurements.

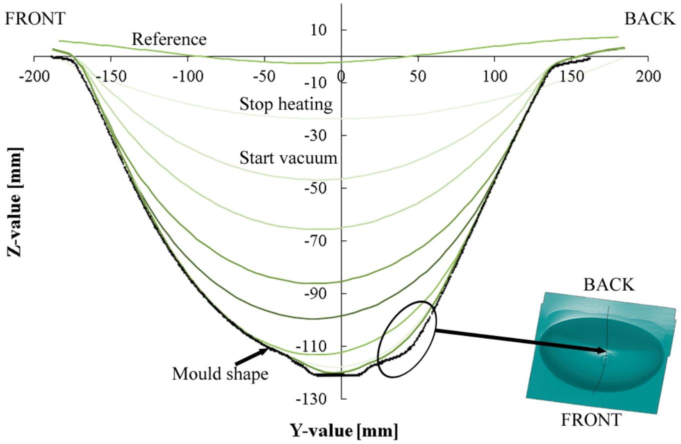

Figure 75 Shape history of a cross section in the length direction (Y-axis) of the incompletely formed washbasin

By using DIC, the problem is defined, the cause is confirmed and the resulting insight leads to a successful modification of the position of the vacuum holes giving good final products, accurately and completely copying the mould (Figure 76).

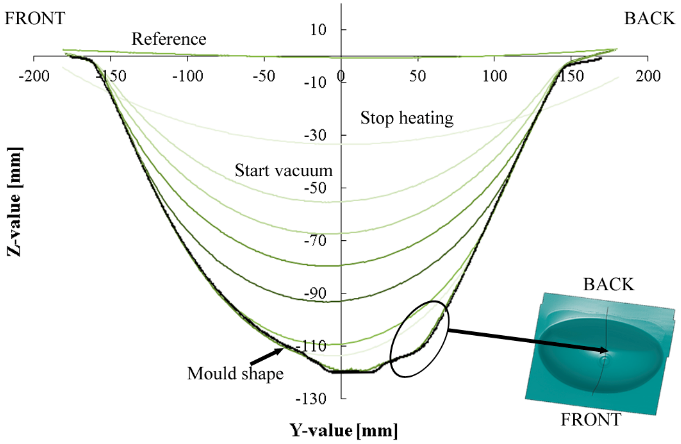

Figure 76 Shape history of a cross section in the length direction (Y-axis) of the completely formed washbasin

The difference in initial ("reference") and sagged ("stop heating") shape between Figure 75 and Figure 76 is because in the latter, a 2 mm thick sheet is used instead of a 1 mm sheet. The initial stiffness is therefore higher in that case and less initial deformation is measured. The sagging is more pronounced although the top temperature is in both cases 150 °C because the temperature gradient in the 2 mm sheet is higher. It is confirmed however that overheating a 1 mm or forming the 2 mm sheet in the initial mould does not influence the product quality and the final conclusions.

In this example only the shape of the product is taken into account and not the product thickness. When the product is offset according to its real thickness distribution instead of using the initial thickness as is the case in this example, the match will be more accurate. An example of such a match is provided in section 5.5.3.

5.5.2 Material friction

As pointed out in the state of the art (Section 2.3.1), the assumption on the (Coulomb) friction (μ) conditions is important for the prediction of the thickness distribution. Most of the researchers assume stick conditions (no slip or unlimited friction) as this is easier to model. Moreover, they are not aware of what really happens during the experiments. Again, applying DIC during forming provides a solution. This is demonstrated by using the same setup (washbasin) as that of the (in)complete forming process in Section 5.5.1. By looking in detail at the shape and the thickness of the sheet at three specific points in time - two points during forming and one point at the end of the process- and comparing the thicknesses of the sheet when it makes contact to the mould, derived from the shape, some interesting results are found (Figure 77).

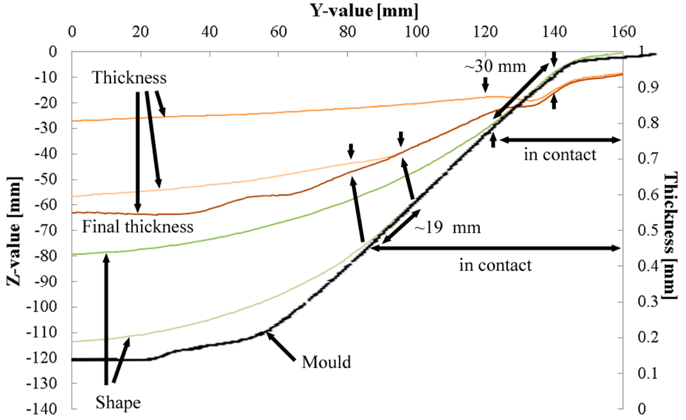

Figure 77 Shape and thickness at three different points in time reveal that slipping is occurring to a certain extent. The final shape as measured by DIC is that of the mould and is therefore not represented.

When looking at the first time point in the figure (highest "shape" line) and matching the shape to that of the final shape (mould), it can be seen that to a certain extent the sheet is in contact with the mould. When looking at the thickness of that contact zone it can be seen that although it is in contact with the mould, it still thins over a length of approximately 30 mm meaning that in that area the sheet slips and no sticking conditions may be assumed. The same is valid when looking at the next time step where a zone of approximately 19 mm slips (and thins) after mould contact. The slipping zone is decreasing in this case since the distance to the vacuum hole is smaller and the amount of time until the product is completely formed is smaller. Moreover, the sheet temperature is at that time already lower (convection losses) and will therefor provide more resistance to strain.

5.5.3 Mould and product matching

The match between the formed product shape and the mould is another important quality aspect of a thermoformed product. Equally, matching the formed product thickness to a required or expected thickness can be another quality goal in the thermoforming process. Since DIC provides both shape and thickness information, both aspects can be combined in a single measurement.

To illustrate the shape matching, the suitcase mould is used to form a (HIPS) shell while performing DIC measurements. In this example, no bubble inflation is used. The process and DIC settings are comparable to those used in Section 5.4. The approach is to align the coordinate systems of the (meshed) 3D CAD drawing of the mould and that of the measured shape. Next, the top sheet surface, which is measured by DIC, is offset by its thickness to form the bottom surface of the sheet which is in contact with the mould. Figure 78 shows the results of this approach at a moment right before vacuum (left) and at the end of the process (right).

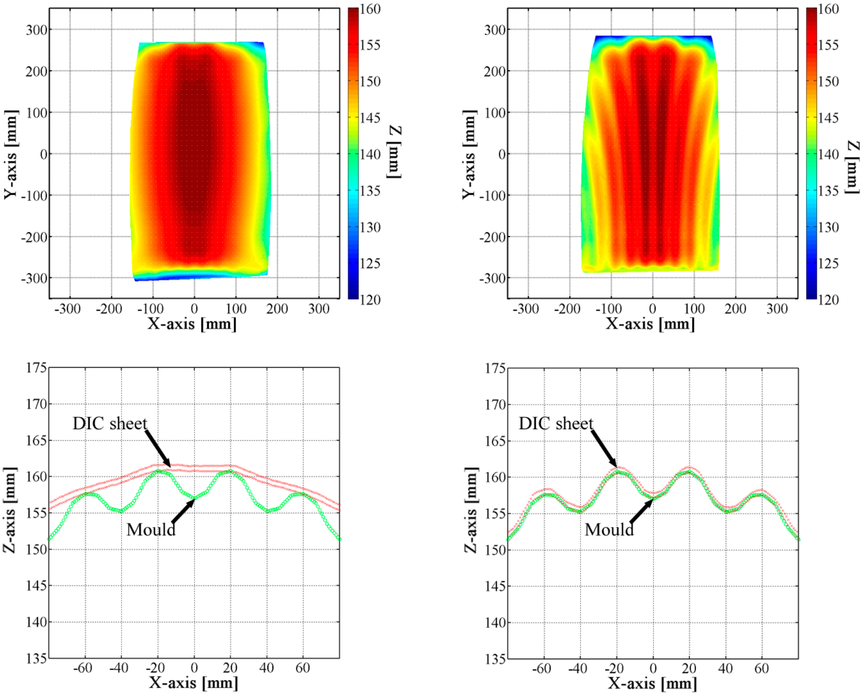

Figure 78 Top: shape of top surface of the suitcase shell right before vacuum (left) and after vacuum (right); bottom: comparison of a central cross section along the x-direction measured by DIC and compared to the mould shape

It can be seen that before vacuum is applied the sheet is stretched by the movement of the mould and is resting on top of the ribs. The vacuum takes care of the formation of the rib valleys. The small differences between the mould and the shape of the sheet can be attributed to several data processing factors. The first being the coarse mesh of the mould, the second, the coordinate alignment procedure and the third, the accuracy of the DIC system. Therefore the match between the mould and he part is reasonably good. Shape deviations over the entire top surface are within ±1 mm (see Figure 85, top right). The main advantage of this approach is however the ability to visualise the process step responsible for the final thickness distribution of the product. This visualisation not only improves process knowledge but makes it easier to set up and check the accuracy of the results of simulation or to modify simulation parameters until agreement with experimental data is found (cf. Chapter 6).

5.6 Conclusions

In this chapter, detailed examples were used to demonstrate that the newly developed methodology provides valuable information on every step of the thermoforming process:

- The ***clamping quality*** and ***sheet slip*** can be visualised, quantified and optimised.
- The consequences of ***extrusion anisotropy*** and the clamping direction have been thoroughly explained.
- A simplified thermal model has been developed and validated making it possible to predict in ***real-time*** the ***through-thickness temperature distribution*** of heavy gauge sheet.
- Examples have been provided showing that the ***effect of (a)symmetric heating*** on sagging, bubble inflation and forming can be adequately quantified. The measuring approach makes it easier for the thermoformer to define the ideal heating for his application.
- Realistic values for the ***heat transfer coefficients*** during free cooling, bubble inflation and forming are calculated taking into account the sheet thinning during the process, providing useful ***input values for simulation***.
- It is possible to define the ***necessary pressure*** for sag compensation and the ***effect of pressure*** on bubble height during inflation and ***final wall thickness distribution***.
- Detailed examples have proven that ***(in)complete forming can be quantified, sheet slip at the mould wall*** can be visualised and that the product shape can be matched to the shape of the mould.

All these new insights provide the thermoformer strongly improved means to optimise the process.

Chapter 6 - Methodology application for the optimisation of simulations

6.1 Introduction

More and more companies try to use simulations to improve their manufacturing processes, as computer processing power is not really an issue anymore and experimental optimisation methods are ever more expensive. The thermoforming industry is no exception and although thermoforming simulation software already exists for a while - the first attempts to simulate thermoforming go back to the 1970's - it is still not used to its full potential. It is mostly used only for comparative studies and prediction of relative wall thickness. One of the major reasons is the difficulty to correctly define and measure all necessary material data and process parameters, required as input for the simulation software. When trying to simulate a thermoforming process based on estimated or literature parameters, the results will often not correspond accurately with experimental measurements and therefore simulations are often poorly assessed.

Besides direct process optimisation as discussed in Chapter 5, the combined measurement approach elaborated in this thesis can also be used to:

- identify specific thermoforming simulation parameters,
- establish the link between simulation and process parameters,
- facilitate the comparison of simulation results with results from experiments or production.

The main purpose of the methodology is to provide means to minimise parameter uncertainties so that the primary focus can be on the remaining parameters and the process optimisation itself. In that way thermoforming simulation can be used for what is intended to. This can be either optimisation of the product design taking into account the final performance of the product or optimisation of the process parameters. The quality of simulation results however depends on the accuracy of the model with respect to the real process, and the quality of the input data. The more the simulation parameters agree with the process parameters, the more reliable the simulation results will be.

The best known dedicated thermoforming simulation software platforms are: Accuform's T-Sim, Rheoware's Formview, ESI's PAM-FORM and Ansys's Polyflow. The input data for simulation consists, next to a number of physical and thermal material characteristics (specific heat capacity, density, thermal conductivity) that can be measured on a lab scale, of material model data and of sheet, mould and process characteristics. DIC can be used as a key-enabling technology to define these parameters and this is explained in current chapter.

6.2 Identification of thermoforming simulation parameters

Although there are slight differences in the definition of the simulation parameters between the different software packages, the methodology for defining the parameters is generic.

6.2.1 Sheet characteristics

The most important sheet characteristics are the sheet dimensions (length, width, thickness), the temperature distribution after heating, the heat transfer coefficient to the environmental air and the heat transfer to the mould. Sheet dimensions are obvious, but an inspection of the initial thickness is recommended, since variations are common.

6.2.1.1 Sheet temperature distribution after heating

The sheet temperature (distribution) is of main importance and should be integrated in detail in a good simulation. Since all thermoforming simulations rely on a membrane (or shell) approximation, the through-thickness temperature distribution cannot be set as a starting condition. The best way to define the overall temperature distribution is to combine the thermal model developed in Section 5.3.1 with a thermal camera. The thermal model is based on the finite difference method and is used to predict the temperature of the core of the sheet, based on the measurement of the top and bottom temperature of the sheet in a single spot. The mean of these three temperatures at the end of the heating step (or after equilibration) can be taken as a point value at the location of the thermal sensors. At the moment the heaters retract and the sheet comes into the field of view of the thermal camera, a snapshot of the in-plane surface temperature distribution is captured. This full-field measurement is then scaled according to the temperature measured by the centrally located thermal sensor. The difference between the temperature measured by this pyrometer and the calculated mean through-thickness temperature at the centre location is then assumed to be proportional to the in-plane temperature difference. For example (see Figure 79), if a difference of 9 °C (96 °C – 87 °C) is calculated at the centre location (*p1*) and a surface temperature of 89 °C is measured with the thermal camera on another location (*p2*), the mean temperature at the latter can be calculated with Equation (43):

$$T_{p2mean} = T_{p2} - \left(\frac{T_{p2}}{T_{p1}} \left(T_{p1} - T_{p1mean} \right) \right) \tag{43}$$

where *p1* represents the location measured by the pyrometer in the centre and *p2* the location where the mean temperature is required. This procedure can be automated for the complete temperature grid from the thermal camera. A small error is introduced with this approach since during heater retraction the surface already starts to cool and the core temperature can even become greater than the surface temperature (cf. Figure 57). It is therefore advised to retract the heaters as fast as possible to minimise this effect. If a full-field thermal image is not available, the central point temperature can be linked to the temperature or power settings of the heating elements. This option does not take into account any surrounding influences and heat losses and will be less accurate.

Also the temperature decrease during equilibration can be measured and matched to the predicted temperature by the simulation making sure that at the moment of forming (or during bubble inflation) the right thermal boundary conditions are taken into account.

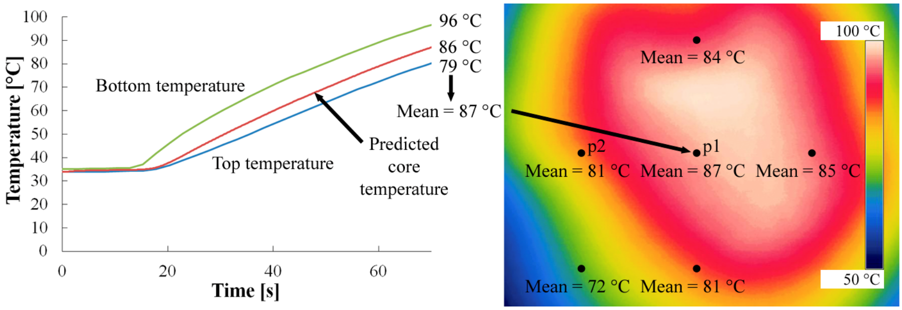

Figure 79 Methodology for the estimation of the initial in-plane temperature distribution. Left: the through-thickness temperature as function of time; right: a 2D infrared image representing the in-plane temperature distribution of the bottom surface of the sheet right after heater retraction.

6.2.1.2 Heat transfer coefficients to the environment and the mould

The way to define realistic values for the convection coefficients between sheet and ambient air and the heat transfer coefficient from sheet to mould has been explained in detail in section 5.3.3. A critical remark has to be made concerning the ambient temperature. The slope of the curves and the calculated heat transfer coefficients are in direct relation with the ambient temperature and the air velocity. Care has to be taken to use the right ambient temperature. Moreover the temperature of the air around the top surface and the bottom surface can be different, especially when the machine is running in a steady state, leading to different heat transfer rates. For that reason, the thermal model has the possibility to include a different temperature for upper and lower environment.

6.2.2 Mould characteristics

Next to the sheet characteristics also the mould properties are of major importance. Key parameters are the mould shape, the temperature distribution, the mould position and the temperature dependent friction which is affected by the contact pressure and the surface roughness of the mould. Thermal conductivity and heat capacity values of the mould are typically not included within dedicated thermoforming simulation software. It is mostly assumed that the thermal inertia of the mould is much bigger than that of the sheet (cf. Table 8).

6.2.2.1 Mould shape

When a new product is developed, the first aspect to take into account is the shape of the mould. Slight modifications to corner radii, design features that increase the stiffness,... can greatly improve product performance. For this reason it is of major importance for the designers to know what the effect of a modified design is on the wall thickness distribution after thermoforming. Nowadays the products are formed and thickness measurements are performed on a number of critical locations of the final product. When DIC is used, the full-field thickness is defined in a single experiment. This approach makes comparison of different designs much easier, more comprehensive and faster.

6.2.2.2 Mould temperature

In simulation, the mould temperature can either be set to be homogeneous with a specific heat transfer coefficient or the possibility exists to assign different temperatures and heat transfer coefficients to certain parts of the mould in order to locally affect the thickness by making use of the locally modified friction (see Section 6.2.2.4) or sheet temperature (Section 6.2.1.1).

6.2.2.3 Mould position

The importance of the mould displacement speed and position is sometimes underestimated in a simulation since it is a tangible parameter that seems not that difficult to set. In simulation it is defined either by setting a position as function of time (T-Sim, Formview) or by setting a velocity as function of time (Polyflow). In most thermoforming machines, the mould position as function of time is defined by a velocity as function of its position meaning that start and stop accelerations and decelerations are unknown. The conversion from machine parameter to simulation is thus not that easy and straightforward. Besides, the exact moment at which the mould makes contact with the sheet and the in-plane position where it makes contact is important and in most cases cannot be distinguished visually since the process is too quick. DIC allows to determine the exact moment and position where the sheet makes contact to the mould. This is especially interesting when the sheet is heavily sagged, a bubble is blown or asymmetric heating is used to validate the simulation model to reality.

6.2.2.4 Mould friction

It is well known that the temperature difference between mould and sheet, pressure of the sheet on the mould and mould roughness all greatly affect the coefficient of friction. Using zero friction in simulation means that the sheet will continue to slide over the surface after contact and that it can continue to stretch (and thin) until the end of the process. On the other hand, a high coefficient of friction means sticking contact and stops the sheet from thinning from the moment it makes contact with the mould. For the thermoformer willing to simulate his process it is not an easy task to define the right coefficient of friction. The proposed methodology in this thesis does not directly specify which value for the coefficient of friction to use, but visualises the real process with all its boundary conditions at any point of time. With this insight and by closely following the displacement and strain progress as function of time, as explained in Section 5.5.2, case specific coefficients of friction (including temperature and strain rate dependence) can be defined until simulation corresponds (exactly) to experimental measurements.

Simulation specific parameters related to contact conditions such as the penalty coefficient and the penetration accuracy (Polyflow) can then be fine-tuned but should not lead to significant differences in the final result since they should be more related to simulation stability rather than to accuracy.

6.2.3 Process characteristics

The process characteristics are the simulation settings, not directly related to the material or the mould: i.e. the air pressure and the vacuum pressure as function of time and the ambient air temperature.

6.2.3.1 Air pressure and vacuum level

Since a pressure sensor is part of the measurement setup, the actual pressure occurring under the sheet (sag compensation, bubble inflation) can be measured and linked to a specific setting of the pressure valve. By being able to use the correct pressure in the simulation software and relating this pressure to an amount of sagging or a bubble height, an additional source of uncertainty is eliminated.

A vacuum sensor is not included in the setup since this sensor should be built in the mould or in the vacuum suction line making the setup mould or machine-dedicated and not standalone. The availability of a vacuum sensor is nevertheless an added value since without it assumptions need to be made on the force acting on the sheet while it is under vacuum. On the other hand, since the strain distribution as function of time is known from DIC measurements, the strain rate, which is necessary to link the deformation data to the material model, can be extracted. This makes the availability of a vacuum sensor less critical.

6.2.3.2 Ambient air

It is already mentioned that the surrounding air temperature is important to correctly predict the cooling rate of a polymer sheet. Since the temperature of the sheet is continuously measured, either the starting temperature of the sheet at the moment it is positioned in the machine or the temperature at the moment it is completely cooled down can be taken as a good estimate. The temperature of the air between the heaters and the sheet during heating is unknown but less critical when using the thermal model developed in section 5.3.1 to predict the core temperature and the temperature distribution.

6.2.4 Material model data

One of the most challenging tasks when trying to simulate a thermoforming process is the choice of the right material model. Each simulation software has its own built in models (see Table 8) and there is no clear definition available in literature stating which material model to use for which kind of deformation or material. Besides, every model has its positive and negative aspects (cf. Section 2.3). When a model (or software) is chosen, the next task is to define the strain rate and temperature dependent material parameters. Fortunately the thermoforming software suppliers provide a limited material database for the most common materials as a starting point. Nevertheless, without process insight it is hard to evaluate if a material model is adequate for a certain deformation. A way to check this compatibility is to use the methodology from this thesis and to compare the results from thermal, pressure and DIC measurements to the simulation. By doing so, the only unknown parameter that remains in the simulation is the material. The simulation can be performed with the default material model parameters as initial values. If the simulation does not correspond to experimental measurements, the material model and/or parameters can be modified until good agreement with the experiment is found.

The approach on how to set up a simulation and compare the data to experiments is shown in the next paragraphs for two cases. The first is a bubble inflation experiment, the second is a forming process. Both simulations are performed in the dedicated software from Rheoware: Formview V9.1 but could have been done in any software. A similar study between simulation (T-Sim) and experiments was already published by the present author in Express Polymer Letters, Vol. 9 (2015) [181].

6.2.4.1 Simulation of bubble inflation

To obtain accurate input parameters for the simulation software, most of the tools as described in Chapter 5 are used. A 1 mm HIPS sheet is clamped (850 x 670 mm), heated with the bottom heater until the top surface temperature reaches approximately 150 °C and after retraction of the heaters, a bubble is inflated (pressure valve setting 3). The temperature, pressure and deformation is recorded during the process until the bubble is cooled down to ambient temperature. Three repeats of this test proved to deliver similar results. From the measurements the mean through-thickness temperature of the centre of the sheet is calculated (151 °C following the procedure of Section 6.2.1) and used as a uniform starting temperature of the sheet in the simulation since the in-plane temperature is within 151±5 °C. Next, the initial sagged shape (25 mm in the centre) and the thickness after sagging (0.93 mm) are used as the starting point for the simulation. The sheet is meshed with 9120 triangular shell elements. The pressure profile as recorded by the pressure sensor is entirely entered into the simulation software. An ambient temperature of 25 °C was chosen and a convective heat transfer coefficient of 24 W/m^{2}K was determined by fitting the cooling curve. The physical (density) and thermal (specific heat, conductivity) parameters of the material are entered as defined in Section 3.2.5. Last but not least, the HIPS material parameters for the K-BKZ viscoelastic model are extracted from the built-in material database (see Table 7 in Section 3.2.5.4). The simulation is performed with a time step of 0.1 s. Afterwards, the temperature, pressure, (vertical) W-displacement and thickness of a node in the centre is plotted as function of time and compared with experimental data (Figure 80).

Figure 80 shows that although the temperature and the pressure agree well, the displacement height in the simulation overestimates the experimental data. As a consequence the sheet thinning is also slightly overestimated (0.83 mm in simulation versus 0.87 mm in reality). One could conclude that for this kind of deformation (strain, strain rate, temperature), the model provides thickness results within 5 % accuracy, which is in general an acceptable result for simulation. For other process conditions, the model needs of course to be additionally validated.

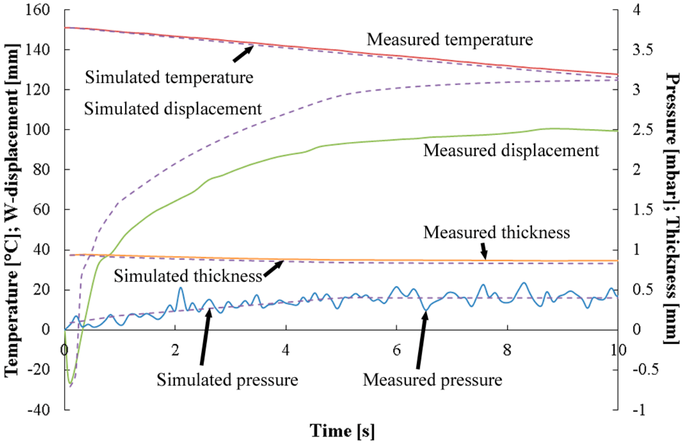

Figure 80 Temperature, W-displacement, pressure and thickness comparison of a central node between DIC and Formview simulation software for a bubble inflation experiment with valve setting 3

If one is looking for exact correspondence, the material parameters can be iteratively modified until a perfect match is found. A possible way to do this is based on the approach of Baumgaertel and Winter [220, 221]: instead of defining relaxation times and relaxation moduli from dynamic mechanical data, the approach is reversed. The storage and loss moduli are plotted based on the material parameters from the simulation software database. Care has to be taken to shift the curves to the forming temperature since this does not necessarily correspond to the reference temperature at which the parameters have been defined. This can be repeated for different materials from the software database. Upon comparing the material behaviour in the simulation (for example bubble height) to that of the DIC measurements and by combining it with the knowledge on the occurring strain rate (also from DIC), idealised storage and loss modulus curves as function of strain rate can be derived. These curves can then again be discretised into relaxation times and moduli following the procedure of Baumgaertel and Winter.

Figure 81 shows the displacement and thickness as function of time during inflation with pressure valve setting 3 (identical to Figure 80) for the standard HIPS material from the database, for the HIPS material using the material parameters from ABS and for an optimised material parameter set defined following the procedure described above. Since this only serves as a proof of concept a single relaxation modulus (0.1 MPa) and relaxation time (1 s) is chosen, but obviously more couples could have been defined. The development of an (automated) material parameter estimator based on this approach is not the purpose of this research, but could be an interesting topic for future projects. These specific values were chosen to obtain material behaviour in between those of ABS and HIPS. The ABS material shows more resistance to deformation than the standard HIPS material leading to a bubble that is a little lower than in reality with a less pronounced thickness reduction. The optimised parameter set captures the height within 5 %.

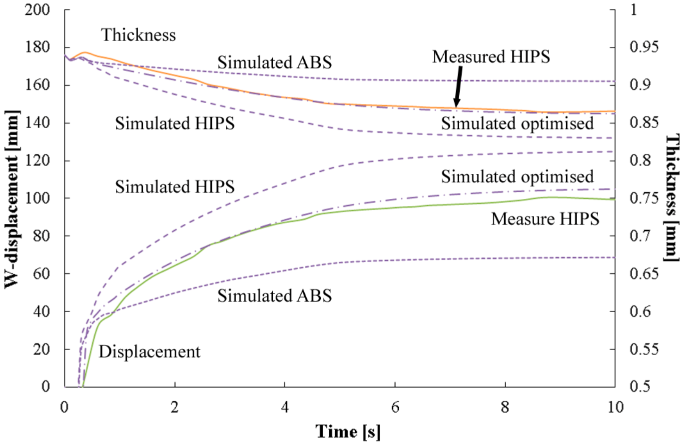

Figure 81 W-displacement and thickness of a central node during bubble inflation with valve setting 3 measured by DIC and compared to simulation in Formview using the generic HIPS and ABS parameters from the material database and the optimised parameters

The optimised parameter set is also used to simulate a bubble inflation with valve setting 5 (higher pressure and strain rate) and is compared to experiments in Figure 82.

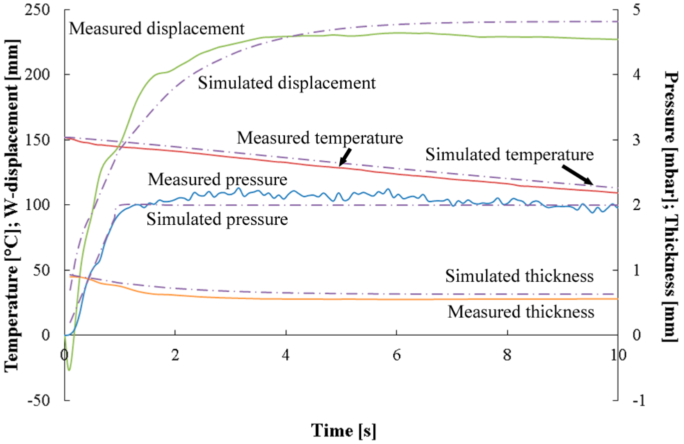

Figure 82 Comparison of the temperature, W-displacement, pressure and thickness of a central node between DIC measurements and Formview simulation with the optimised material parameters for a bubble inflation with valve setting 5

The standard HIPS model parameters overestimate the bubble height by almost 50 % (not show in figure), the optimised parameter set predicts the correct height and thickness within 6 %. Not only the height of a central node of the bubbles in the simulation corresponds to the experimental data but also the shape of the complete bubble. The real advantage of using DIC is that it provides full-field measuring data instead of single point data. The latter is currently industrially obtained with height acquisition devices or a light curtain. Full-field data allows to determine, next to the height of the bubble, also asymmetries created by extrusion anisotropy (cf. 5.2.2) or un-uniform heating in plane (cf. 5.3.2).

6.2.4.2 Simulation of forming

Similar to the first example, a simulation is matched to experiments but this time a bubble is inflated (ideal bubble height: 160 mm) and a suitcase shell (cf. Section 5.4.2) is formed. The method for defining pressure and temperature profiles is identical to the first example, as is the choice of the material parameters. The mould temperature is set to 25 °C and the heat transfer coefficient to 200 W/m²K (cf. Figure 68). Friction is not included in this example, the material is free to slide over the surface, since this corresponds to the behaviour of the top surface of the sheet observed during DIC measurements. Here again, the temperature, pressure, displacement and thickness of a node in the centre is plotted as function of time and compared to experimental data (Figure 83). Similar to the bubble inflation experiment, the bubble height simulated with the HIPS material from the Formview's materials database overestimates the experimental values. At the moment the mould makes contact with the sheet in simulation (5 s), the cooling slope increases, something that is also seen in experiments except that it is delayed by half a second due to secondary effects (cf. Section 5.4.1) caused by a late switchover from inflation to vacuum. These effects induce a localised strain (thinning) in the centre. This is the primary reason why the simulated final thickness in the centre is in this case an overestimation of the reality (0.73 mm versus 0.65 mm respectively) although the inflated bubble is higher.

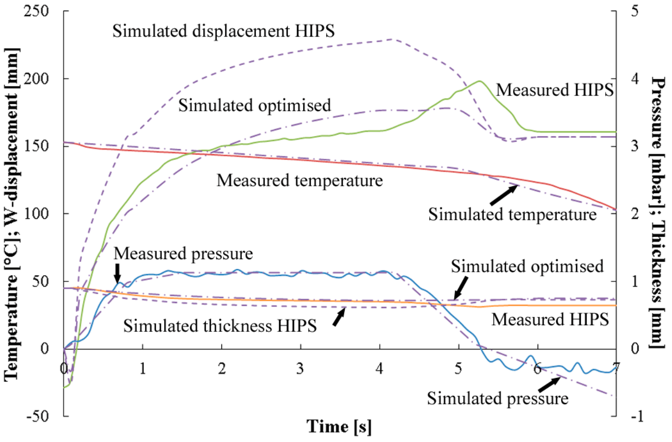

Figure 83 Comparison of the temperature, W-displacement, pressure and thickness of a central node between DIC measurements and Formview simulations with the generic HIPS material parameters from the database and with the optimised parameters for the bubble inflation and the forming of a suitcase shell

When on the other hand the process is simulated with the optimised material parameters, as defined during bubble inflation (Section 6.2.4.1), the bubble height corresponds more accurately to the experimental one but the thickness difference stays comparable due to the aforementioned secondary effects. It is expected that when these unwanted effects are omitted, the thickness difference would have been within a 5 % deviation. When comparing the complete thickness distribution of both simulations instead of the centre point values, the effect of the changing bubble height can also be distinguished clearly (Figure 84). The sheet is draped over the complete top surface in the case of the highest bubble, leading to a quasi-uniform thickness distribution, whereas a circular central part of the sheet is separated from the rest in the lower bubble. The latter case is definitely more representative when comparing the thickness distribution and the wrinkles at the corners, which are less pronounced, to experiments for this pressure level.

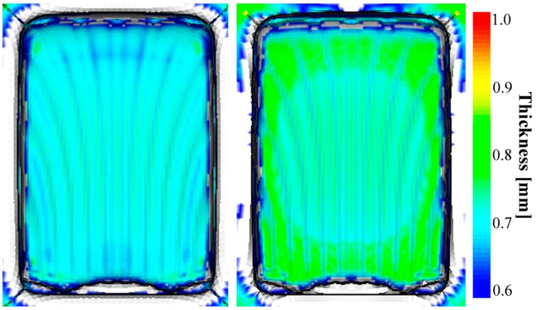

Figure 84 Final thickness distribution in Formview with the generic HIPS material parameters from the database (left) and with the optimised material parameters (right)

The two preceding cases show that when all but the material parameters are known, it is possible to perform a rather adequate simulation, even with material parameters from the material database. Results are within an allowable tolerance (less than 10 %) and the material model for the simulated strain rates and temperatures is appropriate. Of course this is case dependent and a good match is not always obtained. When looking at the example of section 5.5.3 where a suitcase is formed without bubble inflation and comparing the product shape and thickness before and after vacuum between simulated and experiments, significant thickness differences are found (Figure 85). The reason for these differences are mainly related to the fact that when no bubble inflation is used, the thickness of the centre of the sheet is influenced by two phenomena. The first being the thinning due to the forces of the mould acting against the sheet when moving up (~40 %). The second is the additional thinning in between the rib tops during vacuum (~10 %). In simulation, the software assumes that the ribs of the top surface are forming during the upwards movement of the mould and that the sheet is freely draped on the top surface instead of being forced, independently of the slip conditions. The final thickness of the top surface of the suitcase shell in simulation is therefore already determined before vacuum is switched on and the thinning is limited to approximately 10 %, instead of the 50 % measured in reality. Changing the slip coefficient had no influence whatsoever on this phenomenon. The tops of the ribs however are correctly predicted. The significant difference in thickness at the valleys of the ribs can be attributed to either the material model, the model parameters, penalty coefficients of the contact formulation, the solution method or to mesh related issues such as the bending rigidity. The real cause of the difference is however not yet uncovered.

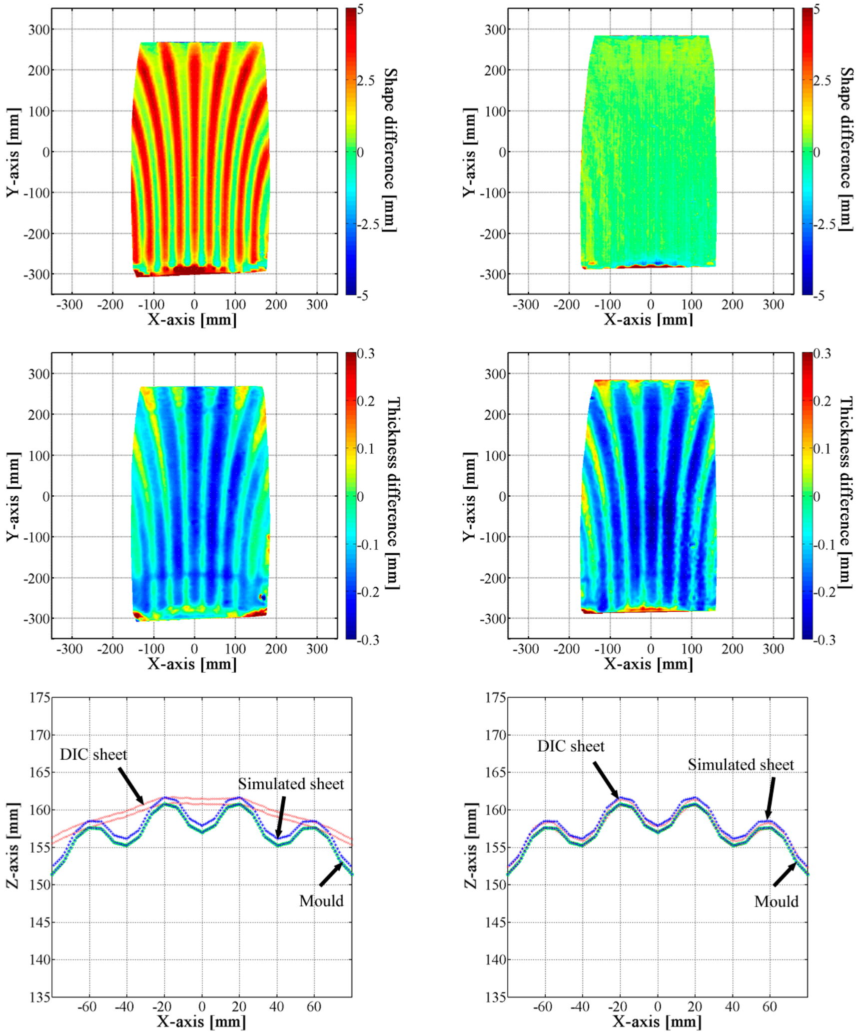

Figure 85 Top: difference in shape between simulated and measured suitcase shell right before vacuum (left) and after vacuum (right);middle row: thickness difference between simulated and measured sample. Negative values mean an overestimation in simulation. Bottom row: comparison of a central cross section along the x-direction measured by DIC and compared to the mould shape and the simulated shape.

6.3 Conclusions

Forgoing examples show that simulation of the thermoforming process is not straightforward and that without detailed knowledge of the process parameters it is an almost impossible task to perform simulations with acceptable accuracy. Besides, even when the parameters are known, discrepancies between simulation and experiments are still observed. The combined measuring methodology reduces the number of unknown parameters and allows to compare simulation to experiments in order to match simulation to reality. In this way, simulation can be used more reliably for in-process and design optimisation.

Chapter 7 - Conclusions

7.1 Conclusions

7.1.1 Introduction

A critical review of the literature has learned that in order to improve the thermoforming process in an efficient way (both experimentally and through simulations), a significant amount of knowledge on what is really happening ***during*** the process is still lacking.

The thermoforming companies have no adequate means to quantify the effects of parameter changes on the part quality, since there is currently no process monitoring system available to follow the process step by step. The only way to judge the effect of a modified (process)parameter is to (manually) measure the thickness of the final product. This is mostly done in a tactile way and on cross-sectional cuts of the thermoformed part. The influence of the quality of raw sheet material, the in-plane and through-thickness temperature distribution, sagging effects,... cannot be directly quantified. Moreover, a significant amount of literature on the effect of process parameters is available, but most of the studies are too specific for a certain machine, process variant, material, parameter combination,... making the results not transferable to a different industrial context.

Even though several thermoforming simulation tools have been developed in the past two decades, they are currently not used to their full potential because the link between the simulation input data and the real, industrial process and machine settings is unclear.

7.1.2 Developed methodology

To overcome abovementioned shortcomings, a new in-situ experimental approach has been proposed. This novel combined measuring methodology, including in-situ deformation, real-time temperature and pressure measurements provides insight in every step of the thermoforming process. The method consists of simultaneous measurement of pressure, (full-field) temperature and deformation. The deformation measurements are based on stereo digital image correlation (DIC) and produce full-field displacements, strains and changes in thickness of the entire sheet during the process. The conversion from strain to thickness is based on a constant volume assumption. The application of DIC to thermoforming, which often implies large deformations, has been thoroughly studied and solutions have been provided to overcome the difficulties that arise such as the speckle pattern, the uniformity of lighting and possible influences of temperature on the digital image correlation results. A tool has been developed to define in advance the correct measurement setup taking into account results from correlation, and the necessary field of view and depth of field of the cameras. On the thermal side, a methodology is proposed to monitor in real-time the through-thickness temperature distribution based on surface temperature measurements, either by full field thermography, or by the pyrometers installed in the heater banks of the thermoforming machine. This thermal tool generates relevant temperature data that can be used during start-up optimisation or for on-line quality control purposes during a continuous production. Typical unwanted start-up phenomena due to the heating of the environment, jeopardising the process stability and requiring an operator intervention for the adjustment of the process parameters, will be identified and potentially solved. Finally, a methodology has been proposed to define realistic heat transfer coefficients to the environment, during bubble inflation and to the mould. These coefficients are essential for simulation purposes.

By adopting the methodology and the developed tools, perspectives for easier process optimisation and minimum setup times are offered. The overall thermoforming process can be improved by minimising the trial and error on start-up, reducing the downtimes during production and making thermoforming simulation software a valuable alternative to optimise the process parameters instead of using experimental optimisation.

The methodology has a number of advantages compared to current (trial and error) approaches.

- As digital image correlation is a ***non-tactile*** measurement, there is no dependency on the applied measuring force as is the case when measuring the thickness in a tactile way.
- The methodology is ***full-field*** meaning that there is no need to measure only in cross-sections and assume (axi)symmetry.
- The measurement is ***fast***, the correlation speed depends on the chosen area of interest, step size, subset size and the correlation algorithm complexity and can be chosen as function of the required spatial resolution.
- The developed thermal model is even meant to provide ***real-time through-thickness temperatures***.
- The measurements are performed ***during the process*** and not only on the final product, in this way ***transient effects can be quantified***.
- All measurements can be performed ***on industrial machines with realistic moulds and surrounding conditions***. There is no need to perform the tests under laboratory conditions or with academic shapes.
- When using the proposed thermal model based on pyrometer measurements there is ***no need to define heater specifications, environmental temperatures or convection coefficients*** to estimate the through-thickness temperature distribution of the sheet during heating.
- Finally, the methodology is ***generic*** and does not require a predefined soft- and hardware. The user is free to choose whatever hardware and whatever DIC and simulation software he wishes to purchase.

7.1.3 Methodology application

By means of detailed example experiments, the new methodology has been validated for the different **steps of the thermoforming process**.

- It has been shown that it can be used to visually quantify the ***slip of the sheet*** in the clamping frame and the influence of the ***clamping direction***, and thus ***extrusion anisotropy***, on sheet sagging and forming. The insights on the effect of extrusion anisotropy can be used to define the most optimal direction to position the sheet in the thermoforming machine.
- The ***amount of sagging and the buoyancy effect*** during heater retraction can also easily be quantified. It is also proven that by combining the full-field displacement data with pressure measurements, important information can be gathered on ***sheet sag compensation*** and ***bubble inflation*** making it easier to find the right pressure (valve) setting depending on the desired thickness distribution.
- The methodology provides a fast and easy solution to define the ***effect of pattern heating***, something which is highly time consuming and therefore currently not being fully exploited. Major insight on which step is responsible for which amount of thinning due to symmetric or asymmetric heating is created in that way.
- The methodology can also be used during and after the forming step due to its ability to ***reconstruct the 3D shape*** and to provide the ***full-field thickness distribution***. The shape and/or the thickness can then be compared to an 'ideal' product and well-considered choices can be made concerning the process parameters to be set on the thermoforming machine.
- Last but not least, it provides information whether or not the sheet is ***sticking*** to the mould wall or an amount of ***slip*** is occurring.

When applying the methodology for the optimisation of **thermoforming simulations**, unknown parameters that have to be estimated or that are currently based on experience can accurately be defined. ***All but the material parameters can be quantified leaving less variables influencing the simulation accuracy***. Additionally it is shown that decent simulations can be run when using optimised material parameters derived from the generic material parameters that are available in dedicated simulation software material databases. This was shown by the simulation of a bubble inflation step and a forming step. An additional asset is that the methodology offers a way to compare experimental results to simulation results (thickness, strain, strain rate, forming mechanisms, contact,...), making it easier to define inconsistencies in simulation.

7.2 Further developments and future perspectives

Some thoughts on possible future developments of the methodology and on future perspectives on the applications of the measuring methodology can be formulated.

7.2.1 Further developments

The proposed method has some limitations. They are however not insurmountable and can offer interesting topics for further development of the technology.

As a stereo camera setup is used, the system is only suitable for ‘visible’ processes and parts. The product to be formed should always be within the field of view of both cameras during the process. It cannot be applied when heaters block the sight of the cameras, nor for closed mould processes.

For deep parts and steep walls, there could be a need for more than two cameras to capture at all times the complete area of interest of the product. Multi-camera DIC systems are commercially available for this purpose.

In applications where very high strains are expected, care has to be taken that the frame rate of the cameras is sufficiently high to limit the amount of deformation between two consecutive images. The maximum amount of deformation depends on the kind of deformation and the chosen correlation settings. However, this has not yet been translated in a straightforward guideline.

DIC relies on pattern matching of a random speckle pattern. If the material itself does not show such a speckle pattern, it must be applied prior to the process. For each new substrate material, the bonding of the speckle paint must be investigated.

Validation of the DIC thickness calculation is performed on specimens in different steps of the forming process but always in the cooled state. An interesting topic for future research would be to correlate the in-situ thickness results from DIC measurements to the ‘real’ thickness of the sheet in heated state.

Although steps have been taken to improve simulation accuracy by applying the methodology, further developments of simulation software can be envisaged. Until now, the consequences of the extrusion anisotropy, secondary effects after bubble inflation or forming discrepancies (cf. Section 6.2.4.2) are not yet included in the process models even though this research has demonstrated they significantly affect the wall thickness distribution and thus the part quality.

Although the methodology has been thoroughly validated for one type of material (and thickness) only, it should be applicable to a wide range of materials. Nevertheless, some remarks have to be formulated.

DIC is a surface measuring technique and it is assumed that the measurements at the surface of the sheet reflect what is happening through the thickness of the sheet and at the opposite side. When using heavier gauge sheet, there is a risk that this assumption is no longer valid. The thicker the sheet, the more the possibility exists that through-thickness shear deformation occurs. The accurate thickness prediction and the visualisation of slip (friction) should in those cases carefully be validated.

The thickness calculations are based on the assumption of volume conservation during deformation and although this assumption is valid for many materials, it must be checked when applying the methodology on other materials. The method has also not yet been applied on heterogeneous materials like composites or microcellular materials. Using (short) fibre reinforced thermoplastic sheets in thermoforming could be an interesting extension of the research since the use of it is rather limited due to the additional difficulties that the fibres entail. Perspectives are that using reinforced sheets will allow the downgauging of the sheets. The methodology could in a more straightforward way define if the use of reinforced sheets is indeed beneficial.

Simulation results showed that reasonable accuracies could be obtained when optimising material parameters starting from the material parameters available in the simulation software database, however sometimes higher accuracy is needed. Therefore, an iterative experimental-numerical method can then be used to define the material parameters (and the material model if necessary) corresponding to the observed material behaviour. This can be done by performing a number of bubble inflation experiments at different pressures (strain rates) and different temperatures, fitting the results to a number of material models and choosing the model that provides the best match between simulation and experiments. This kind of identification could be done on the thermoforming machine itself or on a dedicated setup. The latter is however expected to yield more accurate results. Besides, it can also be used to define thermoformability (cf. Section 2.2.1.1) or as an easy and fast method for the quality control of newly supplied material batches (e.g. by visualising the effect of the residual stresses on the displacement of the sheet during heating).

7.2.2 Future perspectives

Further industrial valorisation of the developed methodology requires two additional steps. First, the methodology from this doctoral study must be made as generic as possible so it can be used with little to no effort in a broad range of equipment and applications, also outside the thermoforming business. It is necessary to develop additional optimisation tools and programs that are not yet available in industry. Secondly, the generic system must be implemented and validated in a real industrial environment, both as part of a new product start-up and as a quality control tool during continuous production. The two aforementioned steps will be performed during an Innovation Mandate funded by the Flemish government agency for Innovation by Science and Technology. The biggest challenge in this project will be to define the link between a certain phenomenon during the process and the process parameter responsible for that phenomenon.

The results of this research have the potential to be used by all (thermoforming) companies where a multi-sensor in process quality control system can mean an added value. It is believed that this will result in higher product quality and a shorter time-to-market. Besides, companies related to vision applications or companies that develop thermoforming simulation software may also benefit from the proposed approach.

Bibliography

[1] J. L. Throne, *Technology of thermoforming*: Hanser, 1996.

[2] J. J. M. Cormont, "Differences between amorphous and crystalline plastics with respect to thermoforming," *Advances in polymer technology,* vol. 5, pp. 209-218, 1985.

[3] D. Hylton, "Laboratory techniques for predicting material thermoformability: a review," in *SPE Antec*, Montreal, 1991, pp. 580-583.

[4] M. Yamaguchi and K. Suzuki, "Enhanced strain hardening in elongational viscosity for HDPE/crosslinked HDPE blend. II. Processability of thermoforming," *Journal of Applied Polymer Science,* vol. 86, pp. 79-83, Oct 2002.

[5] H. Munstedt, S. Kurzbeck, and J. Stange, "Importance of elongational properties of polymer melts for film blowing and thermoforming," *Polymer Engineering and Science,* vol. 46, pp. 1190-1195, Sep 2006.

[6] D. Laroche and F. Erchiqui, "Experimental and theoretical study of the thermoformability of industrial polymers," *Journal of Plastic Film & Sheeting,* vol. 15, pp. 287-296, 1999.

[7] N. J. M. Martin, J. F. Lappin, E. M. A. Harkin-Jones, and P. J. Martin, "The use of hot impact testing in the simulation of the plug-assisted thermoforming process," in *SPE Antec*, Orlando, 2000.

[8] D. Laroche and F. Erchiqui, "Experimental and theoretical study of the thermoformability of industrial polymers," *Journal of Reinforced Plastics and Composites,* vol. 19, pp. 230-239, 2000.

[9] B. Hegemann, "Deformationsverhalten von Kunststoffen beim Thermoformen - experimentelle und virtuelle Bestimmung," PhD, Institut für Kunststoffkunde und Kunststoffprüfung, University of Stuttgart, Stuttgart, 2004.

[10] P. J. Martin, C. W. Tan, K. Y. Tshai, R. McCool, G. Menary, C. G. Armstrong*, et al.*, "Biaxial characterisation of materials for thermoforming and blow moulding," *Plastics Rubber and Composites,* vol. 34, pp. 276-282, 2005.

[11] C. P. J. O'Connor, G. Menary, P. J. Martin, and E. McConville, "Finite element analysis of the thermoforming of polypropylene," *International Journal of Material Forming,* vol. 1, pp. 779-782, Apr 2008.

[12] H. C. Lau, S. N. Bhattacharya, and G. J. Field, "Melt strength of polypropylene: Its relevance to thermoforming," *Polymer Engineering and Science,* vol. 38, pp. 1915-1923, Nov 1998.

[13] D. Hylton. (2011) Thermoforming index - A new test for sheet. *Thermoforming Quarterly*. 12-14.

[14] A. J. De Vries and C. Bonnebat, "Uni- and biaxial stretching of chlorinated pvc sheets. A fundamental study of thermoformability," *Polymer Engineering and Science,* vol. 16, pp. 93-100, 1976.

[15] M. N. Charalambides, L. Wanigasooriya, J. G. Williams, and S. Chakrabarti, "Biaxial deformation of dough using the bubble inflation technique. I. Experimental," *Rheologica Acta,* vol. 41, pp. 532-540, Oct 2002.

[16] C. Galliot and R. H. Luchsinger, "Uniaxial and biaxial mechanical properties of ETFE foils," *Polymer Testing,* vol. 30, pp. 356-365, Jun 2011.

[17] D. J. Hitt and M. Gilbert, "A machine for the biaxial stretching of polymers," *Polymer Testing,* vol. 13, pp. 219-237, 1994.

[18] A. Dharia, "Novel method for rapid determination of thermoformability," in *SPE Antec*, Boston, 2005, pp. 1214-1219.

[19] F. Beilharz, C. Bonten, and P. Eyerer, "Influence of processing conditions on the thermoformability of PP-sheet material," in *SPE Antec*, Boston, 2011, pp. 2504-2508.

[20] S. S. Morye, "A comparison of the thermoformability of a PPE/PP blend with thermoformable ABS. Part I: Small deformation methods," *Polymer Engineering and Science,* vol. 45, pp. 1369-1376, Oct 2005.

[21] L. R. Schmidt and J. F. Carley, "Biaxial stretching of heat-softened plastic sheets using an inflation technique," *International Journal of Engineering Science,* vol. 13, pp. 563-578, 1975.

[22] N. J. MacAuley, E. M. A. Harkin-Jones, and W. R. Murphy, "The influence of nucleating agents on the extrusion and thermoforming of polypropylene," *Polymer Engineering and Science,* vol. 38, pp. 516-523, Mar 1998.

[23] F. G. Torres and S. F. Bush, "Sheet extrusion and thermoforming of discrete long glass fibre reinforced polypropylene," *Composites Part A: Applied Science and Manufacturing,* vol. 31, pp. 1289-1294, 2000.

[24] A. D. Gotsis, B. L. F. Zeevenhoven, and A. H. Hogt, "The effect of long chain branching on the processability of polypropylene in thermoforming," *Polymer Engineering and Science,* vol. 44, pp. 973-982, May 2004.

[25] P. Jacoby, "The use of beta nucleation to improve the properties and lower the cost of polypropylene geogrids," in *4th Asian Regional Conference on Geosynthetics*, Shanghai, 2008, pp. 74-77.

[26] D. Drummer and A. Seefried, "Thermoformability of radiation cross linked polyamide 12," in *SPE Antec*, Boston, 2011, pp. 2520-2526.

[27] A. Seefried, M. Fuchs, and D. Drummer, "Radiation crosslinking of semicrystalline thermoplastics: a novel approach to modifying a material's thermoformability," *Plastics Engineering,* vol. 68, pp. 14-22, Nov-Dec 2012.

[28] H. C. Lau, S. N. Bhattacharya, and G. J. Field, "Influence of rheological properties on the sagging of polypropylene and ABS sheet for thermoforming applications," *Polymer Engineering and Science,* vol. 40, pp. 1564-1570, Jul 2000.

[29] T. W. Womer, "Optimizing sheet extrusion conditions to minimize internal stresses in thermoformed sheet," *Plastic Film & Sheeting,* vol. 8, pp. 26-38, 1992.

[30] N. J. MacAuley, E. M. A. Harkin-Jones, and W. R. Murphy, "The influence of extrusion parameters on the mechanical properties of polypropylene sheet," *Polymer Engineering and Science,* vol. 38, pp. 662-673, Apr 1998.

[31] G. W. Harron, E. M. A. Harkin-Jones, and P. J. Martin, "An experimental investigation of the plug assist thermoforming process," in *SPE Antec*, Dallas, 2001.

[32] S. Wang, A. Makinouchi, T. Tosa, K. Kidokoro, M. Okamoto, T. Kotaka, *et al.*, "Numerical simulation of acrylonitrile-butadiene-styrene material's vacuum forming process," *Journal of Materials Processing Technology,* vol. 91, pp. 219-225, Jun 1999.

[33] Y. Dong, R. J. T. Lin, and D. Bhattacharyya, "Determination of critical material parameters for numerical simulation of acrylic sheet forming," *Journal of Materials Science,* vol. 40, pp. 399-410, Jan 2005.

[34] J. Levey and J. Pylant, "Selective heating and drawing of plastics," 1962.

[35] H. F. Nied and A. T. Chen, "Method and apparatus for differentially heating and thermoforming a polymer sheet ", 1992

[36] R. Claus, M. Stein, S. Bach, J.-P. Majschak, U. Partsch, and H. Griessmann, "An innovative contact heating method in the thermoforming process," in *Eurotec*, Lyon, France, 2013, pp. 691-697.

[37] B. Neubig and C. Bonten, "Local heating using laser radiation for improved wall thickness distribution of thermoformed parts," in *The 28th international conference of the polymer processing society (PPS-28)*, Pattaya, Thailand, 2012.

[38] B. Neubig and C. Bonten, "Model-based temperature measurement for thermoforming applications," in *SPE Antec*, Orlando, 2015.

[39] R. Modirnia and B. Boulet, "Model-Based virtual sensors and core-temperature observers in thermoforming applications," *Ieee Transactions on Industry Applications,* vol. 49, pp. 721-730, Mar-Apr 2013.

[40] R. C. Progelhof, J. Franey, and T. W. Haas, "Absorption coefficient of unpigmented poly(methyl methacrylate), polystyrene, polycarbonate, and poly(4-methylpentene-1) sheets," *Journal of Applied Polymer Science,* vol. 15, pp. 1803-1807, 1971.

[41] R. C. Progelhof, J. Quintiere, and J. L. Throne, "Temperature distribution in semitransparent plastic sheets exposed to symmetric, unsymmetric, and pulsed radiant heating and surface cooling," *Journal of Applied Polymer Science,* vol. 17, pp. 1227-1252, 1973.

[42] J. E. Cunningham, P. F. Monaghan, M. T. Brogan, and S. F. Cassidy, "Modelling of pre-heating of flat panels prior to press forming," *Composites Part a-Applied Science and Manufacturing,* vol. 28, pp. 17-24, 1997.

[43] J. E. Cunningham, P. F. Monaghan, and M. T. Brogan, "Predictions of the temperature profile within composite sheets during pre-heating," *Composites Part a-Applied Science and Manufacturing,* vol. 29, pp. 51-61, 1998.

[44] S. Monteix, F. Schmidt, Y. Le Maoult, R. Ben Yedder, R. W. Diraddo, and D. Laroche, "Experimental study and numerical simulation of preform or sheet exposed to infrared radiative heating," *Journal of Materials Processing Technology,* vol. 119, pp. 90-97, Dec 2001.

[45] F. M. Schmidt, Y. Le Maoult, and S. Monteix, "Modelling of infrared heating of thermoplastic sheet used in thermoforming process," *Journal of Materials Processing Technology,* vol. 143, pp. 225-231, Dec 2003.

[46] A. Yousefi, A. Bendada, and R. Diraddo, "Improved modeling for the reheat phase in thermoforming through an uncertainty treatment of the key parameters," *Polymer Engineering and Science,* vol. 42, pp. 1115-1129, May 2002.

[47] F. M. Duarte and J. A. Covas, "On the use of the heating stage to control the thickness distribution in thermoformed parts," *International Polymer Processing,* vol. 19, pp. 186-198, Jun 2004.

[48] B. Moore, B. Boulet, N. Aouf, P. Girard, and R. DiRaddo, "Multivariable H-infinity control of the thermoforming reheat process," *Dynamics of Continuous Discrete and Impulsive Systems-Series B-Applications & Algorithms,* pp. 330-335, 2003.

[49] P. Girard, R. DiRaddo, V. Thomson, and B. Boulet, "Advanced in-cycle and cycle-to cycle on-line adaptive control for thermoforming of large thermoplastic sheets," in *SAE World Congress & Exhibition*, Detroit, 2005.

[50] B. Boulet, V. Thomson, P. Girard, R. DiRaddo, and A. Haurani, "On-line adaptive control for thermoforming of large thermoplastic sheets," in *Intelligent Processing and Manufacturing of Materials*, California, 2005.

[51] G. Gauthier, M. Ajersch, B. Boulet, A. Haurani, P. Girard, and R. DiRaddo, "A new absorption based model for sheet reheat in thermoforming," in *SPE Antec*, Boston, 2005, pp. 353-357.

[52] B. Cosson, F. Schmidt, Y. Le Maoult, and M. Bordival, "Infrared heating stage simulation of semi-transparent media (PET) using ray tracing method," *International Journal of Material Forming,* vol. 4, pp. 1-10, Mar 2011.

[53] G. N. Labeas, V. B. Watiti, and C. V. Katsiropoulos, "Thermomechanical simulation of infrared heating diaphragm forming process for thermoplastic parts," *Journal of Thermoplastic Composite Materials,* vol. 21, pp. 353-370, Jul 2008.

[54] S. A. Khan, P. Girard, N. Bhuiyan, and V. Thomson, "Improved mathematical modeling for the sheet reheat phase during thermoforming," *Polymer Engineering and Science,* vol. 52, pp. 625-636, Mar 2012.

[55] J. F. Puehringer and G. Zitzenbacher, "The influence of thermal material properties on the heating step of pipe belling," in *PPS*, Cyprus, 2009.

[56] J. F. Puehringer, G. Zitzenbacher, and C. Spreitzer, "Study of heat absorption in thermoforming for transparent and filled polystyrene," *International Polymer Processing,* vol. 28, pp. 14-23, Mar 2013.

[57] C. A. Taylor, H. G. DeLorenzi, and D. O. Kazmer, "Experimental and numerical investigations of the vacuum-forming process," *Polymer Engineering and Science,* vol. 32, pp. 1163-1173, Aug 1992.

[58] M. J. Parisi, M. E. Ryan, and J. M. Charrier, "Experimental study on the dynamics of thermoforming of polystyrene," *Polymer Engineering and Science,* vol. 34, pp. 102-108, Jan 1994.

[59] A. Aroujalian, M. O. Ngadi, and J. P. Emond, "Effect of processing parameters on compression resistance of plug-assist vacuum thermoformed container," *Advances in Polymer Technology,* vol. 16, pp. 129-134, Sum 1997.

[60] A. Aroujalian, M. O. Ngadi, and J. P. Emond, "Wall thickness distribution in plug-assist vacuum formed strawberry containers," *Polymer Engineering and Science,* vol. 37, pp. 178-182, Jan 1997.

[61] Y. H. Song, K. F. Zhang, F. X. Diao, M. L. Fang, and Z. R. Wang, "Study on the warpage of plastics vacuum-forming process," *Journal of Reinforced Plastics and Composites,* vol. 18, pp. 931-941, 1999.

[62] Z. Ayhan and Q. H. Zhang, "Wall thickness distribution in thermoformed food containers produced by a Benco aseptic packaging machine," *Polymer Engineering and Science,* vol. 40, pp. 1-10, Jan 2000.

[63] J. K. Lee, T. L. Virkler, and C. E. Scott, "Influence of initial sheet temperature on ABS thermoforming," *Polymer Engineering and Science,* vol. 41, pp. 1830-1844, Oct 2001.

[64] P. Collins, P. Martin, E. Harkin-Jones, and D. Laroche, "Experimental investigation of slip in plug-assisted thermoforming," in *SPE Antec*, Dallas, 2001.

[65] P. Collins, E. M. A. Harkin-Jones, and P. J. Martin, "The role of tool/sheet contact in plug-assisted thermoforming," *International Polymer Processing,* vol. 17, pp. 361-369, Dec 2002.

[66] C. Yang and S. W. Hung, "Optimising the thermoforming process of polymeric foams: an approach by using the Taguchi method and the utility concept," *International Journal of Advanced Manufacturing Technology,* vol. 24, pp. 353-360, 2004.

[67] S. J. Liu, "Process optimization of thermoforming PP/CaCO3 composites," *International Polymer Processing,* vol. 14, pp. 98-102, Mar 1999.

[68] M. K. Pettersen, M. Gallstedt, and T. Eie, "Oxygen barrier properties of thermoformed trays manufactured with different drawing methods and drawing depths," *Packaging Technology and Science,* vol. 17, pp. 43-52, Jan-Feb 2004.

[69] A. Tulsian, J. Mead, S. Orroth, and N. Tessier, "Computer simulation of the effect of coefficient of friction in plug assist thermoforming," in *SPE Antec*, Chicago, 2004.

[70] C. Y. Yang and S. W. Hung, "Modeling and optimization of a plastic thermoforming process," *Journal of Reinforced Plastics and Composites,* vol. 23, pp. 109-121, 2004.

[71] P. J. Martin and P. Duncan, "The role of plug design in determining wall thickness distribution in thermoforming," *Polymer Engineering and Science,* vol. 47, pp. 804-813, Jun 2007.

[72] S. C. Chen, S. T. Huang, M. C. Lin, and R. D. Chien, "Study on the thermoforming of PC films used for in-mold decoration," *International Communications in Heat and Mass Transfer,* vol. 35, pp. 967-973, Oct 2008.

[73] R. McCool and P. J. Martin, "The role of process parameters in determining wall thickness distribution in plug-assisted thermoforming," *Polymer Engineering and Science,* vol. 50, pp. 1923-1934, Oct 2010.

[74] M. Labonte and C. Dubois, "Optimization of molding conditions of a plug-assisted thermoformed thin containers in a high speed and volume production context," in *SPE Antec*, Boston, 2011, pp. 2515-2519.

[75] M. Ghobadnam, P. Mosaddegh, M. R. Rejani, H. Amirabadi, and A. Ghaei, "Numerical and experimental analysis of HIPS sheets in thermoforming process," *International Journal of Advanced Manufacturing Technology,* vol. 76, pp. 1079-1089, Feb 2015.

[76] F. Soriano, G. Morales, R. D. de Leon, and F. A. Belmontes, "Thermoformability study of virgin and regrind high impact polystyrene coextruded sheets: influence of the number of processing cycles on the processing parameters," *Polymer Engineering and Science,* vol. 46, pp. 503-509, Apr 2006.

[77] R. A. Morales, M. V. Candal, O. O. Santana, A. Gordillo, and R. Salazar, "Effect of the thermoforming process variables on the sheet friction coefficient," *Materials & Design,* vol. 53, pp. 1097-1103, Jan 2014.

[78] P. J. Martin, R. McCool, C. Harter, and H. L. Choo, "Measurement of polymer-to-polymer contact friction in thermoforming," *Polymer Engineering and Science,* vol. 52, pp. 489-498, Mar 2012.

[79] R. W. Ogden, "Large deformation isotropic elasticity - on the correlation of theory and experiment for incompressible rubberlike solids," *Proceedings of the Royal Society of London Series a-Mathematical and Physical Sciences,* vol. 326, pp. 565-&, 1972 1972.

[80] M. Mooney, "A theory of large elastic deformation," *Journal of Applied Physics,* vol. 11, 1940.

[81] E. M. Arruda and M. C. Boyce, "A three-dimensional model for the large stretch behavior of rubber elastic materials," *Journal of the Mechanics and Physics of Solids,* vol. 41, pp. 389-412, 1993.

[82] B. Bernstein, E. A. Kearsley, and L. J. Zapas, "A study of stress relaxation with finite strain," *Journal of Rheology,* vol. 7, p. 391, 1963.

[83] V. H. Rolon-Garrido and M. H. Wagner, "The damping function in rheology," *Rheologica Acta,* vol. 48, pp. 245-284, Apr 2009.

[84] N. Rosenzweig, M. Narkis, and Z. Tadmor, "Wall thickness distribution in thermoforming," *Polymer Engineering and Science,* vol. 19, pp. 946-951, 1979.

[85] R. J. Crawford and S. K. L. Lui, "Prediction of wall thickness distribution in thermoformed mouldings," *European Polymer Journal,* vol. 18, pp. 699-705, 1982.

[86] H. G. DeLorenzi and H. F. Nied, "Blow molding and thermoforming of plastics: finite element modeling," *Computers & Structures,* vol. 26, pp. 197-206, 1987.

[87] H. F. Nied, C. A. Taylor, and H. G. DeLorenzi, "Three-dimensional finite element simulation of thermoforming," *Polymer Engineering and Science,* vol. 30, pp. 1314-1322, Oct 1990.

[88] H. G. DeLorenzi, H. F. Nied, and C. A. Taylor, "A numerical/experimental approach to software development for thermoforming simulations," *Journal of Pressure Vessel Technology-Transactions of the Asme,* vol. 113, pp. 102-114, Feb 1991.

[89] W. N. Song, F. A. Mirza, and J. Vlachopoulos, "Finite element analysis of inflation of an axisymmetric sheet of finite thickness," *Journal of Rheology,* vol. 35, pp. 93-111, Jan 1991.

[90] G. J. Nam, K. H. Ahn, and J. W. Lee, "Three-dimensional simulation of thermoforming process and its comparison with experiments," *Polymer Engineering and Science,* vol. 40, pp. 2232-2240, Oct 2000.

[91] T. Azdast, A. Doniavi, S. R. Ahmadi, and E. Amiri, "Numerical and experimental analysis of wall thickness variation of a hemispherical PMMA sheet in thermoforming process," *International Journal of Advanced Manufacturing Technology,* vol. 64, pp. 113-122, Jan 2013.

[92] K. Kouba and J. Vlachopoulos, "Modeling of thermoforming and blow moulding," in *International Congress on Rheology*, Brussels, 1992, pp. 374-376.

[93] K. Kouba, O. Bartos, and J. Vlachopoulos, "Computer simulation of thermoforming in complex shapes," *Polymer Engineering and Science,* vol. 32, pp. 699-704, May 1992.

[94] H. G. DeLorenzi and C. A. Taylor, "The role of process parameters in blow molding and correlation of 3-D finite element analysis with experiment," *International Polymer Processing,* vol. 8, pp. 365-374, Dec 1993.

[95] P. Bourgin, I. Cormeau, and T. SaintMatin, "A first step towards the modelling of the thermoforming of plastic sheets," *Journal of Materials Processing Technology,* vol. 54, pp. 1-11, Oct 1995.

[96] B. L. Koziey, M. O. Ghafur, J. Vlachopoulos, and F. A. Mirza, "Computer simulation of thermoforming," in *Composite sheet forming,* D. Bhattacharyya, Ed., ed: Elsevier Science B.V., 1997 pp. 75-89

[97] R. E. Khayat and P. Raducanu, "A coupled boundary/finite-element approach for the three-dimensional simulation of air venting in blow molding and thermoforming," *International Journal for Numerical Methods in Engineering,* vol. 43, pp. 151-174, Sep 1998.

[98] R. DiRaddo, D. Laroche, A. Bendada, and T. Ots, "Optimization of thermoforming with process modelling," in *SPE Antec*, New York City, 1999.

[99] M. J. Stephenson, G. F. Dargush, and M. E. Ryan, "Application of one-dimensional mechanical formulations to model the sagging behavior of a polymer sheet," *Polymer Engineering and Science,* vol. 39, pp. 2199-2221, Nov 1999.

[100] F. Erchiqui, A. Gakwaya, and M. Rachik, "Dynamic finite element analysis of nonlinear isotropic hyperelastic and viscoelastic materials for thermoforming applications," *Polymer Engineering and Science,* vol. 45, pp. 125-134, Jan 2005.

[101] F. Erchiqui, "Finite element analysis of transversely isotropic viscoelastic material for thermoforming process," *Journal of Reinforced Plastics and Composites,* vol. 24, pp. 1229-1246, 2005.

[102] F. Erchiqui, "Thermodynamic approach of inflation process of K-BKZ polymer sheet with respect to thermoforming," *Polymer Engineering and Science,* vol. 45, pp. 1319-1335, Oct 2005.

[103] F. Erchiqui and A. Derdouri, "Experimental and numeric analysis of the behaviour of thermoplastic membranes in abs and hips in the thermoformage process," *Canadian Journal of Chemical Engineering,* vol. 83, pp. 527-536, Jun 2005.

[104] F. Erchiqui, "A new hybrid approach using the explicit dynamic finite element method and thermodynamic law for the analysis of the thermoforming and blow molding processes for polymer materials," *Polymer Engineering and Science,* vol. 46, pp. 1554-1564, Nov 2006.

[105] F. Erchiqui, "A new thermodynamical approach for the simulation of thermoforming process using the quasi-static finite element method," *Journal of Reinforced Plastics and Composites,* vol. 25, pp. 235-261, 2006.

[106] H. Xu, J. Wysocki, D. Kazmer, P. Bristow, B. Landa, J. Riello*, et al.*, "Shrinkage study of thermoformed parts," in *SPE Antec*, New York, 1999.

[107] H. Xu and D. O. Kazmer, "Thermoforming shrinkage prediction," *Polymer Engineering and Science,* vol. 41, pp. 1553-1563, Sep 2001.

[108] P. Collins, J. F. Lappin, E. M. A. Harkin-Jones, and P. J. Martin, "Effects of material properties and contact conditions in modelling of plug assisted thermoforming," *Plastic Rubber and Composites,* vol. 29, pp. 349-359, 2000.

[109] D. Laroche, P. Collins, and P. Martin, "Modelling of the effect of slip in plug-assisted thermoforming," in *SPE Antec*, Dallas, 2001.

[110] J. K. Lee, T. L. Virkler, and C. E. Scott, "Effects of rheological properties and processing parameters on ABS thermoforming," *Polymer Engineering and Science,* vol. 41, pp. 240-261, Feb 2001.

[111] G. Marckmann, E. Verron, and B. Peseux, "Finite element analysis of blow molding and thermoforming using a dynamic explicit procedure," *Polymer Engineering and Science,* vol. 41, pp. 426-439, Mar 2001.

[112] G. Sala, L. Di Landro, and D. Cassago, "A numerical and experimental approach to optimise sheet stamping technologies: polymers thermoforming," *Materials & Design,* vol. 23, pp. 21-39, Feb 2002.

[113] S. A. D. Wiesche, "Industrial thermoforming simulation of automotive fuel tanks," *Applied Thermal Engineering,* vol. 24, pp. 2391-2409, Nov 2004.

[114] R. McCool, P. J. Martin, and E. Harkin-Jones, "Process modelling for control of product wall thickness in thermoforming," *Plastics Rubber and Composites,* vol. 35, pp. 340-347, Oct 2006.

[115] Y. Dong, R. J. T. Lin, and D. Bhattacharyya, "Finite element simulation on thermoforming acrylic sheets using dynamic explicit method," *Polymers & Polymer Composites,* vol. 14, pp. 307-328, 2006.

[116] F. Erchiqui, M. Souli, and R. Ben Yedder, "Nonisothermal finite-element analysis of thermoforming of polyethylene terephthalate sheet: Incomplete effect of the forming stage," *Polymer Engineering and Science,* vol. 47, pp. 2129-2144, Dec 2007.

[117] A. J. Giacomin, A. W. Mix, and O. Mahmood, "Sag in Thermoforming," *Polymer Engineering and Science,* vol. 50, pp. 2060-2068, Oct 2010.

[118] H. M. Baek, A. J. Giacomin, and M. J. Wurz, "Sag in commercial thermoforming," *Aiche Journal,* vol. 60, pp. 1529-1535, Apr 2014.

[119] Y. W. Chang and J. H. Cheng, "Numerical and experimental investigation of polycarbonate vacuum-forming process," *Journal of the Chinese Institute of Engineers,* vol. 36, pp. 831-841, 2013.

[120] A. Makradi, S. Belouettar, S. Ahzi, and S. Puissant, "Thermoforming process of amorphous polymeric sheets: Modeling and finite element simulations," *Journal of Applied Polymer Science,* vol. 106, pp. 1718-1724, Nov 2007.

[121] P. Girard, Z. Benrabah, and H. Mir, "Controlling the forming of thermoplastics through forming power," in *SAE World Congress & Exhibition*, Detroit, 2013.

[122] T. Brepols, I. N. Vladimirov, and S. Reese, "Numerical comparison of isotropic hypo- and hyperelastic-based plasticity models with application to industrial forming processes," *International Journal of Plasticity,* vol. 63, pp. 18-48, Dec 2014.

[123] L. M. Yang, V. P. W. Shim, and C. T. Lim, "A visco-hyperelastic approach to modelling the constitutive behaviour of rubber," *International Journal of Impact Engineering,* vol. 24, pp. 545-560, Jun-Jul 2000.

[124] X. T. Pham, F. Thibault, and L. T. Lim, "Modeling and simulation of stretch blow molding of polyethylene terephthalate," *Polymer Engineering and Science,* vol. 44, pp. 1460-1472, Aug 2004.

[125] L. R. G. Treloar, "Stress-strain data for vulcanised rubber under various types of deformation," *Transactions of the Faraday Society,* vol. 40, pp. 59-70, 1944.

[126] B. Van Mieghem, P. Lava, D. Debruyne, A. Van Bael, and J. Ivens, "Digital image correlation for on-line wall thickness measurements in thick gauge thermoforming," *Key Engineering Materials,* vol. 554-557, pp. 1583-1591, 2013.

[127] B. Van Mieghem, A. Van Bael, and J. Ivens, "Impact assessment of extrusion anisotropy on quality of thermoformed products," in *Composites Week @ Leuven and TEXCOMP-11 Conference*, Leuven, Belgium, 2013, pp. 1-8.

[128] P. J. Martin, T. Keaney, and R. McCool, "Development of a multivariable online monitoring system for the thermoforming process," *Polymer Engineering and Science,* vol. 54, pp. 2815-2823, Dec 2014.

[129] uVuTechnologies. (2014). *ToolVu*. http://www.uvutechnologies.com/

[130] M. A. Sutton, J. Orteu, and H. Schreier, *Image correlation for shape, motion and deformation measurements*: Springer, 2009.

[131] MatchID. (2014). *MatchID3D*. http://www.matchidmbc.be/

[132] P. L. Reu, "Experimental and numerical methods for exact subpixel shifting," *Experimental Mechanics,* vol. 51, pp. 443-452, Apr 2011.

[133] Correlated-Solutions. (2009). *VIC-2D*. http://www.correlatedsolutions.com/

[134] GOM. (2009). *Aramis*. http://www.gom.com

[135] Z. Y. Zhang, "A flexible new technique for camera calibration," *Ieee Transactions on Pattern Analysis and Machine Intelligence,* vol. 22, pp. 1330-1334, Nov 2000.

[136] P. Lava, S. Cooreman, S. Coppieters, M. De Strycker, and D. Debruyne, "Assessment of measuring errors in DIC using deformation fields generated by plastic FEA," *Optics and Lasers in Engineering,* vol. 47, pp. 747-753, Jul-Aug 2009.

[137] B. Pan, K. M. Qian, H. M. Xie, and A. Asundi, "Two-dimensional digital image correlation for in-plane displacement and strain measurement: a review," *Measurement Science and Technology,* vol. 20, Jun 2009.

[138] P. Reu, "All about speckles: speckle size measurement," *Experimental Techniques,* vol. 38, pp. 1-2, Nov-Dec 2014.

[139] P. Reu, "All about speckles: aliasing," *Experimental Techniques,* vol. 38, pp. 1-3, Sep-Oct 2014.

[140] Y. Q. Wang, M. A. Sutton, H. A. Bruck, and H. W. Schreier, "Quantitative error assessment in pattern matching: effects of intensity pattern noise, interpolation, strain and image contrast on motion measurements," *Strain,* vol. 45, pp. 160-178, Apr 2009.

[141] C. A. Sciammarella and J. A. Gilbert, "Strain analysis of a disk subjected to diametral compression by means of holographic interferometry," *Applied Optics,* vol. 12, pp. 1951-1956, 1973 1973.

[142] Y. Y. Hung and H. P. Ho, "Shearography: an optical measurement technique and applications," *Materials Science & Engineering R-Reports,* vol. 49, pp. 61-87, Apr 21 2005.

[143] M. R. Viotti, A. E. Dolinko, G. E. Galizzi, and G. H. Kaufmann, "A portable digital speckle pattern interferometry device to measure residual stresses using the hole drilling technique," *Optics and Lasers in Engineering,* vol. 44, pp. 1052-1066, Oct 2006.

[144] Y. Y. Hung, Y. S. Chen, S. P. Ng, L. Liu, Y. H. Huang, B. L. Luk*, et al.*, "Review and comparison of shearography and active thermography for nondestructive evaluation," *Materials Science & Engineering R-Reports,* vol. 64, pp. 73-112, May 1 2009.

[145] V. J. Parks, "Strain-measurement using grids," *Optical Engineering,* vol. 21, pp. 633-639, 1982 1982.

[146] J. S. Sirkis and T. J. Lim, "Displacement and strain-measurement with automated grid methods," *Experimental Mechanics,* vol. 31, pp. 382-388, Dec 1991.

[147] P. J. Rae, H. T. Goldrein, N. K. Bourne, W. G. Proud, L. C. Forde, and M. Liljekvist, "Measurement of dynamic large-strain deformation maps using an automated fine grid technique," *Optics and Lasers in Engineering,* vol. 31, pp. 113-122, Feb 1999.

[148] H. Chalal, S. Avril, F. Pierron, and F. Meraghni, "Experimental identification of a nonlinear model for composites using the grid technique coupled to the virtual fields method," *Composites Part a-Applied Science and Manufacturing,* vol. 37, pp. 315-325, 2006 2006.

[149] X. Li, Z. Zhang, L. Qin, X. Feng, Z. Feng, L. He*, et al.*, "High strain gradient measurements using modified automated grid technique," *Optics and Lasers in Engineering,* vol. 52, pp. 140-144, Jan 2014.

[150] F. Kreith, R. M. Manglik, and M. S. Bohn, *Principles of heat transfer*, 7 ed. Stamford, USA: Cengage Learning, 2011.

[151] P. Novotny, P. Saha, and K. Kouba, "Fitting of K-BKZ model parameters for the simulation of thermoforming," *International Polymer Processing,* vol. 14, pp. 291-295, Sep 1999.

[152] M. H. Wagner, "Analysis of time-dependent nonlinear stress-growth data for shear and elongational flow of a low-density branched polyethylene melt," *Rheologica Acta,* vol. 15, pp. 136-142, 1976.

[153] M. L. Williams, R. F. Landel, and J. D. Ferry, "The temperature dependence of relaxation mechanisms in amorphous polymers and other glass-forming liquids," *Journal of the American chemical society,* vol. 77, pp. 3701-3707, 1955.

[154] R. G. Larson, *Constitutive equations for polymer melts and solutions.* Butterworths, Boston: Butterworth Publishers, 1988.

[155] M. H. Wagner and A. Demarmels, "A constitutive analysis of extensional flows of polyisobutylene," *Journal of Rheology,* vol. 34, pp. 943-958, Aug 1990.

[156] A. C. Papanastasiou, L. E. Scriven, and C. W. Macosko, "An integral constitutive equation for mixed flows - viscoelastic characterization," *Journal of Rheology,* vol. 27, pp. 387-410, 1983 1983.

[157] J. Nixon and G. H. Menary, "Determining volumetric strain in biaxial deformation of PET at temperatures and strain rates for stretch blow moulding," *Key Engineering Materials,* vol. 651-653, pp. 869-873, 2015.

[158] W. H. Peters and W. F. Ranson, "Digital imaging techniques in experimental stress-analysis," *Optical Engineering,* vol. 21, pp. 427-431, 1982.

[159] W. H. Peters, W. F. Ranson, M. A. Sutton, T. C. Chu, and J. Anderson, "Application of digital correlation methods to rigid body mechanics," *Optical Engineering,* vol. 22, pp. 738-742, 1983.

[160] M. A. Sutton, W. J. Wolters, W. H. Peters, W. F. Ranson, and S. R. McNeill, "Determination of displacements using an improved digital correlation method," *Image and Vision Computing,* vol. 1, pp. 133-139, 1983.

[161] T. C. Chu, W. F. Ranson, M. A. Sutton, and W. H. Peters, "Applications of digital-image-correlation techniques to experimental mechanics," *Experimental Mechanics,* vol. 25, pp. 232-244, 1985.

[162] M. A. Sutton, M. Q. Cheng, W. H. Peters, Y. J. Chao, and S. R. McNeill, "Application of an optimized digital correlation method to planar deformation analysis," *Image and Vision Computing,* vol. 4, pp. 143-150, Aug 1986.

[163] Z. L. Sun, J. S. Lyons, and S. R. McNeill, "Measuring microscopic deformations with digital image correlation," *Optics and Lasers in Engineering,* vol. 27, pp. 409-428, Jul 1997.

[164] H. W. Schreier, J. R. Braasch, and M. A. Sutton, "Systematic errors in digital image correlation caused by intensity interpolation," *Optical Engineering,* vol. 39, pp. 2915-2921, Nov 2000.

[165] J. Brillaud and F. Lagattu, "Limits and possibilities of laser speckle and white-light image-correlation methods: theory and experiments," *Applied Optics,* vol. 41, pp. 6603-6613, 2002.

[166] F. Lagattu, J. Brillaud, and M. C. Lafarie-Frenot, "High strain gradient measurements by using digital image correlation technique," *Materials Characterization,* vol. 53, pp. 17-28, Sep 2004.

[167] B. Pan, A. Asundi, H. Xie, and J. Gao, "Digital image correlation using iterative least squares and pointwise least squares for displacement field and strain field measurements," *Optics and Lasers in Engineering,* vol. 47, pp. 865-874, Jul-Aug 2009.

[168] C. Cofaru, W. Philips, and W. Van Paepegem, "Evaluation of digital image correlation techniques using realistic ground truth speckle images," *Measurement Science & Technology,* vol. 21, May 2010.

[169] C. Cofaru, W. Philips, and W. Van Paepegem, "A novel speckle pattern-Adaptive digital image correlation approach with robust strain calculation," *Optics and Lasers in Engineering,* vol. 50, pp. 187-198, Feb 2012.

[170] M. A. Sutton, S. R. McNeill, J. D. Helm, and Y. J. Chao, "Advances in two-dimensional and three-dimensional computer vision," *Photo-Mechanics,* vol. 77, pp. 323-372, 2000.

[171] S. Avril, M. Bonnet, A.-S. Bretelle, M. Grediac, F. Hild, P. Ienny, *et al.*, "Overview of identification methods of mechanical parameters based on full-field measurements," *Experimental Mechanics,* vol. 48, pp. 381-402, Aug 2008.

[172] P. Lava, S. Cooreman, S. Coppieters, and D. Debruyne, "Sources of systematic errors in the determination of heterogeneous strain fields obtained via DIC," in *SEM Annual Conference*, Indianapolis, Indiana USA, 2010, pp. 271-281.

[173] P. Lava, S. Cooreman, and D. Debruyne, "Study of systematic errors in strain fields obtained via DIC using heterogeneous deformation generated by plastic FEA," *Optics and Lasers in Engineering,* vol. 48, pp. 457-468, Apr 2010.

[174] P. Lava, S. Coppieters, Y. Wang, P. Van Houtte, and D. Debruyne, "Error estimation in measuring strain fields with DIC on planar sheet metal specimens with a non-perpendicular camera alignment," *Optics and Lasers in Engineering,* vol. 49, pp. 57-65, Jan 2011.

[175] I. De Baer, W. Van Paepegem, N. Lammens, P. Lava, D. Debruyne, C. Corafu, *et al.*, "Experimentally induced errors in Digital Image Correlation measurement of small strains with large gradients," in *Emerging Technologies in Non-Destructive Testing V*, C. Press, Ed., ed, 2012, pp. 441-446.

[176] S. Ma, J. Pang, and Q. Ma, "The systematic error in digital image correlation induced by self-heating of a digital camera," *Measurement Science & Technology,* vol. 23, Feb 2012.

[177] P. Lava, W. Van Paepegem, S. Coppieters, I. De Baere, Y. Wang, and D. Debruyne, "Impact of lens distortions on strain measurements obtained with 2D digital image correlation," *Optics and Lasers in Engineering,* vol. 51, pp. 576-584, May 2013.

[178] T. N. Nguyen, J. M. Huntley, R. L. Burguete, and C. R. Coggrave, "Multiple-view shape and deformation measurement by combining fringe projection and digital image correlation," *Strain,* vol. 48, pp. 256-266, Jun 2012.

[179] L. Wittevrongel, P. Lava, S. V. Lomov, and D. Debruyne, "A self adaptive global digital image correlation algorithm," *Experimental Mechanics,* vol. 55, pp. 361-378, Feb 2015.

[180] B. Van Mieghem, R. Appermont, H. Vanhove, J. Duflou, A. Van Bael, and J. Ivens, "Single point incremental formed molds and digital image correlation in heavy gauge thermoforming," in *Eurotec*, Lyon, France, 2013, pp. 713-717.

[181] B. Van Mieghem, F. Desplentere, A. Van Bael, and J. Ivens, "Improvements in thermoforming simulation by use of 3D digital image correlation," *Express Polymer Letters,* vol. 9, pp. 119-128, Feb 2015.

[182] A. Seefried and D. Drummer, "The effects of radiation cross-linking and process parameters on the behavior of polyamide 12 in vacuum thermoforming," *Polymer Engineering and Science,* vol. 52, pp. 884-892, 2012.

[183] D. Lecompte, A. Smits, S. Bossuyt, H. Sol, J. Vantomme, D. Van Hemelrijck*, et al.*, "Quality assessment of speckle patterns for digital image correlation," *Optics and Lasers in Engineering,* vol. 44, pp. 1132-1145, Nov 2006.

[184] D. Lecompte, S. Bossuyt, S. Cooreman, H. Sol, and J. Vantomme, "Study and generation of optimal speckle patterns for DIC," in *SEM Annual conference and exposition on experimental and applied mechanics*, Springfield, Massachusetts, USA, 2007, pp. 1643-1649.

[185] S. Yaofeng and J. H. L. Pang, "Study of optimal subset size in digital image correlation of speckle pattern images," *Optics and Lasers in Engineering,* vol. 45, pp. 967-974, Sep 2007.

[186] B. Pan, H. Xie, Z. Wang, K. Qian, and Z. Wang, "Study on subset size selection in digital image correlation for speckle patterns," *Optics Express,* vol. 16, pp. 7037-7048, May 12 2008.

[187] B. Pan, Z. X. Lu, and H. M. Xie, "Mean intensity gradient: An effective global parameter for quality assessment of the speckle patterns used in digital image correlation," *Optics and Lasers in Engineering,* vol. 48, pp. 469-477, Apr 2010.

[188] T. Hua, H. M. Xie, S. M. Wang, Z. X. Hu, P. W. Chen, and Q. M. Zhang, "Evaluation of the quality of a speckle pattern in the digital image correlation method by mean subset fluctuation," *Optics and Laser Technology,* vol. 43, pp. 9-13, Feb 2011.

[189] S. Craig. (2013) Direct digital UV imaging for deep draw thermoforming. *Thermoforming Quarterly*. 24-26.

[190] Fujifilm. (2014). *Uvijet UV.* http://www.fujifilm.eu/

[191] G. Vendroux and W. G. Knauss, "Submicron deformation field measurements: Part 2. Improved digital image correlation," *Experimental Mechanics,* vol. 38, pp. 86-92, Jun 1998.

[192] J. S. Lyons, J. Liu, and M. A. Sutton, "High-temperature deformation measurements using digital-image correlation," *Experimental Mechanics,* vol. 36, pp. 64-70, Mar 1996.

[193] B. M. B. Grant, H. J. Stone, P. J. Withers, and M. Preuss, "High-temperature strain field measurement using digital image correlation," *Journal of Strain Analysis for Engineering Design,* vol. 44, pp. 263-271, May 2009.

[194] X. Chen, N. Xu, L. X. Yang, and D. Xiang, "High temperature displacement and strain measurement using a monochromatic light illuminated stereo digital image correlation system," *Measurement Science & Technology,* vol. 23, Dec 2012.

[195] M. A. Sutton, J. H. Yan, V. Tiwari, H. W. Schreier, and J. J. Orteu, "The effect of out-of-plane motion on 2D and 3D digital image correlation measurements," *Optics and Lasers in Engineering,* vol. 46, pp. 746-757, Oct 2008.

[196] L. Stroebels, I. Current, J. Compton, and R. D. Zakia, *Basic photographic materials and processes*, 2 ed.: Focal press, 2000.

[197] A. R. Greenleaf, *Photographic optics*. New York: The Macmillan Company, 1950.

[198] R. E. Jacobson, S. F. Ray, G. G. Attridge, and N. R. Axford, *The manual of photography: photographic and digital imaging*, 9 ed.: Focal Press, 2000.

[199] P. Reu, "All about speckles: edge sharpness," *Experimental Techniques,* vol. 39, pp. 1-2, Mar-Apr 2015.

[200] M. A. Biot, *Mechanics of incremental deformations*. London: J. Wiley & Sons, 1964.

[201] L. E. Malvern, *Introduction to the mechanics of a continuous medium*. Englewood Cliffs, New Jersey: Prentice-Hall Inc., 1969.

[202] A. Kaye, R. F. T. Stepto, W. J. Work, J. V. Aleman, and A. Y. Malkin, "Definition of terms relating to the non-ultimate mechanical properties of polymers," *Pure and Applied Chemistry,* vol. 70, pp. 701-754, Mar 1998.

[203] Correlated-Solutions. (2012). *VIC-3D*. http://www.correlatedsolutions.com

[204] GOM. *GOM Inspect (V7.5 ed.)*.

[205] "International vocabulary of metrology - Basic and general concepts and associated terms (VIM)," 2012.

[206] M. Grediac and F. Sur, "Effect of sensor noise on the resolution and spatial resolution of displacement and strain maps estimated with the grid method," *Strain,* vol. 50, pp. 1-27, Feb 2014.

[207] Y. Wang, "Uncertainty quantification of digital image correlation and the impact on material identification," KU Leuven, 2015.

[208] Y. Q. Wang, M. A. Sutton, X. D. Ke, H. W. Schreier, P. L. Reu, and T. J. Miller, "On error assessment in stereo-based deformation measurements - Part I: theoretical developments for quantitative estimates," *Experimental Mechanics,* vol. 51, pp. 405-422, Apr 2011.

[209] X. D. Ke, H. W. Schreier, M. A. Sutton, and Y. Q. Wang, "Error assessment in stereo-based deformation measurements - Part II: experimental validation of uncertainty and bias estimates," *Experimental Mechanics,* vol. 51, pp. 423-441, Apr 2011.

[210] P. L. Reu, "A study of the influence of calibration uncertainty on the global uncertainty for digital image correlation using a Monte Carlo approach," *Experimental Mechanics,* vol. 53, pp. 1661-1680, Nov 2013.

[211] A. Willems, S. V. Lomov, I. Verpoest, D. Vandepitte, P. Harrison, and W. R. Yu, "Forming simulation of a thermoplastic commingled woven textile on a double dome," *International Journal of Material Forming,* vol. 1, pp. 965-968, Apr 2008.

[212] B. Vanleeuw, "Experimental and numerical studies of a flax quasi-unidirectional woven fabric formability," Master of Science, KU Leuven, 2014.

[213] B. Buffel, M. Amerijckx, M. Hamblok, B. Van Mieghem, F. Desplentere, and A. Van Bael, "Experimental and computational analysis of the heating step during thermoforming of thermoplastics," *Key Engineering Materials,* vol. 651-653, pp. 1003-1008, 2015.

[214] R. Courant, K. Friedrichs, and H. Lewy, "On the partial difference equations of mathematical physics," *IBM Journal of Research and Development,* vol. 11, pp. 215-234, 1967.

[215] P. Manselli and K. Miller, "Calculation of the surface temperature and heat flux on one side of a wall from measurements on the opposite side," *Annali di Matematica Pura ed Applicata,* vol. 123, pp. 161-183, 1980.

[216] L. Guo and D. Murio, "A mollified space-marching finite-different algorithm for the two-dimensional inverse heat conduction problem with slab symmetry," *Inverse Problems,* vol. 7, pp. 247-259, 1991.

[217] T. L. Bergman, F. P. Incropera, and A. S. Lavine, *Fundamentals of heat and mass transfer*, 7 ed.: John Wiley & Sons, 2011.

[218] G. Linteris, M. Zammarano, B. Wilthan, and L. Hanssen, "Absorption and reflection of infrared radiation by polymers in fire-like environments," *Fire and Materials,* vol. 36, pp. 537-553, Nov 2012.

[219] H. L. Choo, P. J. Martin, and E. M. A. Harkin-Jones, "Measurement of heat transfer for thermoforming simulations," *International Journal of Material Forming,* vol. 1, pp. 1027-1030, Apr 2008.

[220] M. Baumgaertel and H. H. Winter, "Determination of discrete relaxation and retardation time spectra from dynamic mechanical data," *Rheologica Acta,* vol. 28, pp. 511-519, Nov-Dec 1989.

[221] M. Baumgaertel and H. H. Winter, "Interrelation between continuous and discrete relaxation time spectra," *Journal of Non-Newtonian Fluid Mechanics,* vol. 44, pp. 15-36, Sep 1992.

Appendices

Appendix A - Practical guideline for the application of DIC in thermoforming applications
Appendix B – Characteristic temperatures of thermoformable polymers
Appendix C - Correlation settings used for the various validation examples

Appendix A – Practical guideline for the application of DIC in thermoforming applications

The following is a step by step explanation on how to set-up a system on a thermoforming machine for combined pressure, temperature and deformation measurements. It is outlined as a comprehensive roadmap that gathers the steps that need to be taken to successfully implement the methodology in an industrial environment.

- Download the depth of field and field of view calculator from the Matlab file exchange website (http://www.mathworks.com/matlabcentral/fileexchange/)
- Follow the procedure to characterise the camera/lens combination for DOF/FOV prediction. This needs to be done once for each available camera/lens combination (cf. Section 4.2.4.2).
- Choose the machine, the material and the mould (width, length, height).
- Use the DOF/FOV calculator to define which camera, lens, aperture and starting distance to choose that yields the desired resolution and depth of field.
- Install the cameras at the suggested distance with an inter-camera angle between 10° and 30° to have good sensitivity to out-of-plane motion while maintaining modest perspective differences between corresponding image subsets [130]. However, if large stand-off distances are required and out-of-plane sensitivity is of importance, as is the case in thermoforming, angles of 60° or higher can be employed at the expense of in-plane accuracy.
- Install the pressure measurement in the lower cabinet of the machine.
- Install a thermal measurement system (camera, pyrometer). Take care with the setting of the emissivity and make sure the camera is in focus. For emissivity measurements see Section 3.2.5.2.
- Synchronise the cameras, the temperature and the pressure sensor
- Generate a speckle target (DOF/FOV calculator) based on the camera/lens and starting distance combination. If the subject is moving away from the camera, use a speckle that is larger than the 3 x 3 pixels minimum rule of thumb.
- Print the generated speckle pattern on the sheet: ink suppliers that can deliver highly stretchable inks are EFI and Fujifilm.
- Choose a frame rate and shutter time as function of the rate of deformation. Higher frame rates will result in more stable incremental correlation since the difference between two consecutive pictures will be smaller but comes at the cost of a longer processing time and an increased error since in an incremental approach the errors are summed up. Smaller shutter times will reduce the occurrence of motion blur but will also reduce the amount of incident light. Add or remove light sources until a grey value histogram is achieved with a wide base and no grey values fall outside the dynamic range (see Figure 24 in Section 4.2.2.1).

- Clamp the speckled sheet in the thermoforming machine.
- Focus the cameras on the target using the smallest aperture f-stop number (smallest DOF) and after focussing switch back to the predefined aperture as suggested by the DOF/FOV calculator.
- Take pictures of a calibration target that is approximately 25-35 % smaller than the FOV and that is rotated under different angles. 15 to 25 different pictures are recommended. Run the pictures through a camera calibration software and define the intrinsic and extrinsic camera parameters.
- Take several pictures (10-50) of the static, unheated sheet and perform an image noise evaluation (self-correlation test). Make sure that the noise is as low as possible; values below 1 % are achievable in normal conditions and with decent hardware. To reduce the effect of noise, an averaged image (for both cameras) can be saved and used as the reference picture.
- Take pictures during the heating and forming process.
- Post-process the pictures: load the reference pictures, load the deformed pictures, make sure the correct calibration file is chosen, define the region of interest, the subset size, the step size and the correlation settings. Run the correlation.
- Export the results and plot the desired value from the image correlation against the temperature and pressure results.

When all steps are successfully followed, a similar plot as the one represented in Figure 86 for a bubble inflation process can be drawn.

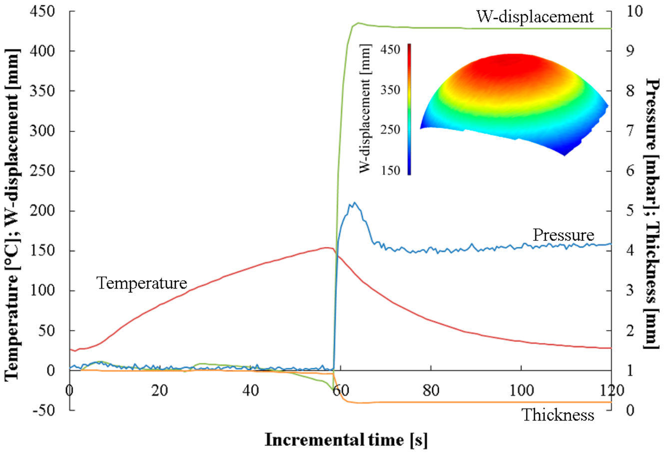

Figure 86 Typical plot containing temperature, displacement, pressure and thickness data of a point in the centre of the bubble inflated with pressure valve setting7. Also the full-field 3D (vertical) W-displacement is represented.

Appendix B – Characteristic temperatures of thermoformable polymers (Table 2.5 from [1])

Polymer	Glass transition temperature (°C)	(°F)	Melt temperature (°C)	(°F)	Heat distortion temperature (0.46 N/mm²/ 66 psi) (°C)	(°F)	Set and mold temperature (°C)	(°F)	Lower forming temperature (°C)	(°F)	Orienting temperature (°C)	(°F)	Normal forming temperature (°C)	(°F)	Upper forming temperature (°C)	(°F)
Amorphous polymers																
Polystyrene	94	200	–	–	68–96	155–204	85	185	127	260	135	275	149	300	182	360
PMMA	100	212	–	–	74–113	165–235	85	185	149	300	163	325	177	350	193	380
PMMA/PVC alloy	105	221	–	–	81	177	79	175	143	290	154	310	171	340	182	360
ABS	88–120	190–248	–	–	77–113	170–235	82	180	127	260	137	280	146	295	182	360
Polycarbonate	150	300	–	–	138	280	132	270	168	335	177	350	191	375	204	400
Rigid PVC	77	170	–	–	57–82	135–180	66	150	104	220	118	245	138	280	154	310
Modified PPO	104–110	219–230	–	–	110	230	99	210	165	325	182	360	188	375	204	400
Polysulfone	190	374	–	–	181	358	163	325	191	375	213	415	246	475	302	575
Polyethersulfone (PES)	230	445	–	–	216	420	204	400	274	525	293	560	316	600	343	650
20% GR PES	225	437	–	–	216	420	210	410	279	535	293	560	316	600	357	675
Polyamide-imide	275	527	–	–	302	575	232	450	357	675	371	700	404	760	427	800
Crystalline polymers																
LOPE	−25	−13	115	239	40–44	104–112	66	150	116	240	129	265	132	270	168	335
EVA	–	–	107	225	62	114	77	170	127	260	138	280	146	295	182	360
HDPE	−110	−166	134	273	79–91	175–196	77	170	127	260	132	270	146	295	182	360
Cellulose acetate	70, 100	158, 212	230	445	52–93	125–200	71	160	127	260	141	285	154	310	182	360
Cellulose butyrate	120	248	140	284	54–108	130–227	79	175	127	260	138	280	146	295	182	360
Cellulose propionate	–	–	190	374	64–121	147–250	88	190	127	260	137	280	146	295	182	360
Polypropylene, homo-	5	41	168	334	107–121	225–250	88	190	132	270	138	280	154–163	310–325	166	330
Polypropylene, co-	−20	−4	150–175	302–347	85–104	185–220	88	190	143	290	177	350	185	365	193	380
40% GR PP	5	41	168	334	166	330	91	195	129	265	141	285	204	400	232	450
Polymethyl pentene	47	117	235	455	85	185	77	170	260	500	274	525	277	530	288	550
PVDC	0	32	160	320	68	155	66	150	163	325	177	350	182	360	199	390
Acrylonitrile	95	203	135	275	78	172	82	180	127	260	137	280	149	300	182	360
PET	70	158	255	490	49	120	77	170	121	250	138	280	149	300	166	330
PBT, neat	−80, 70	−112, 158	245	473	185	365	177	350	260	500	274	525	274	525	288	550
Nylon 6 (PA 6)	58	136	220	428	80	176	91	195	216	420	224	435	227	440	238	460
Nylon 66 (PA 66)	78	169	255	491	105	221	104	220	249	480	260	500	274	525	288	550
POM, copolymer	−55	−67	165	329	110–125	230–257	99	210	163	325	177	350	182	360	204	400
30% GR POM	−50	−58	166	331	163	325	104	220	163	325	177	350	182	360	204	400
PTFE	−55	−67	327	621	46	115	99	210	234	435	249	480	260	500	282	540
FEP	−55	−67	275	527	70	158	149	300	232	450	246	475	260	500	279	535
PEEK	100, 149	212, 300	334	633	140	284	160	320	399	750	413	775	418	785	427	800
Foams																
Polystyrene foam	70–85	158–185	–	–	55–65	131–149	50	122	88	190	96	205	104	220	113	235
Rigid PVC foam	70	158	–	–	65	149	66	150	110	230	124	255	143	290	171	340

Appendix C – Correlation settings

Correlation settings used for the validation of the printed vs. the sprayed patterns (Section 4.2.1.3), the effect of changing light and the application of the equalisation function (Section 4.2.2.2) and the depth of field tests (Section 4.2.4.2)

Technique used	**2D Digital Image Correlation**
Camera brand	Allied Vision Technologies
Camera type	Stingray F-201B
Lens focal length [mm]	25
Aperture f-stop number	f/1.4
Approximated distance to target [mm]	150 / 300 / 500
Field of view [mm]	42 x 32 / 85 x 64 / 142 x 107
Depth of field [mm]	0.4 / 1.9 / 5.6
Pixel resolution as function of FOV [px/mm]	37.5 / 18.75 / 11.2
Noise Camera 0 [%]	<0.76%
Noise Camera 1 [%]	N/A
Pre-Filtering	Gaussian – Kernel 5
Subset [px * px]	58
Step [px]	9
Correlation criterion	ZNSSD
Shape function	Affine
Stereo shape function	N/A
Interpolation function	Bicubic polynomial
Correlation threshold	0.9
Progress history	Spatial + update reference
Number of measurement points	19965 (5984 Histeq)
Total number of images	Various
Pixel to mm conversion [mm/px]	N/A
Displacement	
Spatial resolution [px]	58
Spatial resolution [mm]	N/A
In-plane resolution [mm]	0.0048 (300mm)
Out-of-plane resolution [mm]	NA
Strain	
Smoothing method	Bilinear quadrilateral
Strain tensor	Log. Euler-Almansi
Strain window [px]	15
Virtual strain gauge [px]	127
Virtual strain gauge [mm]	N/A
Spatial resolution [px]	184
Spatial resolution [mm]	N/A
Resolution [µm/m]	43 (300mm)

Correlation settings used for the characterisation of the heat waves (Section 4.2.3.1)

Technique used	**2D Digital Image Correlation**
Camera brand	Allied Vision Technologies
Camera type	Stingray F-201B
Lens focal length [mm]	25
Aperture f-stop number	f/1.4
Approximated distance to target [mm]	1200
Field of view [mm]	341 x 256
Depth of field [mm]	33
Pixel resolution as function of FOV [px/mm]	4.7
Noise Camera 0 [%]	<0.79%
Noise Camera 1 [%]	N/A
Pre-Filtering	Gaussian – Kernel 5
Subset [px * px]	21
Step [px]	10
Correlation criterion	ZNSSD
Shape function	Affine
Stereo shape function	N/A
Interpolation function	Bicubic polynomial
Correlation threshold	0.9
Progress history	Spatial
Number of measurement points	10780
Total number of images	50
Pixel to mm conversion [mm/px]	N/A
Displacement	
Spatial resolution [px]	21
Spatial resolution [mm]	N/A
In-plane resolution [mm]	0.0131
Out-of-plane resolution [mm]	NA
Strain	
Smoothing method	Bilinear quadrilateral
Strain tensor	Log. Euler-Almansi
Strain window [px]	10
Virtual strain gauge [px]	91
Virtual strain gauge [mm]	N/A
Spatial resolution [px]	111
Spatial resolution [mm]	N/A
Resolution [µm/m]	83

Correlation settings used for the validation of the thickness calculation (Section 4.2.5.2)

Technique used	**Stereo Digital Image Correlation**
Camera brand	Allied Vision Technologies
Camera type	Stingray F-201B
Lens focal length [mm]	25
Aperture f-stop number	f/8
Approximated distance to target [mm]	1190
Field of view [mm]	338 x 254
Depth of field [mm]	185
Pixel resolution as function of FOV [px/mm]	4.7
Noise Camera 0 [%]	<0.80%
Noise Camera 1 [%]	<0.85%
Pre-Filtering	Gaussian – Kernel 5
Subset [px * px]	21
Step [px]	3
Correlation criterion	ZNSSD
Shape function	Affine
Stereo shape function	Affine
Interpolation function	Bicubic polynomial
Correlation threshold	0.9
Progress history	Spatial + update reference
Number of measurement points	119556
Total number of images	41
Pixel to mm conversion [mm/px]	0.228
Displacement	
Spatial resolution [px]	21
Spatial resolution [mm]	4.788
In-plane resolution [mm]	0.0014
Out-of-plane resolution [mm]	0.0173
Strain	
Smoothing method	Bilinear quadrilateral
Strain tensor	Log. Euler-Almansi
Strain window [px]	9
Virtual strain gauge [px]	25
Virtual strain gauge [mm]	5.7
Spatial resolution [px]	45
Spatial resolution [mm]	10.26
Resolution [µm/m]	359

Correlation settings used for the validation of the clamping quality and the extrusion anisotropy (Section 5.2)

Technique used	**Stereo Digital Image Correlation**
Camera brand	Allied Vision Technologies
Camera type	Stingray F-201B
Lens focal length [mm]	25
Aperture f-stop number	f/8
Approximated distance to target [mm]	1190
Field of view [mm]	338 x 254
Depth of field [mm]	185
Pixel resolution as function of FOV [px/mm]	4.7
Noise Camera 0 [%]	<0.80%
Noise Camera 1 [%]	<0.85%
Pre-Filtering	Gaussian – Kernel 5
Subset [px * px]	21
Step [px]	10
Correlation criterion	ZNSSD
Shape function	Affine
Stereo shape function	Affine
Interpolation function	Bicubic polynomial
Correlation threshold	0.9
Progress history	Spatial + update reference
Number of measurement points	10780
Total number of images	+/-45
Pixel to mm conversion [mm/px]	0.228
Displacement	
Spatial resolution [px]	21
Spatial resolution [mm]	4.788
In-plane resolution [mm]	0.0014
Out-of-plane resolution [mm]	0.0173
Strain	
Smoothing method	Bilinear quadrilateral
Strain tensor	Log. Euler-Almansi
Strain window [px]	10
Virtual strain gauge [px]	91
Virtual strain gauge [mm]	20.748
Spatial resolution [px]	111
Spatial resolution [mm]	25.308
Resolution [µm/m]	46

Correlation settings used for sagging and the influence of subset, step and strain window size (Section 5.3.1.5).

Technique used	**Stereo Digital Image Correlation**
Camera brand	Allied Vision Technologies
Camera type	Stingray F-201B
Lens focal length [mm]	8
Aperture f-stop number	f/2
Approximated distance to target [mm]	1200
Field of view [mm]	1063 x 798
Depth of field [mm]	482
Pixel resolution as function of FOV [px/mm]	1.5
Noise Camera 0 [%]	<0.70%
Noise Camera 1 [%]	<0.70%
Pre-Filtering	Gaussian – Kernel 5
Subset [px * px]	21
Step [px]	1, 5, 10
Correlation criterion	ZNSSD
Shape function	Affine
Stereo shape function	Affine
Interpolation function	Bicubic polynomial
Correlation threshold	0.9
Progress history	Spatial
Number of measurement points	344974, 13752, 3468
Total number of images	2
Pixel to mm conversion [mm/px]	0.63
Displacement	
Spatial resolution [px]	21
Spatial resolution [mm]	13.23
In-plane resolution [mm]	0.0049
Out-of-plane resolution [mm]	0.021
Strain	
Smoothing method	Bilinear quadrilateral
Strain tensor	Log. Euler-Almansi
Strain window [px]	From 3 to 491
Virtual strain gauge [px]	From 3 to 491
Virtual strain gauge [mm]	From 1.89 to 309.33
Spatial resolution [px]	From 23 to 511
Spatial resolution [mm]	From 14.49 to 321.93
Resolution [µm/m]	59

Correlation settings used for the validation of (a)symmetric heating, transfer and cooling (Section 5.3) and for sag compensation (Section 5.4.1)

Technique used	Stereo Digital Image Correlation
Camera brand	Allied Vision Technologies
Camera type	Stingray F-201B
Lens focal length [mm]	8
Aperture f-stop number	f/2
Approximated distance to target [mm]	1200
Field of view [mm]	1063 x 798
Depth of field [mm]	482
Pixel resolution as function of FOV [px/mm]	1.5
Noise Camera 0 [%]	<0.72%
Noise Camera 1 [%]	<0.77%
Pre-Filtering	Gaussian – Kernel 5
Subset [px * px]	21
Step [px]	10
Correlation criterion	ZNSSD
Shape function	Affine
Stereo shape function	Affine
Interpolation function	Bicubic polynomial
Correlation threshold	0.9
Progress history	Spatial + update reference
Number of measurement points	3562
Total number of images	426
Pixel to mm conversion [mm/px]	0.63
Displacement	
Spatial resolution [px]	21
Spatial resolution [mm]	13.23
In-plane resolution [mm]	0.0037
Out-of-plane resolution [mm]	0.0564
Strain	
Smoothing method	Bilinear quadrilateral
Strain tensor	Log. Euler-Almansi
Strain window [px]	10
Virtual strain gauge [px]	91
Virtual strain gauge [mm]	57.33
Spatial resolution [px]	111
Spatial resolution [mm]	69.93
Resolution [µm/m]	50

Correlation settings used for bubble inflation and forming with and without inflation (Section 5.4.2).

Technique used	**Stereo Digital Image Correlation**
Camera brand	Allied Vision Technologies
Camera type	Stingray F-201B
Lens focal length [mm]	8
Aperture f-stop number	f/2
Approximated distance to target [mm]	1200
Field of view [mm]	1063 x 798
Depth of field [mm]	482
Pixel resolution as function of FOV [px/mm]	1.5
Noise Camera 0 [%]	<0.70%
Noise Camera 1 [%]	<0.70%
Pre-Filtering	Gaussian – Kernel 5
Subset [px * px]	21
Step [px]	3
Correlation criterion	ZNSSD
Shape function	Affine
Stereo shape function	Affine
Interpolation function	Bicubic polynomial
Correlation threshold	0.9
Progress history	Spatial
Number of measurement points	Around 45000
Total number of images	From 20 to 120
Pixel to mm conversion [mm/px]	0.63
Displacement	
Spatial resolution [px]	21
Spatial resolution [mm]	13.23
In-plane resolution [mm]	0.0049
Out-of-plane resolution [mm]	0.021
Strain	
Smoothing method	Bilinear quadrilateral
Strain tensor	Log. Euler-Almansi
Strain window [px]	10
Virtual strain gauge [px]	28
Virtual strain gauge [mm]	17.64
Spatial resolution [px]	48
Spatial resolution [mm]	30.24
Resolution [µm/m]	59

Correlation settings used for DIC measurements during forming of the washbasin (Section 5.5.1).

Technique used	**Stereo Digital Image Correlation**
Camera brand	Allied Vision Technologies
Camera type	Stingray F-201B
Lens focal length [mm]	25
Aperture f-stop number	f/4
Approximated distance to target [mm]	2000
Field of view [mm]	567 x 425
Depth of field [mm]	264
Pixel resolution as function of FOV [px/mm]	2.8
Noise Camera 0 [%]	<0.65%
Noise Camera 1 [%]	<0.65%
Pre-Filtering	Gaussian – Kernel 5
Subset [px * px]	40
Step [px]	6
Correlation criterion	ZNSSD
Shape function	Affine
Stereo shape function	Affine
Interpolation function	Bicubic polynomial
Correlation threshold	0.9
Progress history	Spatial + update reference
Number of measurement points	40274
Total number of images	110
Pixel to mm conversion [mm/px]	0.36
Displacement	
Spatial resolution [px]	40
Spatial resolution [mm]	14.4
In-plane resolution [mm]	0.0081
Out-of-plane resolution [mm]	0.04
Strain	
Smoothing method	Bilinear quadrilateral
Strain tensor	Log. Euler-Almansi
Strain window [px]	10
Virtual strain gauge [px]	55
Virtual strain gauge [mm]	19.8
Spatial resolution [px]	94
Spatial resolution [mm]	33.84
Resolution [µm/m]	75

List of publications

The following is an overview of contributions to papers that are related to thermoforming.

IT (Articles in internationally reviewed academic journals)

Van Mieghem, B., Desplentere, F., Van Bael, B., Ivens, J. (2015). Improvements in thermoforming simulation by use of 3D digital image correlation. Express Polymer Letters, 9 (2), 119-128.

Pazmino, J., Carvelli, V., Lomov, S., Van Mieghem, B., Lava, P. (2014). 3D digital image correlation measurements during shaping of a non-crimp 3D orthogonal woven E-glass reinforcement. International Journal of Material Forming, 7 (4), 439-446.

Van Mieghem, B., Ivens, J., Van Bael, A. Consistency of strain fields and thickness reduction in thermoforming experiments through 3D DIC. Experimental Techniques. (submitted for publication in 2015).

AT-p (Articles in other professionally oriented journals)

Van Mieghem, B., Hamblok, M., Van Bael, A., Buffel, B., Amerijckx, M., Desplentere, F., Ivens, J. (2015). On the potential of stereo digital image correlation in thermoforming. Thermoforming Quarterly, 34 (2), 20-28.

Van Mieghem, B., Appermont, R. (2014). Pressing concerns. Film and Sheet Extrusion (March), 11-14.

Appermont, R., Van Mieghem, B., Van Bael, A., Vanhove, H., Duflou, J., Ivens, J. (2013). Sneller thermovormen met minder energie!. Visie op Kunststof, 3 (4), 26-27.

IC (Papers at international scientific conferences and symposia, published in full in proceedings)

Buffel, B., Amerijckx, M., Hamblok, M., Van Mieghem, B., Desplentere, F., Van Bael, A. (2015). Experimental and computational analysis of the heating step during thermoforming of thermoplastics. Key Engineering Materials: Vol. 651-653. ESAFORM 2015, Annual Conference on Material Forming. Graz, Austria, 15-17 April 2015 (pp. 1003-1008) Trans Tech Publications.

Van Mieghem, B., Hamblok, M., Van Bael, A., Buffel, B., Amerijckx, M., Desplentere, F., Ivens, J. (2015). On the potential of stereo digital image correlation in thermoforming. ANTEC 2015. ANTEC. Orlando, 23-25 March 2015 (pp. 2665-2672) Society of Plastics Engineers.

Van Mieghem, B., Appermont, R., Vanhove, H., Duflou, J., Van Bael, A., Ivens, J. (2013). Single point incremental formed molds and digital image correlation in heavy gauge thermoforming. EUROTEC 2013 - Proceedings of the 2nd European Technical Conference & Exhibition. Eurotec. Lyon, France, 04-05 July 2013 (pp. 713-717) Society of Plastics Engineers.

Van Mieghem, B., Van Bael, A., Ivens, J. (2013). Impact assessment of extrusion anisotropy on quality of thermoformed products. In Lomov, S. (Ed.), Composites Week @ Leuven and TEXCOMP-11 Conference. Composites Week @ Leuven. Leuven, Belgium, 16-20 September 2013 (art.nr. PB8) (pp. 1-8).

Van Mieghem, B., Lava, P., Debruyne, D., Van Bael, A., Ivens, J. (2013). Digital image correlation for on-line wall thickness measurements in thick gauge thermoforming. Key Engineering Materials: Vol. 554-557. ESAFORM 2013, Annual Conference on Material Forming. Aveiro, Portugal, 22-24 April 2013 (pp. 1583-1591) Trans Tech Publications.

Appermont, R., Van Mieghem, B., Van Bael, A., Bens, J., Ivens, J., Vanhove, H., Behera, A., Duflou, J. (2012). Sheet-metal based molds for low-pressure processing of thermoplastics. In Cardon, L. (Ed.), Proceedings of the 5th Bi-Annual PMI Conference: Vol. 5. Polymers and Mould Innovations Conference. University College Ghent, Belgium, 12-14 September 2012 (art.nr. 74) (pp. 383-388). Ghent: University College Ghent.

IMa (Meeting abstracts, presented at international scientific conferences and symposia, published or not published in proceedings or journals)

Van Mieghem, B., Desplentere, F., Van Bael, A., Ivens, J. (2014). Improvements in heavy gauge thermoforming simulation by use of 3D digital image correlation. European Thermoforming Conference. Prague, Czech Republic, 03-04 April 2014.

Van Mieghem, B., Lava, P., Debruyne, D., Ivens, J., Van Bael, A. (2014). Consistency of strain fields and thickness reduction in thermoforming experiments through 3D DIC. International conference on experimental mechanics. Cambridge, 07-11 July 2014.

Van Mieghem, B., Van Bael, A., Ivens, J. (2013). An intelligent experimental approach for the optimisation of the process parameters for the thermoforming of plastics and composites. KU Leuven MRC - Annual Research Meeting 2013. Leuven, Belgium, 26 February 2013.

IMa-p (Meeting abstracts, presented at international professionally oriented conferences and symposia, published or not published in proceedings or journals)

Van Mieghem, B., Appermont, R., Bens, J., Vanhove, H., Duflou, J., Ivens, J., Van Bael, A. (2012). Metaalplaatgebaseerde matrijzen voor lagedrukvormgevings-technieken van kunststoffen en composieten. Kunststoffen 2012. Veldhoven, The Netherlands, 26-27 September 2012

WP (Science popularisation)

Van Mieghem, B., Appermont, R., Bens, J., Vanhove, H., Duflou, J., Ivens, J., Van Bael, A. (2012). Een kunststofmatrijs van dunne plaat. Vraag en Aanbod, 38 (59), 15.

Curriculum vitae

Contact information

Name: Bart Van Mieghem

Working address: Wetenschapspark 27
3590 Diepenbeek
Belgium

Tel.: +32(0)11/278825

Fax.: +32(0)11/278826

E-mail: bart.vanmieghem@kuleuven.be

Personal information

Place - Date of birth: Merksem, Belgium - 17/09/1981

Marital status: Married

Children: 3

Work related interests: Polymers, thermoforming, composites, engineering, R&D, FEA

Personal interests: Traveling, movies, wine

Education

2004 - 2005	Master of Science Industrial polymer processing *KHBO – Oostende, Belgium* Thesis: “Properties positioning of new polyolefins versus styrenic based polymers” Graduated magna cum laude
2000 - 2004	Master of Science in Industrial Engineering *De Nayer Instituut – Sint-Katelijne-Waver, Belgium* Thesis: “Development of wear test for injection moulding moulds” Graduated cum laude

Working experience

Sep. 2011 – Present	KU Leuven, Technology Campus Diepenbeek, Belgium PhD student in Engineering Technology *Thesis:* An intelligent experimental approach for the optimisation of the process parameters for the thermoforming of plastics and composites.

Jan. 2011 – Aug. 2011	KU Leuven, Technology Campus Diepenbeek, Belgium Project Engineer polymer department *Main activities / responsibilities:* Project engineer in the TEchnology TRAnsfer (TETRA) project: “Sheet metal based moulds for low-pressure processing of plastics and composites”. Responsible for the thermoforming part of the project.
May 2006 – Dec. 2010	Helvoet Pharma, Alken, Belgium Project Engineer *Main activities / responsibilities:* Helvoet Pharma, now a division in the Swiss Datwyler group is one of the biggest pharmaceutical sealing solution providers worldwide. My task was to manage infrastructural and production related projects by determining the most effective way to use the basic factors of production – people, machines, materials, information and energy. This was done in close collaboration with the purchasing, quality and R&D department and with respect to budget and planning.
Aug. 2005 – April 2006	Materialise, Leuven, Belgium Project Manager Industrial services *Main activities / responsibilities:* Materialise is a world leading company in the field of 3D rapid manufacturing. My role as a project manager was to: capture technical needs of customers and advise on the best possible solution, manage projects within budget, time-schedule and quality requirements and define corrective actions on complaints.

FACULTY OF ENGINEERING TECHNOLOGY
TECHNOLOGY CAMPUS DIEPENBEEK
Technology Cluster Materials Technology
Cel Kunststoffen - Wetenschapspark 27
B-3590 DIEPENBEEK, BELGIUM
tel: +32 11 27 88 25
bart.vanmieghem@kuleuven.be
www.kuleuven.be/kunststoffen